U.S. Department
of Transportation
Federal Railroad
Administration

Office of Research,
Development and Technology
Washington, DC 20590

Side Impact Test and Analyses of a DOT-113 Surrogate Tank Car with Water

DOT/FRA/ORD-21/35

Final Report | December 2021

REPORT DOCUMENTATION PAGE

Form Approved
OMB No. 0704-0188

1. REPORT DATE *(DD-MM-YYYY*	**2. REPORT TYPE**	**3. DATES COVERED** *(From - To)*
December 2021	Technical Report	June 2020

4. TITLE AND SUBTITLE

Side Impact Test and Analyses of a DOT-113 Surrogate Tank Car with Water

5a. CONTRACT NUMBER
DTFR53-11-D-00008

5b. GRANT NUMBER

5c. PROGRAM ELEMENT NUMBER

6. AUTHOR(S)
Nicholas Wilson* – 0000-0003-1140-7108
Michael Carolan** – 0000-0002-8758-5739
Shawn Trevithick* – 0000-0001-6155-5526
Shaun Eshraghi** – 0000-0002-8152-0838

5d. PROJECT NUMBER

5e. TASK NUMBER
Task Order 008

5f. WORK UNIT NUMBER

7. PERFORMING ORGANIZATION NAME(S) AND ADDRESS(ES)
*Transportation Technology Center, Inc.
55500 DOT Road, Pueblo, CO 81001-0130
**Volpe National Transportation Systems Center
55 Broadway, Cambridge, MA 02142

8. PERFORMING ORGANIZATION REPORT NUMBER

9. SPONSORING/MONITORING AGENCY NAME(S) AND ADDRESS(ES)
U.S. Department of Transportation
Federal Railroad Administration
Office of Railroad Policy and Development
Office of Research, Development and Technology
Washington, DC 20590

10. SPONSOR/MONITOR'S ACRONYM(S)

11. SPONSOR/MONITOR'S REPORT NUMBER(S)
DOT/FRA/ORD-21/35

12. DISTRIBUTION/AVAILABILITY STATEMENT
This document is available to the public through the FRA website.

13. SUPPLEMENTARY NOTES
COR: Francisco González, III

14. ABSTRACT

The Federal Railroad Administration (FRA) conducted a side impact test of a surrogate DOT-113 tank car at Transportation Technology Center, Inc. (TTCI) to evaluate its performance under dynamic impact conditions and to provide data for the verification and refinement of a computational model. The tank car surrogate was filled with water to approximately 82.4 percent of its volume, then sealed and pressurized to approximately 50 psig. The tank car surrogate was impacted by a 297,200-pound ram car traveling at 17.3 mph fitted with a 12-inch by 12-inch indenter. The ram car impacted the tank car 2 feet off-center toward the A-End. The tank car was not punctured.
The Volpe National Transportation Systems Center (Volpe) performed pre-test finite element (FE) modeling to estimate the overall response of the tank to the impact. The pre-test models gave results that were in reasonable agreement with the test results. After the test, the pre-test FE model was updated to represent the measured speed of the ram car, resulting in excellent agreement with the measured test data.
The overall goal of the DOT-113 side impact test series is to analyze the side impact performance of a DOT-113 tank car carrying liquefied natural gas (LNG) under typical service conditions.

15. SUBJECT TERMS
Impact test, prototype DOT-113 tank car, tank car performance, transportation safety, hazardous materials, surrogate

16. SECURITY CLASSIFICATION OF:			**17. LIMITATION OF ABSTRACT**	**18. NUMBER OF PAGES**	**19a. NAME OF RESPONSIBLE PERSON**
a. REPORT	**b. ABSTRACT**	**c. THIS PAGE**			Francisco González, III
Unclassified	Unclassified	Unclassified		200	**19b. TELEPHONE NUMBER** *(Include area code)* 202-689-4316

Standard Form 298 (Rev. 8/98)
Prescribed by ANSI Std. Z39.18

METRIC/ENGLISH CONVERSION FACTORS

ENGLISH TO METRIC

LENGTH (APPROXIMATE)

1 inch (in)	=	2.5 centimeters (cm)
1 foot (ft)	=	30 centimeters (cm)
1 yard (yd)	=	0.9 meter (m)
1 mile (mi)	=	1.6 kilometers (km)

AREA (APPROXIMATE)

1 square inch (sq in, in^2)	=	6.5 square centimeters (cm^2)
1 square foot (sq ft, ft^2)	=	0.09 square meter (m^2)
1 square yard (sq yd, yd^2)	=	0.8 square meter (m^2)
1 square mile (sq mi, mi^2)	=	2.6 square kilometers (km^2)
1 acre = 0.4 hectare (he)	=	4,000 square meters (m^2)

MASS - WEIGHT (APPROXIMATE)

1 ounce (oz)	=	28 grams (gm)
1 pound (lb)	=	0.45 kilogram (kg)
1 short ton = 2,000 pounds (lb)	=	0.9 tonne (t)

VOLUME (APPROXIMATE)

1 teaspoon (tsp)	=	5 milliliters (ml)
1 tablespoon (tbsp)	=	15 milliliters (ml)
1 fluid ounce (fl oz)	=	30 milliliters (ml)
1 cup (c)	=	0.24 liter (l)
1 pint (pt)	=	0.47 liter (l)
1 quart (qt)	=	0.96 liter (l)
1 gallon (gal)	=	3.8 liters (l)
1 cubic foot (cu ft, ft^3)	=	0.03 cubic meter (m^3)
1 cubic yard (cu yd, yd^3)	=	0.76 cubic meter (m^3)

TEMPERATURE (EXACT)

[(x-32)(5/9)] °F = y °C

METRIC TO ENGLISH

LENGTH (APPROXIMATE)

1 millimeter (mm)	=	0.04 inch (in)
1 centimeter (cm)	=	0.4 inch (in)
1 meter (m)	=	3.3 feet (ft)
1 meter (m)	=	1.1 yards (yd)
1 kilometer (km)	=	0.6 mile (mi)

AREA (APPROXIMATE)

1 square centimeter (cm^2)	=	0.16 square inch (sq in, in^2)
1 square meter (m^2)	=	1.2 square yards (sq yd, yd^2)
1 square kilometer (km^2)	=	0.4 square mile (sq mi, mi^2)
10,000 square meters (m^2)	=	1 hectare (ha) = 2.5 acres

MASS - WEIGHT (APPROXIMATE)

1 gram (gm)	=	0.036 ounce (oz)
1 kilogram (kg)	=	2.2 pounds (lb)
1 tonne (t)	=	1,000 kilograms (kg)
	=	1.1 short tons

VOLUME (APPROXIMATE)

1 milliliter (ml)	=	0.03 fluid ounce (fl oz)
1 liter (l)	=	2.1 pints (pt)
1 liter (l)	=	1.06 quarts (qt)
1 liter (l)	=	0.26 gallon (gal)
1 cubic meter (m^3)	=	36 cubic feet (cu ft, ft^3)
1 cubic meter (m^3)	=	1.3 cubic yards (cu yd, yd^3)

TEMPERATURE (EXACT)

[(9/5) y + 32] °C = x °F

QUICK INCH - CENTIMETER LENGTH CONVERSION

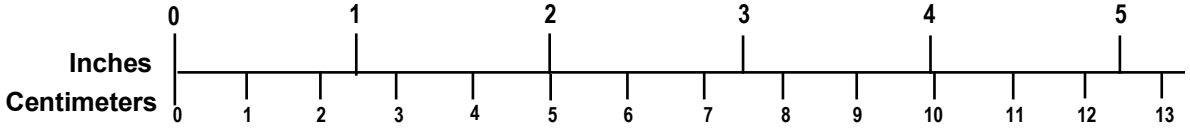

QUICK FAHRENHEIT - CELSIUS TEMPERATURE CONVERSIO

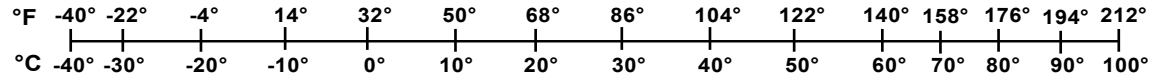

For more exact and or other conversion factors, see NIST Miscellaneous Publication 286, Units of Weights and Measures. Price $2.50 SD Catalog No. C13 10286

Updated 6/17/98

Acknowledgements

The authors of this report gratefully acknowledge the cooperation and assistance of Hector Villarreal and Devangkumar Patel of Taylor-Wharton Americas in providing engineering drawings and design information for the DOT-113 tank car surrogate used in this test. The authors also gratefully acknowledge the assistance provided by A.D. McKisic of Trinity Rail in obtaining design information and material test data for the outer tank of the tank car surrogate used in this test.

The authors of this report gratefully acknowledge the technical assistance of the Volpe National Transportation Systems Center's (Volpe) Senior Engineer Benjamin Perlman. Volpe's Mechanical Engineer Aswani Krishnamurthy assisted with developing and executing the finite element models described in this report. Additionally, inputs from Francisco González, III of the Federal Railroad Administrations (FRA) Office of Research, Development and Technology were valuable in developing this testing program. The authors also gratefully acknowledge technical discussions and assistance in developing the testing plan from Mark Maday and Dr. Phani Raj of FRA's Office of Railroad Safety, and Leonard Majors and Alex Cheng of Pipeline and Hazardous Materials Safety Administration (PHMSA) Office of Engineering. The authors also gratefully acknowledge technical discussions held with PHMSA's Associate Administrator for Hazardous Materials Safety William Schoonover.

Contents

Illustrations

Tables

Equations

Executive Summary

The tests and analyses described in this report support the overall objective of the Federal Railroad Administration's (FRA) research program to improve transportation safety for tank cars. This report documents the combined efforts of Transportation Technology Center, Inc. (TTCI) and the Volpe National Transportation Systems Center (Volpe) to test and analyze the side impact puncture performance of a surrogate DOT-113 tank car. This was the second test in a planned series of four tests on DOT-113 tank cars.

FRA conducted the impact test on June 11, 2020, at the Transportation Technology Center (TTC) to evaluate the performance of the tank car surrogate and to provide data for the verification and refinement of a computational model. All test requirements were met. Volpe performed pre-test and post-test analyses of the impact response to evaluate, validate, and improve the puncture modeling capabilities.

The tank car surrogate was filled with water to approximately 82.4 percent of its volume (i.e., 17.6 percent outage), then sealed and pressurized to approximately 50 psig to replicate the conditions used in the first test of a legacy DOT-113 tank car conducted on November 19, 2019. The target test speed for the June 2020 test was 17.2 mph ± 0.5 mph to be close to but not less than the November 2019 test speed of 16.7 mph.

The tank car surrogate was impacted by a 297,200-pound ram car traveling at 17.3 mph fitted with a 12-inch by 12-inch indenter. The impact resulted in a significant amount of deformation but did not puncture the inner or outer tank of the tank car surrogate. Pre-test finite element (FE) modeling was used to estimate the overall response of the tank car surrogate to the impact for test planning. After the test, the pre-test FE model was updated to represent the measured speed of the ram car, resulting in excellent agreement with the measured test data. The FE model analyses predicted that a speed near 19.5 mph would be necessary to puncture the tank car surrogate given the test conditions.

The results and lessons learned from the material characterization and FE model validation from this test will be applied during the next test in the DOT-113 tank car side impact test series that will feature a tank car surrogate filled with liquid nitrogen (LN2). A series of post-test tensile characterizations was conducted on coupons from the T304 stainless steel inner tank at various combinations of strain rates and temperatures in preparation for the next test. It is expected that the stainless steel will have a significantly different structural response at cryogenic temperature than at ambient temperature which may affect the puncture behavior of the inner tank.

The overall goal of the DOT-113 side impact test series is to analyze the side impact performance of a DOT-113 tank car carrying liquefied natural gas (LNG) under typical service conditions. A DOT-113 tank car cannot be directly tested with LNG due to safety concerns regarding a full-scale side impact test. In lieu of a test with LNG, FRA has planned a series of four tests with DOT-113 tank cars and surrogate tank cars going from water to cryogenic LN2 with companion FE analyses. Once confidence in the FE model is achieved, this model will be used to estimate the puncture resistance of a DOT-113 tank car carrying LNG.

1. Introduction

This report documents the analyses and test results for a side impact test performed on a DOT-113 tank car surrogate. A DOT-113 is a specially designed tank car intended to transport cryogenic liquid commodities. The DOT-113 surrogate described in this report included the features of a DOT-113 tank car essential to evaluating its impact response (e.g., typical tank materials, thicknesses, and diameters) but did not include features such as couplers, brake rigging, and other tank car specific features that would not affect the impact response. Previously tested tank cars in the Federal Railroad Administration's (FRA) side impact testing program typically had an exterior jacket that was much thinner than the commodity tank. The DOT-113 tank car surrogate used in this test featured an outer tank made of 9/16-inch carbon steel and an inner tank made of 1/4-inch stainless steel. This report documents the impact test and describes the finite element (FE) model development and pre-test estimates, the comparisons of the test and analyses, and the subsequent post-test analyses.

1.1 Background

In the past decade, significant research has been conducted to analyze and improve the impact behavior and puncture resistance of railroad tank cars. Ultimately, the results of this research will be used by Federal regulatory agencies—i.e., FRA and Pipeline and Hazardous Materials Safety Administration (PHMSA) in the United States—to establish performance-based testing requirements and to develop methods to evaluate the crashworthiness and structural integrity of different tank car designs when subjected to a standardized shell impact scenario. A performance-based requirement for tank car head impact protection has already been defined within the current regulations [1], and an optional performance-based requirement for tank car shell impact resistance is applicable to DOT-117P tank cars [2].

FRA has a continuing research program to provide the technical basis for rulemaking on enhanced and alternative performance standards for tank cars and a review of new and innovative designs that are developed by the industry and other countries. In support of this ongoing research program, full-scale tests are necessary to provide the technical information to validate modeling efforts and inform regulatory activities. These tests will evaluate the crashworthiness performance of tank cars used in the transportation of hazardous materials under standardized, repeatable conditions.

A DOT-113 tank car is a specialized tank car that is designed to transport cryogenic liquids.[1] A cryogenic liquid is "a refrigerated liquefied gas having a boiling point colder than -90 °C (-130 °F) at 101.3 kPa (14.7 psia) absolute."[2] DOT-113 tank cars are "tank-within-a-tank" cars, where the inner tank is in contact with the cryogenic material and resists the pressure exerted by the lading, and an outer tank surrounds the inner tank and insulating materials and carries the in-train forces. The DOT-113 tank car surrogate used in this test was constructed specifically for use in this shell impact test. The surrogate included design features representative of a

[1] Pipeline and Hazardous Materials Safety Administration, DOT. Title 49 Code of Federal Regulations (CFR) Section 179.302. Subpart F – Specification for Cryogenic Liquid Tank Car Tanks and Seamless Steel Tanks (Classes DOT-113 and 107A).

[2] 49 CFR § 173.115(g)

specification DOT-113 tank car, including typical materials of construction for the inner and outer tanks, typical diameters for the inner and outer tank shells, typical thicknesses for the inner and outer tanks, and typical pressure relief valve (PRV) arrangements. The surrogate did not include features required of tank cars that would not influence the puncture response during a shell impact, such as couplers, trucks, brake piping, or safety appliances. The terms "surrogate" and "tank car surrogate" are used interchangeably throughout this report.

At the time that this test was being planned, the Hazardous Materials Regulations (HMR) permitted the transportation of several cryogenic liquids via DOT-113 tank cars, including argon and ethylene. Refrigerated liquid methane (more commonly referred to as liquefied natural gas, or LNG) was not authorized for transportation via DOT-113 tank cars. However, there has been considerable interest in transporting this commodity via DOT-113 tank cars. PHMSA and FRA published a Notice of Proposed Rulemaking (NPRM) in October 2019[3] that would permit LNG to be transported in DOT-113 tank cars. Because the existing fleet of DOT-113 tank cars is small compared to the overall tank car fleet, and there is limited accident data regarding the performance of these tank cars in derailments or collisions, a series of full-scale shell impact tests was planned to provide technical information on the puncture resistance of the DOT-113 tank car. Researchers performed the first test in this series in November 2019 [3]. In the November 2019 test (Test 10), a "legacy" DOT-113C120W tank car that had been removed from service was struck by a 297,000-pound ram car equipped with a 12-inch by 12-inch indenter at 16.7 mph. As a result of the impact, both the inner and outer tanks of the test car were punctured.

DOT-113 tank cars include several unique design features that are not found on unpressurized (e.g., DOT-117) or pressurized (e.g., DOT-105) tank cars because of the particular properties of cryogenic materials. The inner tank of a DOT-113 tank car will be exposed to cryogenic temperatures, and thus must be constructed of either American Society for Testing and Materials (ASTM) A240 Type 304 or Type 304L stainless steel [4]. These grades of steel maintain desirable properties at cryogenic temperatures.

Since the inner tank and lading must be kept at cryogenic temperatures during transit, the inner tank must be surrounded by highly effective insulation. This insulation may take the form of expanded perlite[4] (e.g., a granular, lightweight, and natural mineral) or multiple layers of "super" insulating materials (e.g., multi-layer insulation [MLI]). Additionally, a vacuum is typically used in conjunction with either perlite or MLI to further reduce heat transfer into the inner tank. The specification defines a maximum rate of heat transfer that is permissible through the insulation system. The inner tank and insulation must be surrounded by an external tank to contain the insulation, maintain the vacuum, and carry the in-train forces.

1.2 Objectives

The objective of this test was to quantify the deformation mode, impact load-time history, and puncture resistance of a tank car surrogate in a side impact. Moreover, the impact conditions were developed so that the side impact test was: 1) safe, 2) repeatable, and 3) analyzable. The test conditions were intended to be representative of planned service conditions, subject to the

[3] Pipeline and Hazardous Materials Safety Administration. Proposed Rule: Hazardous Materials: Liquefied Natural Gas by Rail. Federal Register/Vol 84, No. 206/Thursday, October 24, 2019.

[4] The DOT-113 car used in Test 10 was equipped with perlite insulation.

limitation that LNG was not permitted to be carried via DOT-113 tank cars at the time the test conditions were developed. This test was intended to subject a new surrogate DOT-113 tank car with a 9/16-inch-thick TC-128B steel outer tank to an impact of slightly higher kinetic energy than the previous test of a "legacy" DOT-113 tank car in November 2019. The overall objective of this test series is to examine the potential improvement in shell puncture resistance for a DOT-113 tank car with an outer shell made of 9/16-inch TC-128B steel compared to a baseline DOT-113 tank car constructed from 7/16-inch A516-70 steel under LNG service conditions.

The objective of the pre- and post-test analyses was to provide estimates of the tank car impact response both for pre-test planning and for the validation of tank car impact and puncture modeling capabilities.

The lessons learned from the modeling efforts in this test will be applied to the next test in the series. This research program plans to conduct a series of tests of DOT-113 tank cars and DOT-113 tank car surrogates. Each test is planned to increase in both complexity and realism over the previous test in an incremental approach to representing planned service conditions.

1.3 Overall Approach

Prior to this test, FRA has conducted similar shell impact tests on DOT-105, DOT-111, DOT-112, DOT-117, and DOT-113 tank cars. These previous tests were all accompanied by companion FE analysis. These previous tests covered a wide range of tank car designs (e.g., capacities, shell diameter, shell thickness, vintage, manufacturer, outage level, outage pressure, etc.) The goal of the tank car shell impact testing and modeling program is to understand how a particular tank car performs under a standardized impact scenario that is representative of typical service conditions. For a DOT-113 tank car, typical service conditions mean a cryogenic commodity within the inner tank.

The overall approach to understanding the behaviors of a DOT-113 tank car under impact conditions and the potential for improving its performance through design changes uses full-scale and laboratory testing with companion FE modeling of increasing complexity. This testing ultimately represents a DOT-113 tank car under LNG service conditions subjected to a shell impact that punctures both the inner and outer tanks. The planned approach includes future tests and corresponding analyses to examine the influence of different materials and thicknesses used for the tank shell to 1) examine the effect(s) of modeling both the lading and the inner tank steel using properties at cryogenic conditions and 2) to ultimately model a DOT-113 tank car under "representative" conditions expected for LNG service.

Observations, lessons learned, and data collected during the first impact test of a DOT-113 tank car were used as a starting point for modeling the DOT-113 surrogate tank car used in this test. An additional complexity for designs such as the DOT-113 tank car is the consideration of the puncture of one or both tanks. For the impact test described in this report, the desired outcome of the test was the non-puncture of both the inner and outer tanks at a speed no lower than the speed of the previous DOT-113 tank car impact test. Such a test would be an experimental demonstration of the improved puncture resistance of the DOT-113 surrogate tank car compared to the legacy DOT-113 tank car tested previously.

The Volpe National Transportation Systems Center (Volpe), Transportation Technology Center, Inc. (TTCI), and FRA collaborated before the test to determine the target test speed based on the model estimates, the desired outcome of the test, and such factors as ambient conditions (e.g.,

wind speed influencing actual impact speed) at the time of the test. After the test, material coupon test data from both the inner and outer shells of the tank car, the measured internal pressure, and the measured test speed were used to update the pre-test FE model to reflect the actual test conditions. Finally, the post-test FE model results were compared to the test measurements.

1.4 Scope

This report introduces the DOT-113 tank car surrogate used in this test and compares it to the DOT-113 tank car used in the previous test. It includes a discussion of developing and executing the FE models used in this program. Aspects of developing and executing the FE models include modeling the tank car steels, modeling the water within the tank, and modeling the gas phase outage within the tank. This report discusses the execution of the test, summarizes the overall results of the test, and includes a discussion of the post-test modeling adjustments. Finally, the report presents a comparison between the test measurements and the model results.

This report does not include any results from further analyses using the DOT-113 tank car model, such as impact conditions outside of the conditions of the test. While this report refers to previously performed shell impact tests on tank cars of different specifications [3] [5] [6] [7] [8] [9], no comparison of results from those tests is included within the scope of this report. Research into the puncture resistance of DOT-113 tank cars is ongoing, and further simulations or comparisons may be presented in future work. Further testing and simulations of the puncture responses of DOT-113 tank cars under varied impact conditions (e.g., varied outage level, varied impact speeds, varied tank thicknesses, cryogenic lading conditions, etc.) are planned in this testing and analysis program, and they will be documented in a future report.

1.5 Organization of the Report

Section 1 introduces the research and work conducted.

Section 2 describes the tank car undergoing testing and analysis, and it describes the shell impact test setup.

Section 3 describes the instrumentation used during the test and its placement. This description includes discussion of the cameras used to capture the impact event.

Section 4 presents the results of the test. These results include a description of the actual conditions of the impact, a description of the test itself, and a summary of the measured test data.

Section 5 describes the development of the FE models used in this program. This section describes the geometry used in the model, the different material models developed, and modeling techniques used in the pre-test and post-test models.

Section 6 presents test measurements alongside the corresponding estimates from the pre-test FE models.

Section 7 includes a summary of the report and concluding remarks.

Appendix A describes the positions of the cameras and targets used in the test.

Appendix B contains the full set of time history data measured during the test. The appendix also contains the material data measured during the tensile coupon tests for the T304 stainless steel and TC-128B carbon steel making up the car's inner and outer tanks respectively.

Appendix C contains a full set of comparisons between test measurements and FE estimates. This appendix contains comparisons for pre-test models using two different material behaviors, and for the post-test model using the actual TC-128B behavior.

Appendix D describes the geometry and mesh on each part used in the FE models.

Appendix E contains a description of the modeling techniques that were used in both the pre-test and post-test FE models.

Appendix F contains a description of how each material behavior was developed in the FE models.

Appendix G provides the parametric analyses of the tank length and structural supports.

2. Test Conditions

Researchers performed the side (shell) impact test on June 11, 2020, at the Transportation Technology Center (TTC) in Pueblo, CO. The test was performed by sending a ram car into the side of a surrogate DOT-113 tank car that was mounted on skids and backed by a rigid impact barrier. This section describes the tank car that was used in this test and the overall test setup used in the side impact testing program.

2.1 DOT-113C120W Tank Car Specification and Features

The DOT-113 tank car used in this test was a surrogate tank car designed to be superior to a DOT-113C120W tank car from a crashworthiness perspective. The commodity-carrying inner tank and insulation must be surrounded by an external tank to contain the insulation, maintain vacuum, and carry the in-train forces. The DOT-113C120W specification requires that the outer tank be made of a carbon steel or stainless steel that is approved for use in tank car construction [10] and is a minimum of 7/16-inch thick.

Notably, the surrogate DOT-113 featured a 9/16-inch TC-128 Grade B steel outer shell, compared to a 7/16-inch A516-70 steel shell in the previously tested DOT-113C120W. The surrogate also featured a shorter overall length compared to the previously tested DOT-113. The surrogate tank car did not have all the piping, valves, fittings, insulation,[5] etc. that would be included in a tank car meeting the full DOT-113 tank car specification as defined in 49 CFR Part 179 Subpart F [11]. The lack of piping, valves, fittings was not expected to have a significant effect on the puncture response of the tank car's shell. A description of the alphanumeric code making up the DOT-113C120W tank car specification is given in Table 1.

Table 1. Description of Specification DOT-113C120W Tank Car

DOT	113	C	120	W
Car built to meet a U.S. Department of Transportation specification	Specification 113	Inner tank design service temperature of -260 °F	Inner tank test pressure of 120 psig	Welded tank

2.1.1 DOT-113C120W9 Tank Car Specification and Features

After this test was conducted, PHMSA promulgated a final rule (85 FR 44994)[6] on July 24, 2020, to authorize the transportation of refrigerated liquid methane, (i.e., more commonly referred to as LNG) by rail tank car. In the final rule, enhanced outer tank requirements were specified for DOT-113C120W tank cars with the specification suffix "9" (DOT-113C120W9). This suffix denotes that the outer tank shall be 9/16 inch thick instead of 7/16 inch thick. Additionally, a specification DOT-113C120W9 tank car must have its outer shell constructed of

[5] A small (8-foot) section of MLI was installed around the inner tank of the surrogate in the vicinity of the impact, but most of the surrogate's inner tank was left uninsulated.

[6] Pipeline and Hazardous Materials Safety Administration (PHMSA). (2020). Hazardous Materials: Liquefied Natural Gas by Rail. Washington, DC: U.S. Department of Transportation.

normalized Association of American Railroads (AAR) Specification Tank Car-128, Grade B (TC-128B) carbon steel.

Table 2 presents a summary of the outer tank requirements from the NPRM and final rule.

Table 2. Summary of Tank Car Properties from NPRM and Final Rule for LNG

Property	NPRM	Final Rule
Tank Car Specification	113C120W	113C120W9
Minimum Wall Thickness of the Outer Tank Shell	7/16 inch	9/16 inch
Minimum Wall Thickness of the Outer Tank Heads	1/2 inch	9/16 inch
Required Outer Tank Steel Type(s)	As specified in AAR Specifications for Tank Cars, Appendix M[7]	AAR TC-128B normalized steel plate

2.2 Description of DOT-113 Tank Car Surrogate Used in Test

The surrogate DOT-113 tank car used in this test was constructed solely for the purpose of this side impact test, whereas all the other tank cars used in the previous tests in this program were designed and constructed to be used in service.

The inner tank was made of ASTM A240, Type 304 (T304) stainless steel [12] with a nominal thickness of 1/4 inches. The outer tank was made of TC-128B high strength carbon-manganese steel [10] in the normalized condition with a nominal thickness of 9/16 inches.

According to its manufacturer, the outer tank of the surrogate was originally intended to be the commodity tank in a DOT-117 tank car. A DOT-117 tank car features a 9/16-inch-thick tank shell made of TC-128B steel and a diameter similar to the diameter of the outer tank of the DOT-113 tank car used in the previous test. Since one purpose of the impact test was to evaluate the potential crashworthiness improvements associated with an outer tank made of 9/16-inch-thick TC-128B steel and the dimensions were appropriate, the DOT-117 tank was determined to be a suitable outer tank for the DOT-113 surrogate used in the test.

As part of the typical fabrication processes used to manufacture a DOT-117 tank car, the entire outer tank was put through a post-weld heat treatment (PWHT) process. Following this PWHT, the outer tank was cut apart circumferentially at two locations. The outer tank had cutouts in it to accommodate the planned nozzles and appurtenances of a DOT-117 tank car. These shell sections were removed from the center of the tank car as they are not typically found on a DOT-113 outer tank. Removing the shell sections containing these cutouts reduced the overall length of the outer tank to approximately 45 feet over the outside of the heads, which is one reason the DOT-113 surrogate had a smaller overall length than the previously tested DOT-113 tank car. Reducing the outer tank's shell length provided the test team with an opportunity to

[7] AAR TC-128B steel normalized or ASTM A516, Grade 70 (A516-70)

conduct material characterization testing on the pieces of the outer tank's steel removed from the shell (see Section 4.5).

The inner tank was purpose-built for installation in the surrogate DOT-113. Its diameter, thickness, and material were consistent with the previously tested DOT-113. Its length was limited by the length of the outer tank of the DOT-113 surrogate and the need to maintain an empty space between the inner and outer tanks that would typically be used to insulate the inner tank. The inner tank had a length over its heads of approximately 43 feet 8 inches. As the inner tank was fabricated specifically for this research program, samples of the inner tank's material were also available for material characterization prior to the impact test (see Section 4.5). The inner tank had a nominal capacity of 19,300 gallons of water at room temperature.[8] The car was equipped with a PRV that had a start-to-discharge (STD) pressure of 75 psig.

The two tanks were nested together and separated by a 6-inch gap. The inner tank had a section approximately 100 inches long, wrapped in MLI, and centered on the impact region (see Figure 1); however, the annular space was not held under vacuum, i.e., openings were present in the outer tank to maintain atmospheric conditions in the annular space. The MLI was added to the impact region to investigate if it would play a noticeable structural role in the side impact. The previously tested DOT-113 tank car used perlite and a vacuum in the annular space, and post-test modeling demonstrated that perlite contributed to the structural response of the impacted tank car [3].

Figure 1. T304 Stainless Steel Inner Tank Wrapped in MLI

The test was performed by sending a ram car into the side of the tank car that was mounted on skids and backed by a rigid impact barrier as shown in Figure 2.

[8] Due to thermal contraction, the inner tank would have a lower capacity of cryogenic material based on the temperature of that material.

Figure 2. DOT-113 Surrogate Tank Car Mounted on Support Skids

2.2.1 Test Arrangement

An overhead view of the test setup is shown in Figure 3 with annotations indicating: 1) the A-end and B-end of the tank car, 2) the east and west sides of the test site, and 3) the direction of travel of the ram car.

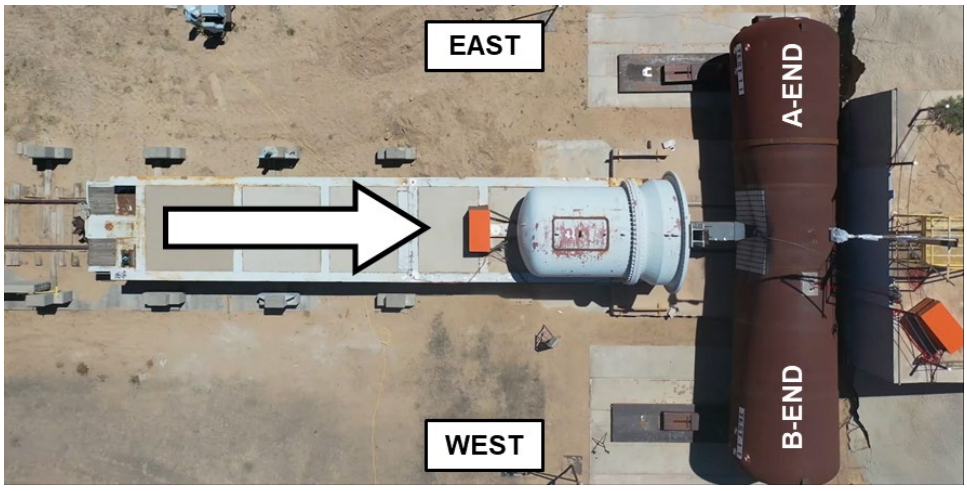

Figure 3. Overhead View of Test Setup Extracted from Drone Video

The DOT-113 surrogate tank car was offset by approximately 2 feet toward the west, resulting in an off-center impact. A centered impact would have placed the edge of the impactor near a closure weld in the outer tank. Figure 4 shows an annotated photo of the closure weld and a diagram of the nesting process in which the outer tank (brown) is closed around the inner tank (grey). The closure weld is a unique circumferential weld that is formed using a single welded butt joint with a backing strip on the inside of the joint instead of a fusion double welded butt joint per 49 CFR § 179.400-11. This weld is unique because it is not possible to weld from the

inside of the outer tank after the inner tank is nested. This makes the closure weld the only circumferential weld in the inner and outer tank that is not a double-sided weld. Additionally, a PWHT of the entire tank car is not possible once the inner tank is nested. Thus, the double-sided welds on the two halves of the outer tank go through a global PWHT, but the closure weld is not required to undergo a PWHT by 49 CFR § 179.400-12. The tank car was offset by 2 feet to avoid this weld because the objective of the test was to evaluate the overall performance of the tank car surrogate in a side impact, not the performance of a particular design feature, e.g., the closing weld. Post-test material testing included samples of the outer tank's TC-128B steel taken from the base (unwelded) plate, from double-sided welds in the outer tank, and from the closure weld in the outer tank (see Section 4.5.2). The purpose for these material tests were to investigate whether the closure weld's mechanical properties differed significantly from either the unwelded plate or the double-sided welded joints in the outer tank.

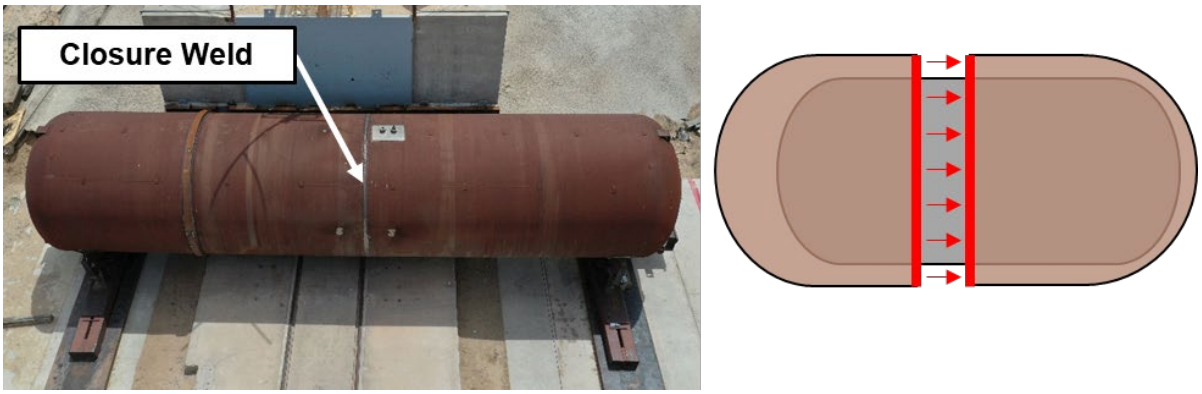

Figure 4. Photo of Closure Weld (left) and Diagram of Nesting Process (right)

Figure 5(a) shows one of the skids that the tank car was placed on oriented parallel to the track with one end near the impact barrier. Two sections of I-beams were welded to each skid and to the tank car for attachment, as Figure 5(b) shows. The tank car with skids attached was placed on 1-inch steel plates. These steel plates were placed on four 3/4-inch-thick stacks of plywood to raise the tank car above the concrete slab in which the rails are embedded at the impact wall. This test configuration was designed to minimize the tank car rollback and allow the tank car on the skids to slide on the steel plates during the impact without contacting the concrete slab.

(a) Support Skids (b) Welded I-beam Connection

Figure 5. Tank Support Skid System

The desired level of water in the tank car was calculated based on the nominal dimensions and capacity of the inner tank. Because the manway was located in the head of the tank, it was necessary to devise an alternate method for determining when the proper innage for the test had been reached. A 1/2-inch pipe which passed through the inner and outer shell of the tank car was located such that once the desired 17.6 percent outage had been achieved, water would begin to flow out of the pipe. This pipe was also used to pressurize the outage to approximately 50 psig. Figure 6 shows the pipe used for setting the outage and pressurizing the tank car.

Figure 6. Pipe Used for Setting Innage and Pressurizing the Tank Car

The indenter was positioned to align with the mid height of the target tank car as closely as possible. The ram car was a modified flat car with an 8-foot ram installed on the leading end. This ram car was used in previous tank car tests and has a shortened tank attached to the ram end. Figure 7 shows the ram car, which is an image from a previous test. For this test, a 12-inch by 12-inch indenter with 1.0-inch radii on the edges and corners was used. The same indenter was used in the impact test of a DOT-111 tank car [5], a DOT-112 tank car [13], a DOT-117 tank car [7], a DOT-105 tank car [8], and a second DOT-111 tank car meeting voluntary industry standard CPC-1232 [14].

Figure 7. Ram Car and Head

Figure 8 shows the 12-inch by 12-inch indenter attached to the ram car in an image taken from a prior test, and Figure 9 shows the ram car aligned with the tank car taken from a high-speed video. The ram car was weighed before the test to confirm the actual weight. The measured weight was 297,200 pounds.

Figure 8. Ram Arm with 12-inch by 12-inch Indenter

Figure 9. Ram Arm with 12-inch by 12-inch Indenter Aligned with Impact Zone on the Tank Car

Prior to the previous test of a DOT-113 tank car in November 2019, it was determined that one of the reinforcement rings would interfere with the typical interaction of the tank car with the crash wall. Because the reinforcement ring was on the outside of the outer tank, the initial point of contact between the DOT-113 tank car and the rigid wall during impact would be at this reinforcement ring. The decision was made to add sections of 4-inch-thick plate steel to the wall to allow the entire outer tank to be initially in contact with the rigid wall, typical of the setup used in the previous tests. Five-foot-wide sections of plate were mounted to the existing plate across the width of the wall with a 1-foot gap between the plates at one end to accommodate the structural ring. Figure 10 shows the layout of this plate on the wall.

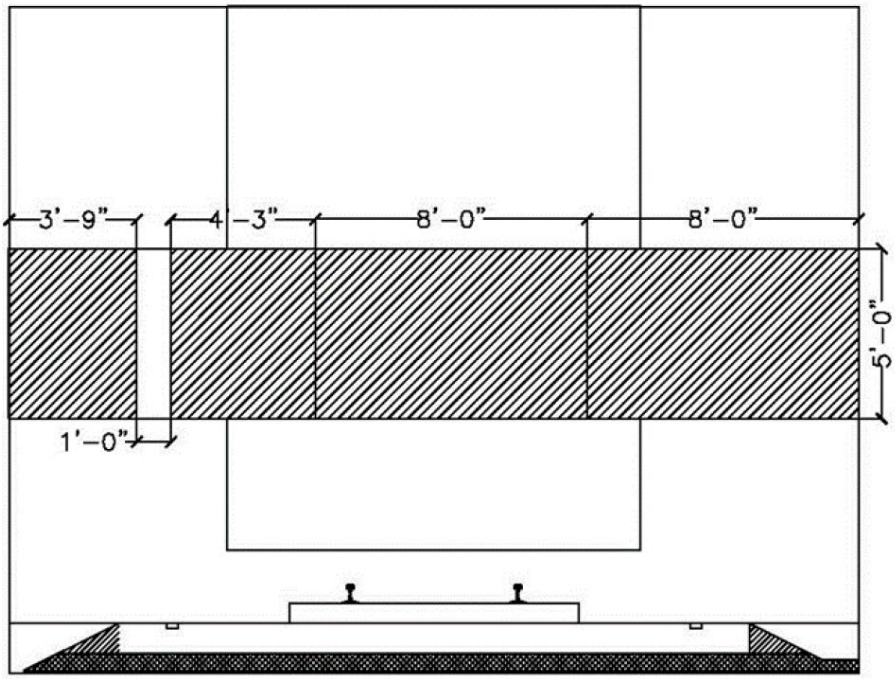

Figure 10. Offset Plate Layout

The surrogate DOT-113 tank car in this test had a stiffener added in the same longitudinal position relative to the impact location as in Test 10. However, the stiffener was only designed to extend 270 degrees around the impact side of the tank car to ensure that there would be no interaction between the stiffener ring and the crash wall.

2.2.2 Lading and Outage Conditions

Three lading conditions needed to be defined prior to the test. First, the lading to be used had to be selected. Second, the volume of lading (and thus, the volume of air space or "outage") to be placed in the tank car had to be chosen. Third, the desired pressure for the outage had to be chosen. This section discusses each of these three aspects and the values targeted for the test.

Careful consideration of the safety, environmental, logistical, and technical ramifications were given to the lading that would be used in the tank car during this test. While testing using a cryogenic liquid in the tank car would have presented a more realistic test condition, this test used water as the lading in the tank car. As this was the second impact test using a DOT-113 type tank car performed to-date, water was chosen over a cryogenic liquid in an effort to reduce the number of unknowns and additional safety precautions necessary for this test. As previously described in Section 2.1, a DOT-113 tank car contains several unique design features that FRA has tested previously but that were not present, and therefore not examined, in the pressurized and unpressurized tank cars. Another benefit to using water was that water made it easier to compare this test of a DOT-113 surrogate to the previous November 2019 test of a DOT-113.

While using water simplified the test setup in several ways, when compared to using a cryogenic liquid, water also introduced several additional challenges into test implementation. Water has a weight density of approximately 8.3 pounds per gallon [15]. Liquid methane has a density of approximately 3.5 pounds per gallon [17]. Thus, since the tank car surrogate was filled to the same level with water as it would have been filled with a cryogenic liquid, the inner tank was carrying a load that exceeded a typical service load. This extra load, in turn, resulted in higher stresses to the inner tank, the inner tank's attachments to the outer tank, and the outer tank at the start of the test.

Using water at ambient temperature also influences the material behavior of the inner tank. The material of construction for the inner tank, T304 steel, has different mechanical properties at cryogenic temperatures, e.g., -260 °F, than at ambient temperature. While the outer tank of a properly functioning DOT-113 tank car should not reach this temperature, the inner tank will be at the same temperature as the lading. The mechanical properties of T304, namely the strength and ductility, are expected to differ when the tank is at ambient temperature versus cryogenic temperature. As a means of addressing this difference, post-test material coupons excised from the inner tank were subjected to tensile testing at -320, -80, and 70 °F. These material tests were also conducted over a range of strain rates. This was done based on the lesson learned from the first DOT-113 impact test—the stainless-steel inner tank may have a rate sensitivity that influences its puncture behavior. These material test results are discussed in Section 4.5.

Another aspect of the lading and outage conditions to be determined prior to the test was the filling level for the tank car. For cryogenic materials authorized to be transported by DOT-113

tank cars, 49 CFR § 173.319(d)(2) contains a table of maximum permitted filling densities[9] for different commodities, initial pressures, specification tank cars, and STD pressures for the tank car's PRV. Because the tank was filled with water during the test, a target filling density had to be chosen based on the in-service condition expected to be encountered for a particular commodity.

At the time when the first two DOT-113 side impact tests were conducted in 2019 and 2020, LNG could only be transported via DOT-113 tank car under a Special Permit (DOT-SP 20534). PHMSA had published a Notice of Proposed Rulemaking (NPRM) in the Federal Register [17] that proposed to allow the transportation of LNG by DOT-113C120W tank cars. This NPRM included a proposed updated version of the table contained in 49 CFR § 173.319(d)(2) that set out the filling conditions for LNG. Note that the test conditions were based on the proposed requirements in the NPRM. These requirements are different from the those in the final rule published after the completion of the second test (85 FR 44994). Table 3 summarizes the requirements from the NPRM and final rule.

Table 3. Summary of Pressure Control Valve Settings from NPRM and Final Rule for LNG

Property	NPRM	Final Rule
Tank car specification	113C120W	113C120W9
Maximum STD	75 psig	75 psig
Maximum pressure when offered for transportation	15 psig	15 psig
Design service temperature	-260 °F	-260 °F
Maximum permitted filling density (% by weight) methane	32.5%	37.3%

Because the DOT-113 tank car tests in 2019 and 2020 took place before the final rule was published, a filling density of 32.5 percent was used to determine the outage volume percentage and pressure for both of these tests.

To make it easier to compare this 2020 test of a DOT-113 surrogate with the 2019 test of a DOT-113C120W tank car, the lading and outage conditions were matched as closely as possible. A more detailed discussion on the choice of lading (water) and outage conditions is provided in the test report on the 2019 DOT-113 side impact test [3]. The DOT-113 surrogate test's target outage of 17.6 percent and pressure of 50 psig were chosen to match the previous DOT-113 test.

Table 4 summarizes the target lading and outage conditions chosen for the test.

[9] 49 CFR § 173.319(d)(1) states: "For purposes of this section, 'filling density' is defined as the percent ratio of the weight of lading in the tank to the weight of water that the tank will hold at the design service temperature."

Table 4. Summary of Lading and Outage Conditions for Test

Loading Parameter	Target Value for Test
Commodity in tank	Water
Outage volume	17.6%
Outage pressure	50 psig

2.3 Comparison of DOT-113 Tank Car Test Conditions

Table 5 summarizes the test conditions in the November 2019 test of a DOT-113C120W tank car and the June 2020 test of a DOT-113 surrogate tank car. The highlighted cells call attention to the conditions that changed from test-to-test. The initial pressure, outage, lading, inner tank thickness, and material remained consistent between the two tests. The insulation was changed from perlite to MLI to be more representative of a modern DOT-113 tank car. To simplify the design and construction of the surrogate tank car, the annular space was held at atmospheric pressure because a vacuum was not expected to have a significant effect on puncture. The inner tank's volume and the length over the heads of the surrogate were reduced to simplify the design and construction of the surrogate tank car. Reducing the length of the tank was expected to be a conservative simplification, as a shorter distance between bolsters and heads would stiffen the impact response of the tank, compared to a longer tank span. For the same diameter and thickness of tank material, a stiffer tank was expected to puncture at a lower speed than a more flexible tank. A pre-test parametric modeling study was conducted to examine the influence of tank length on global response. This study is described in Appendix G.

Table 5. Summary of DOT-113 Tank Car Side Impact Test Conditions

Test Date	November 19, 2019	June 11, 2020
Test Number	Test 10	Test 11
Test Article	DOT-113C120W	DOT-113 Surrogate
Thickness (Outer Tank)	7/16 inch	9/16 inch
Material (Outer Tank)	A516-70 Carbon Steel	TC-128B Carbon Steel
Diameter (Outer Tank)	~119 inches	~120 inches
Length (Outer Tank)	~74 feet	~45 feet
Thickness (Inner Tank)	1/4 inch	1/4 inch
Material (Inner Tank)	T304 Stainless Steel	T304 Stainless Steel
Diameter (Inner Tank)	~106 inches	~106 inches
Volume (Inner Tank)	32,900-gal H_2O	19,300-gal H_2O
Tank Lading	Water	Water
Outage Volume	17.6%	17.6%
Pressure	50 psig	50 psig

Test Date	November 19, 2019	June 11, 2020
Insulation	Perlite	Multilayer Insulation
Annular Pressure	Vacuum	Atmospheric
Impact Speed	16.7 mph	17.3 mph

The outer tank of the DOT-113 surrogate was intentionally changed from a 7/16-inch A516, Grade 70 (A516-70) carbon steel to a 9/16-inch TC-128B carbon steel. This change was made to evaluate the potential crashworthiness improvement from using a higher strength, thicker steel in the outer tank. The target speed for the June 2020 test was 17.2 mph, and the actual speed was 17.3 mph. The November 2019 test used a target speed of 16.5 mph, and the actual speed was 16.7 mph. The target speed for the June 2020 test was chosen to ensure that the actual speed would be no less than the actual speed of the November 2019 test.

Note that the combined changes to the insulation material and outer tank thickness and material specifications were expected to have a large effect on the structural response of the DOT-113 surrogate tank car. Post-test FE analyses performed after the November 2019 test indicated that the presence of perlite in the annular space stiffened the force versus impactor travel response of the tank car and resulted in puncture at a lower impactor velocity than predicted in analyses without perlite. While it is desirable to change only one variable (i.e., insulation type or outer tank steel) between tests, both variables were changed between the November 2019 test and the June 2020 test due to the high cost and time commitment associated with running a full-scale side impact test. However, once confidence is built in a validated FE model of a DOT-113 tank car side impact test, the FE model can be used to carefully investigate the individual effects of each test variable on the structural response of the tank car to a side impact collision.

3. Test Instrumentation

3.1 Overview

The test configuration and instrumentation were consistent with the specifications of the test implementation plan [18]. Table 6 lists all instrumentation used for this test. Additional descriptions of the various types of instrumentation are provided in the following subsections.

Table 6. Instrumentation Summary

Type of Instrumentation	Channel Count
Accelerometers	11
Speed sensors	2
Pressure transducers	13
String potentiometers	10
Laser displacement transducers	15
Total data channels	51
Digital video	10 cameras (including 4 high-speed cameras)

3.2 Ram Car Accelerometers and Speed Sensors

The local acceleration coordinate systems were defined relative to the ram car. Positive x, y, and z directions are forward, left, and up relative to the lead end of the ram.

Three triaxial accelerometers were mounted on the longitudinal centerline of the ram car at the front, rear, and near the middle of the car. Two uniaxial accelerometers were mounted on the left and right sides of the car to supplement recording of longitudinal acceleration. The positions of these accelerometers are illustrated in Figure 11. A summary of the ram car accelerometer ranges and positions is provided in Table 7.

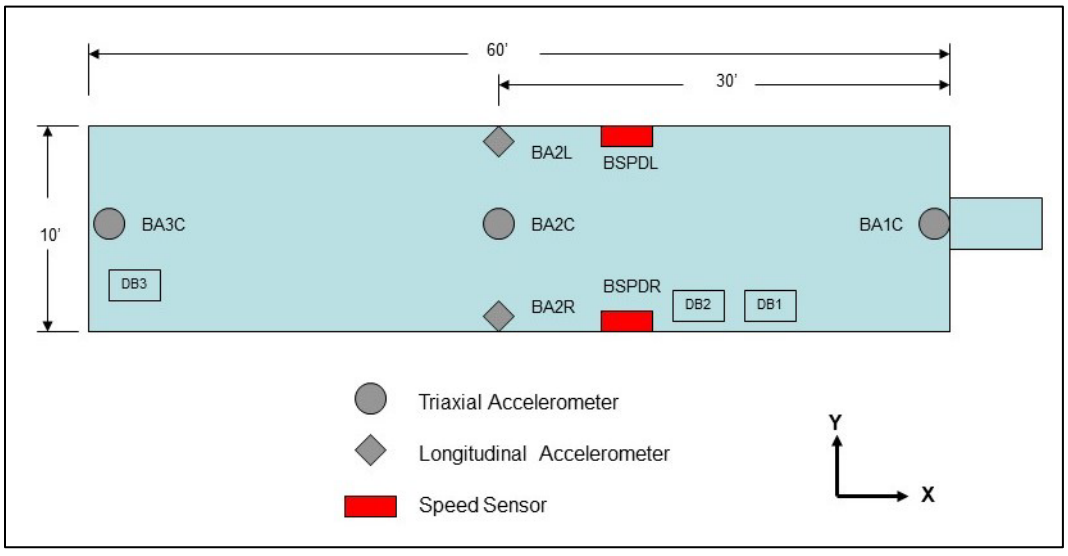

Figure 11. Ram Car Instrumentation

Table 7. Ram Car Accelerometers

Channel Name	Sensor Description	Range
BA1CX	Leading end, centerline, X accel	200 g
BA1CY	Leading end, centerline, Y accel	100 g
BA1CZ	Leading, centerline, Z accel	200 g
BA2LX	Middle, left side X accel	100 g
BA2CX	Middle, centerline, X accel	50 g
BA2CY	Middle, centerline, Y accel	50 g
BA2CZ	Middle, centerline, Z accel	50 g
BA2RX	Middle, right-side X accel	100 g
BA3CX	Trailing end, centerline, X accel	200 g
BA3CY	Trailing end, centerline, Y accel	100 g
BA3CZ	Trailing end, centerline, Z accel	200 g

Speed sensors were mounted on both sides of the ram car to provide an accurate measurement of the car's velocity within 20 inches of the impact point. The speed sensors were reflector-based light sensors, using reflectors on the ground separated by a known distance in conjunction with light sensors mounted on the ram car. These sensors were triggered as the ram car passed over the reflectors. The last reflector was positioned to align with the sensor when the ram head was within a few inches of the impact point. The time interval between passing the reflectors was recorded, and the speed was calculated from distance and time. A handheld radar gun was also used to take supplemental speed measurements.

3.3 Tank Car String Potentiometers and Pressure Transducers

The local displacement coordinate systems (except for the tank heads) were defined relative to the tank car. Positive x, y, and z directions are forward, right (away from the wall), and up relative to the A-end of the tank car. Tank head displacements were positive toward the impact wall.

Six string potentiometers were used to measure the tank crush displacements around the immediate impact zone during the test. Five string potentiometers measured the dent formation of the tank at the center of impact and at locations 24 and 48 inches to either side of the impact point. The sixth string potentiometer measured the vertical deformations of the tank at the center of impact. Four external string potentiometers were used to measure the tank motions. These string potentiometers were attached to each of the tank skids and to the center of the tank heads at both ends of the car. Fixed anchor positions were established so that these measurements were limited to the longitudinal motions of the tank heads and skids. Table 8 lists all string potentiometers attached to the tank car. Figure 12 and Figure 13 show their placement.

Table 8. Tank Car String Potentiometers

Area	Location	Axis	Channel Name	Range (inches)
Impact area	B-end, 48-inch offset	Y	TD1Y	50
Impact area	B-end, 24-inch offset	Y	TD2Y	50
Impact area	Center	Y	TD3Y	50
Impact area	Center	Z	TD3Z	50
Impact area	A-end, 24-inch offset	Y	TD4Y	50
Impact area	A-end, 48-inch offset	Y	TD5Y	50
Tank head	A-end	Y	TDAend	50
Tank head	B-end	Y	TDBend	50
Skid	A-end	Y	TDAskid	50
Skid	B-end	Y	TDBskid	50

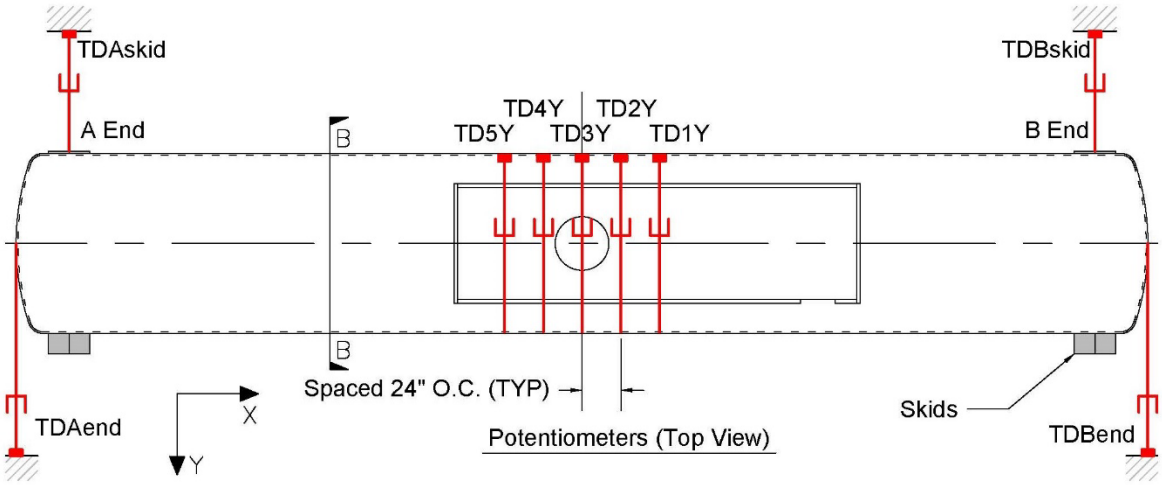

Figure 12. Tank Car String Potentiometers (top view)

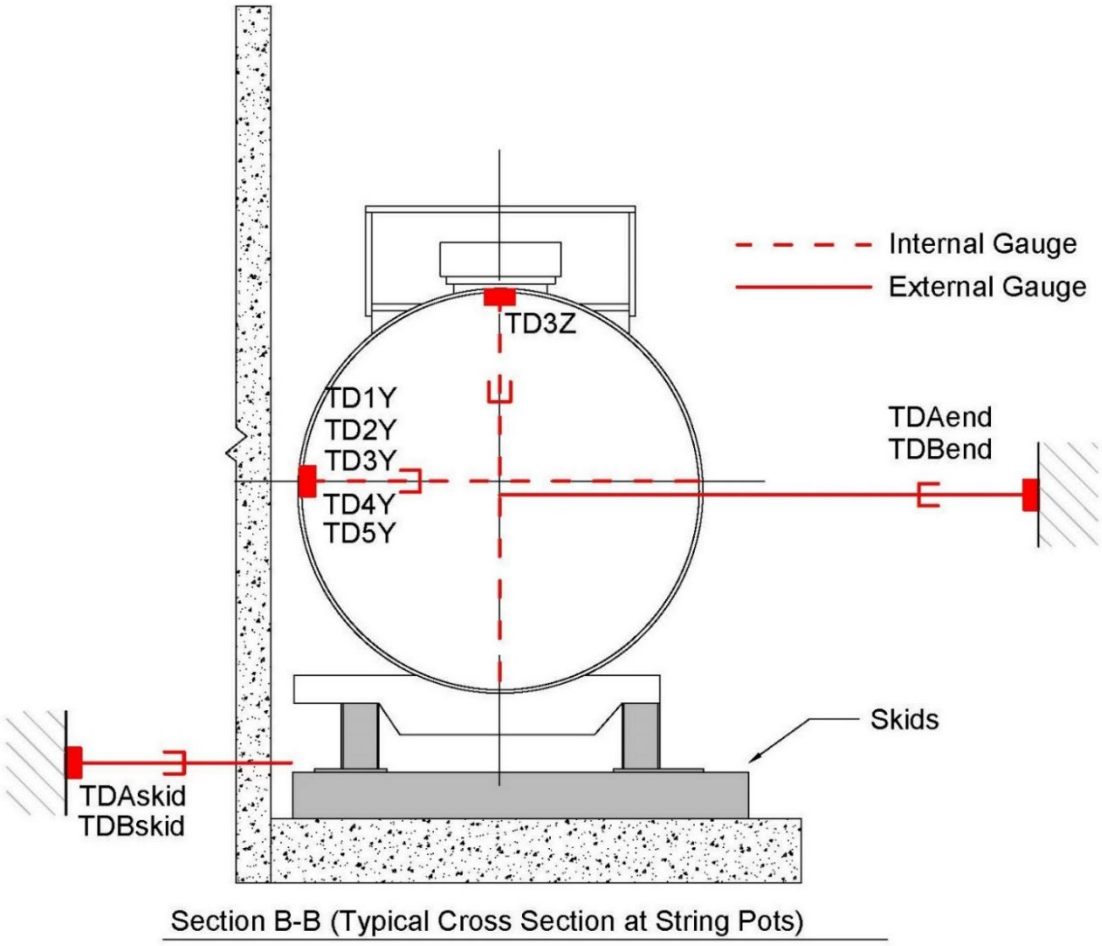

Figure 13. Tank Car String Potentiometers (end view)

An array of 12 pressure transducers was set up within the tank to record the pressure in the lading and the outage. They were mounted on the top, sides, and bottom of the inner tank between the B-end of the car and the impact centerline. A pressure transducer was also mounted immediately downstream from the pressure relief valve to record a discharge if it occurred. Table 9 lists all the pressure transducers used for the tank car. Figure 14 and Figure 15 show their placement.

Table 9. Tank Car Pressure Transducers

Location	Channel Name	Sensor Description	Range (psi)
B top	TP1000	B-End top pressure	300
B back wall	TP1090	B-End back wall pressure	300
B floor	TP1180	B-End floor pressure	300
B front wall	TP1270	B-End front wall pressure	300
M top	TP2000	Mid-length top pressure	300
M back wall	TP2090	Mid-length back wall pressure	300

Location	Channel Name	Sensor Description	Range (psi)
M floor	TP2180	Mid-length floor pressure	300
M front wall	TP2270	Mid-length front wall pressure	300
C top	TP3000	Center top pressure	300
C back wall	TP3090	Center back wall pressure	300
C floor	TP3180	Center floor pressure	300
C front wall	TP3270	Center front wall pressure	500
PR valve	TPRV	Pressure relief valve	500

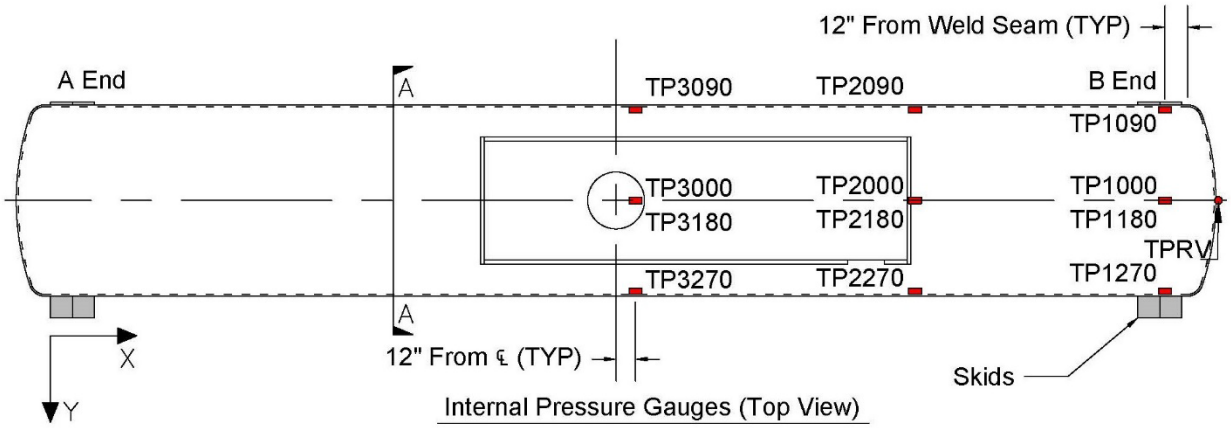

Figure 14. Tank Car Pressure Transducers (top view)

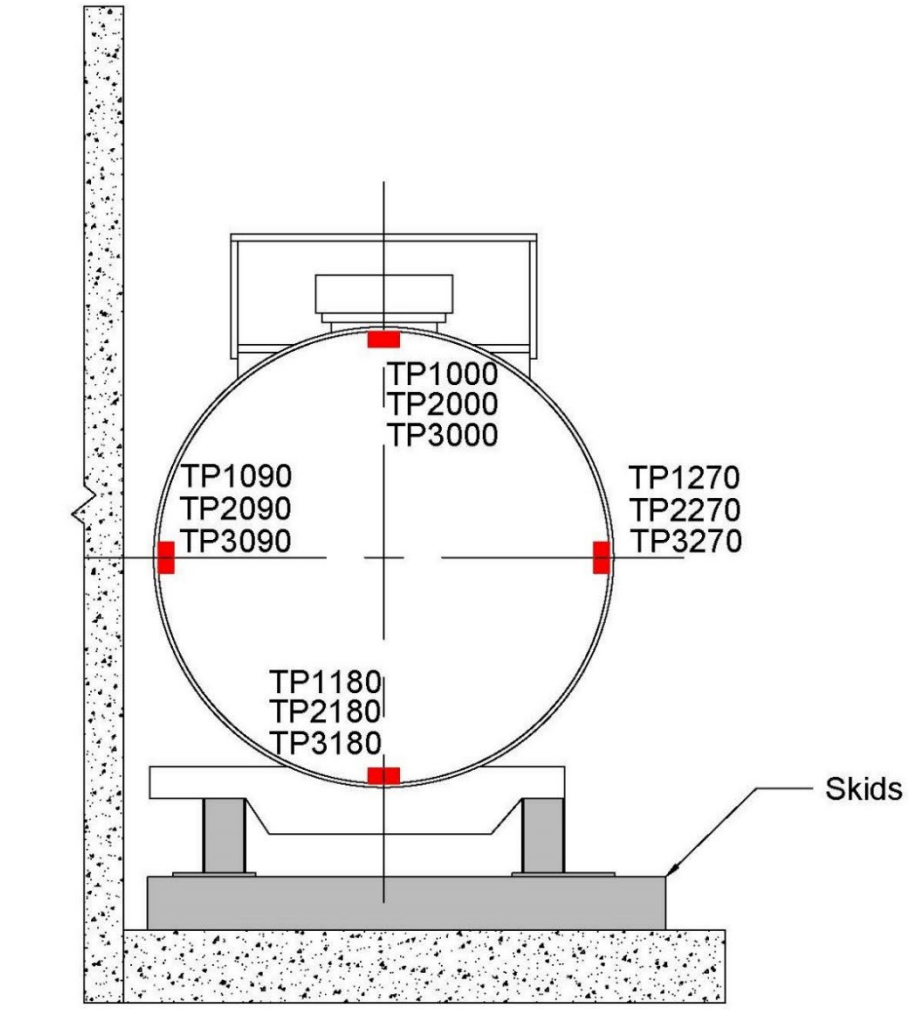

Figure 15. Tank Car Pressure Transducers (end view)

3.4 Laser Displacement Transducers

In addition to the string potentiometers, a series of lasers mounted to the face of the ram car and in the recesses cut into the offset plate mounted to the crash wall were used to record the tank car response. The data that was recorded was also used to calculate the deformation of the tank car at positions that were 24 and 48 inches on either side of the center of impact. The overall positional reference for these calculations was provided by a laser that was mounted at the top of the ram car and aimed at the crash wall to record the distance between the ram car and the crash wall. Table 10 lists the laser displacement transducers used during the test. Figure 16 shows the position of the lasers mounted to the ram car. Figure 17 shows the lasers mounted to the crash wall, and Figure 18 shows the relative positions of these lasers.

Table 10. Laser Displacement Transducers

Location	Channel Name	Sensor Description	Range (mm)
Ram car	BD1Y	Displacement EAST	50 to 12,000
Ram car	BD2Y	Displacement second from EAST	50 to 12,000
Ram car	BD3Y	Displacement third from EAST aimed at crash wall above tank car	50 to 12,000
Ram car	BD4Y	Displacement fourth from EAST	50 to 12,000
Ram car	BD5Y	Displacement fifth from EAST	50 to 12,000
Crash wall	TD1YS	Displacement short range EAST	35 to 110
Crash wall	TD1YL	Displacement long range EAST	100 to 1,000
Crash wall	TD2YS	Displacement short range second from EAST	35 to 110
Crash wall	TD2YL	Displacement long range second from EAST	100 to 1,000
Crash wall	TD3YS	Displacement short range third from EAST	35 to 110
Crash wall	TD3YL	Displacement long range third from EAST	100 to 1,000
Crash wall	TD4YS	Displacement short range fourth from EAST	35 to 110
Crash wall	TD4YL	Displacement long range fourth from EAST	100 to 1,000
Crash wall	TD5YS	Displacement short range fifth from EAST	35 to 110
Crash wall	TD5YL	Displacement long range fifth from EAST	100 to 1,000

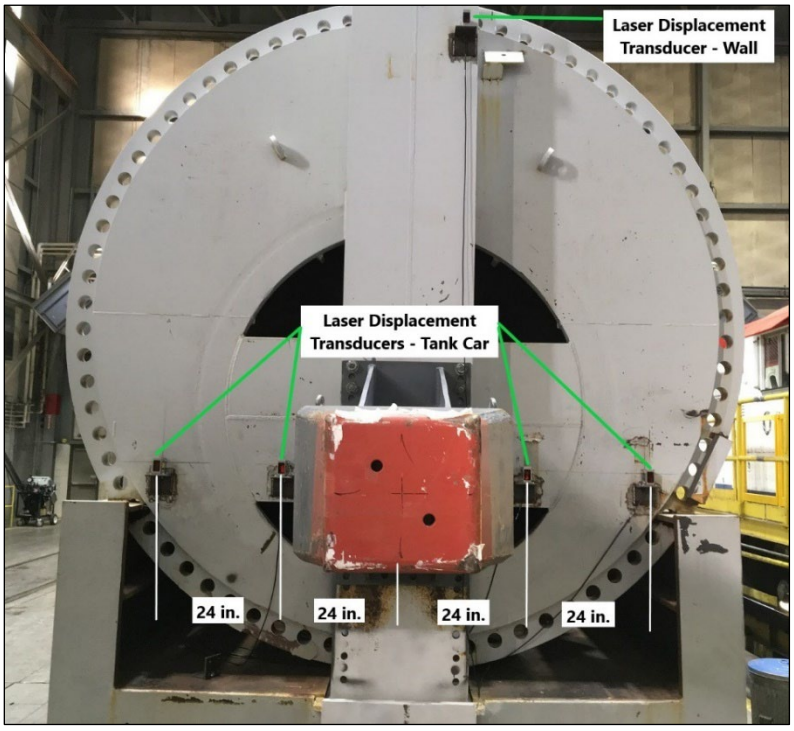

Figure 16**. Lasers Displacement Transducers on Ram Car**

Figure 17. Lasers Displacement Transducers on Crash Wall

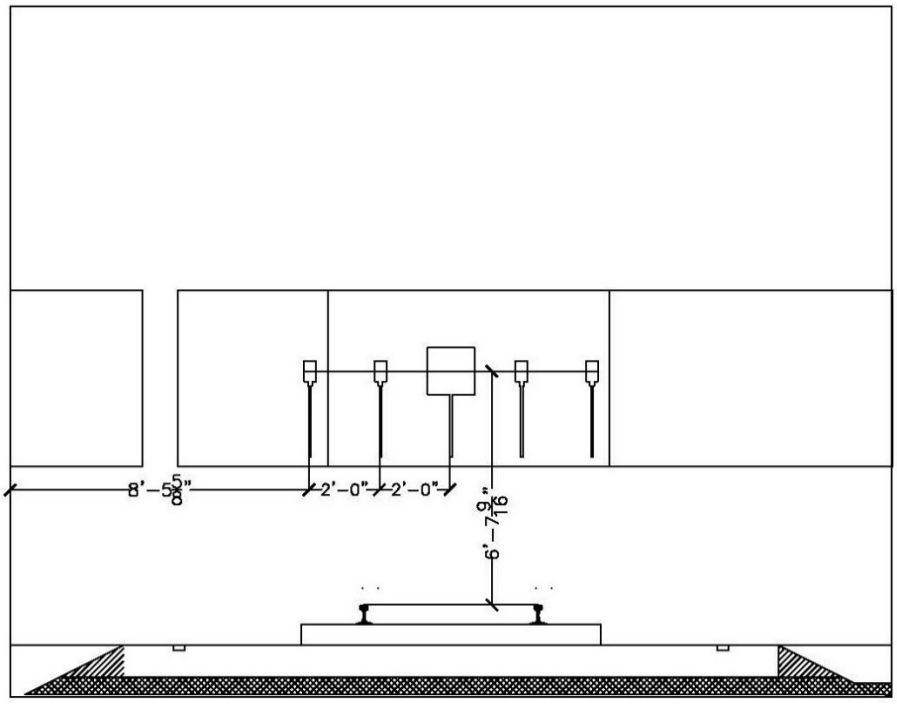

Figure 18. Relative Positions of Crash Wall Laser Transducers

3.5 Real Time and High-Speed Photography

Four high-speed and six real time high-definition video cameras were used to document the impact event. All high-speed cameras used were crashworthy and rated for peak accelerations of 100 g. The ram car and the impact barrier were painted with flat light gray. The tip of the indenter was painted red. High contrast targets were applied to the ram car and the indenter. Appendix A contains a schematic of the locations of the cameras and positions of the targets.

3.6 Data Acquisition

A set of eight-channel battery-powered onboard data acquisition systems was used to record the data from the instrumentation mounted on the ram car. These systems provided excitation to the instrumentation, analog anti-aliasing filtering of the signals, analog-to-digital conversion, and recording of each data stream. A similar set of ground-based data acquisition systems was used to record data from the pressure transducers and string potentiometers on the tank car.

The data acquisition systems were GMH Engineering Data BRICK Model III units. Data acquisition complied with the appropriate sections of SAE J211 [19]. Data from each channel was anti-alias filtered at 1,735 Hz, then sampled and recorded at 12,800 Hz. Data recorded on the data bricks was synchronized to time zero when the tape switches were closed by the initial impact. The time reference came from closure of the tape switches on the front of the test vehicle. Each data brick was ruggedized for shock loading up to at least 100 g. Onboard battery power was provided by GMH Engineering 1.7 Amp-hour 14.4 Volt NiCad Packs. Tape Switches, Inc., model 1201-131-A provided the initial event contact.

Software in the data bricks was used to determine zero levels and calibration factors rather than relying on set gains and expecting zero drift. The data bricks were set to record 1 second of data before initial impact and 4 seconds of data after initial impact. This data collection method has been used for all tests since Test 3 on July 16, 2014.

4. Results

This section describes the actual conditions of the test, some of which varied from the target conditions summarized in Sections 2. This section presents the results of the test in the form of photographs and a discussion of the damage to the tank car, as well as graphs of the test data. The results of post-test laser scans of the inner and outer tanks are also presented in this section.

4.1 Test Conditions

As described in Sections 2 and 3, this test was a side impact on a surrogate DOT-113 tank car, performed on June 11, 2020. The test involved a 17.3 mph side impact from a structurally rigid 297,200-pound ram car with a 12-inch by 12-inch indenter into the side of the tank car that was backed by a rigid impact barrier. After being filled to approximately 82.4 percent capacity with water to simulate standard commodity lading volume of a DOT-113 tank car, the tank car was then pressurized to approximately 50 psig.

At the time of the test, the ambient conditions included a wind speed of 3 mph out of the W-NW and an air temperature of 79 °F.

4.2 Details of Test

Pre-test simulations estimated a puncture speed range of 18 to 20 mph based on estimated material properties. The target speed for the test was 17.2 mph ± 0.5 mph. The objective in choosing this target test speed was to ensure the actual impact speed was below the threshold puncture/non-puncture speed while being no lower than the impact speed measured in the previous DOT-113 tank car test. Section 6 contains a discussion of the pre-test simulations used to help select the target test speed. The actual calculated impact speed from the speed sensors was 17.3 mph.

The ram car was brought to a stop during the test. Subsequently, both the ram car and the DOT-113 surrogate rebounded from the impact wall as the surrogate tanks recovered their elastic energy. The ram car separated from the DOT-113 surrogate and continued to roll back up the impact track until its brakes engaged. The inner and outer tanks did not puncture during the test.

Figure 19 shows the damage to the impacted side of the tank car. Figure 20 shows a detailed view of the impact zone on the outer tank. The impactor footprint is apparent in this figure. The upper left, lower left, and lower right corners of the impactor have transferred paint onto the outer tank. In the upper right corner of the impactor, some evidence of local plastic flow can be seen. Figure 21 shows the post-test position of the tank car relative to the supporting wall.

Figure 19. Tank Car After the Impact (impact side)

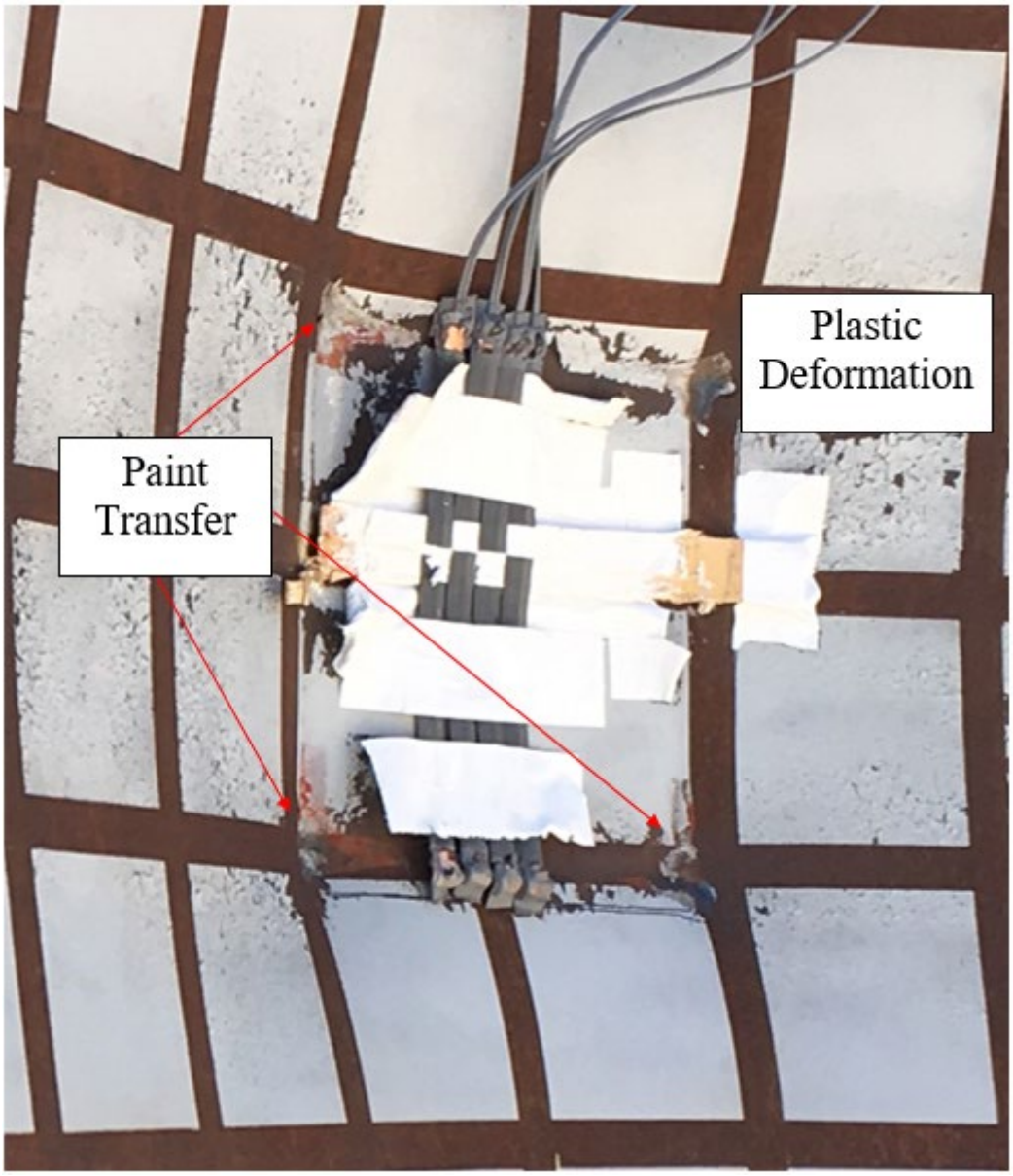

Figure 20. Detail View of Impact Zone with Annotations in Corners of Impactor Footprint

Figure 21. Post-test Position of Tank Car (wall side)

Figure 22 contains a still frame extracted from the isometric high-speed video taken during the test with an additional annotation. During the test, a small cover plate at the top of the tank was dislodged due to the impact. This plate originally covered the connectors used to pass instrumentation wiring through into the inner tank. The dislodging of this plate pulled on the instrumentation cabling but did not compromise the inner tank's pressure-retaining integrity during the test.

Figure 22. Still Frame from High-speed Video Taken at 0.195 Seconds

Figure 23 contains a still frame extracted from the isometric high-speed video of the test. This frame was extracted at 0.329 seconds, which is approximately the time at which the maximum forward motion of the ram car occurred. This photograph shows the extent of the indentation that occurred during the test.

Figure 23. Still Frame from High-speed Video Taken at Approximate Time of Maximum Indentation (0.329 seconds)

4.3 Laser Scanning

Following the test, complete light detection and ranging (LIDAR) scans of the inside of the tested tank car were performed to document the deformation that occurred during the test. Figure 24 shows the post-test scan of the inner tank. The area of impact is shown on the left side of the tank in this figure. The area of the inner tank that was cut away for material characterization (see Section 4.5) is shown at the right end of the tank.

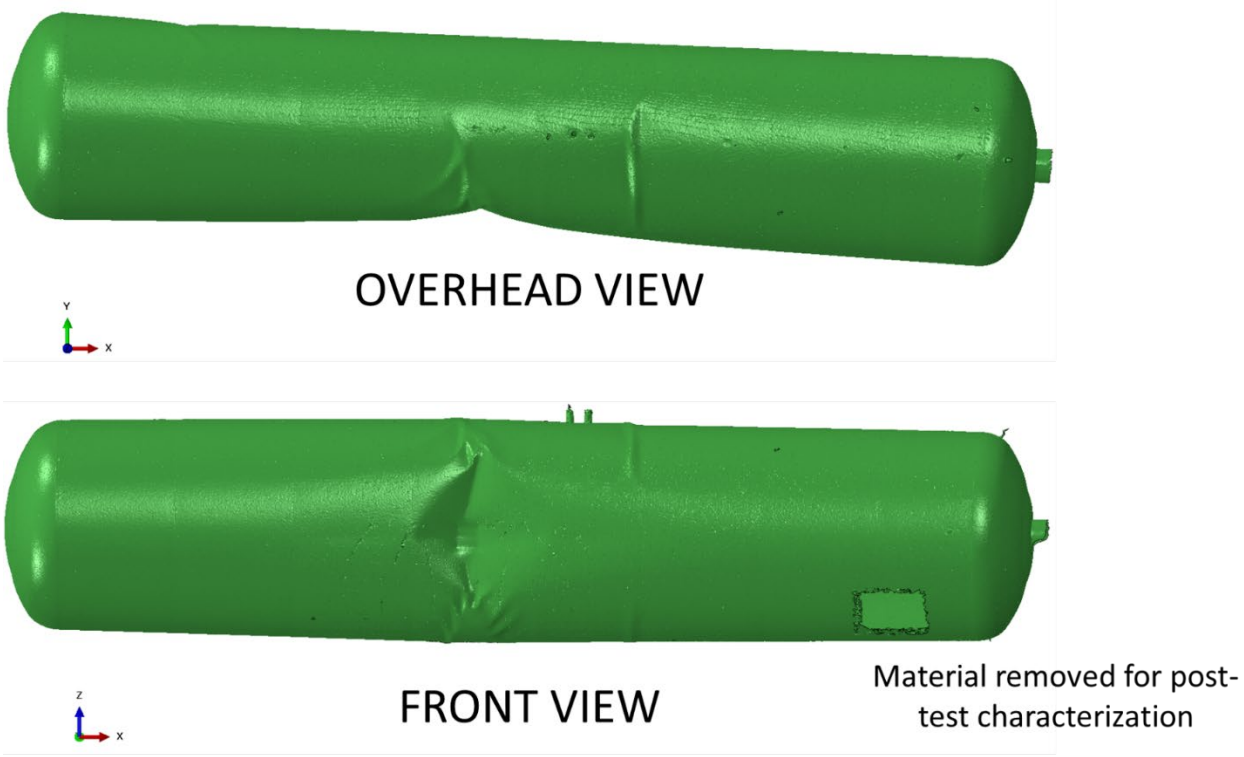

Figure 24. Two Views of Post-test LIDAR Scan of Inner Tank

Using the laser scanned data, a contour plot was generated as follows: 1) the approximate center of the impact zone was aligned with the global origin (0,0,0), and 2) the coordinates of each node in the point cloud from the scan was then superimposed on the resulting scan geometry. In the LIDAR scan cloud's coordinate system, the "Y" or "2" direction corresponds with the direction of the impact. Figure 25 shows the front of the tank with the contours of indentation depth measured in inches. The red "x" symbol indicates the approximate origin from which all indentation is measured. In the coordinate system used, most of the indentation area that is visible is negative because it is measured relative to the point of maximum indentation from impact.

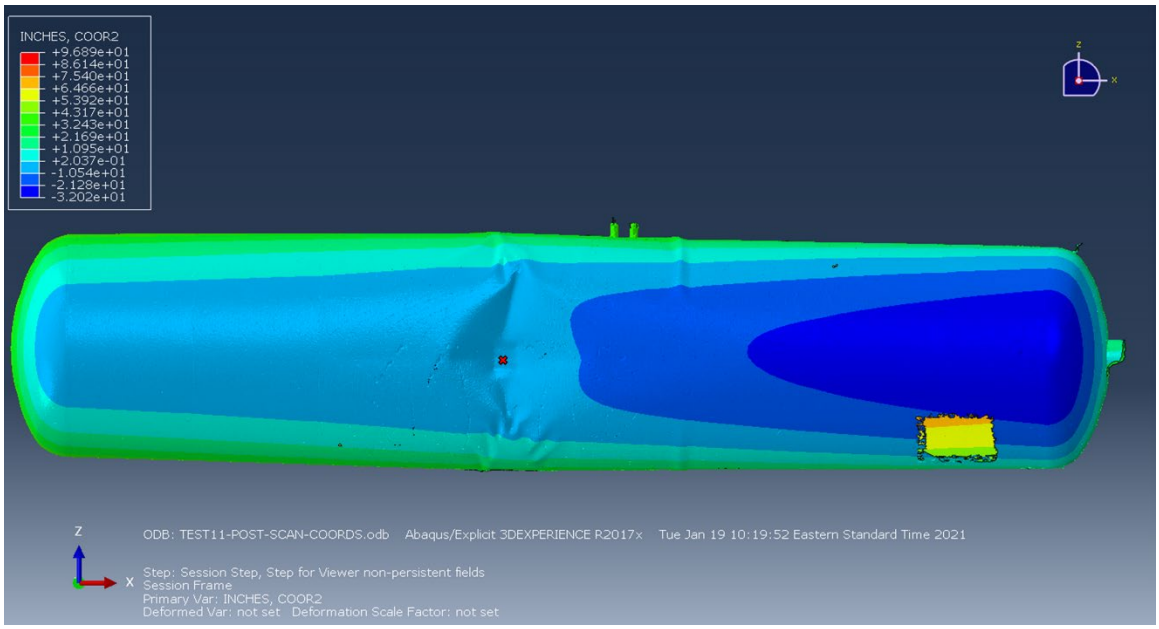

Figure 25. Contours of Indentation Measured Relative to Center of Impact, Post-test LIDAR Scan Cloud

Figure 26 shows the contour plot of indentation focused on the impact zone. The legend has been re-scaled to better illustrate the local variation in indentation in the vicinity of the impact. The contours of maximum indentation approximate the shape and size of the 12-inch by 12-inch indenter that was used in the test. These contours illustrate a residual "crease" that formed in the hoop (Z) direction around the tank with a gradual decrease in indentation moving along the tank in the axial (X) direction.

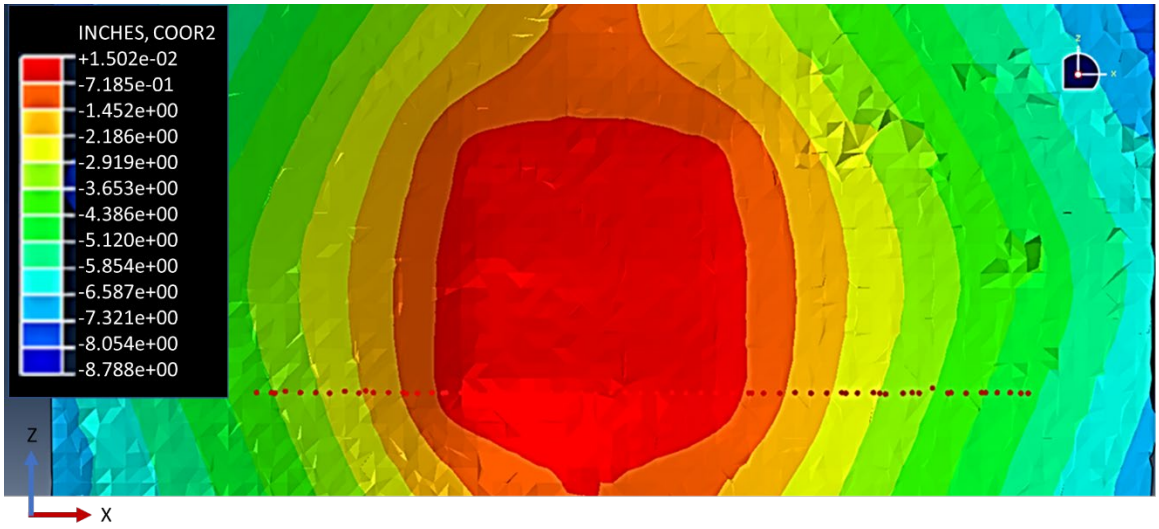

Figure 26. Contours of Indentation Measured Relative to Center of Impact in Impact Zone, Post-test LIDAR Scan Cloud

The individual points shown across the bottom of the indenter footprint in the previous image were used to generate a plot showing a "slice" of the deformation across this area. The exact extent of the impactor footprint is not known because the impactor made contact with the outer

tank which pressed against the inner tank. Because the outer tank did not puncture during this test, however, the inner tank was not directly contacted by the impactor. Figure 27 shows the slice of indentation across the bottom edge of the impactor footprint. This figure also shows a 12-inch by 12-inch indenter with 1-inch radii edges, similar to what was used in the impact test even though the impactor did not make direct contact with the inner tank in the test. In this figure, the horizontal axis shows the distance from the left-most point shown in Figure 26.

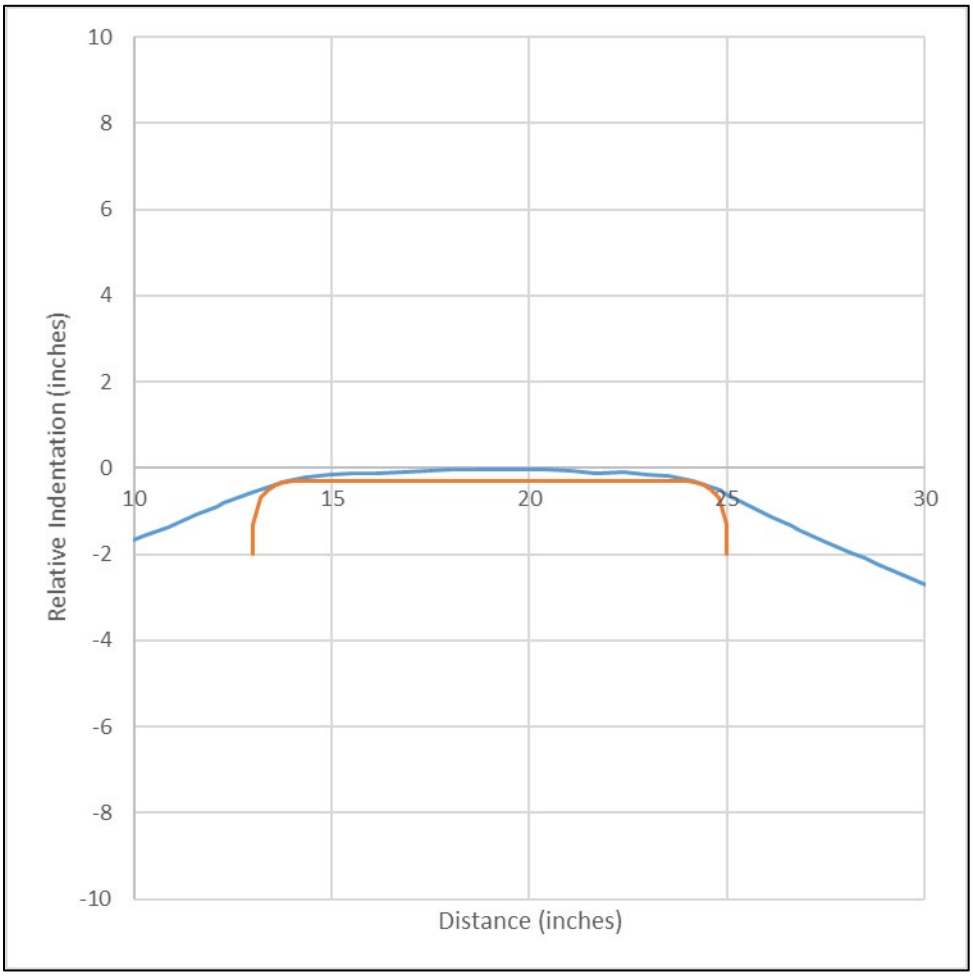

Figure 27. Deformed Shape of Tank along Bottom Edge of Impactor with Impactor Profile Overlaid

Figure 27 demonstrates that the indentation of the inner tank did not exhibit a sharp increase in deformation marking the edges of the impactor as observed in the outer tank (Figure 20). The outer tank appears to have blunted the edges of the impactor, thus the inner tank experienced a less sharp impactor compared to the outer tank.

4.4 Measured Data – Impact Test

The data collected in the test was initially processed (e.g., offset corrections, filtering, etc.) by TTCI and provided to Volpe for comparison to the FE analyses. The offset adjustment procedure ensured that the data that was plotted and analyzed included only impact-related accelerations and strains and excluded electronic offsets or steady biases in the data. To determine the necessary

offset, the data was collected before the impact was averaged. This offset was then subtracted from the entire data set for each channel. This post-test offset adjustment was independent of, and in addition to, the pre-test offset adjustment made by the data acquisition system.

The post-test filtering of the data was accomplished with a phaseless four-pole digital filter algorithm consistent with the requirements of SAE J211 [19]. A 60 Hz channel frequency class (CFC) filter was applied for the filtered acceleration data shown in this report. This section provides a brief summary of the measured data. Appendix B contains the plots of filtered data from all transducers.

The longitudinal acceleration of the ram car was one of the primary measurements in the test. Multiple accelerometers were used on the ram car to capture this data. The data was used to derive the impact energy, the deceleration of the ram car, and the contact forces between the ram and target tank car. The ram car's average longitudinal acceleration history from all the on-board accelerometers is shown in Figure 28.

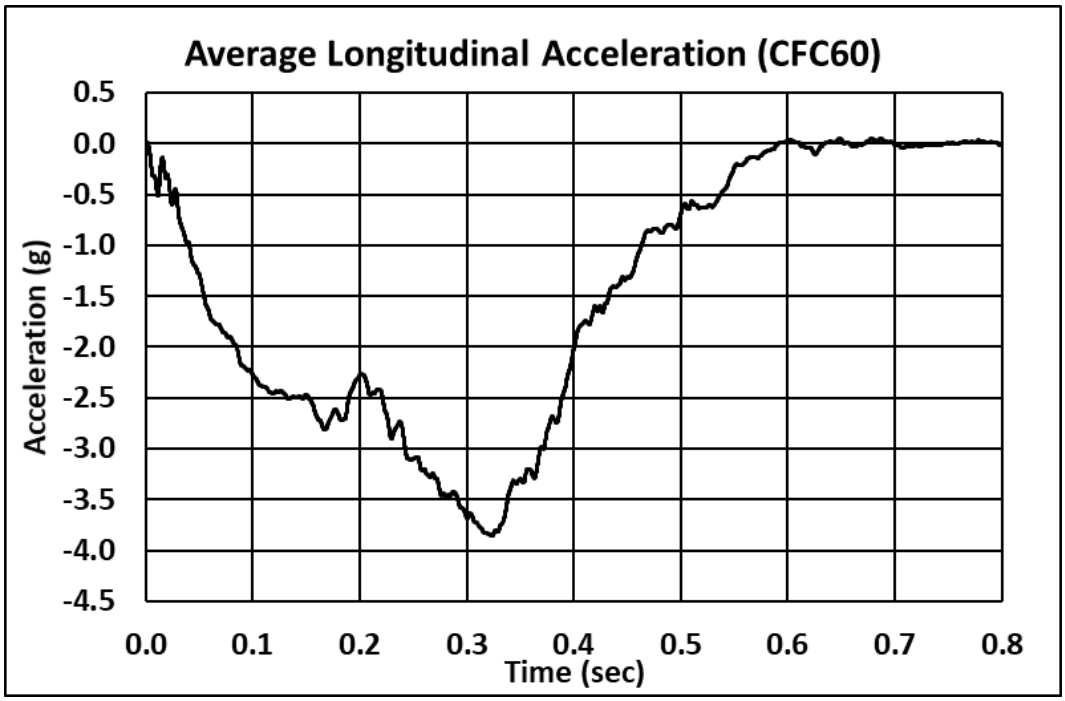

Figure 28. Longitudinal Acceleration Data (averaged)

The ram car velocity history for this test was calculated by integrating the average longitudinal acceleration of the ram car and using the impact speed measurement as an initial condition. Contact forces between the ram and target tank car were calculated as the product of the average acceleration and the mass of the ram car. Figure 29 shows both the force-time and velocity-time histories. The negative velocity is the speed of the rebounding ram car.

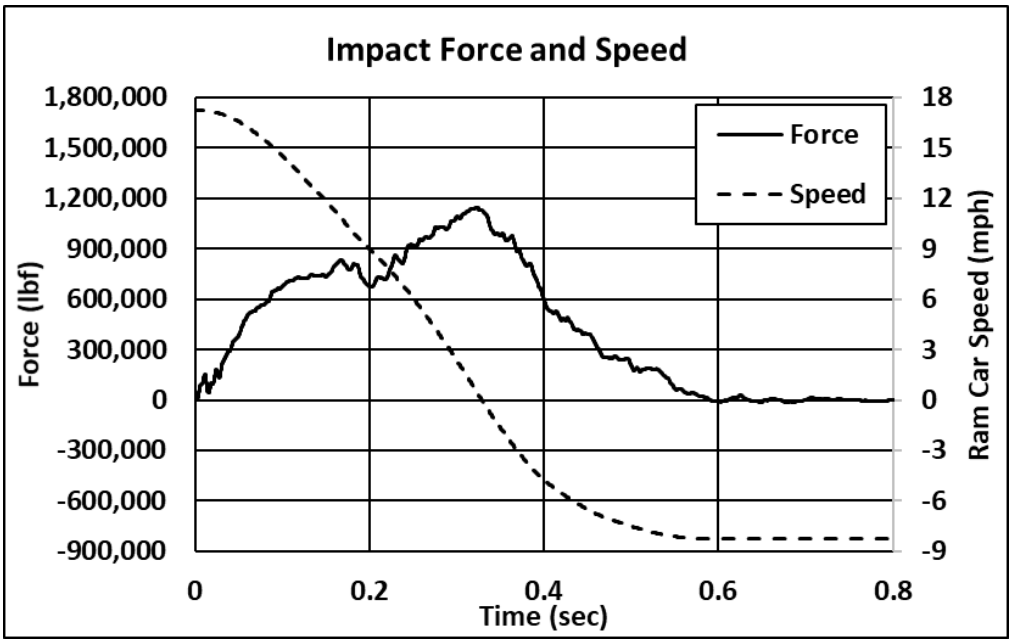

Figure 29. Impact Force and Ram Car Speed (averaged)

Similarly, the kinetic energy for the ram car was calculated from its speed-time history and mass. The energy absorbed by the tank car is calculated as the difference between the ram car's current kinetic energy and its kinetic energy at the time of impact. Figure 30 shows the ram car's kinetic energy time history and the energy absorbed by the tank car. The energy absorbed by the tank car reaches its maximum when the forward motion of the ram car ends, approximately 0.329 seconds after impact.

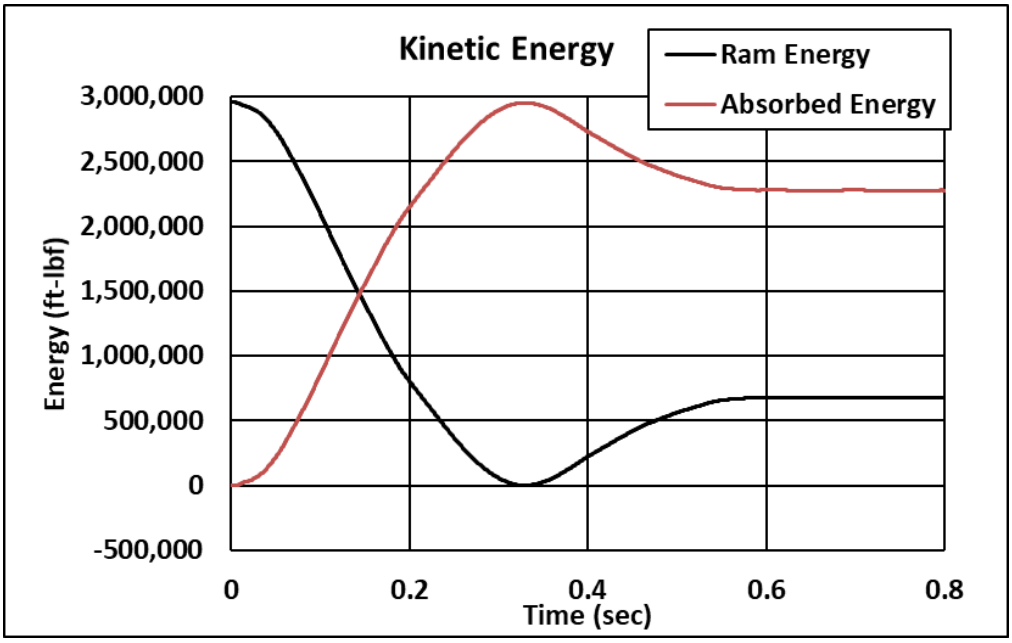

Figure 30. Kinetic Energy Time-history of Ram Car

The total kinetic energy of the ram car was approximately 2.96 million ft-lbf, and the energy absorbed by the tank car just prior to rebound was approximately 2.95 million ft-lbf. The

difference between the initial kinetic energy and the energy absorbed by the tank before rebound was approximately 2,300 ft-lbf or approximately 0.079 percent of the total kinetic energy. This insignificant difference is likely the result of the round-off during numerical integration, the averaging of multiple accelerometer channels, or the filtering the accelerometer signal.

Another significant impact response measured in the test was the effect of the internal pressure as the tank indentation formed and reduced the volume of the tank. The tank was filled to approximately a 17.6 percent outage volume with water and then pressurized to 50 psi above atmospheric pressure. Water can be approximated as incompressible for the impact behavior. As a result, the small air volume in the outage, initially at 50 psig, was compressed as the dent formation reduced the tank volume. This caused the internal pressure to rapidly increase. As described in Section 3.3, pressure transducers were mounted at several locations inside the tank car, both within the water and in the outage.

Figure 31 shows pressure data near the center of the tank car (i.e., transducers TP3000 at the top of the inner tank, TP3090 on the back wall of the inner tank, TP3180 on the bottom, and TP3270 on the front wall of the inner tank). Pressure transducer TP3090 started out with a +30 psi offset above the nominal 50 psig initial pressure, and the readings quickly became unrealistic before the channel eventually quit responding. It is believed that this was due to a faulty transducer that was not detected until after the tank car had been filled and pressurized. The early spike seen in pressure transducer TP3270 corresponds to the point at which the gap between the outer and inner shell was closed and the outer shell contacted the inner shell. It should also be noted that the power/data wires from the transducers in the tank car were dislodged from their tie-offs along the walls of the tank car during the impact. When the tank car was entered to retrieve the transducers after the test, the wires were found to be hanging down from the top of the tank car and somewhat tangled together. The severe spikes seen in the data beginning at around 0.17 seconds are most likely the result of the dislodged wires being “yanked” around during the impact. Ignoring the bad transducer and the large spikes, the data indicates that the overall pressure in the tank car rose to about 77 psig. Additionally, the sloshing motions of the water in the tank created local pressure variations of up to 45 psi. Although the pressure reached 77 psig, the data does not indicate that the pressure relief valve opened—the PRV was set to discharge at 75 psig.

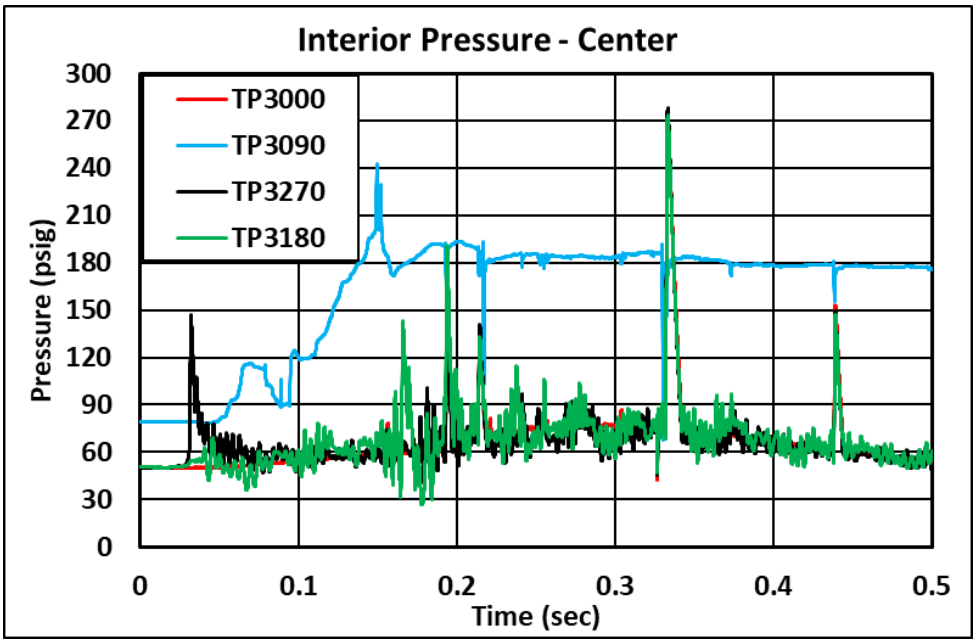

Figure 31. Pressure Data Measured Near the Center of the Tank Car

The remaining quantitative measurements made for the tank car impact behavior were displacement histories recorded with string potentiometers and laser displacement transducers. These measurements included internal tank deformations (i.e., measured with string potentiometers), external tank deformations (i.e., measured with lasers), and external tank movements at both ends of the tank (i.e., also measured with string potentiometers). The layout of the string potentiometers was described in Section 3.3, and the layout of the lasers was described in Section 3.4.

The measured displacements for the tank car internal string potentiometers (i.e., TD1Y through TD5Y) are shown in Figure 32. TD1Y (i.e., 48 inches from center B-end) began to deviate from its counterpart TD5Y (i.e., 48 inches from center A-end) at around 0.16 seconds and never recovered. During the post-test instrumentation retrieval, it was noted that TD1Y's string became dislodged from its anchor point on the opposite wall of the tank. The signal from TD3Y was also compromised around 0.35 seconds. These problems are most likely the result of the loose wiring inside the tank. TD2Y and TD4Y (i.e., 24 inches from center B-end and 24 inches from center A-end) had almost identical responses throughout most of the impact. However, TD2Y did indicate greater plastic deformation than TD4Y.

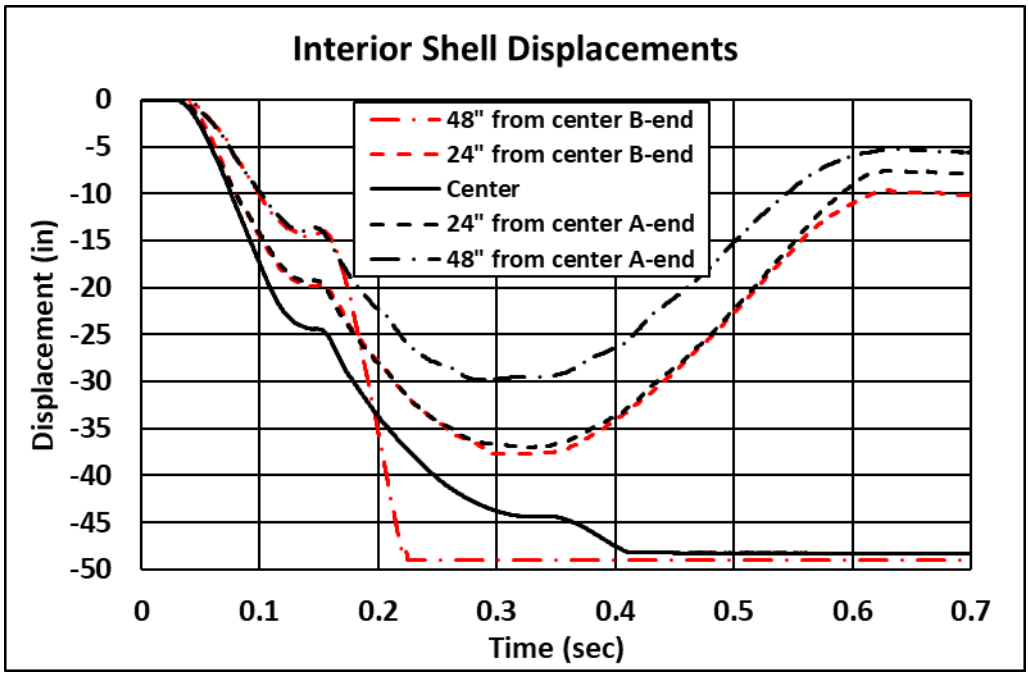

Figure 32. Internal Longitudinal Displacements

TD3Z recorded the vertical tank deformation during impact, presented in Figure 33. The data became extremely unstable at approximately 0.23 seconds and did not recover until approximately 1.6 seconds after impact, corresponding closely to the time when the rebounding tank car came to a stop. During the post-test instrumentation retrieval, it was noted that the shielding around the data wire had been damaged during the impact.

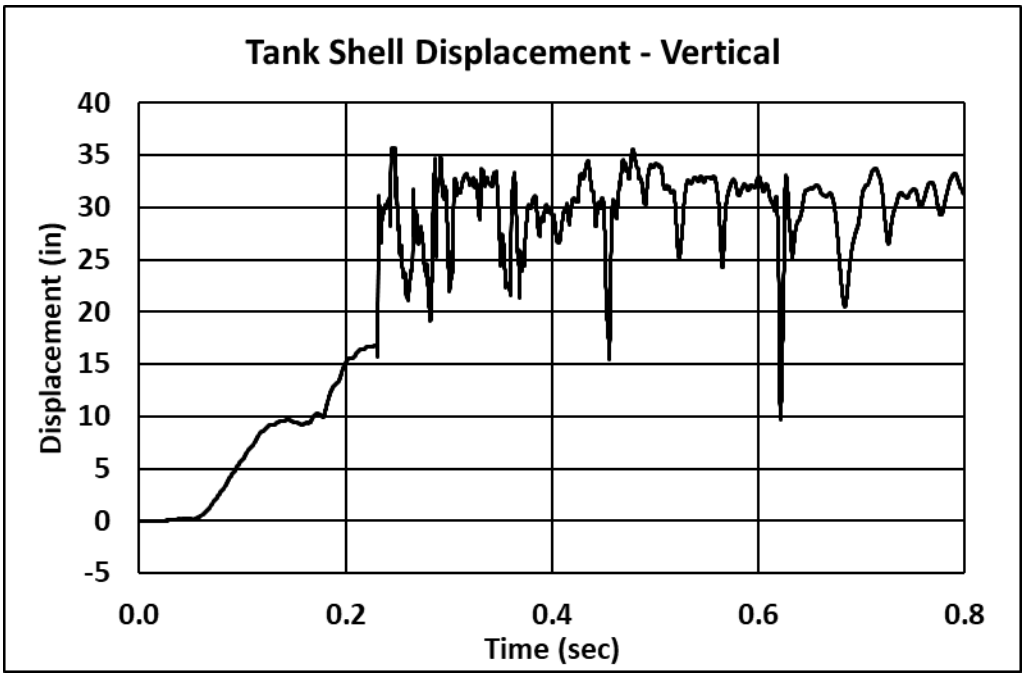

Figure 33. Internal Vertical Displacement

Deformation of the tank around the impact was also calculated using the lasers on the front of the ram car as shown in Figure 34. The data series "Deformation Measured at BD1Y" and "Deformation Measured at BD5Y" show the magnitude of the tank car's deformation at positions 48 inches to the left and right of the center of impact, respectively, over time. "Deformation Measured at BD2Y" and "Deformation Measured at BD4Y" show the magnitude of the tank car's deformation at positions 24 inches to the left and the right of the center of impact, respectively. By measuring the distance between the front of the ram car and the crash wall and distance between the front of the ram car and the front of the tank car, the distance between the front of the tank and crash wall—and correspondingly the longitudinal deformation of the tank car—can be easily calculated. The maximum longitudinal deformation is expected to correspond to the time at which the forward motion of the ram car stopped (i.e., at approximately 0.329 seconds after impact).

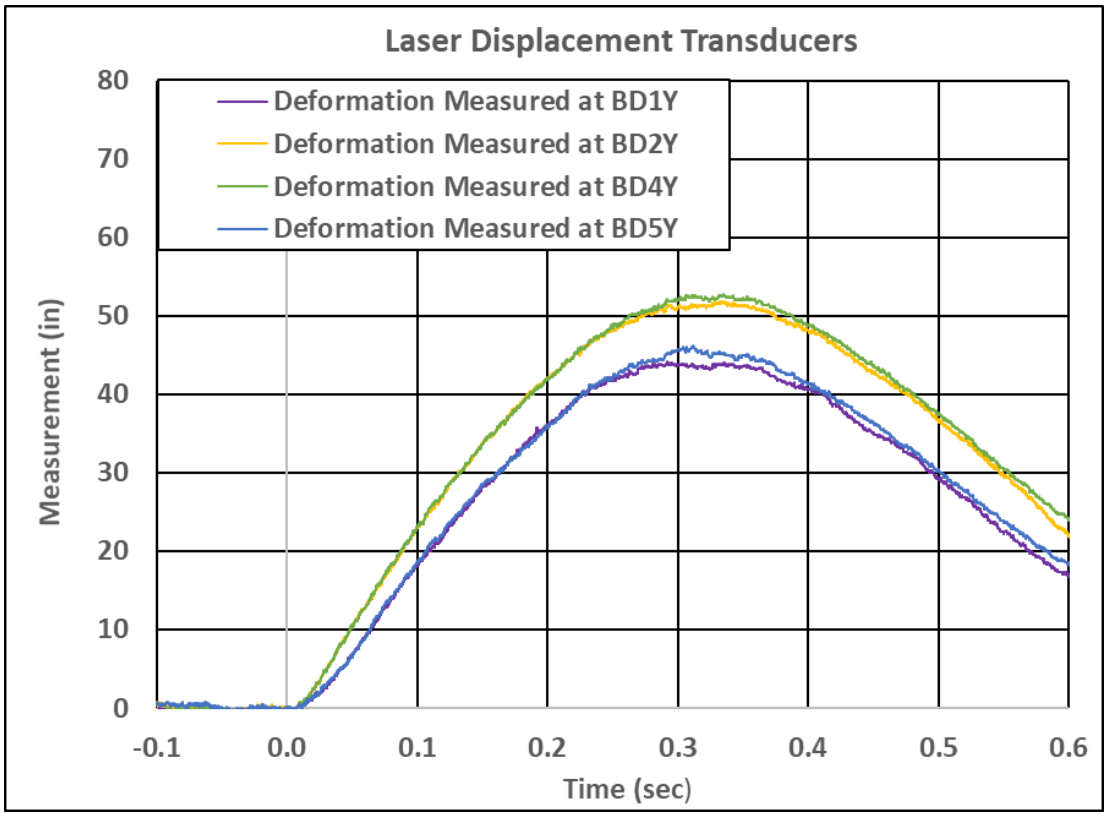

Figure 34. Tank Car Deformation Measured with Laser Displacement Transducers

The measured displacements for the tank car external string potentiometers are shown in Figure 35 and Figure 36. The displacements of the ends of the tank car were significantly delayed from the motions in the impact zone and little displacement is seen for the first 0.1 seconds of the response. The string potentiometers intended to measure the displacements at the tank car heads were rendered inoperable when the strings on the string potentiometers exceeded their range and broke about 0.18 seconds after the ram made contact with the tank car. The reason for the string breakage was determined to be the result of incorrectly setting the zero locations of the string potentiometers which did not leave sufficient string travel room to account for the full forward motion of the tank car after impact. However, the string potentiometers used to measure the displacement at the skids recorded data throughout the test. The responses at the

two ends are noticeably different with the A-end showing a momentary reversal of direction after the initial rebound from the crash wall and the B-end ending up further from the crash wall after the rebound.

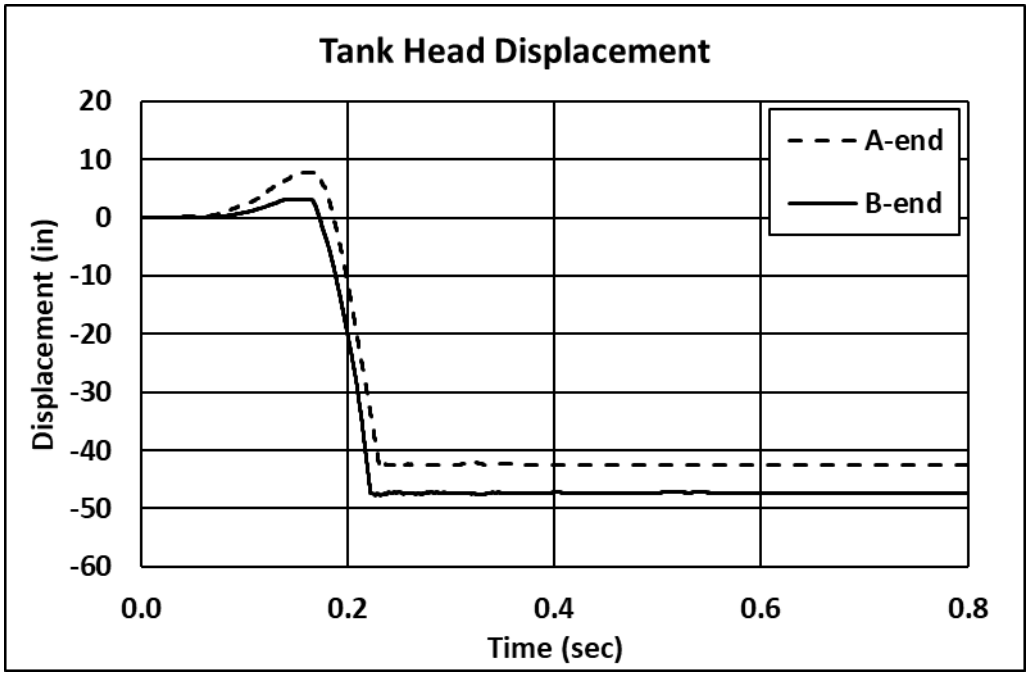

Figure 35. External Longitudinal Displacements – Tank Car Heads

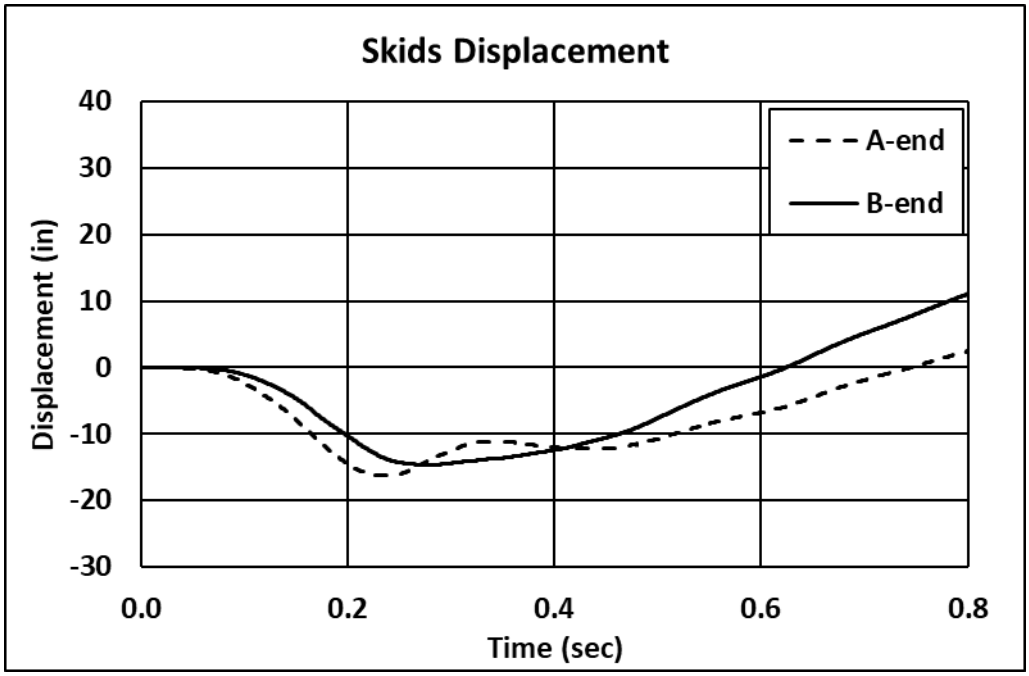

Figure 36. External Longitudinal Displacements – Skids

4.5 Measured Data – Material Testing

In previous side impact tests, the tensile properties of the steels composing the tanks were not measured prior to the tests due to the risk of compromising the structure of the tank. Tensile coupons were cut after the test, and the pre-test FE model was updated with the actual material properties. Because this was the first side impact test in the test program with a surrogate tank car constructed specifically for the purpose of a side impact test, tensile coupons could be cut prior to the test during the tank car's construction to determine the material properties of the inner and outer tanks. Pre-test material characterizations were performed on the inner tank's stainless steel and the outer tank's TC-128B steel, both in the unwelded condition (i.e., parent material).

Following the test, additional material characterization was performed on the inner and outer tank materials. The outer tank had additional coupons cut from a base (unwelded) TC-128B plate (parent material), from a circumferential joint that had been welded as part of the original outer tank's fabrication (factory weld), and from the circumferential joint that closed the outer tank after the inner tank was installed (closure weld). The inner tank had additional coupons cut and subjected to tensile testing at various combinations of strain rates and cryogenic temperatures. Coupons from both tanks were also subjected to Charpy V-notch (CVN) testing. The outer tank's TC-128B was CVN tested in the parent material, in the heat-affected zone (HAZ) of each weld type, and in each weld type. The inner tank's T304 stainless steel was CVN tested at different cryogenic temperatures.

4.5.1 Pre-test Material Characterization

The manufacturer of the outer tank excised a representative section of the 9/16-inch outer shell in the PWHT condition and machined 2-inch gage length smooth round bar (SRB) tensile specimens. TTCI cut 2-inch gage length flat rectangular (e.g., dogbone or DB) coupons from a sample of the 1/4-inch inner tank provided by the inner tank's manufacturer. All pre-test coupons were tested according to the requirements of ASTM E-8 [20] at room temperature.

The results of the pre-test tensile characterization revealed that the TC-128B outer tank and T304 inner tank met their respective requirements in AAR Specifications for Tank Cars Appendix M-1002[10] and ASTM A240 [4], respectively, for yield strength (YS), ultimate tensile strength (UTS), and elongation at break with a 2-inch gage length (EB-2in). Table 11 summarizes the average mechanical properties from eight TC-128B samples and three T304 samples.

Table 11. Summary of Average YS, UTS, and EB-2in from Tensile Tests at Room Temperature Conducted Pre-impact

Steel	**YS**	**UTS**	**EB-2in**
	ksi	*ksi*	*%*
T304 Stainless Steel	56.7	96.3	64.1
TC-128B Carbon Steel	64.9	88.8	31.5

These tensile test results were used, in part, to develop the material properties input regarding the pre-test FE model. Appendix B4 contains properties for the individual tensile specimens.

4.5.2 Post-test Material Characterization

Following the impact test, additional post-test material characterization testing was conducted on both the inner tank's T304 stainless steel and the outer tank's TC-128B steel. These tests were conducted to provide additional data for input to future FE models and to study whether different welding processes used on the outer tank resulted in a measurable difference in material properties around each type of weld.

Outer Tank – TC-128B

The outer tank did not experience any puncture or weld failure in the June 2020 test. However, there has been interest in the behavior of welded joints in tank cars during impact events from various stakeholders during previous full-scale impact tests. As discussed in Section 2.2, the DOT-113 surrogate features two different types of circumferential welds on its outer tank. Due to the unique nature of the closure weld on a DOT-113 tank car, there is further interest in understanding whether this weld exhibits any difference in mechanical properties compared to the remaining "factory" welds on the outer tank that are typical to multiple specifications of tank car. Thus, a series of post-test material characterization tests on the two different types of circumferential welds on the outer tank was conducted.

Post-test TC-128B steel testing focused on investigating the following: 1) whether the circumferentially welded TC-128B steel exhibited any considerable mechanical differences compared to the parent TC-128B steel, and 2) whether the "factory" circumferential welds and the circumferential closure weld exhibited any considerable mechanical differences when compared to each other.

This section contains a summary of the post-test TC-128B carbon steel material test results. Appendix B4.2 discusses the complete set of results. Following the impact test, tensile coupons were excised from the outer tank in areas that experienced limited permanent deformation. These coupons were excised from areas parallel to the axis of the tank such that tension would be applied across a weld. The parent TC-128B steel was found to have similar properties to those reported during pre-impact tensile tests.

Regardless of the type of weld, all welded specimens fractured both outside the gage and outside the weld itself. One welded coupon taken from the closure weld was rejected by the lab due to a lack of fusion on the interior of the weld. Because the fracture occurred outside of the gage marks, accurate measurements of the EB-2in could not be made for the welded coupons. Additionally, YS was not reported for all coupons tested in the first round of testing. Table 12 contains a summary of the average UTS for each TC-128B steel material condition tested in the axial orientation in the first round of tensile testing. The UTS was found to be within the specification requirements at all conditions tested. The parent TC-128B steel was also found to have similar properties to those reported during pre-impact tensile tests, indicating the material was not significantly strain-hardened by the impact test.

Table 12. Summary of Average UTS from Axial Orientation Tensile Tests on Steel in Welded Condition

Type -	UTS *ksi*
Parent material	86.5
Factory weld	84.8
Closure weld	87.0
Specification requirement	81–101

A second group of tensile test specimens were cut from the outer tank and oriented parallel to the hoop direction of the tank. These specimens were cut from the weld, the HAZ adjacent to the weld, and the parent plate beyond the HAZ. This was done to ensure that the source of the material (i.e., weld, HAZ, or parent material) that ultimately fractured in each coupon was unambiguous. Additionally, CVN tests of TC-128B steel in each material condition were conducted to understand whether the energy to fracture the material varied significantly across the different conditions. The second round of testing also included metallography performed on several coupons that had been tensile tested in the longitudinal direction (i.e., the first round of testing). Appendix B4.2 includes the complete second-round testing report.

Table 13 contains the average YS, UTS, and EB-2in values from the post-test TC-128B steel in each material condition tested in the second round of tensile testing. The average values were within the requirements of the specification for TC-128B steel in each condition tested. It should be noted that because the coupons were tested with tension applied in the hoop direction, they had initial curvature in them due to the curvature of the tank's shell. This curvature caused the initial response measured during the tensile test to appear "soft," as the initial response to a tensile load was to straighten the curvature, not to uniformly extend the gage area. In its report, the testing lab noted that three of the four closure weld tensile test specimens exhibited an apparent lack of fusion and porosity defects.

Table 13. Average Post-impact TC-128B Steel Material Properties in Hoop Direction

Material Source	Type -	YS *ksi*	UTS *ksi*	EB-2in *%*
Post-impact, Hoop Direction	Parent Material	58.9	82.9	31.5
Post-impact, Hoop Direction	Factory Weld	54.7	84.8	27
Post-impact, Hoop Direction	HAZ - Factory Weld	60	82.8	33.5
Post-impact, Hoop Direction	Closure Weld	77.4	92.9	33.1
Post-impact, Hoop Direction	HAZ - Closure Weld	58.5	83.4	31.9
Specification Requirement		*50 min*	*81–101*	*22 min*

Table 14 contains the average CVN energy values from the post-test TC-128B in each material condition tested.

Table 14. Post-impact TC-128B Steel CVN Energies

Material Source	Type -	Average CVN Energy *(foot-pounds)*
Post-impact	Parent material	111.8
Post-impact	Factory weld	112.3
Post-impact	HAZ - factory weld	121.8
Post-impact	Closure weld	76.3
Post-impact	HAZ - closure weld	103.8

The second round of test results showed that the TC-128B steel taken from the closure weld had an average absorbed CVN energy that was significantly lower than TC-128B steel in any of the other material conditions. At the same time, the tensile test results did not indicate that the TC-128B steel taken from the closure weld had lower than average yield strength, UTS, or EB-2in when compared with TC-128B steel in any other tested material condition. Taken together, these results suggest that further study of the closure weld may be appropriate, as the CVN and tensile test results appear to lead to different conclusions. Taken on its own, the CVN test results would indicate that the closure weld behaves significantly differently from the other material conditions that were tested, absorbing significantly less energy for the same CVN test conditions. On the other hand, the tensile results indicate the closure weld did not have a noticeable loss of strength or ductility. Some other effect not being studied in this round of testing (e.g., increased strain-rate sensitivity and increased porosity) may need to be further investigated.

Inner Tank – T304 Stainless

This section contains a summary of the post-test T304 stainless steel material test results. Appendix B4.4 contains the complete set of results. One of the lessons learned following the previously conducted DOT-113 impact test was that the stainless steel used in the inner tank may possess strain-rate effects that could affect the puncture response of the inner tank [3]. This was an area of follow-up that could be investigated using T304 stainless taken from the DOT-113 surrogate. Further, the ultimate goal of the DOT-113 tank car testing program is to develop FE models representative of the DOT-113 tank car in LNG service conditions. One aspect of the LNG service conditions that needs to be accounted for in an FE model is the T304 stainless steel inner tank's mechanical properties at cryogenic temperatures. Thus, the post-test mechanical testing for the DOT-113 surrogate tank included a matrix of tensile tests at various combinations of temperature and strain rate. The target strain rates and temperatures are shown in Table 15. Three coupons were tested at each combination of temperature and strain rate.

Table 15. Temperature and Strain Rate Targets for T304 Post-test Characterizations

Tensile Strain Rate (s^{-1})	Temperature (K)
5×10^{-4} s^{-1}	295, 200, 111, 77
5×10^{-2} s^{-1}	295, 200, 111, 77
5×10^{-1} s^{-1}	295, 200, 111, 77
5×10^{0} s^{-1}	295, 200, 111, 77
5×10^{1} s^{-1}	295, 200, 111, 77

Additionally, CVN testing was planned at each of the four test temperatures used for tensile testing. The CVN test data was expected to be useful in calibrating the FE models of T304 material at various temperatures and strain rates.

The complete set of post-test T304 tensile and CVN data can be found in Appendix B4.4. This section summarizes the results. The testing laboratory encountered several challenges to conducting the tensile tests at the target temperatures and strain rates. Initially, 2-inch (full-size) gage length ASTM E8 tensile coupons were to be used at all temperatures and strain rates indicated in Table 15. Tests were successfully conducted at 295 K and reportedly at all nominal strain rates. However, two limitations were identified following this first round of testing. First, the test chamber could not be maintained at the desired 111 K, but 200 and 77 K were thought to be achievable. Second, based on the strength of the material and the strain rates targeted, the laboratory required subsize specimens to be able to attempt testing at cryogenic temperatures. The subsize coupons featured a reduced length and had their thicknesses reduced from a nominal value of 1/4 inch to approximately 0.06 to 0.07 inch. Table 16 shows the actual strain rates attained for the subsize specimens.

Table 16. Actual Temperature and Strain Rate for T304 Post-test Characterizations

Tensile Strain Rate (s^{-1})	Temperature (K)
5×10^{-4} s^{-1}	295, 210, 77
5×10^{-2} s^{-1}	295, 210, 77
5×10^{-1} s^{-1}	295, 210, 77
5×10^{0} s^{-1}	295, 210, 77
1.6×10^{1} s^{-1}	295, 210, 77

Additionally, the test laboratory measured strain using a strain gage installed in the center of the gage length of each coupon. At the two highest strain rates (i.e., approximately 5 and 16 s^{-1}), there appeared to have been substantial dynamic effects that influenced the strain measurements.

Three tensile coupons were tested at each combination of strain rate and temperature for a total of 45 tensile coupons. The mechanical properties (YS, UTS, and EB-2in) of the stainless-steel samples at each temperature and strain rate are summarized in Table 17. The full-size coupons used a 2-inch gage length, and the subsize coupons used a 1 1/2-inch gage length.

Table 17. Summary of Average YS, UTS, and EB-2in from Tensile Tests of Stainless Steel

	Nominal Tensile Strain Rate (s^{-1})	Average Actual Tensile Strain Rate[10] (s^{-1})	Full-size Coupon 295 K 71 °F	Sub-size Coupon 295 K 71 °F	Sub-size Coupon 210 K -82 °F	Sub-size Coupon 77 K -321 °F
Average YS (1,000 psi)	5×10^{-4}	4.3×10^{-4}	Not reported	47.3	61.5	75.6
	5×10^{-2}	5.0×10^{-2}	Not reported	54.3	70.9	77.0
	5×10^{-1}	5.5×10^{-1}	Not reported	56.8	76.9	85.9
	5×10^{0}	4.9×10^{0}	Not reported	61.8	92.8	107.5
	5×10^{1}	1.6×10^{1}	Not reported	73.3	98.1	114.1
Average UTS (1,000 psi)	5×10^{-4}	4.3×10^{-4}	96.5	95.0	147.8	233.5
	5×10^{-2}	5.0×10^{-2}	95.6	88.2	132.9	179.3
	5×10^{-1}	5.5×10^{-1}	99.1	90.2	129.5	176.9
	5×10^{0}	4.9×10^{0}	101.1	95.4	133.7	177.2
	5×10^{1}	1.6×10^{1}	101.2	103.6	133.2	180.7
Average EB-2in (%)	5×10^{-4}	4.3×10^{-4}	62.6	63.8	37.2	38.8
	5×10^{-2}	5.0×10^{-2}	52.6	45.1	38.6	29.4
	5×10^{-1}	5.5×10^{-1}	46.6	44.1	39.8	31.2
	5×10^{0}	4.9×10^{0}	54.4	49.5	37.1	35.7
	5×10^{1}	1.6×10^{1}	49.7	47.7	42.1	35.1

The tensile testing demonstrated that the stainless steel in the inner tank exceeded the minimum values of YS, UTS, and EB-2in required of ASTM A240 Type 304 stainless steel at room temperature. The testing also demonstrated that the YS increased with decreasing temperature and with increasing strain rate. The UTS increased with decreasing temperature, but it decreased with increasing strain rate only to a rate of approximately 5×10^{-2} s^{-1}. Beyond that strain rate, the reported UTS remained fairly constant. The average EB-2in is more difficult to generalize as the properties decreased non-monotonically with increasing strain rate. In general, the EB-2in decreased with decreasing temperature.

CVN testing was performed at temperatures of 77 K, 111 K, 200 K, and 295 K according to ASTM E23 [21]. Three coupons were tested at each temperature for a total of 12 CVN tests. CVN testing resulted in partial fracture of each test coupon at each temperature. Tearing initiated at the V-notch, but deformation of the coupon allowed it to slip through the test specimen without fracturing through the full thickness. Figure 37 shows example pre- and post-test CVN specimens.

[10] Full-size specimen strain rates were reported as nominal rate, but the actual rates were unknown. Sub-size specimen results included data on actual strain rates attained during tests.

Figure 37. Pre- (top) and Post-test (bottom) CVN Specimens

Table 18 contains a summary of the results of the CVN testing performed at each temperature. While no exceptions from the CVN procedures given in ASTM E23 were noted, the results of the tests were ambiguous due to the incomplete fracture of every specimen. Typically, the kinetic energy lost by the striker is the energy required to fracture the specimen. In the case of a specimen deforming out of the fixture, a portion of the energy lost by the striker went toward fracture of the specimen, and a portion of the energy went toward accelerating the coupon out of the fixture. Since the specimen did not completely fracture, it is not known how much energy would be necessary to fully fracture each specimen if it were not possible for the specimen to escape from the fixture. Additionally, the results do not demonstrate any clear relationship between absorbed energy and temperature. However, the results do indicate that even at the lowest cryogenic temperature tested (77 K), the T304 stainless steel remained sufficiently ductile to deform and slip out of the fixture before fracturing completely.

Table 18. Summary of T304 CVN Energies at Various Test Temperatures

CVN Energy (ft-lbf)	295 K 71 °F	200 K -100 °F	111 K -260 °F	77 K -321 °F
Average	27	30.5	34	30

5. FE Model Development

Researchers developed FE models of the DOT-113 surrogate tank car prior to the test to help estimate the desired impact speed. The purpose of these pre-test FE models was to provide estimates of the speed range where puncture could be expected to occur while considering uncertainties in the exact puncture speed, lading conditions, etc. Volpe developed the FE models that incorporated and expanded upon several modeling techniques used during simulations of previous tank car impact tests [5] [13] [7] [8] [14] [9]. The DOT-113 models required definition of the tank car geometry, geometry of the impact setup (e.g., impact wall, impactor, etc.), definition of boundary conditions, constraints, initial conditions, and development of several material models. Additionally, modeling features such as element types, mesh sizes, and fluid and structure interactions were selected.

The models were developed using the Abaqus/CAE preprocessor and executed in Abaqus/Explicit [22]. Abaqus/Explicit is a commercially available, general purpose, nonlinear FE solver capable of simulating dynamic impacts involving complex material behaviors such as plasticity and puncture. The solid mechanics simulation features used in the DOT-113 models included defining material models to describe the elastic-plastic and fracture behaviors of the inner and outer steel tanks. To model damage initiation for fracture, the Bao-Wierzbicki (B-W) triaxiality-based damage initiation model was used [23].

The Abaqus software also includes several modeling techniques that can be used to represent the water and air phases of the lading, permitting these two parts to be modeled explicitly. The water and air phases of the tank were modeled using pneumatic cavity and hydraulic cavity approaches, respectively. These fluid modeling techniques had been used in several previous tank car tests, including the previous test of a DOT-113 tank car [3].

5.1 Overview of Models

A DOT-113 tank car presents several unique FE modeling challenges compared to modeling single-walled tank cars. The DOT-113 tank car features an external tank and an internal tank, with a desired FE model capability to puncture both tanks. This required both tanks be modeled with techniques that would simulate puncture.

The pre-test FE model for this test was the first one in FRA's side impact test series where the actual plastic stress-strain responses of both tanks were characterized prior to the test and used as inputs to the model. The development of the FE model material inputs for the TC-128B outer tank material responses is described in detail in Appendix F3. The development of the FE model material inputs for the T304 inner tank material is described in detail in Appendix F4.

Puncture-capable FE models feature more complex material definitions and meshes than non-puncture models. Puncture-capable models include inner and outer tanks with refined meshes in the impactor contact areas, and material modeling behaviors to simulate element degradation and removal. For the DOT-113 surrogate, the refined area was meshed using solid elements on both the inner tank and the outer tank. While the desired outcome of the DOT-113 surrogate test was puncture of neither tank, the pre-test FE model needed to be capable of allowing both tanks to puncture. To simulate the puncture of both tanks, the solid patch of elements on the outer tank needed to be large enough to not only capture the initial tearing of the tank (which typically occurs beneath a corner of the impactor), but also allow the tear to propagate until the point when

the inner tank punctured. This required a much larger solid patch of elements on the outer tank of the modeled DOT-113 surrogate than for standard single-walled tanks. It was important to include a sufficiently large patch of solid elements in the outer tank to allow the tear to propagate fully without being artificially arrested the limits of the solid patch, as that could result in the modeled DOT-113 surrogate placing less demand on the inner tank than would be experienced during an impact test.

While an actual cryogenic tank car would feature insulation around the entire inner tank and a vacuum in the annular space, the DOT-113 surrogate in this test had an 8-foot-by-8-foot section of MLI in the impact region between the tanks and no vacuum, i.e., the annular space was open to atmosphere. The annular space in the FE model was also open to atmosphere, but it was hypothesized that the MLI would not produce a significant structural response, so the FE model did not include a representation of MLI in the annular space. Including MLI in the tested DOT-113 surrogate's impact zone would either confirm or refute the assumption that the MLI's structural properties could be neglected in the FE model.

The point of impact on the tested DOT-113 tank car surrogate was planned to be slightly offset (2 feet) from the centerline of the car. A symmetry boundary condition was used in the pre-test FE models to reduce the mesh size with the shorter half of the tank included in the model. This means that the overall length of the tank was shortened by 2 feet in the symmetric pre-test FE models. This approach was taken because it was expected to be conservative, i.e., result in a lower puncture speed, due to the tank's overall stiffness increasing slightly. The post-test FE models include the full-length of the tank car without a symmetry condition.

The tank car surrogate's geometry was simplified, and structures expected to have an insignificant effect on the puncture speed (e.g., the stub sills) were omitted. These simplifications have a relatively minor effect on the impact response of the tank under the test conditions. Figure 38 shows the symmetric pre-test FE model and full-length post-test FE test model.

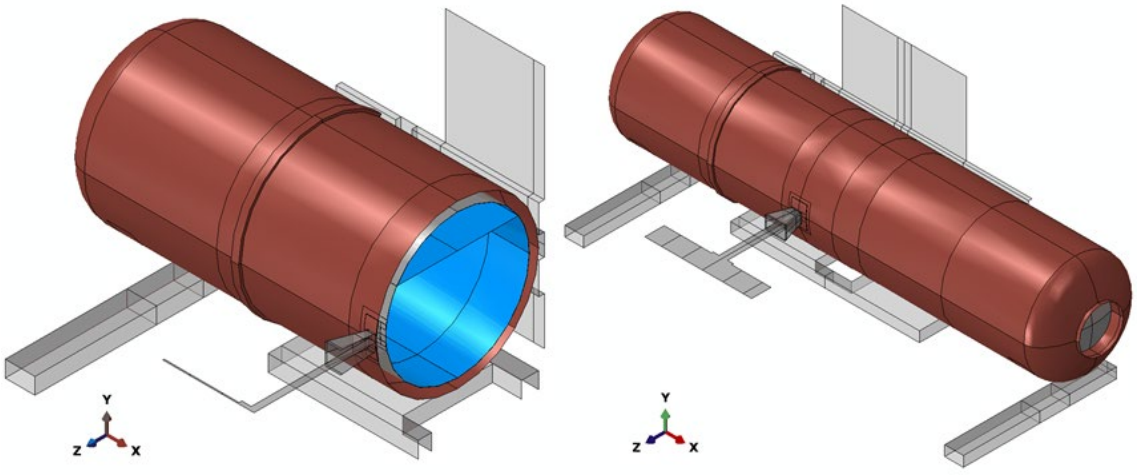

Figure 38. Pre-test (left) and Post-Test (right) FE Models

The lading in the DOT-113 surrogate FE model was represented using a hydraulic cavity for the water phase and a pneumatic cavity for the pressurized air phase. This approach is the same as what was used for the FE models of the two previous tests of DOT-105 tank cars [8] [24] and the test of a DOT-113 tank car in 2019 within the FRA side impact testing program [3]. The cavity approach is a simplified modeling technique that represents the fluid species (either gas or liquid)

using uniform pressure over the entire volume of that species. This uniform pressure will change over the course of the impact simulation as the volume enclosing the pneumatic cavity is reduced through tank deformation. This dual-cavity approach to fluid modeling gave a satisfactory representation of the fluid response seen in this test with a pressurized DOT-113 surrogate tank while offering considerable computational efficiency over an explicit representation of the liquid phase (e.g., Lagrangian, Eulerian, or smoothed particle hydrodynamics [SPH] representations). The cavity approach is sometimes referred to as the uniform pressure method (UPM) in FE models of air bags in automotive crash simulations.

The parts included in the FE model can generally be divided into three categories: rigid bodies, deformable bodies made of steel, and deformable bodies made of other materials (membrane). Figure 39 shows a section view with the cutting plane passing through the center of the impactor. This image includes annotations denoting the various parts making up the assembly of the DOT-113 tank car FE model.

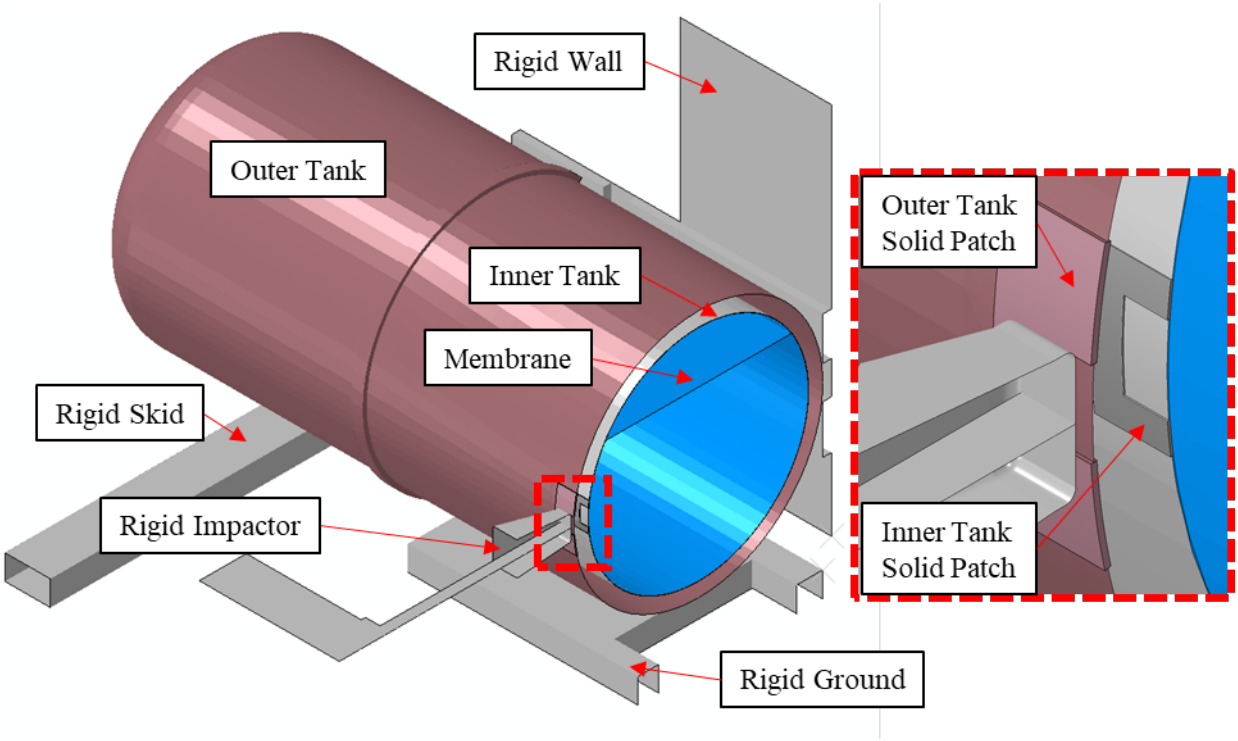

Figure 39. Section View Through Impact Plane with Annotated Parts

Table 19 contains a summary of the parts making up the FE model used in the pre-test puncture simulations. This table contains the weight of the part in the FE model and the number of elements in that part's mesh. Due to adjustments made between the pre-test FE models and the post-test FE models, the meshes and part weights were slightly different between the pre-test and post-test FE models. A full description of each part in the pre-test and post-test FE models can be found in Appendix D.

Table 19. Summary of Parts in Post-Test FE Models

Part Name	Type of Body	Material	Number of Elements	Part Weight (lbf)
Impactor	Rigid	-	86,988	297,200
Wall	Rigid	-	2,378	-
Skid	Rigid	-	368	9,600
Ground	Rigid	-	1,664	-
Outer tank (shell)	Deformable	TC-128B carbon steel	17,541	33,900
Outer Tank (solid)	Deformable	TC-128B carbon steel	434,448	64
Inner Tank (shell)	Deformable	T304 stainless steel	18,964	12,800
Inner Tank (solid)	Deformable	T304 stainless steel	264,000	9
Internal membrane	Deformable	Other	35,718	133,000

From this table, the total weight of the parts in the FE model corresponding to the entire DOT-113 surrogate (e.g., inner and outer tanks, bolsters, and water) would be approximately 199,000 lbf. The single heaviest part in the DOT-113 surrogate FE model is the internal membrane that has water added as a non-structural mass. As previously discussed in Section 2.2.2, water was used in the test to account for both the mass and the dynamic effects of a fluid-filled tank car. As this surrogate tank car was designed to be representative of a DOT-113 tank car that could carry cryogenic materials having a lower density than that of water, the surrogate tank car was intentionally overloaded (by weight) for the test to maintain a filling volume like that expected in cryogenic service. Thus, the FE model was loaded with a volume of water to match the test condition (17.6 percent outage).

5.2 Material Behaviors in FE Models

The same material definitions were used in both the pre-test and post-test FE models: ASTM A240 Type 304 stainless steel, AAR TC-128B carbon steel, a membrane material, air, and water. This section summarizes the material properties input into the FE models. Complete descriptions of the development of the stainless steel and carbon steel material models are given in Appendix F. No material model for MLI was developed as this feature was omitted from the pre-test FE model.

5.2.1 ASTM A240 Type 304 Stainless Steel

A section of the T304 inner tank was cut into flat ASTM E8 tensile coupons, as discussed in Section 4.5. Tensile tests were performed on three coupons having gage dimensions of 2 inches long, 1/2 inch wide, and 1/4 inch thick.

An FE model of the T304 tensile coupons was created in Abaqus/Explicit using similar modeling techniques, i.e., mesh size, step time, mass scaling, etc., to those used in the tank car puncture model to calibrate a material input for that model. A more detailed description of the calibration

procedure of the T304 material input is contained in Appendix F4. Figure 40 shows that the calibrated T304 material input matched the average YS, UTS, and EB-2in results from the tests.

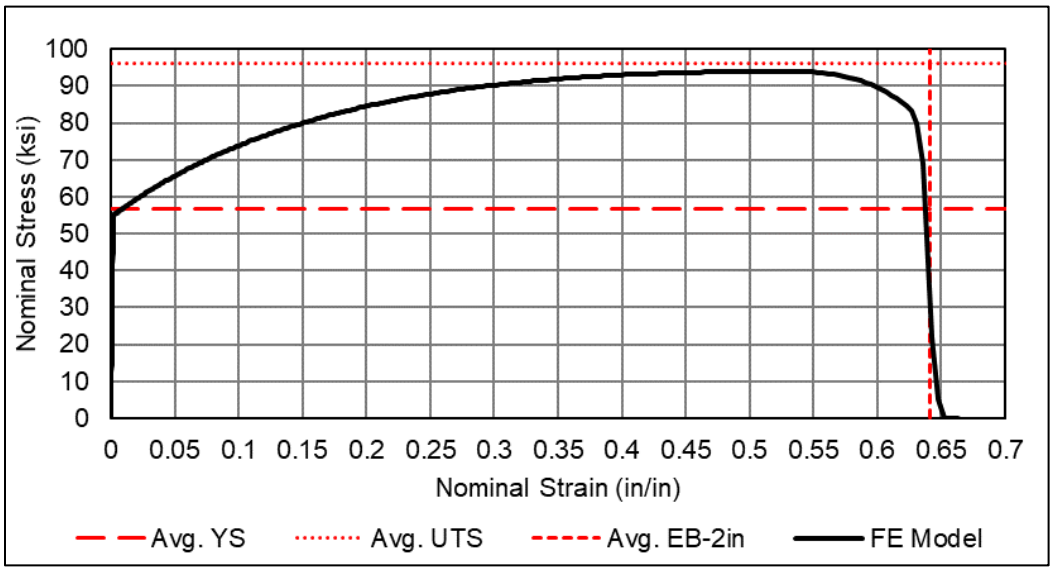

Figure 40. Nominal Stress-Strain Response from the T304 Stainless Steel Coupon FE Model (solid black) and Average Tensile Properties (dashed red)

Table 20 summarizes the material properties used for the T304 stainless steel inner tank in the FE models of the DOT-113 surrogate tank car. Damage progression was only specified for the solid patch.

Table 20. Summary of Material Properties for T304 Stainless Steel

Parameter	Value
Mass density	7.35 x 10^{-4} lbf-s^2/in^4
Modulus of Elasticity	3 x 10^7 psi
Poisson's Ratio	0.25
Plasticity	Piecewise Linear (Appendix F4)
Damage initiation	B-W Envelope (Appendix F4)
Damage progression	Displacement = 0.005 in/in^2, exponent = -2
Mesh implementation	0.05-inch Reduced Integration Brick (C3D8R) Elements

5.2.2 AAR TC-128B Carbon Steel

As discussed in Section 4.5, a section of the TC-128B outer tank removed during construction of the surrogate was cut into smooth round bar ASTM E8 tensile coupons. Tensile tests were performed on eight coupons having gage dimensions of 2 inches long and 1/2 inch in diameter. An FE model of the TC-128B coupon geometry was used to calibrate a material model to match

the average YS, UTS, and EB-2in as depicted in Figure 41. The process of calibrating the material input for TC-128B is described in Appendix F3.

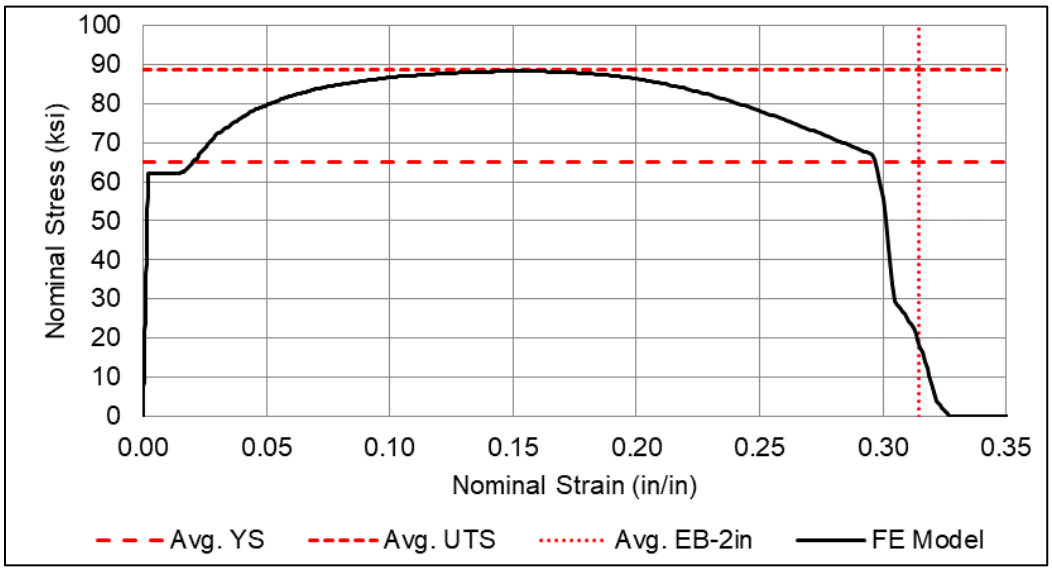

Figure 41. Nominal Stress-Strain Response from the TC-128B Carbon Steel Coupon FE Model (solid black) with Average Tensile Properties (dashed red)

Table 21 summarized the material properties of TC-128B steel used in the outer tank of the FE models. Damage progression was only specified for the solid patch of elements.

Table 21. Summary of Material Properties for TC-128B Carbon Steel

Parameter	Value
Mass density	7.35×10^{-4} lbf-s^2/in.^{4}
Modulus of Elasticity	3×10^7 psi
Poisson's Ratio	0.3
Plasticity	Piecewise nonlinear (Appendix F3)
Damage initiation	B-W Envelope (Appendix F3)
Damage progression	Displacement = 0.005 in./in.^{2}, exponent = -1
Mesh implementation	0.081-in. Reduced Integration Brick (C3D8R) Elements

5.2.3 Membrane

As described in Appendix D9, an artificial surface was modeled within the tank to define the limits of the hydraulic and pneumatic cavities. Because this surface does not correspond to any physical structure within the tank, modeling techniques were chosen to minimize the increase in either mass or stiffness introduced into the model by the membrane while not negatively impacting the FE model's stability or runtime. The membrane material used two different moduli

of elasticity, based on whether the region was constrained by the inner surface of the tank's wall or unconstrained in the center of the tank. Table 22 summarizes the material properties of the membrane.

Table 22. Material Properties Defined for Membrane Material

Parameter	Value
Density	7.35×10^{-6} lbf·s^2/in.^{4}
Modulus of Elasticity	1×10^{4} psi (unconstrained) 1×10^{-6} psi (constrained)

Additionally, a nonstructural mass was added to the membrane around the hydraulic cavity to account for the mass of the water within the tank.

5.2.4 Air

The gas phase of the lading was modeled as air at a gauge pressure of 50 psi because this was the desired internal pressure for the tank car at the beginning of the test. Within Abaqus, the air within the outage was modeled as an ideal gas, using a pneumatic cavity modeling technique. This modeling technique requires a surface to be defined that encloses the cavity, with a reference point defined within this cavity to which initial temperature and pressure can be assigned. The initial pressure and temperature are discussed further in Appendix E9.

The pneumatic cavity approach models the entire cavity with a single uniform pressure and uniform temperature value. The air pressure within the model was allowed to change as the volume of the tank changed due to the impact while the temperature was held constant (isothermal assumption). The modeling inputs defined for the air phase of the model are summarized in Table 23, using the unit system used in the FE models.

Table 23. Properties for Air (Pneumatic Cavity)

Property	Value	Reference
Universal gas constant (R)	73.583 in.-lbf/(mol·K)	[25]
Molecular weight (MW)	1.654×10^{-4} (lbf·s^2/in.)/mol	[26]
Constant Temperature	294 K	
Initial Pressure	50 psig	

The molar specific heat capacity at constant pressure ($c_{p,m}$) for air was calculated according to Equation 1.

Equation 1. Calculation of Molar Specific Heat

$$c_{P.m} = c_P \cdot MW$$

Values for the specific heat capacity of air at constant pressure (c_p) were obtained from published values [27]. Table 24 shows the values calculated for molar specific heat at different

temperatures using Equation 1 that were defined as inputs to the FE models in the unit system used in the FE models.

Table 24. Molar Specific Heat for Air

Temperature *K*	$c_{p,m}$ *in-lbf/(mol·K)*
250	257.2
300	257.7
350	258.5
400	259.7

5.2.5 Water

The target initial conditions for the side impact test of the surrogate DOT-113 tank car were set to an outage volume of 17.6 percent and internal pressure of 50 psig. The liquid phase of the lading was modeled as water at approximately 70 °F (294 K) in the pre-test and post-test models. Within Abaqus, a hydraulic cavity model was used to describe the behavior of the liquid water. The key material properties that must be input to this material model are the material's density and its bulk modulus. Values for density and speed of sound were obtained by interpolating published tabular values to the anticipated test temperature of 70 °F. Initial conditions are discussed further in Appendix E9.

The speed of sound (c) in a fluid can be determined from the fluid's bulk modulus (K) and density (ρ) according to the Newton-Laplace equation given in Equation 2 [28].

Equation 2. Calculation of Bulk Modulus

$$K = c^2\rho$$

Table 25 shows the properties used in the DOT-113 surrogate tank car model. This table includes the specific units used in the unit system of the FE model.

Table 25. Properties of Water Used in FE Models

Property	Value	Reference
Mass density (ρ)	9.42×10^{-5} lbf·s^2/in.^{4}	[15]
Speed of sound (c)	55,930 in./s	[29]
Bulk modulus (K)	294,695 lbf/in.^{2}	Equation 2

While density is among the parameters defined for the water in the hydraulic cavity, this value of density is only used by the solver to calculate the bulk modulus of the liquid in the hydraulic cavity. The mass of the water in the tank was represented as a distributed, nonstructural mass assigned to the membrane surrounding the hydraulic cavity. This nonstructural mass is described further in Appendix D9.

5.3 Modeling Techniques Adjusted Between Pre-test and Post-test FE Models

A few modeling parameters were adjusted from the pre-test to post-test FE models. The adjustments were made based on the actual test conditions and based on considerations of model runtime. Table 26 summarizes these modeling techniques and their adjustments. Note that insulation was not added to the post-test FE model, as the level of agreement between the test measurement and the insulation-less pre-test model indicated MLI could be omitted without affecting the structural response of the model.

Table 26. Summary of Adjustments Made Between Pre- and Post-test FE Models

Modeling Feature	Condition in Pre-test Model	Condition in Post-test Model	Explanation
Impact speed	Varied	17.3 mph	Adjusted to match test speed
Impactor offset	0.25 in.	1.25 in.	Adjusted to account for support of tape switches
Symmetry	Longitudinal symmetry	No symmetry	Removed in post-test models to analyze full-length tank
Laser transducers	None	Included	Added to the post-test model for direct comparison with test

5.3.1 Impact Speed

Pre-test FE models were run to simulate impacts over a range of speeds from 16.7 to 21 mph. The purpose of the pre-test FE models was to aid in test planning by estimating the outcomes (e.g., impact forces, puncture of one or both tanks, etc.) over a range of speeds so that a target impact speed could be chosen. Post-test FE models were run using 17.3 mph, the measured impact speed from the test. The post-test FE models were run at the same speed as the test to facilitate a comparison of test and model results as part of a model validation program.

5.3.2 Impactor Offset and Time Zero

It was observed that the initial rise in impact force occurred approximately 4 milliseconds later in the test results than in the FE results. This delay was attributed to the thickness of the wooden supports for the tape switches on the impactor and outer tank. The tape switches determine time zero in the test and are visible in Figure 8 on the end of the impactor. The pre-test simulations started with the impactor 1/4 inches away from making contact with the outer tank, and the post-test simulations adjusted the initial impactor position to 1 1/4 inches away from the outer tank to account for the early triggering of the tape switches in the test.

5.3.3 Symmetry

Because the pre-test FE model was run incrementally over a range of speeds from 16.7 to 21 mph, a symmetry condition was imposed longitudinally and centered on the impact point to reduce the mesh size and runtime of the model. This approach was taken because it was determined that a symmetrical assumption did not have a significant effect on the puncture speed for this model. The post-test FE model was run without the symmetry condition because it only

needed to be run at the test speed of 17.3 mph, and it allowed for a comparison of the east and west ends of the FE model with the test results.

5.3.4 Displacement Transducers

External laser transducers and internal string potentiometers were not included in the pre-test FE model because the primary purpose of the pre-test model was to determine a threshold puncture speed. Model representations (soft springs) of the laser transducers and string potentiometers were added to the post-test FE model for direct comparison with the test results.

6. Comparison of Test Responses to FE Analyses

This section compares the results from the pre- and post-test FE models with the test measurements. While the post-test model was run at the measured test speed of 17.3 mph, the pre-test models were not run at the measured test speed because this speed was unknown when they were created. The two closest speeds (i.e., 16.7 and 18 mph) from the analyses using the pre-test FE model are presented for comparison with the test measurements in Section 6.1. The post-test FE model was updated from the pre-test version as discussed in Section 5.3, and the results from the post-test FE model are compared with test measurements in Section 6.2.

6.1 Pre-test FE Model Comparison

One of the intended uses of the pre-test FE models was to assist in test planning by estimating the range of impact speeds over which the puncture of both the inner and outer tanks would be likely to occur. The pre-test FE models were run using an iterative approach in an attempt to estimate a speed that would cause the puncture of both tanks without resulting in an excessive amount of residual energy in the impactor at the time of puncture. Using this iterative approach, the models estimated that at a speed of 19 mph only the outer tank would be torn, but at a speed of 19.5 mph, both the inner and outer tanks would be punctured. Therefore, it was expected that the puncture of the inner tank would be a possible outcome for speeds above 19 mph depending on the exact test conditions. Table 27 summarizes the pre-test FE models and their outcomes.

Table 27. Summary of Pre-test FE Model Outcomes

Speed*(mph)*	**Outer Tank State**	**Inner Tank State**	**Impactor State**
16.7	No elements lost	No elements lost	Rebounding
18	Some elements lost	No elements lost	Rebounding
19	Tear along vertical edge of impactor	No elements lost	Rebounding
19.5	Tearing around edges of impactor	Tearing around edges of impactor	Rebounding
20	Tearing around edges of impactor	Tearing around edges of impactor	Penetrating

A large solid patch was used on the outer tank to allow the tear to propagate without artificially arresting its growth. The inner tank, however, had a smaller solid patch because a non-puncture versus puncture outcome could be determined once the inner tank just started to tear under a corner of the impactor.

The chosen target speed for the test was 17.2 ± 0.5 mph (actual impact speed 17.3 mph) on the basis of these pre-test FE results because a non-puncture outcome was desired for this test. A non-puncture outcome was desirable because a previous test of a DOT-113 in 2019 (actual impact speed 16.7 mph) had already resulted in a puncture outcome with an excess residual kinetic energy in the impactor. The target speed of 17.2 ± 0.5 mph was expected to be conservative for the DOT-113 surrogate tank car because the maximum expected speed

(17.7 mph) was still 1.8 mph below the speed that resulted in puncture of both tanks in the pre-test FE model. Additionally, there were fewer uncertainties in the exact material properties of the DOT-113 surrogate tank car because its tensile properties were measured during its construction.

Figure 42 compares the impact force versus impactor travel for the pre-test FE model at speeds both slightly above and below the test speed (16.7 and 18 mph) with the test measurements (17.3 mph). While the FE model used a rigid impactor with a single acceleration-time history, the ram car in the test featured five longitudinal accelerometers. The test force reported is the average of the five longitudinal accelerometer channels. Both the test and FE forces reported in this section were filtered using a CFC-60 filter [19]. Both pre-test FE results are in good agreement with one another and with the test measurements. The initial portion of the force-displacement response does not appear to be significantly affected by the impact speed over the range simulated.

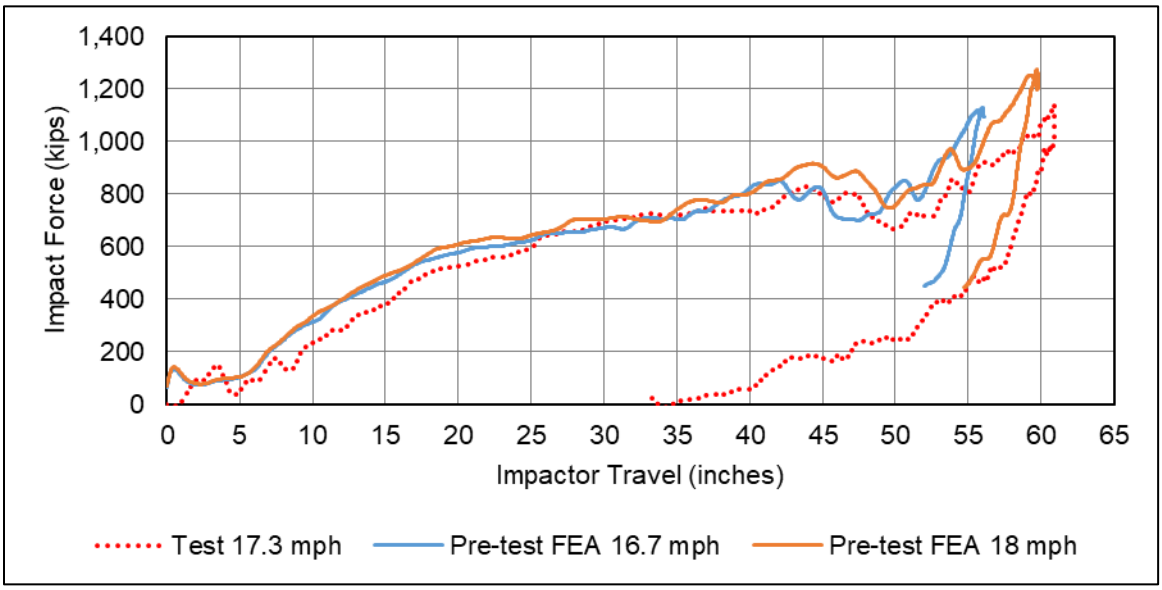

Figure 42. Force-displacement Responses from Pre-test FEAs at 16.7 and 18 mph Compared to Test Results at 17.3 mph

Figure 43 compares the air pressure-time histories from the pre-test FE model at the two closest speeds to the actual test speed (16.7 and 18 mph) with the test measurements (17.3 mph). The test measurements were made using three air pressure transducers (i.e., TP1000, TP2000, and TP3000) placed inside the inner tank at the vertical center at three points along its length. All three pressure transducers had a significant amount of noise, but the pressure response is qualitatively bounded by the pre-test FE model run at speeds below and above the test speed.

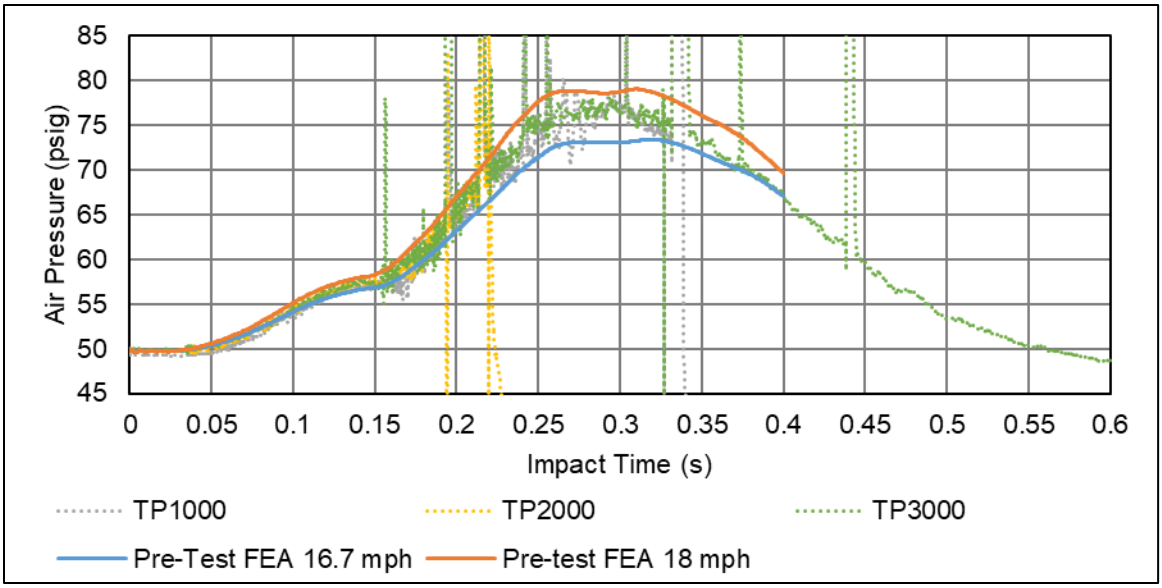

Figure 43. Air Pressure Time History from Pre-test FE Model Run at 16.7 and 18 mph Compared to Three Air Pressure Transducers (TP1000, TP2000, TP3000) from Test at 17.3 mph

Table 28 summarizes the peak results from the pre-test FE models and compares them with the test results. The pre-test FE model underpredicted displacement at maximum force at both speeds and maximum displacement of the east skid. Typically, the maximum air pressure is compared between the FE model and test. However, noise was present in the test measurements, and this noise artificially inflated the maximum pressure, so the average pressure at peak force was used for comparison instead. Overall, the pre-test FE model was in agreement with the test results.

Table 28. Comparison of Peak Results from Pre-test FEA with Lower Estimate of Steels (16.7 and 18 mph) and Test Results (17.3 mph)

Peak Measurement	Test	16.7 mph FEA	16.7 mph FEA	18 mph FEA	18 mph FEA
	Value	Value	%	Value	%
Peak longitudinal acceleration (g)	3.85	3.80	-1.3	4.29	11.6
Global peak force (kip)	1,143	1,128	-1.3	1,275	11.6
Impactor travel at peak force (in.)	60.9	56.0	-8.1	59.7	-2.0
East skid displacement (in.)	16.4	13.0	-20.8	13.1	-19.8
East head displacement (in.)	N/A†	15.7	N/A†	16.1	N/A†
Avg. air pressure at peak force (psi)	74.7	73.1	-2.1	78.6	5.3

†Denotes a sensor that malfunctioned during the DOT-113 surrogate side impact test

Figure 44 shows the state of the solid patch on the outer tank at the end of the pre-test FE simulations (0.4 seconds). The damage initiation criterion (i.e., ductile criterion [DUCTCRT]) is plotted over a range of 0 to 1, where 1 corresponds to the start of damage progression (i.e., element stiffness degradation) that quickly leads to element deletion. No elements are visibly removed from the pre-test FE model at 16.7 mph, and some elements are lost in the pre-test FE

model at 18 mph under the bottom corner of the impactor. It should be noted that the impactor speed needed to be increased to 19.5 mph before elements were lost, i.e., tearing started, in the inner tank.

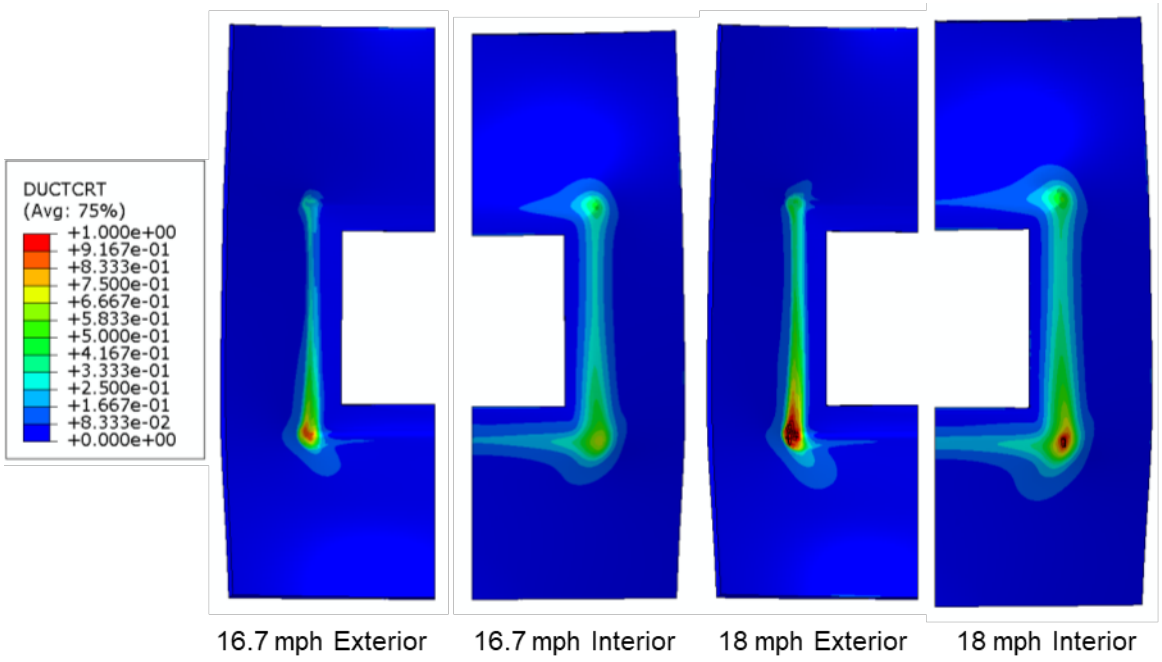

Figure 44. Contour Plots of Damage Initiation Criterion (DUCTCRT) on Outer Tank Solid Patch from 16.7 mph (left) and 18 mph (right) Pre-test FE Models at 0.4 Seconds

From the information presented above puncture of the inner tank was not expected at the target test speed of 17.2 ± 0.5 mph, and the test that occurred at 17.3 mph did not result in puncture of the inner or outer tanks. Pre-test FE simulation results at all speeds are contained within Appendix C1.

6.2 Post-test FE Model Comparison

The pre-test FE model was updated as discussed in Section 5.3 to reflect the actual test speed, offset, and asymmetry conditions and to permit additional comparisons to be made with the test measurements. In this section, comparisons are made between the post-test FE model and the test measurements, and it was found that the post-test FE model was in excellent agreement with the test measurements.

Table 29 provides a summary of the post-test FE model outcomes at the end of the simulation. The post-test FE model had some elements deleted from the exterior surface of the outer tank, but no elements were lost from the interior surface of the outer tank or either surface of the inner tank.

Table 29. Summary of Post-test FE Model Outcomes

Simulated Impact Speed (mph)	Outer Tank State	Inner Tank State
17.3	Some elements lost	No elements lost

Figure 45 compares the impact force versus impactor travel from the post-test FE model with the average test measurements. The post-test FE model exhibits excellent agreement with the shape of the force-displacement curve from the test, but the impactor travel at the time of peak force is slightly under predicted, i.e., the model is slightly too stiff. This difference in stiffness is believed to be due to the simplified representation of the air and water in the FE model.

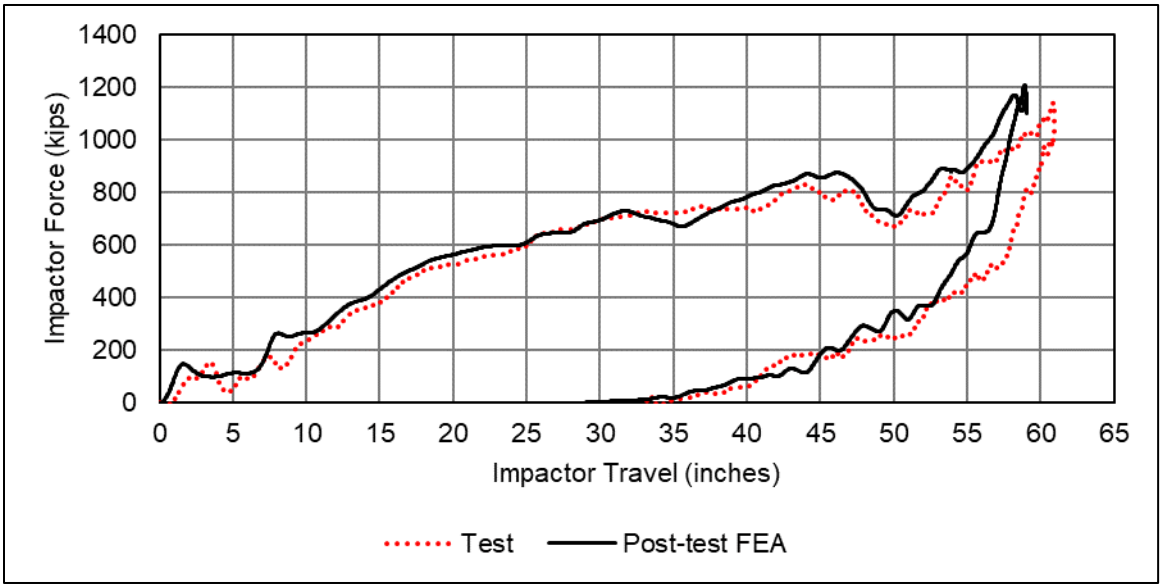

Figure 45. Force-displacement Responses from Post-test FEA Compared to Test Results

Figure 46 compares the air pressure versus time histories from the post-test FE model with the test measurements. The test measurements were made using three air pressure transducers (i.e., TP1000, TP2000, and TP3000) placed inside the inner tank at three points along the length of the vertical center. All three pressure transducers had a significant amount of noise, but the qualitative shape of the pressure curve shows agreement between the model and test. The slight under prediction of peak air pressure is attributed to the higher overall stiffness of the model that results in less of a reduction in volume of the inner tank.

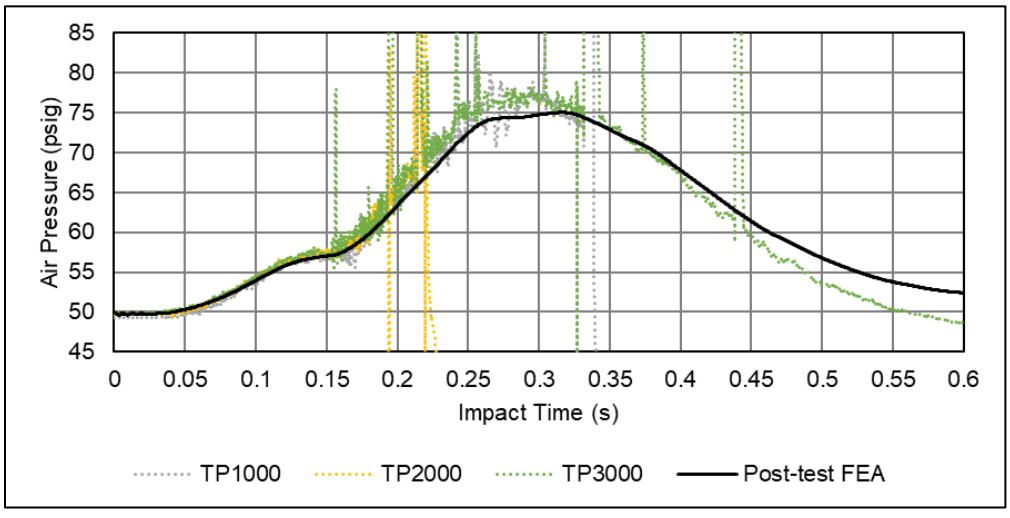

Figure 46. Air pressure Time History from Post-test FE Model Compared to Three Air Pressure Transducers (TP1000, TP2000, TP3000) from the Test

Table 30 summarizes the peak results from the post-test FE model and compares them with the test results. Additional measurements were added to the post-test FE model to make comparisons with all the test measurements, i.e., the internal string potentiometers and external laser transducers. All the external compression measurements were made using laser transducers mounted to the ram car and rigid wall. The laser transducer readings were zeroed at the point of impact, and the wall-mounted transducers were subtracted from the ram-mounted transducers at all positions except for the centered impactor that was aimed at the wall instead of the exterior vertical center of the outer tank.

Table 30. Comparison of Peak Results from Post-test FEA and Test Measurements

Peak Measurement	**Test**	**FEA**	**FEA**
	Value	Value	%
Peak Longitudinal Acceleration (g)	3.85	4.1	5.6
Global Peak Force (kip)	1,143	1,206.4	5.6
Impactor Travel at Peak Force (in)	60.9	58.9	-3.3
East Skid Displacement (in.)	16.4	14.3	-12.9
West Skid Displacement (in.)	14.8	13.5	-8.6
East Head Displacement (in.) †	-	17.1	-
West Head Displacement (in.) †	-	16.2	-
48″ Offset East Internal Compression (in.) †	-	31.5	-
24″ Offset East Internal Compression (in.)	37.7	38.9	3.2
0″ Offset Internal Compression (in.) †	-	45.1	-
24″ Offset West Internal Compression (in.)	36.9	39.6	7.3
48″ Offset West Internal Compression (in.)	29.8	32.7	9.8
0″ Offset Vertical Extension (in.) †	-	20.7	-
48″ Offset East External Compression (in.)	43.9	44.0	0.2
24″ Offset East External Compression (in.)	51.6	51.2	-0.9
0″ Offset External Compression (in.)	60.2	58.9	-2.3
24″ Offset West External Compression (in.)	52.3	51.6	-1.4
48″ Offset West External Compression (in.)	46.1	44.6	-3.4
Avg. Air Pressure at Peak Force (psi)	74.7	73.8	-1.2

†Denotes a sensor that malfunctioned during the DOT-113 surrogate side impact test

The post-test FE model performed similarly to the pre-test FE model in that it underpredicted displacement at maximum force and maximum displacement of the skids when run at the measured test speed. Overall, the post-test model showed excellent agreement with the test results.

Figure 47 shows a plotted comparison between the FE model and the test measurements of maximum percent change in diameter for the inner and outer tanks. The percent change in diameter was calculated using the displacement measurements at the time of peak force. The string potentiometer measurements from the inner tank were divided by the initial inner diameter of the inner tank, and the zeroed laser transducer measurements from the outer tank were divided by the initial outer diameter of the outer tank. East (A-End) corresponds to a negative distance from the

impactor, and west (B-End) corresponds to a positive distance from the impactor on the x-axis of the plot. The 48-inch offset west internal string potentiometer is omitted due to instrumentation failure. Overall, the FE model captures the compression of the inner and outer tanks.

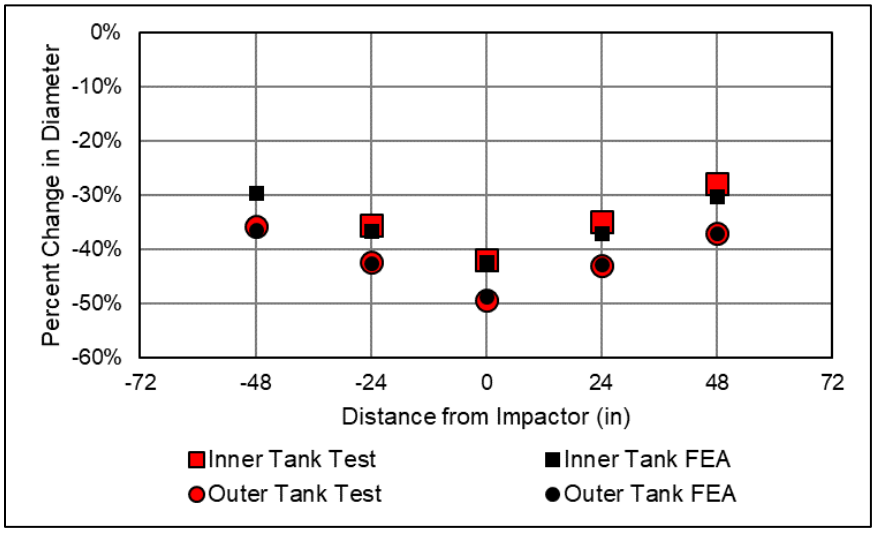

Figure 47. Comparison of Maximum Percentage Change in Diameter of Inner and Outer Tanks Between FE Model and Test Measurements

Figure 48 shows the state of the solid patches on the outer tank and inner tank at the end of the post-test simulation (0.6 seconds). DUCTCRT is plotted over a range of 0 to 1, where 1 corresponds to the start of damage progression (element stiffness degradation) that quickly leads to element deletion. A few elements are visibly lost on the exterior surface of the outer tank under the bottom corners of the impactor, but no elements in the inner tank patch reached the start of damage progression (DUCTCRT=1) by the end of the simulation.

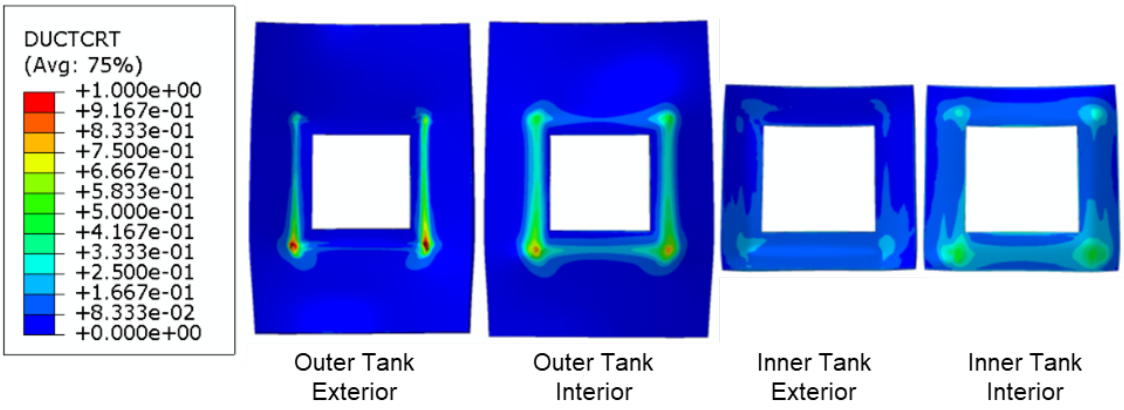

Figure 48. Contour Plots of DUCTCRT on Outer and Inner Tank Solid Patches from 17.3 mph Post-test FE Model at 0.6 Seconds

Appendix C2 presents a complete set of post-test FE simulation results.

7. Discussion

This test was the second test in a planned series of four tests to be conducted on DOT-113 tank cars and tank car surrogates. The objective of this test series is to examine the potential improvement in shell puncture resistance for a DOT-113 tank car with an outer shell made of 9/16-inch-thick TC-128B steel compared to a baseline DOT-113 tank car using 7/16-inch-thick A516-70 steel under LNG service conditions. Four tests are planned, with each test increasing in both complexity and realism compared to the previous test. Companion FE modeling is planned for each test, with the FE model expected to increase in complexity as results and observations from each test are studied and synthesized. Details of the planned testing sequence are summarized in Table 31.

Table 31. Summary of DOT-113 Side Impact Test Conditions

Summary				
Test Number	Test 10	Test 11 (this report)	Test 12	Test 13
Test Date	November 2019	July 2020	TBD, 2021	TBD, 2021/2022
Test Article	DOT-113C120W	DOT-113 surrogate	DOT-113 surrogate	DOT-113C120W9
Thickness (Outer Tank)	7/16 inch	9/16 inch	~0.6 inch	9/16 inch
Material (Outer Tank)	A516-70	TC-128B	TC-128B	TC-128B
Diameter (Outer Tank)	~119 inches	~120 inches	~120 inches	~120 inches
Length (Outer Tank)	~74 feet	~45 feet	TBD	TBD, typical of service
Thickness (Inner Tank)	1/4 inch	1/4 inch	1/4 inch	1/4 inch
Material (Inner Tank)	T304 stainless steel	T304 stainless steel	T304 stainless steel	T304 stainless steel
Diameter (Inner Tank)	~106 inches	~106 inches	~106 inches	~106 inches
Volume (Inner Tank)	32,900	19,300	TBD	TBD, typical of service
Tank Lading	Water	Water	LN2	LN2
Outage	17.6%	17.6%	TBD, typical of service	TBD, typical of service

Summary				
Pressure	50 psig	50 psig	TBD, typical of service	TBD, typical of service
Insulation	Perlite	MLI	MLI	MLI
Annular Pressure	Vacuum	Atmospheric	Vacuum	Vacuum
Impact Speed	16.7 mph (actual)	17.3 mph (actual)	TBD, sufficient to puncture	TBD, sufficient to puncture

Figure 49 compares impactor force versus impactor travel for the test described in this report (Test 11) and the previously performed impact test of a DOT-113 tank car [3]. Annotations on this figure indicate the approximate force and indentation levels corresponding to the puncture of the outer and inner tanks for Test 10. Additional annotations distinguish the motion of the impactor which came to a stop and rebounded in Test 11 but continued to penetrate the tank car following puncture in Test 10. Initially, the two responses were in relative agreement with one another. The force-displacement response in Test 10 climbs steadily to approximately 30 inches, while the response in Test 11 features a plateau in the first 10 inches before beginning to climb. This difference may be attributed to the different insulation schemes used in each tank car.

The DOT-113 tank car used in Test 10 featured an annular space between tanks that was filled with granular perlite under vacuum, while the DOT-113 surrogate tank car used in Test 11 featured an open-to-atmosphere annular space with MLI. However, MLI does not completely fill the annular space. Thus, the outer tank in Test 10 was in contact with insulation as soon as it began to deform from the impact, while the outer tank in Test 11 was free to deform inward until it made contact with the layers of MLI surrounding the inner tank. Once both tanks in Test 11 are in contact (through the MLI), the initial force-displacement responses are of a similar stiffness in the two tests up to the point of outer tank puncture in Test 10. At approximately the same distance as Test 10's outer tank puncture, the Test 11 surrogate has a relatively stable plateau at a force between 700 and 800 kips. After an impactor travel of approximately 50 inches, the force measured in Test 11 begins to climb once again until the impactor comes to a stop.

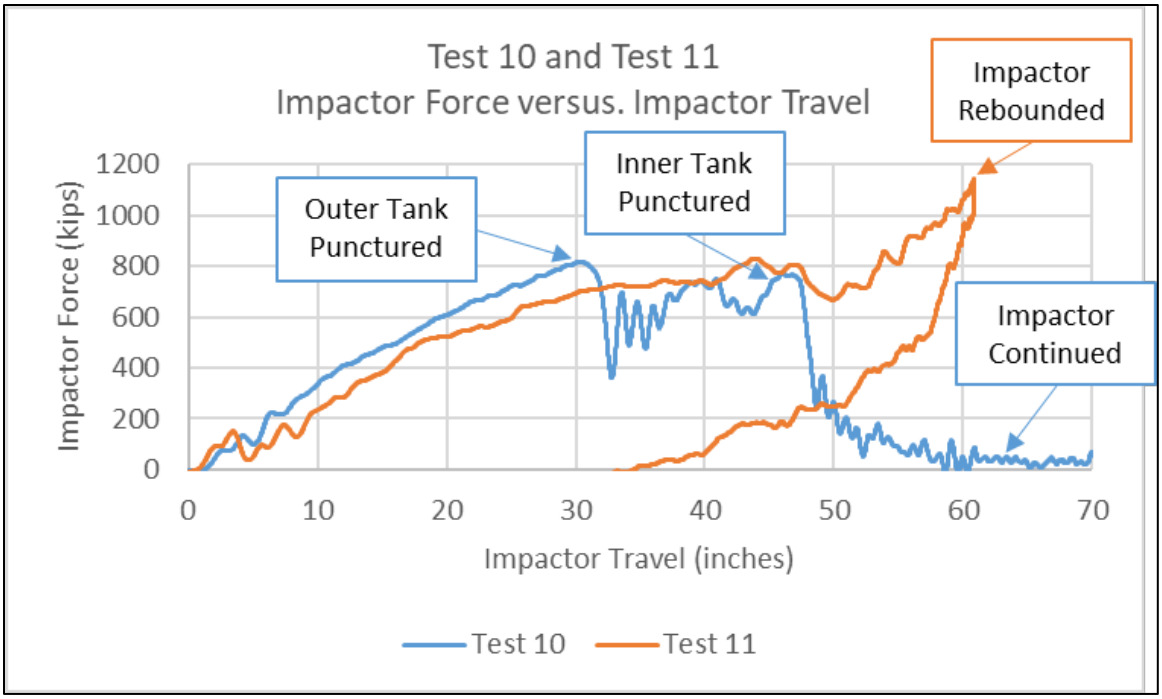

Figure 49. Impactor Force Versus Impactor Travel, Test 10 and Test 11

The inner tanks of the DOT-113 used in Test 10 and the surrogate used in Test 11 were made of the same material (T304) of the same thickness (1/4 inch), rolled into a ring of approximately the same diameter (106 inches). From the above comparison between Test 10 and Test 11, it is apparent that the inner tank punctured in Test 10 after puncture of the outer tank. The force required to puncture the inner tank in Test 10 was exceeded by the two unpunctured tanks in the Test 11 surrogate working together to resist the impactor. The Test 11 surrogate was able to maintain its integrity under a higher-energy impact at least partially because the thicker, TC-128B outer tank did not puncture under the conditions that caused the thinner A516-70 outer tank of the Test 10 car to puncture. Once the Test 10 car's outer tank was punctured, the impact placed more demand on the inner tank. In contrast, the Test 11 surrogate benefitted from the combined energy-absorption contributions of both tanks over the course of the entire impact event. Further, the intact outer tank of the Test 11 surrogate may have served to "blunt" the impactor shape when it made contact with the inner tank, while the punctured outer tank of the Test 10 tank car would have provided little in the way of blunting.

The next test in this planned series (Test 12) will use a DOT-113 surrogate tank having a 0.6-inch outer tank made of TC-128B steel, where the Test 10 DOT-113C120W had a 7/16-inch outer tank made of A516-70 steel. Test 12 will replace the water used in Tests 10 and 11 with a cryogenic liquid, LN2. The outage volume and pressure will be based on the expected in-service conditions for LNG. Beyond Test 12, a fourth test is planned using the newest specification DOT-113C120W9 tank car with LN2 as the lading. This final test is expected to be the closest approximation to LNG in-service conditions to be examined through testing in this program. Following Test 13, additional FEA using LNG in the model and inner tank at LNG temperature are planned to confirm the performance of the DOT-113C120W9 under LNG service conditions.

8. Conclusion

This report documents the combined efforts of TTCI and Volpe to test and analyze the side impact puncture performance of a surrogate DOT-113 tank car. The inner tank was filled with water to approximately 17.6 percent of its volume, then sealed and pressurized to 50 psig. The test was intended to cause a strike to the tank car at a speed high enough to result in significant damage to the inner and outer tanks but not puncture either tank. The tank car was impacted by a 297,200-pound ram car equipped with a 12-inch by 12-inch indenter at a speed of 17.3 mph on June 11, 2020, at the TTC. The impact resulted in approximately 61 inches of compression of the outer tank and an internal pressure rise of approximately 25 psi in the outage.

This testing and analysis support FRA's tank car research program to provide the technical basis for rulemaking on enhanced and alternative performance standards for tank cars. The preliminary findings from this surrogate DOT-113 impact study have been referenced in a July 24, 2020, final rule (see 85 FR 44994, footnote #6) by PHMSA authorizing the transportation of LNG by rail tank car. Two additional tests are planned in this testing series where LN2 will replace water as the liquid used within the tested tank. Further discussion of the results of this test compared to these other tests is planned for a future report.

This test was the first side impact test in FRA's tank car research program where the tensile properties of the impacted tank car were characterized prior to the test. Material test data was used to generate material inputs that were implemented in both the pre-test and post-test FE models.

Pre-test analyses predicted that neither the outer nor the inner tank of the DOT-113 surrogate would tear at the targeted speed range 17.2 ± 0.5 mph. The test resulted in both tanks withstanding the impact. Excellent agreement was observed between the FE model results and the test measurements. The FE modeling performed in this effort used simplified hydraulic cavity and pneumatic cavity modeling techniques to simulate the water and air responses, respectively. The test measurements confirmed that this modeling approach provided a good representation of the fluid behavior within the tank car. The force-indentation response of the tested tank car, however, was slightly softer than that predicted by the FE models.

Both the pre-test and post-test FE models omitted the MLI installed in the impact zone between the two tanks. The high level of agreement between the FE model response and the test measurements demonstrated that the MLI did not have a significant structural effect and could be excluded from future FE models for tank cars using this type of insulation. This lack of structural effect contrasted with what was observed following the previous test of a DOT-113 tank car (Test 10) that used perlite insulation. Perlite insulation was determined to have a significant effect on the structural response of both the tested tank and the FE model.

Post-test material characterization tests were performed on the inner tank's T304 stainless steel and the outer tank's TC-128B carbon steel. Each type of steel was characterized using tensile testing and CVN testing. For the outer tank, the post-test characterization was focused on assessing the weld performance of the outer tank. The tensile testing did not demonstrate a clear difference in YS, UTS, or EB-2in between the parent material, welded material, or HAZ for the factory weld. However, CVN testing indicated that material taken from the closure weld absorbed significantly less energy than any of the other material conditions. Additionally, the testing lab noted apparent weld defects in tensile coupons taken from the closure weld used for

both axial and hoop direction testing. Collectively, these material test results and defect observations may suggest further examination of closure welds should be undertaken in the future. The tensile and CVN test results are planned to be used to develop FE material models of the outer tank welds that can be incorporated into future DOT-113 tank car and surrogate tank car models to examine the effects of impacts in the vicinity of the closure weld.

Post-test characterization of Test 11's inner tank was focused on assessing the effect of the temperature and strain rate on the mechanical properties of the T304 stainless steel. Specifically, the tensile and CVN tests were conducted on parent (unwelded) material at four temperatures between room temperature and 77 K (-320 °F), the saturation temperature of LN2 at 1 atmosphere. The tensile tests were conducted at five different strain rates at each of the three temperatures to better understand the effects of simultaneous cryogenic temperature and elevated strain rate on the mechanical properties of T304 stainless steel. Results from the companion FE model to the previously tested DOT-113 tank car suggested that calibrating a T304 stainless steel material response using only quasi-static strain rate material data could overestimate the puncture response of a stainless-steel inner tank when subjected to a dynamic impact. Ultimately, the strain rate and temperature effects will be incorporated into future FE models of DOT-113 tank cars and surrogates simulating impacts under cryogenic conditions.

Now that the DOT-113 FE model has shown acceptable performance for a test with water, future modeling work will focus on preparing for a DOT-113 surrogate test with a cryogenic liquid. Several technical challenges are anticipated in switching from water to a cryogenic liquid. The modeling team anticipates discovering additional challenges associated with simulating cryogenic liquids as the modeling work progresses. A significant amount of pre-test planning and analyses will be required to prepare for the next side impact test in FRA's tank car research program (Test 12).

9. References

[1] Pipeline and Hazardous Materials Safety Administration, DOT, "Title 49 Code of Federal Regulations Section 179.16, Tank-head puncture-resistance systems," 2015.

[2] Pipeline Hazardous Materials Safety Administration, DOT, "Title 49 Code of Federal Regulations Section 179.202-12, Performance standard requirements (DOT-117P)," 2015.

[3] Trevithick, S., Carolan, M., Eshraghi, S., & Wilson, N., "Side Impact Test and Analyses of a Legacy DOT-113 Tank Car," U.S. Department of Transportation, Federal Railroad Administration, Technical Report No. DOT/FRA/ORD-21/28, Washington, DC, 2021.

[4] ASTM International, ASTM A240/A240M: Standard Specification for Chromium and Chromium-Nickel Stainless Steel Plate, Sheet, and Strip for Pressure Vessels and for General Applications, Conshocken, PA, 2019.

[5] Kirkpatrick, S. W., Rakoczy, P., & MacNeill, R. A., "Side Impact Test and Analyses of a DOT-111 Tank Car," U.S. Department of Transportation, Federal Railroad Administration, Technical Report No. DOT/FRA/ORD/15-30, Washington DC, 2015.

[6] Rakoczy, P., & Carolan, M., "Side Impact Test and Analysis of a DOT-112 Tank Car," U.S. Department of Transportation, Federal Railroad Administration, Technical Report No. DOT/FRA/ORD-16/38, Washington, DC, 2016.

[7] Rakoczy, P., Carolan, M., Gorhum, T., & Eshraghi, S., "Side Impact Test and Analyses of a DOT-117 Tank Car," U.S. Department of Transportation, Washington, DC, Technical Report No. DOT/FRA/ORD-19/13, Washington, DC, 2019.

[8] Carolan, M., & Rakoczy, P., "Side Impact Test and Analyses of a DOT-105 Tank Car," U.S. Department of Transportation, Federal Railroad Administration, Technical Report No. DOT/FRA/ORD-19/12, Washington DC, 2019.

[9] Kirkpatrick, S. W., "Detailed Puncture Analyses of Various Tank Car Designs - Final Report - Revision 1," U.S. Department of Transportation, Federal Railroad Administration, Washington, DC, 2010.

[10] Association of American Railroads, "AAR Manual of Standards of Recommended Practices, Section C-III, Standard M-1002, Specifications for Tank Cars, Appendix M."

[11] Pipeline and Hazardous Materials Safety Administration, DOT, "Title 49 Code of Federal Regulations, Subpart F – Specification for Cryogenic Liquid Tank Car Tanks and Seamless Steel Tanks (Classes DOT-113 and 107A)."

[12] ASTM International, "ASTM A240/A240M-19, Standard Specification for Chromium and Chromium-Nickel Stainless Steel Plate, Sheet, and Strip for Pressure Vessels and for General Applications."

[13] Rakoczy, P., & Carolan, M., "Side Impact Test and Analysis of a DOT-112 Tank Car," U.S. Department of Transportation, Federal Railroad Administration, Technical Report No. DOT/FRA/ORD-16-38, Washington, DC, 2016.

[14] Trevithick, S., Carolan, M., & Eshraghi, S., "Side Impact Test and Analyses of a DOT-111 (CPC-1232) Tank Car," U.S. Department of Transportation, Federal Railroad Administration, Technical Report No. DOT/FRA/ORD-20/43, Washington, DC, 2020.

[15] The Engineering ToolBox, "Water - Density, Specific Weight and Thermal Expansion Coefficient," The Engineering ToolBox, 2003.

[16] The Engineering ToolBox, "Methane - Density and Specific Weight," The Engineering ToolBox, 2020.

[17] Pipeline and Hazardous Materials Safety Administration, "Federal Register/Vol 84, No. 206, Hazardous Materials: Liquefied Natural Gas by Rail," 24 October 2019.

[18] Transportation Technology Center, Inc., "Test Implementation Plan for FRA Tank Car Side Impact, Revision 2," Pueblo, CO, 2019.

[19] SAE International, Instrumentation for Impact Test - Part 1: Electronic Instrumentation, Warrendale, PA: SAE, 2007.

[20] ASTM International, *ASTM E8/E8M: Standard Test Methods for Tension Testing of Metallic Materials*, West Conshocken, PA: American Society for Testing and Materials, 2013.

[21] ASTM International, *ASTM E23-18, Standard Test Methods for Notched Bar Impact Testing of Metallic Materials*, West Conshohocken, PA, 2018.

[22] Dassault Systèmes Simulia Corp., *Abaqus 2017*, Providence, RI, 2017.

[23] Bao, Y., & Wierzbicki, T., "On fracture locus in the equivalent strain and stress triaxiality space," *International Journal of Mechanical Sciences*,*46*(2004), p. 81–98, 2004.

[24] Eshraghi, S., Trevithick, S., Carolan, M., & Rakoczy, P., "Side Impact Test and Analyses of a DOT-105 Tank Car – 6 X 6 Inch Indenter," U.S. Department of Transportation, Federal Railroad Administration, Technical Report No. DOT/FRA/ORD-20/38, Washington, DC, 2020.

[25] The Engineering ToolBox, "Universal and Individual Gas Constants," The Engineering ToolBox, 2004.

[26] The Engineering ToolBox, "Air - Molecular Weight and Composition," The Engineering ToolBox, 2004.

[27] Urieli, I., "Specific Heat Capacities of Air," Engineering Thermodynamics, 2008.

[28] Smits, A. J., A Physical Introduction to Fluid Mechanics, New York: John Wiley and Sons, 2000.

[29] The Engineering ToolBox, "Water - Speed of Sound," The Engineering ToolBox, 2004.

[30] Interrante, C. G., Hicho, G. E., & Harne, D. E., "A Metallugical Analysis of Eleven Steel Plates Taken from a Tank Car Accident near Callao, Missouri," U.S. Department of Transportation, Federal Railroad Administration, Technical Report No. DOT/FRA/ORD-75/49, Washington, DC, 1972.

[31] The Engineering ToolBox, "Air - Density and Specific Volume vs. Altitude," The Engineering ToolBox, 2003.

[32] Swift, H. W., "Plastic instability under plane stress," *Journal of the Mechanics and Physics of Solids*, vol. 1, p. 1–18, 1952.

[33] Voce, E., "The relationship between stress and strain for homogeneous deformations," *Journal of the Institute of Metals*, vol. 74, p. 537–562, 1948.

[34] Lee, Y. -W., & Wierzbicki, T., "Quick Fracture Calibration for Industrial Use," MIT Impact & Crashworthiness Laboratory, Cambridge, MA, 2004.

[35] Lee, Y. -W., "Fracture Prediction in Metal Sheets," Cambridge, MA, 2005.

[36] Paredes, M., Grolleau, V., & Wierzbicki, T., "On Ductile Fracture of 316L Stainless Steels at Room and Cryogenic Temperature Level: An Engineering Approach to Determine Material Parameters," *Materialia*, *10*(100624), p. In Press, 2020.

[37] The Engineering ToolBox, "Ethylene – Density and Specific Weight," The Engineering ToolBox.

[38] Paredes, M., Sarzosa, D., Savioli, R., Wierzbicki, T., Jeong, D., & Tyrell, D., "Ductile Tearing Analysis of TC128 Tank Car Steel Under Mode I Loading," *Theoretical and Applied Fracture Mechanics*, vol. 96, p. 658–675, 2018.

Appendix A.
Camera and Target Positions

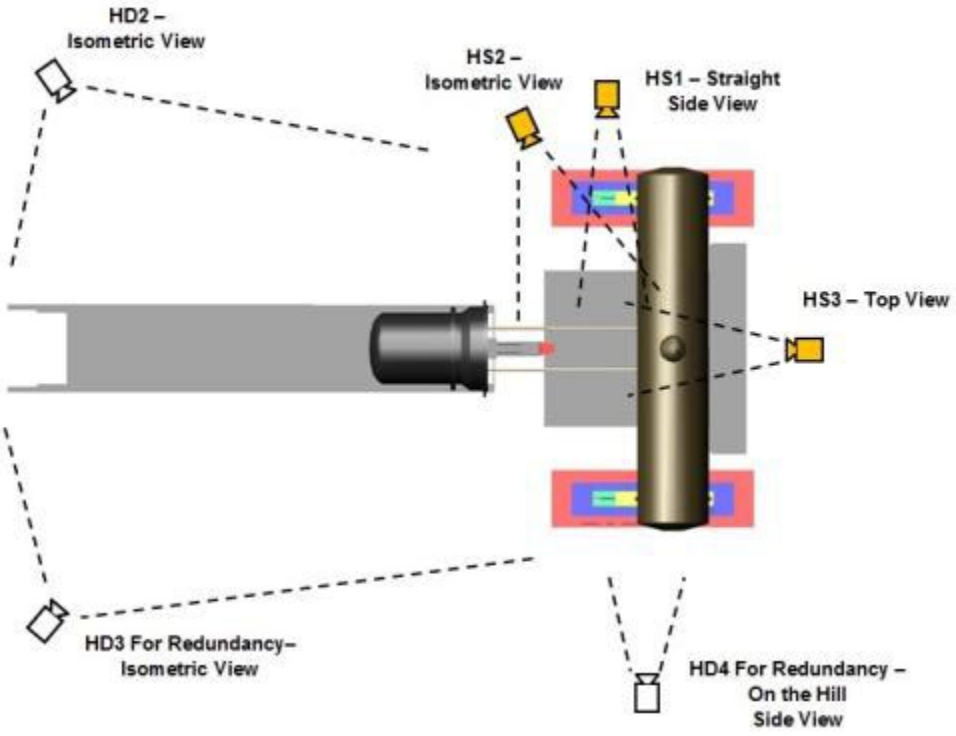

Figure A1. Camera Positions (top) – High-speed (HS), High Definition (HD)

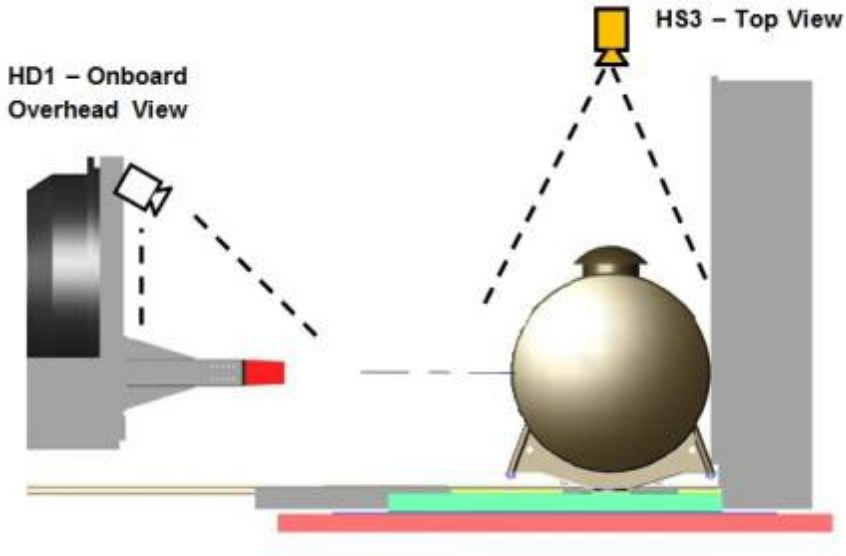

Figure A2. Camera Positions (side) – HS, HD

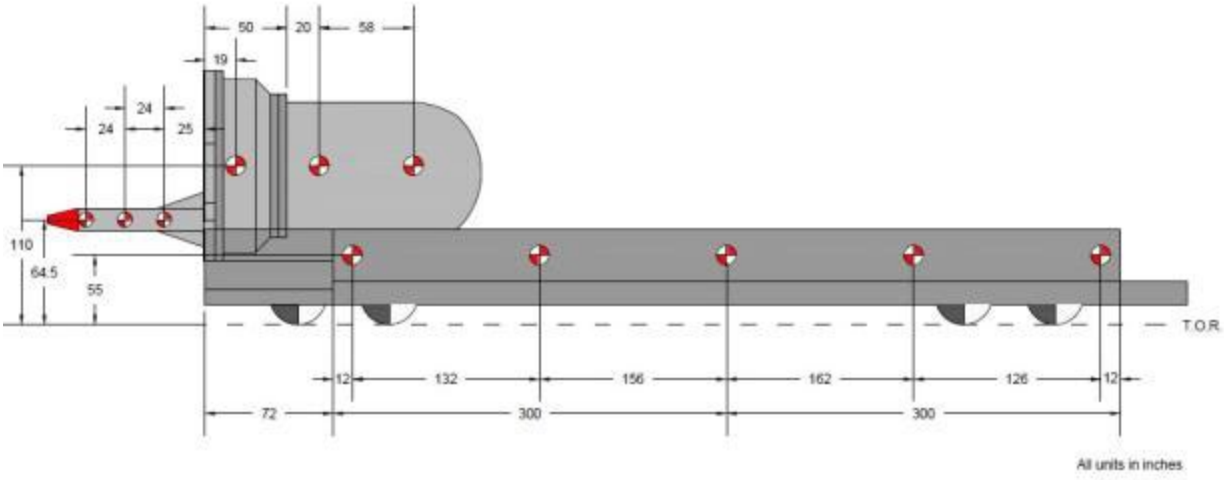

Figure A3. Ram Car Target Positions

Appendix B.
Test Data

This section contains raw and filtered accelerometer data shown in Figures B1 through B11. The raw accelerations measured at different locations on the impact car were processed as follows: 1) the test data from -1 to -0.1 seconds on each channel were averaged, and 2) this value was subtracted from the test measurements to remove any initial offsets in the data. Each channel was then filtered to channel frequency class (CFC) 60 using the procedures given in SAE J211 [19]. Displacement data did not require any filtration.

B.1. Accelerations

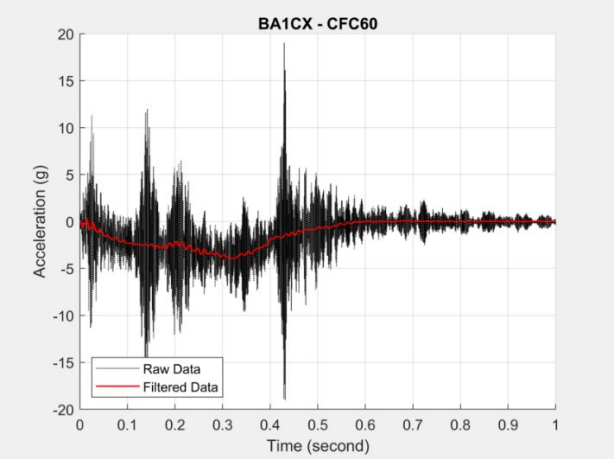

Figure B1. Raw and CFC60 Filtered Acceleration-Time Data from BA1CX

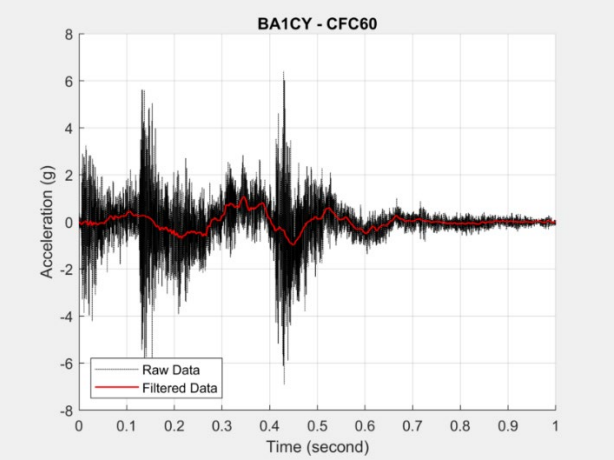

Figure B2. Raw and CFC60 Filtered Acceleration-Time Data from BA1CY

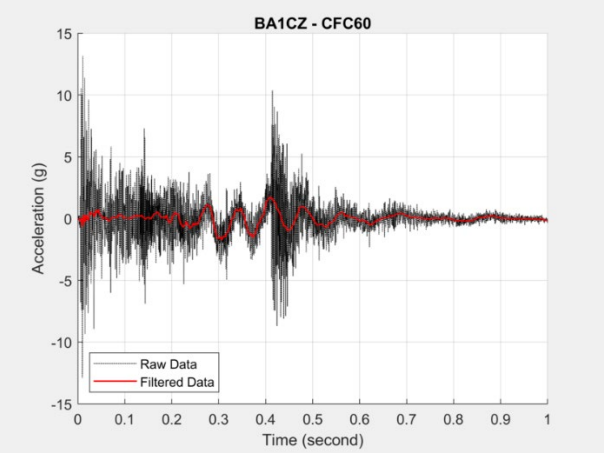

Figure B3. Raw and CFC60 Filtered Acceleration-Time Data from BA1CZ

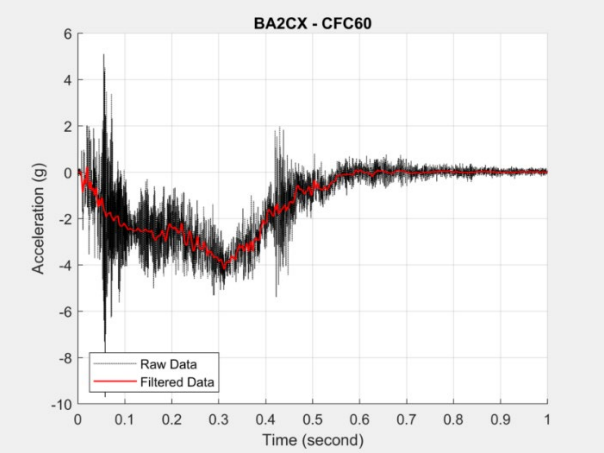

Figure B4. Raw and CFC60 Filtered Acceleration-Time Data from BA2CX

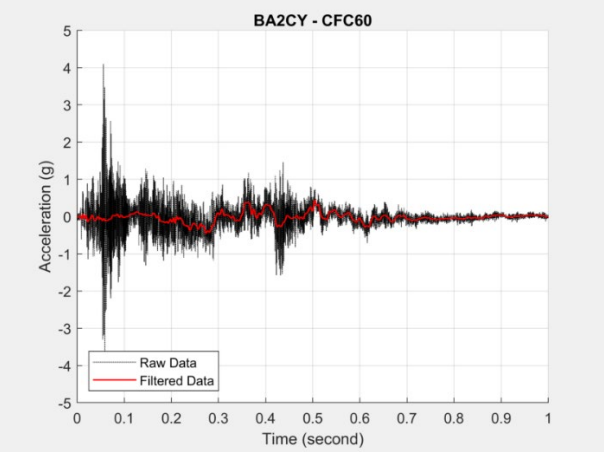

Figure B5. Raw and CFC60 Filtered Acceleration-Time Data from BA2CY

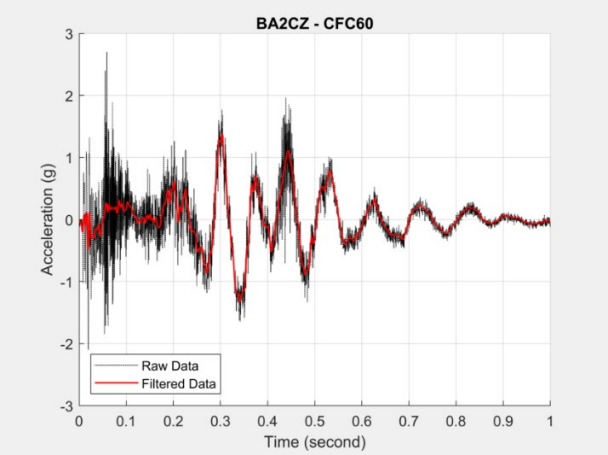

Figure B6. Raw and CFC60 Filtered Acceleration-Time Data from BA2CZ

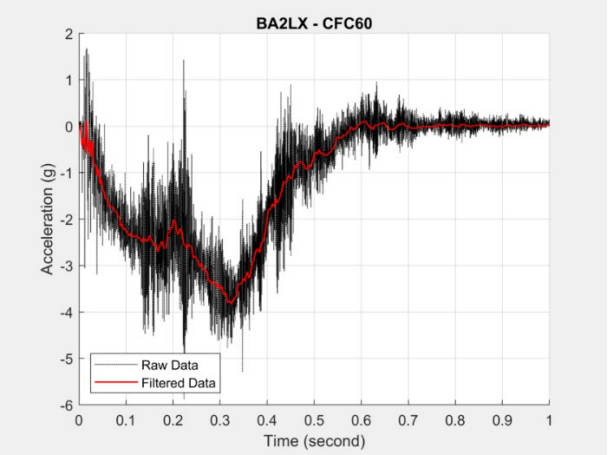

Figure B7. Raw and CFC60 Filtered Acceleration-Time Data from BA2LX

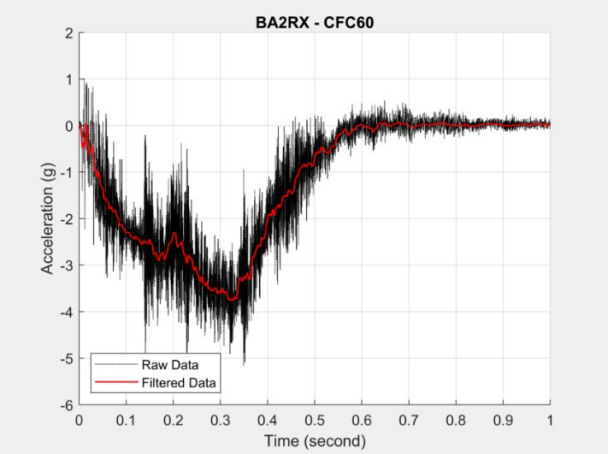

Figure B8. Raw and CFC60 Filtered Acceleration-Time Data from BA2RX

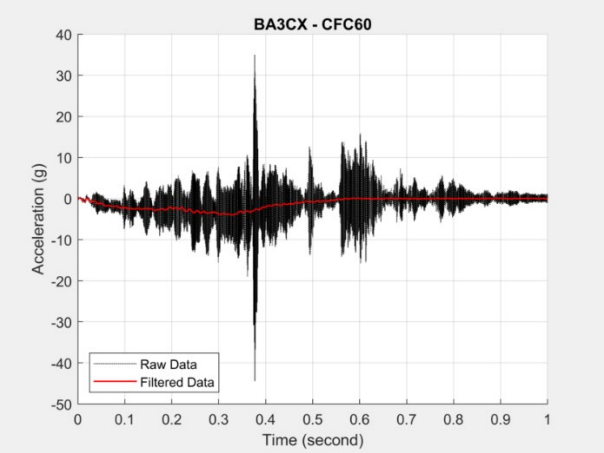

Figure B9. Raw and CFC60 Filtered Acceleration-Time Data from BA3CX

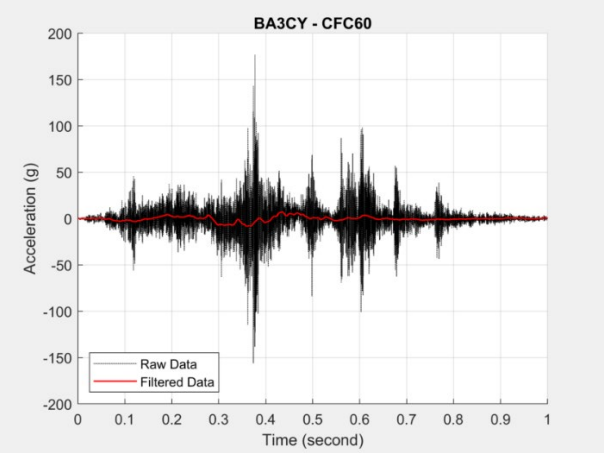

Figure B10. Raw and CFC60 Filtered Acceleration-Time Data from BA3CY

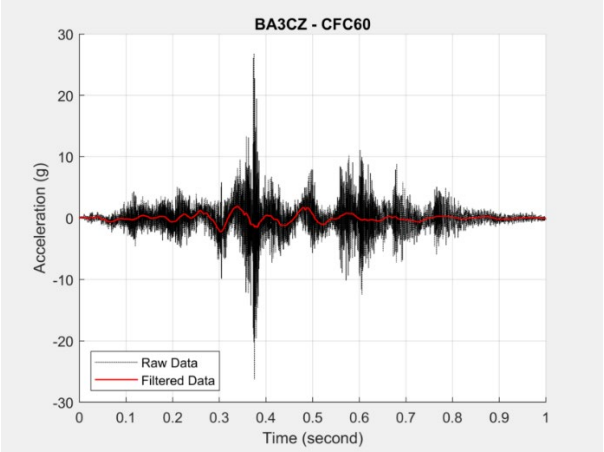

Figure B11. Raw and CFC60 Filtered Acceleration-Time Data from BA3CZ

B2. Pressures

This section contains raw pressure transducer data shown in Figures B12 through B24. The pressure measurements were made at different locations within the inner tank.

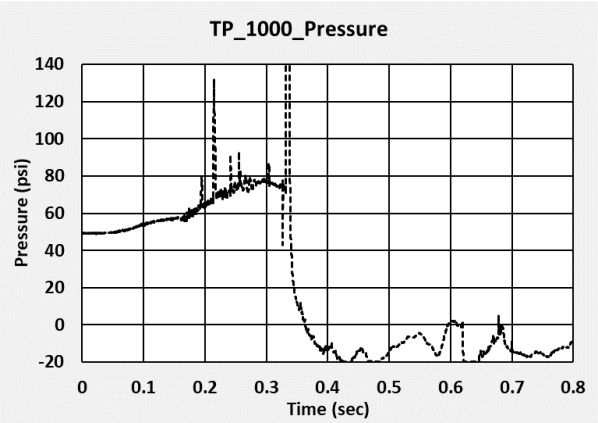

Figure B12. Raw Pressure-Time Data from TP1000

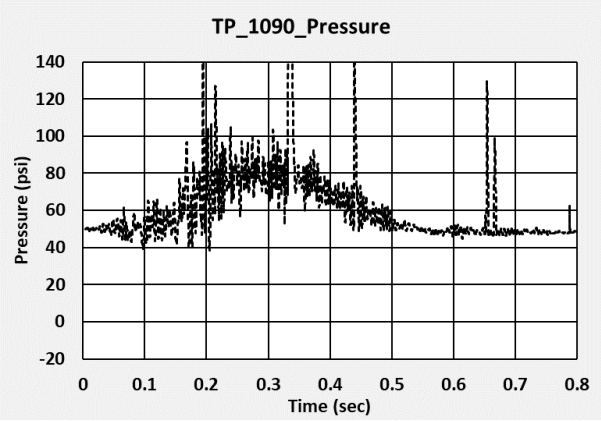

Figure B13. Raw Pressure-Time Data from TP1090

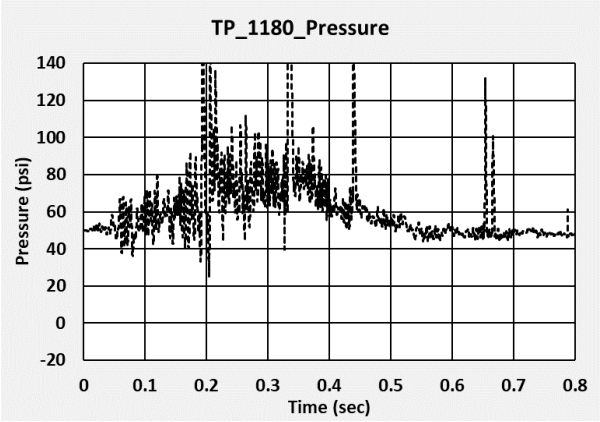

Figure B14. Raw Pressure-Time Data from TP1180

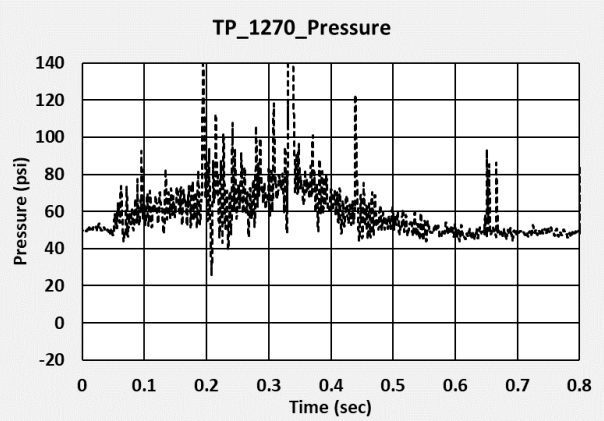

Figure B15. Raw Pressure-Time Data from TP1270

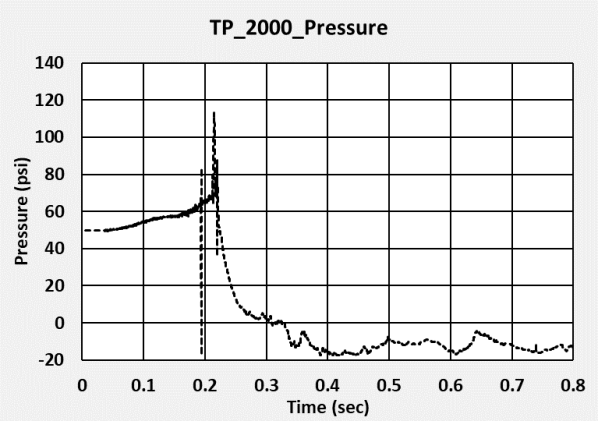

Figure B16. Raw Pressure-Time Data from TP2000

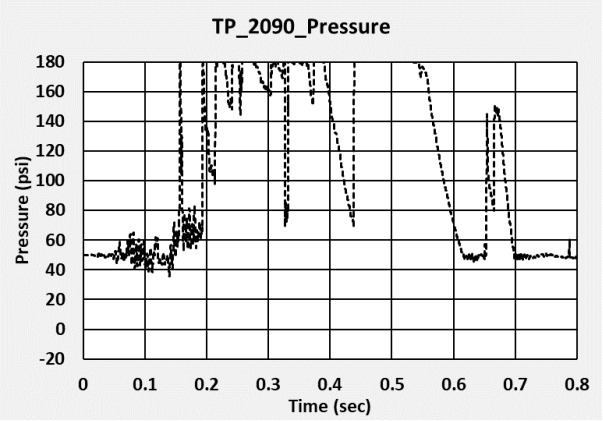

Figure B17. Raw Pressure-Time Data from TP2090

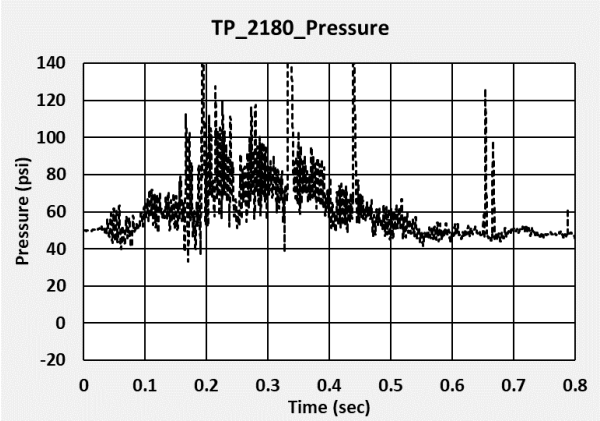

Figure B18. Raw Pressure-Time Data from TP2180

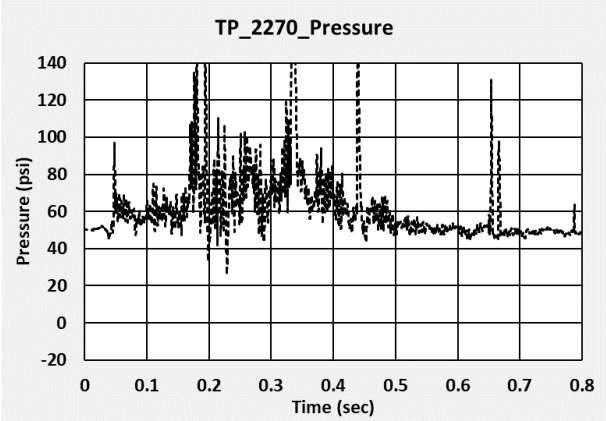

Figure B19. Raw Pressure-Time Data from TP2270

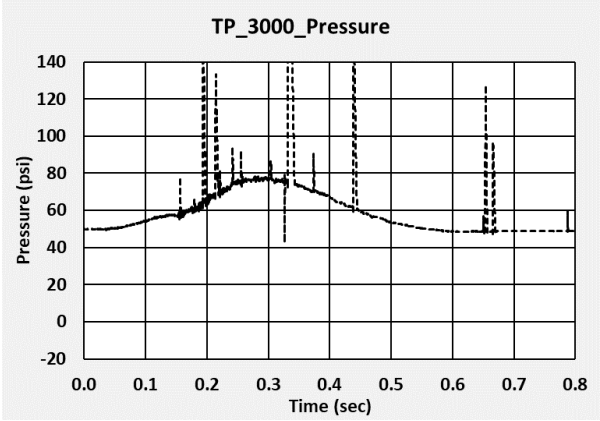

Figure B20. Raw Pressure-Time Data from TP3000

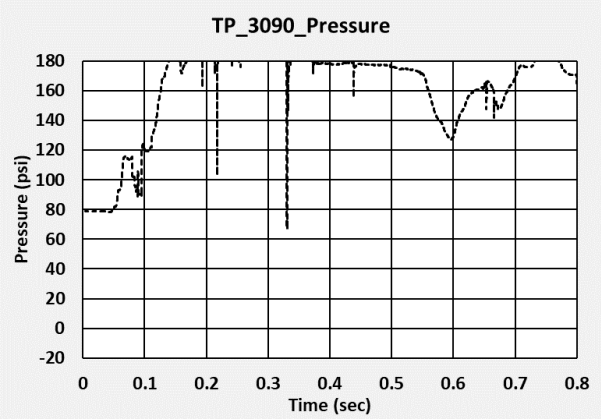

Figure B21. Raw Pressure-Time Data from TP3090

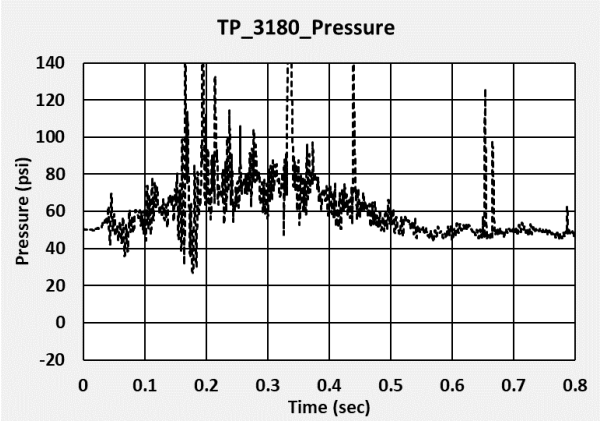

Figure B22. Raw Pressure-Time Data from TP3180

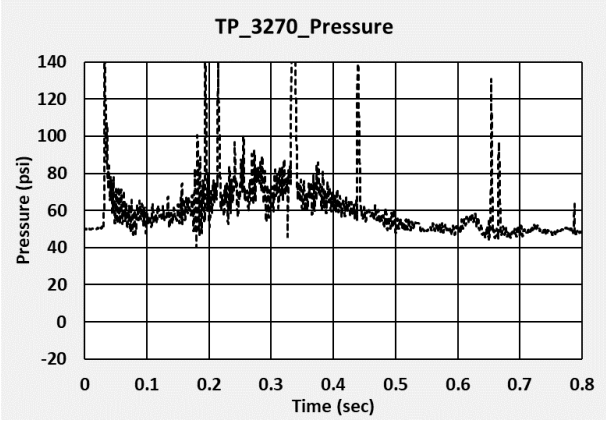

Figure B23. Raw Pressure-Time Data from TP3270

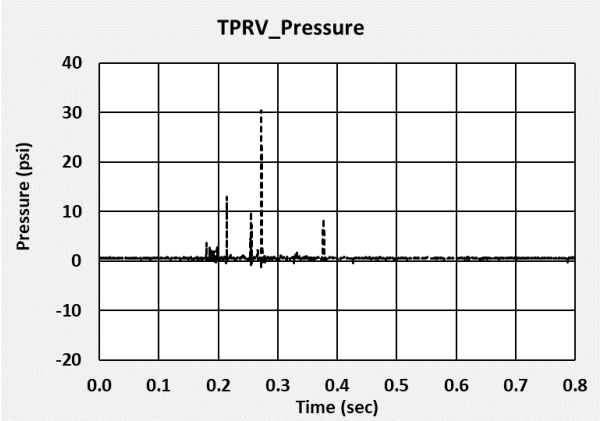

Figure B24. Raw Pressure-Time Data from TPRV

B3. Displacements

This section contains raw pressure displacement transducer data shown in Figures B25 through B49. The displacement measurements were made at different locations inside the tank car, outside of the tank car, and between the ram car and tank car.

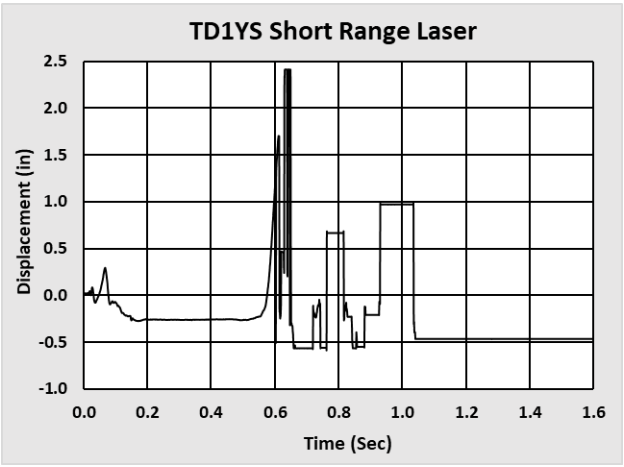

Figure B25. Raw Displacement-Time Data from Short Range Wall Mounted Laser Displacement Transducer (range: 1.4 in. to 4.3 in.)

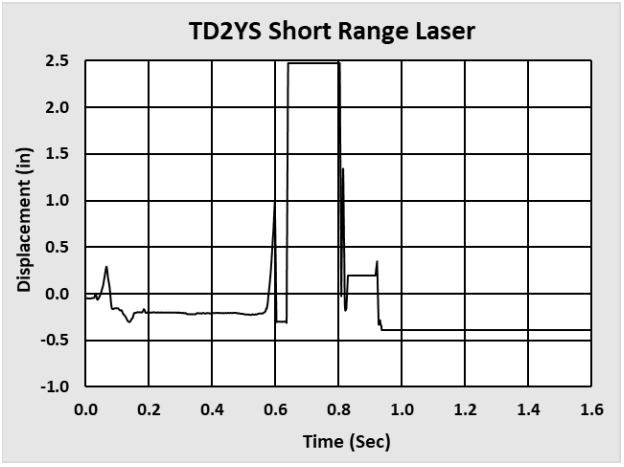

Figure B26. Raw Displacement-Time Data from Short Range Wall Mounted Laser Displacement Transducer (range: 1.4 in. to 4.3 in.)

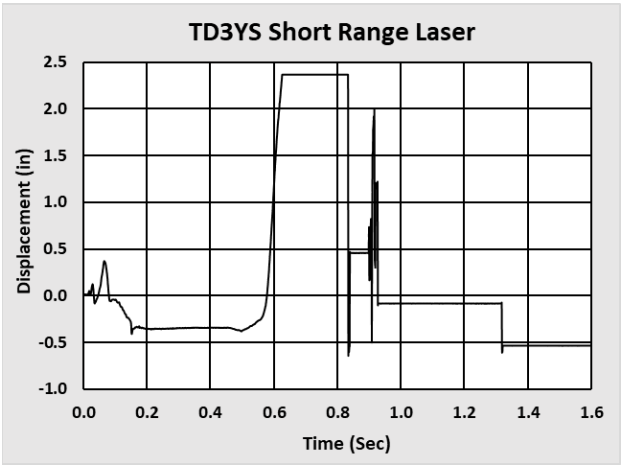

Figure B27. Raw Displacement-Time Data from Short Range Wall Mounted Laser Displacement Transducer (range: 1.4 in. to 4.3 in.)

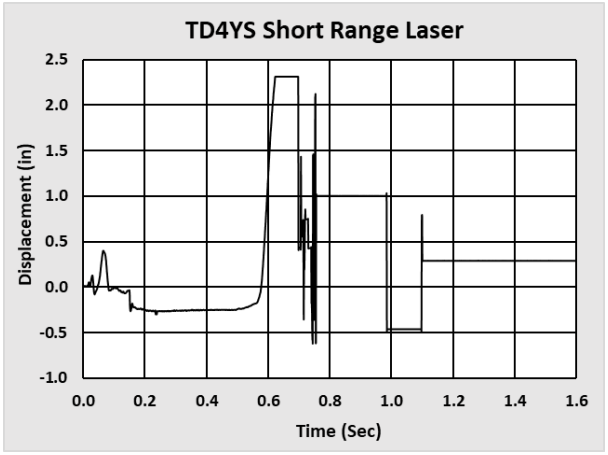

Figure B28. Raw Displacement-Time Data from Short Range Wall Mounted Laser Displacement Transducer (range: 1.4 in. to 4.3 in.)

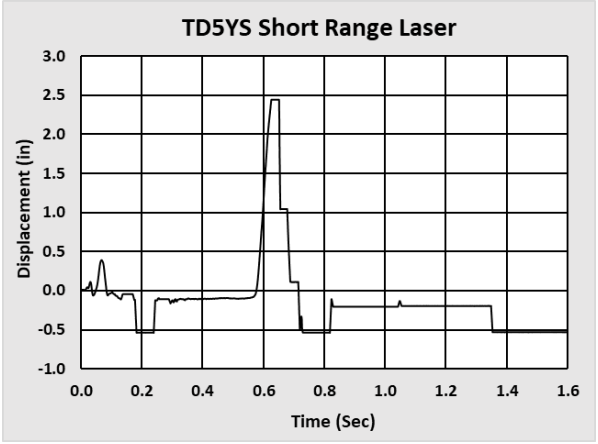

Figure B29. Raw Displacement-Time Data from Short Range Wall Mounted Laser Displacement Transducer (range: 1.4 in to 4.3 in)

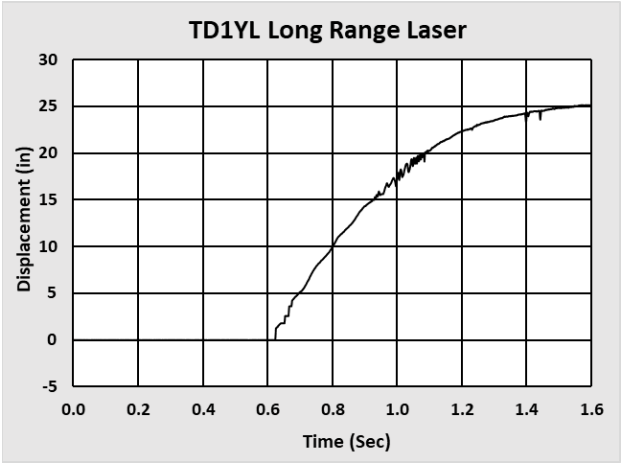

Figure B30. Raw Displacement-Time Data from Long Range Wall Mounted Laser Displacement Transducer (range: 4 in. to 39 in.)

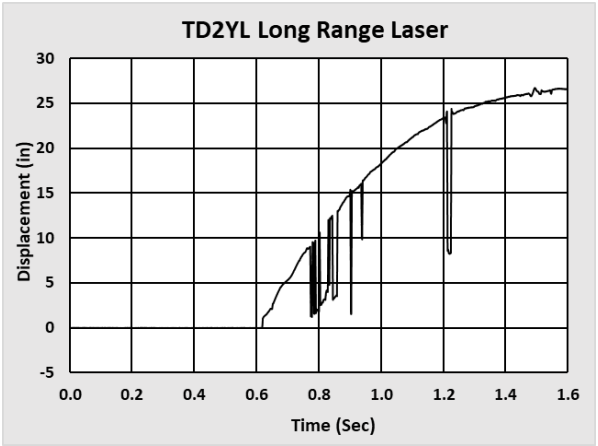

Figure B31. Raw Displacement-Time Data from Long Range Wall Mounted Laser Displacement Transducer (range: 4 in. to 39 in.)

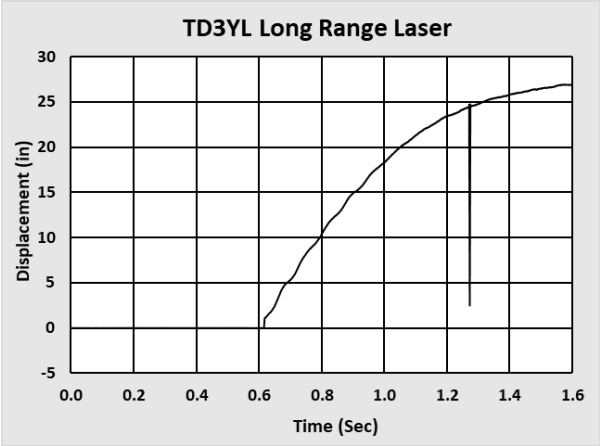

Figure B32. Raw Displacement-Time Data from Long Range Wall Mounted Laser Displacement Transducer (range: 4 in. to 39 in.)

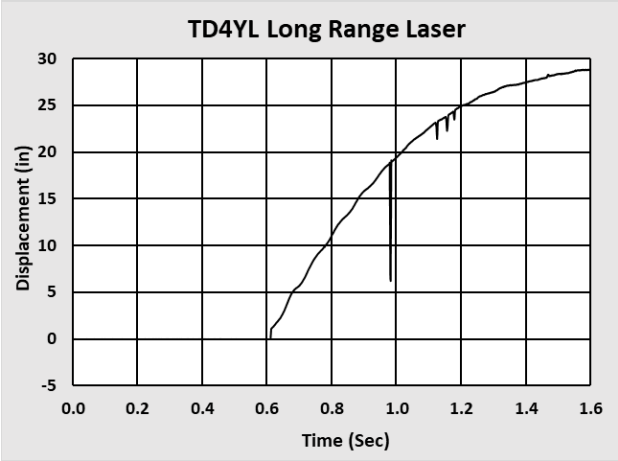

Figure B33. Raw Displacement-Time Data from Long Range Wall Mounted Laser Displacement Transducer (range: 4 in. to 39 in.)

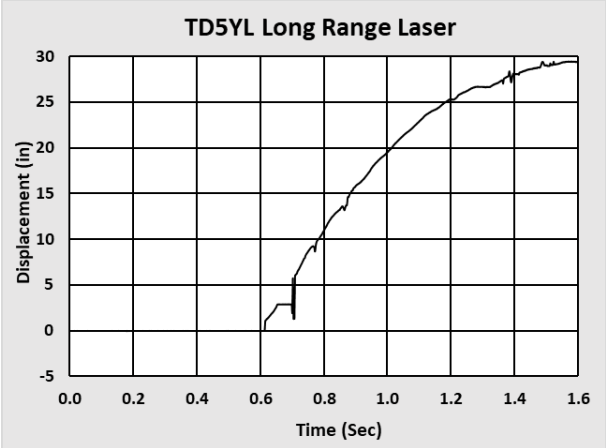

Figure B34. Raw Displacement-Time Data from Long Range Wall Mounted Laser Displacement Transducer (range: 4 in. to 39 in.)

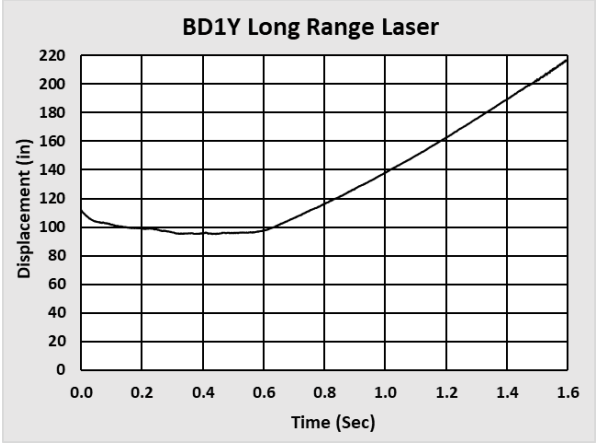

Figure B35. Raw Displacement-Time Data from Long Range Ram Car Mounted Laser Displacement Transducer (range: 2 in. to 39 ft.)

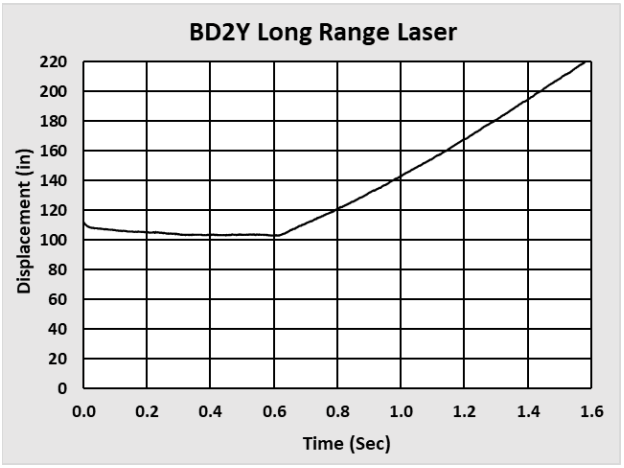

Figure B36. Raw Displacement-Time Data from Long Range Ram Car Mounted Laser Displacement Transducer (range: 2 in. to 39 ft.)

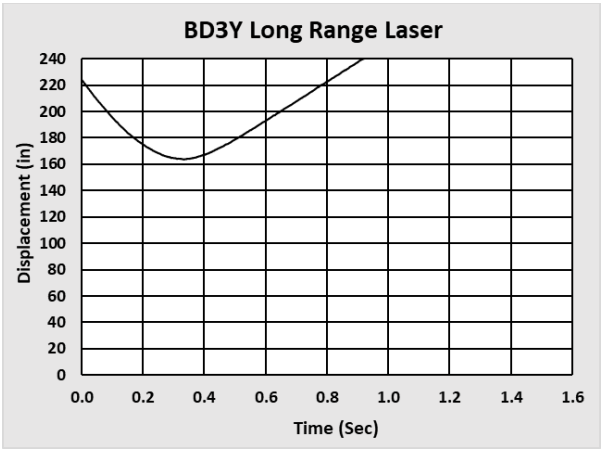

Figure B37. Raw Displacement-Time Data from Long Range Ram Car Mounted Laser Displacement Transducer (range: 2 in. to 39 ft.)

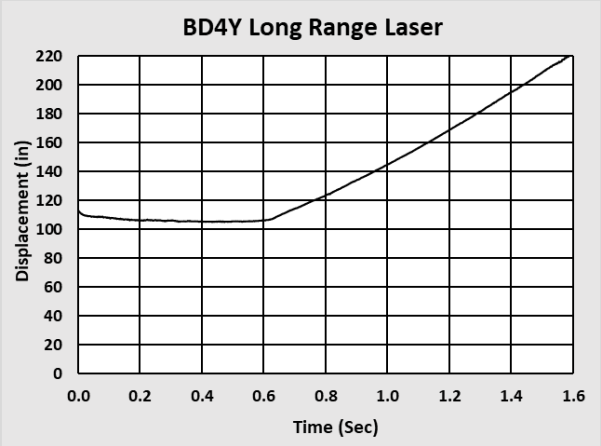

Figure B38. Raw Displacement-Time Data from Long Range Ram Car Mounted Laser Displacement Transducer (range: 2 in. to 39 ft.)

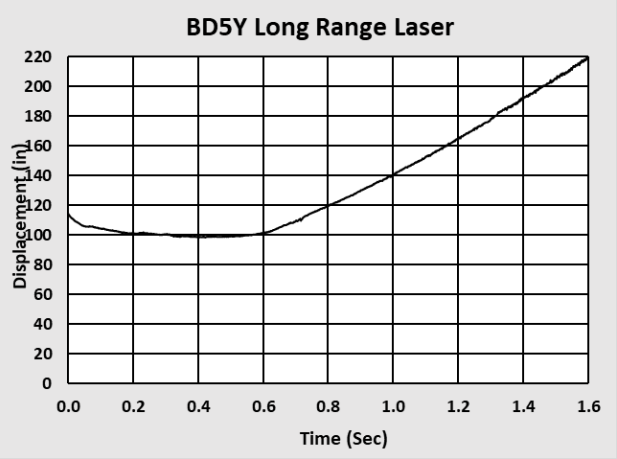

Figure B39. Raw Displacement-Time Data from Long Range Ram Car Mounted Laser Displacement Transducer (range: 2 in. to 39 ft.)

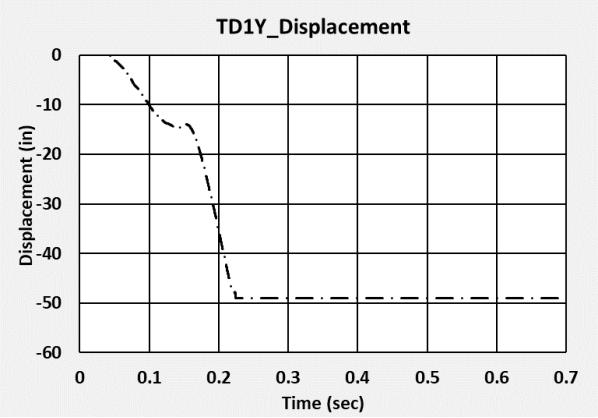

Figure B40. Raw Displacement-Time Data from TD1Y

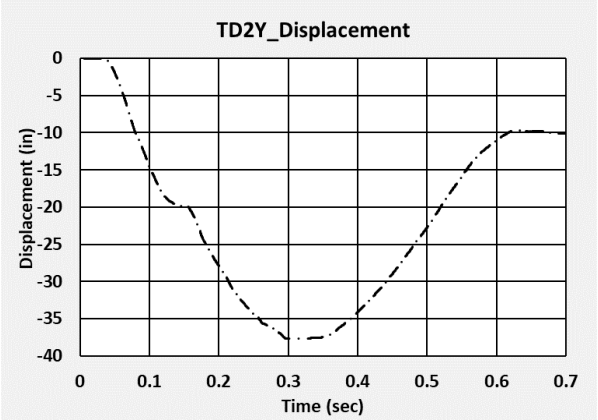

Figure B41. Raw Displacement-Time Data from TD2Y

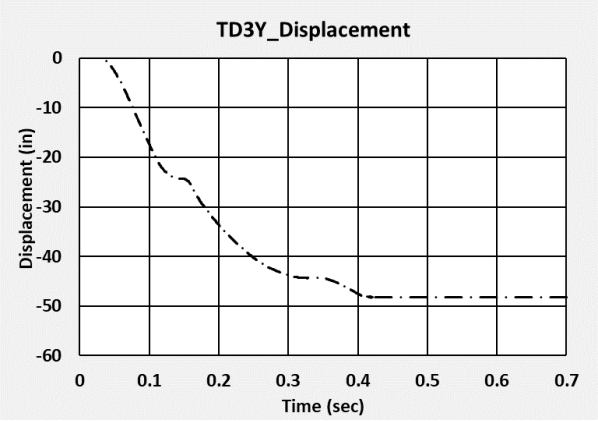

Figure B42. Raw Displacement-Time Data from TD3Y

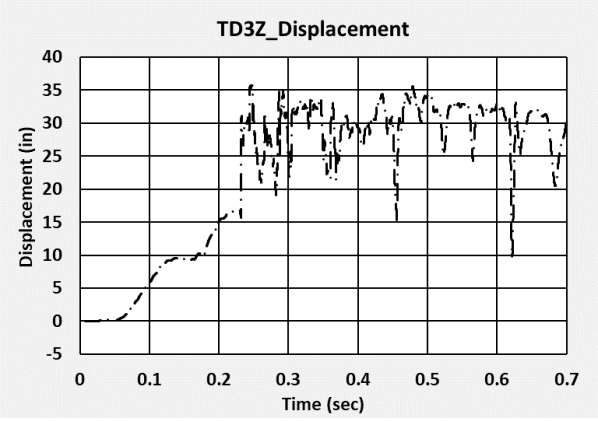

Figure B43. Raw Displacement-Time Data from TD3Z

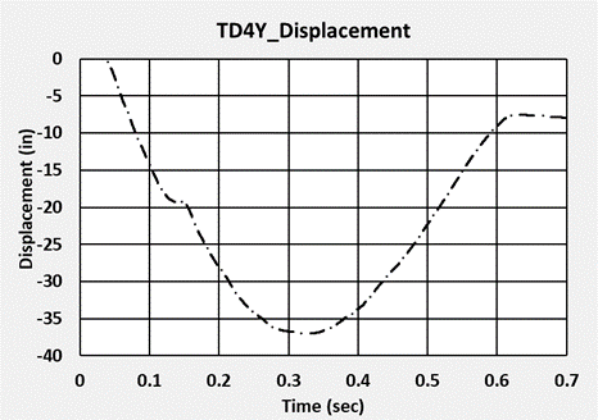

Figure B44. Raw Displacement-Time Data from TD4Y

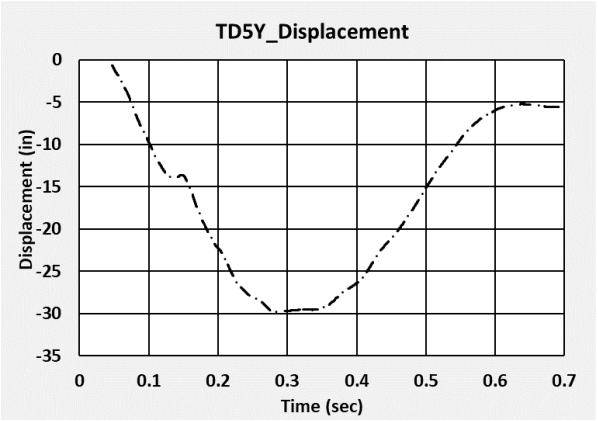

Figure B45. Raw Displacement-Time Data from TD5Y

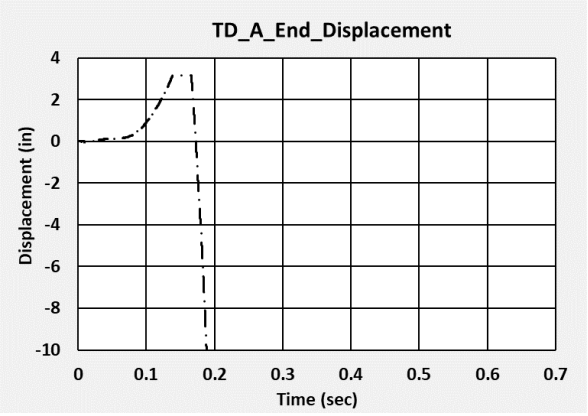

Figure B46. Raw Displacement-Time Data from Displacement Transducer on A-End Head

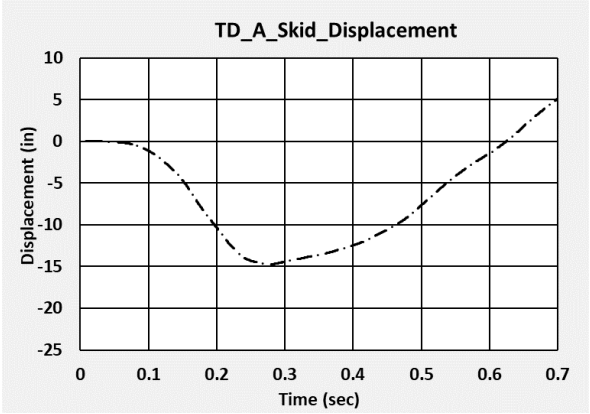

Figure B47. Raw Displacement-Time Data from Displacement Transducer on A-End Skid

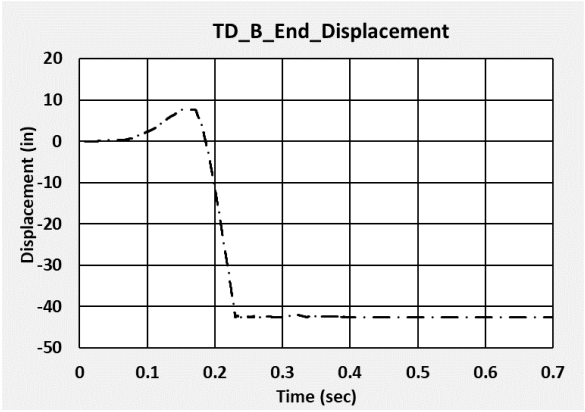

Figure B48. Raw Displacement-Time Data from Displacement Transducer on B-End Head

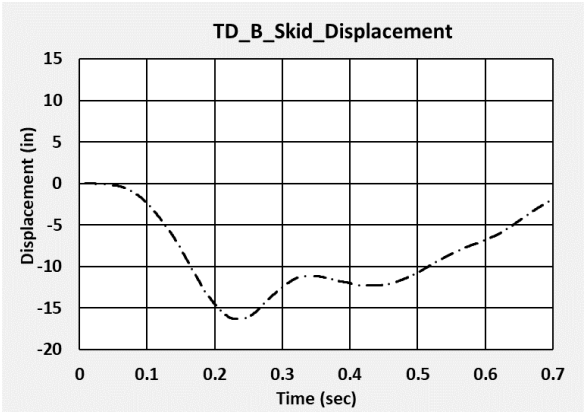

Figure B49. Raw Displacement-Time Data from Displacement Transducer on B-End Skid

B4. Material Characterization Results

Material characterization tests were performed on both the TC-128B carbon steel used in the outer tank and the T304 stainless steel used in the inner tank. Testing was performed on both types of material both before and after the impact test of the DOT-113 surrogate.

B4.1 AAR TC-128B, Carbon Steel (Pre-test)

The manufacturer of the outer tank provided tensile test data from the TC-128B parent material in the post-weld heat treated (PWHT) condition prior to the test. The average tensile properties from the manufacturer were used to calibrate a material model (refer to Appendix F) that was used in all pre-test and post-test modeling of the side impact test. Nominal stress-strain curves were not available for the TC-128B tensile coupons because the extensometer was detached after measuring the elastic modulus. Table B1 provides the tensile properties, i.e., yield strength (YS), ultimate tensile strength (UTS), elongation at break with a 2-inch gage length (EB-2in), and reduction in area (RA) for the pre-test specimens. The ASTM-E8 tensile coupons had a smooth round bar geometry with a 2-inch gage length and 1/2-inch diameter.

Table B1. Summary of AAR TC-128B Steel Tensile Pre-test Results

Specimen	YS	UTS	EB-2in	RA
-	ksi	Ksi	%	%
92106200_1	64.7	87.8	30.2	65.4
92106200_2	64.5	88	31.6	66.2
92106300_1	66.2	90.4	31	64.2
92106300_2	66.1	90.4	30.6	65.7
92106400_1	64.4	87.5	33.1	70
92106400_2	64	87.5	31.8	69.8
92106500_1	64.4	89.3	31.2	68.9
92106500_2	64.9	89.8	32.1	69.3
Average	64.9	88.8	31.4	67.4
Specification	50 min.	81–101	22 min.	-

B4.2 AAR TC-128B, Carbon Steel (Post-test)

Additional post-test mechanical testing on TC-128B carbon steel was conducted to examine the properties of the factory and closure welds on the outer tank. Post-test material testing was also conducted on the "parent," or unwelded, TC-128B to verify that the area selected for post-impact TC-128B coupon removal was unaffected by the tank's permanent deformation. This post-test characterization was conducted in two phases because the results of the first phase of testing required additional testing to be better understood.

In addition to visually inspecting the tank, the post-test FE model was used to identify areas of low plastic strain. Figure B50 uses a contour plot to show a section view of plastic equivalent (PEEQ) strain taken from the post-test FE model run at the test condition. This image guided the decision of where to excise the TC-128B post-test coupons. The areas around the 2 and 5 o'clock position on the tank showed near-zero levels of PEEQ, indicating these areas did not undergo significant permanent deformation during the test. This region also includes both a factory circumferential weld and the closure weld. Unfortunately, due to a misunderstanding, the first set of post-test TC-128B coupons were cut from the 8 o'clock position and not the 2 or 5 o'clock position as originally intended.

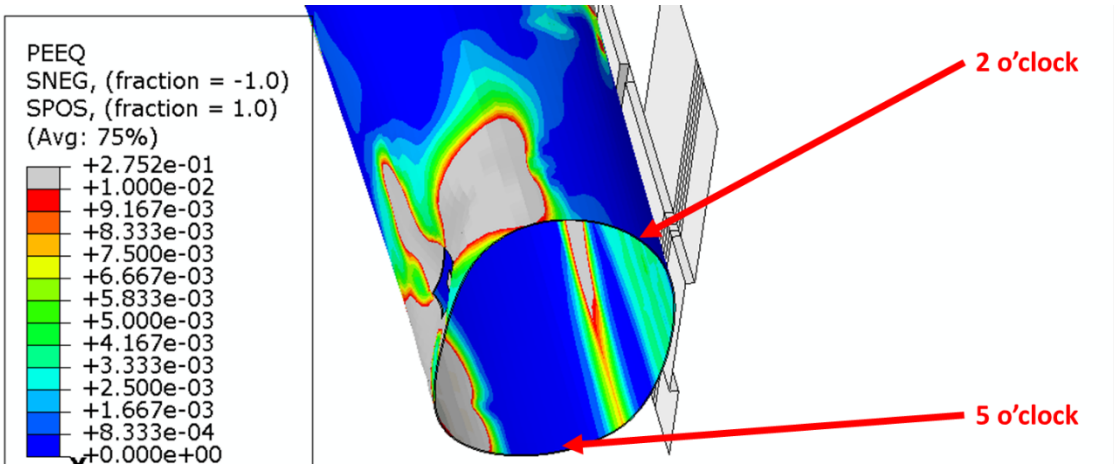

Figure B50. Contours of PEEQ on Post-test FE Model Showing Areas Identified for Weld Coupon Cutting

The longitudinal locations of the closure weld and "factory" weld selected for tensile coupons are shown in Figure B51. The left side of this figure shows the impact zone of the tank, while the right side is a zoomed-in view of the two circumferential welds. The right side also contains an overlay showing, schematically, how tensile test coupons would be excised from the closure weld, parent TC-128B steel, and "factory" weld.

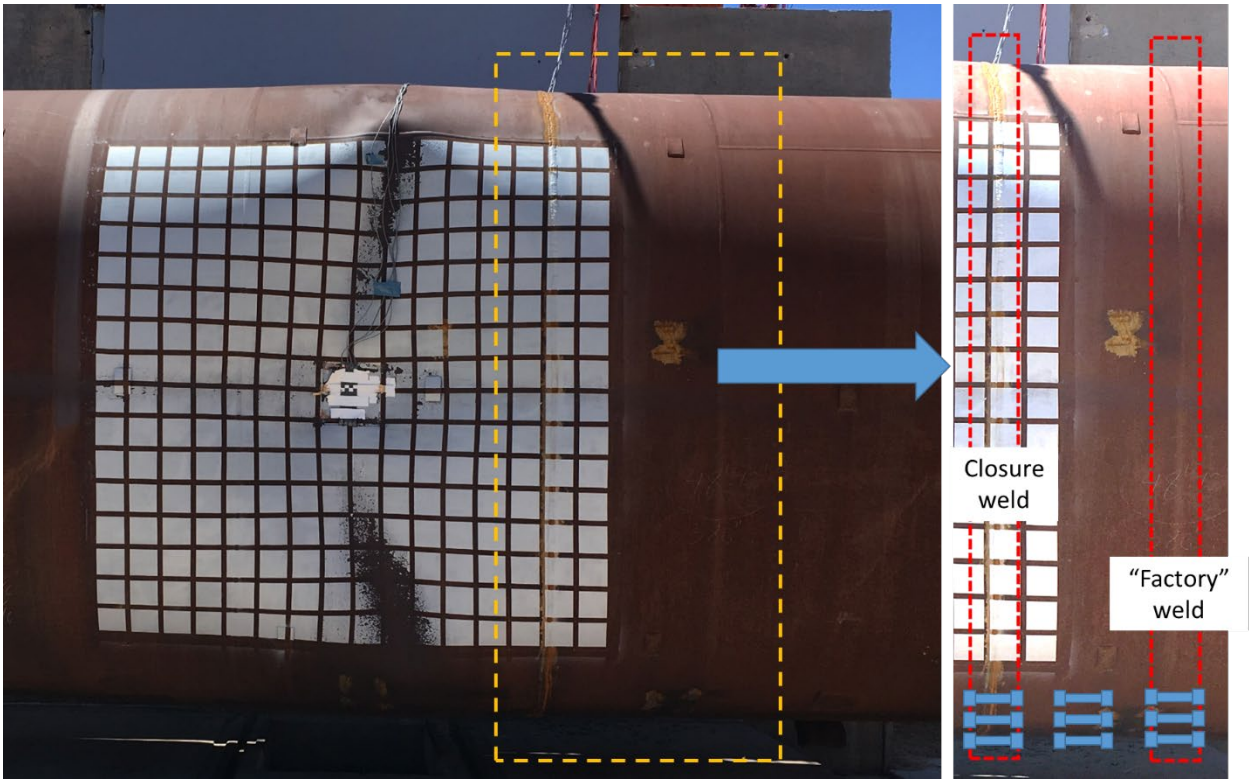

Figure B51. Longitudinal Positions of Closure and Factory Welds for Tensile Testing

The coupon orientation shown on the right side of Figure B51. would be tested with the tensile load applied parallel to the axial direction of the tank. This direction corresponds to the "transverse-to-rolling" direction of the curved plates making up the outer tank's rings. Cutting the welded coupons using this orientation results in a composite material sample, where a single coupon may include TC-128B steel from two parent plates, a weld, and a heat-affected zone (HAZ) between the weld and each parent material. This distribution of materials is illustrated schematically in Figure B52.

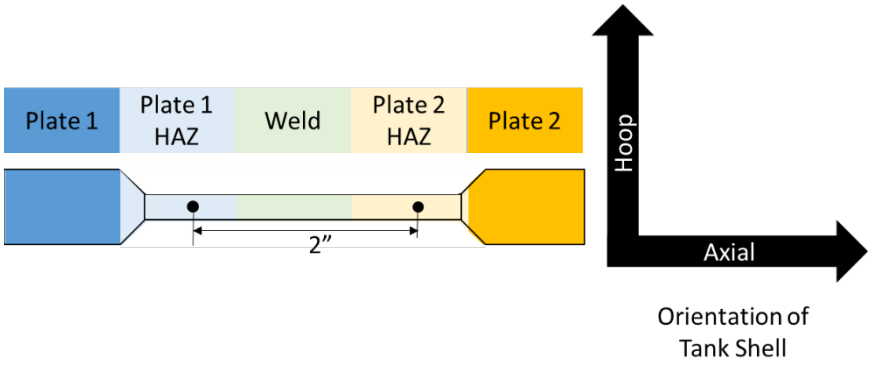

Figure B52. Orientation of Welded Tensile Coupons, Axial Orientation

TTCI provided the lab with five coupons in each material condition, leaving the lab to choose three coupons to test at random. In its report, the lab noted that "[o]ne field [closure] weld specimen was rejected due to the presence of a large lack of fusion defect at the weld." This rejected coupon is shown in Figure B53. The left side of this figure shows the entire coupon,

with a superimposed box indicating the area of detail shown on the right side of the figure. In each photograph, the right side of the coupon features the backing bar, indicating it was originally adjacent to the annular space between the outer and inner tanks. The weld was made on the left side of the figure as that was the outer surface of the outer tank.

Figure B53. Closure Weld Specimen Rejected Due to Lack of Fusion Defect in Weld

The welded coupons exhibited several trends common to both the factory weld and closure weld. None of the welded coupons broke in the weld itself. All the welded coupons broke in an area between the grip section and the weld. All welded samples also broke outside of the 2-inch gage section in the center of the coupon.

The axially oriented tensile tests provided some information on the behaviors of the different types of welds. As noted above, none of the coupons broke in the weld itself, but in an area more than 1 inch away from the center of the weld. This behavior was observed in both the factory and closure welds. The average UTS of both types of welds fell within the acceptable range of UTS per the specification for TC-128B steel. The average UTS of the factory weld was slightly lower (1.7 ksi) than the average UTS of the parent material tested post-impact. The average UTS of the closure weld was slightly higher (0.5 ksi) than the average UTS of the parent material tested post-impact.

Values for YS were not reported by the test lab for coupons in the welded condition. As a result of the break outside the gage section, the elongation at break (EB-2in) values recorded during the tests of welded coupons are not a reliable indication of the ductility of the weld. Significant necking that would not have been captured by measuring the post-break distance between the gage marks may have occurred outside of the gage section prior to the break. These two data limitations prevented any meaningful comparison of YS or EB-2in across the axially oriented tensile test results.

The axially oriented tensile tests did not provide sufficient data to understand whether the welds would be likely to have a different puncture resistance from the parent material or if the two types of welds would be expected to perform differently from one another. While the UTS for TC-128B in each material was comparable, there was insufficient data to make a meaningful comparison of ductility across the three samples. The data collected from the axially oriented tests revealed that the weld itself was not the point of failure in any of the coupons tested. However, the coupons all failed outside of the gage section but within the reduced-width section of the coupon. This section would contain the HAZ from the welded coupons, but it was not known if the HAZ for the two different weld types would perform similarly.

A second set of coupon tests were performed to further investigate the behaviors of the two weld types and the HAZ associated with each type. To ensure that the desired material condition of TC-128B was being tested, the coupon orientation for the second round of testing was rotated 90-degrees from the axial direction, so that the tensile forces were applied in the hoop direction. While this orientation would result in a coupon with a slight curvature from the tank's circular cross-section, coupons could be machined entirely out of parent plate, HAZ, or welded condition TC-128B as shown in Figure B54.

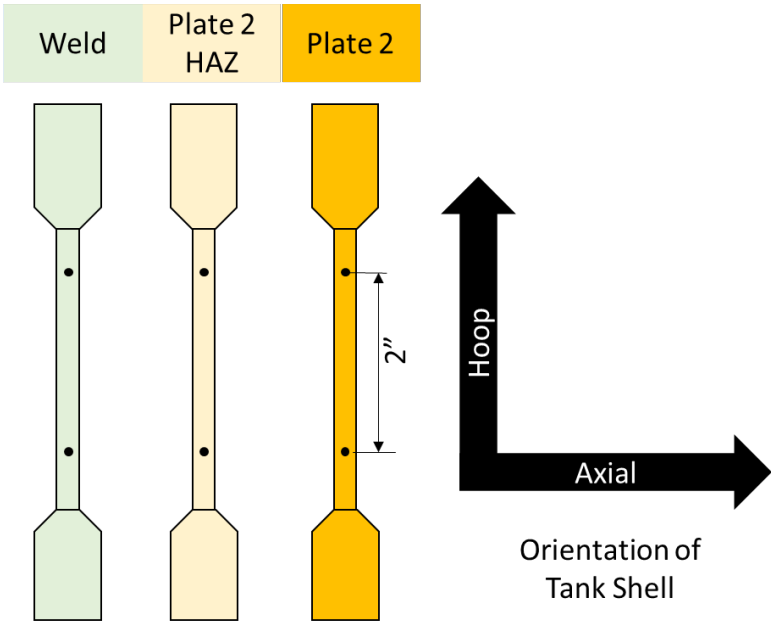

Figure B54. Orientation of Welded Tensile Coupons, Hoop Orientation

In addition to conducting tensile tests, the second round of testing on the outer tank's TC-128B steel also included CVN testing on material in different conditions. CVN testing is performed to evaluate the energy necessary to fracture a sample subjected to an impact from a standardized pendulum. It was thought that CVN data would be useful for comparing the performance of the different TC-128B steel conditions associated with the welds and with calibrating any future FE material models of TC-128B steel in welded condition.

CVN testing can be performed using a coupon excised in numerous orientations from the tank's plate. For the weld tests, the coupons were cut with their long direction parallel to the axial direction of the tank and the V-notch cut into the thickness of the tank plate from the face of the shell that would face the inner tank. Thus, during the CVN test the striker made contact with the

face of the coupon that corresponded with the outer surface of the tank's shell. This orientation is referred to as the T-S orientation, where "T" is parallel to the transverse-to-rolling direction of the tank shell's plate and "S" is the through-thickness direction [30]. Figure B55 shows a schematic diagram of T-S orientation coupons for TC-128B steel in the welded, HAZ, and parent plate conditions. While the weld and HAZ coupons included material in another condition due to the length in the axial direction, the V-notch was cut into the material in the condition of interest for a given test as that is the region where failure will occur.

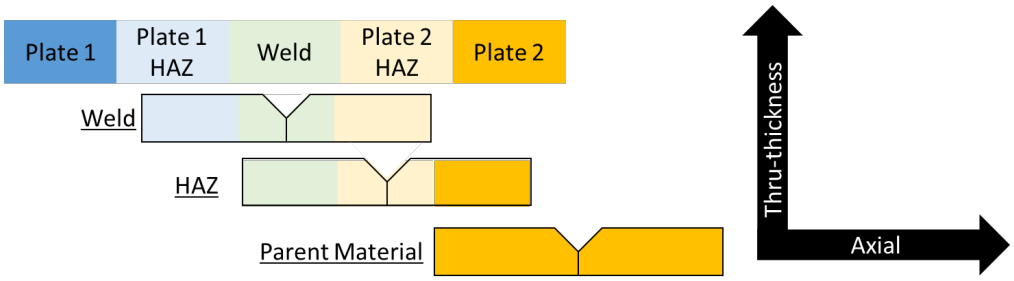

Figure B55. T-S Orientation of CVN Coupons

First Phase of Testing Results

After the test, TTCI extracted tensile coupons from three locations on the outer tank just above the low-PEEQ area to characterize the properties of the parent material, the circumferential factory weld, and the closure weld. The closure weld is depicted in Figure B51. The tensile coupons were all oriented transverse to the rolling direction of the plates (i.e., along the long axis of the tank) meaning that they were cut across circumferential welds. TTCI contracted an independent test lab to conduct the tensile tests. The ASTM-E8 flat specimens had a gage section measuring 2 inches long, 1/2 inch wide, and 9/16 inch thick.

Figure B56 shows the post-test condition of the three coupons of parent TC-128B steel. These coupons all fractured within the gage section, and the extent of the fractures are indicated by two small indentations visible on each bar.

Figure B56. Post-test Parent Material ASTM-E8 Tensile Coupons

Figure B57 shows the post-test condition of the three coupons cut across the factory weld seam. The weld itself is visible in the center of each coupon. There were two observations of interest

made regarding the failure behaviors of these samples. First, each coupon failed outside of the weld itself. Second, the failure occurred outside of the gage section in each coupon.

Figure B57. Post-test Factory Weld ASTM-E8 Tensile Coupons

Figure B58 shows the post-test condition of the three coupons cut across the closure weld seam. The weld itself is visible in the center of each coupon. There were two observations of interest made regarding the failure behaviors of these samples. First, each coupon failed outside of the weld itself. Second, the failure occurred outside of the gage section in each coupon. These observations are consistent with the observations made for the coupons containing the factory weld.

Figure B58. Post-test Closure Weld ASTM-E8 Tensile Coupons

The mechanical properties of the post-impact TC-128B were similar to the pre-impact TC-128B test data provided by the outer tank's manufacturer. This indicates that the post-impact coupons were excised from the outer tank at an area that did not experience a substantial amount of permanent deformation that could have affected the TC-128B steel's mechanical properties. The pre-impact and post-impact TC-128B parent material properties are compared in Table B2.

Table B2. Comparison of Average Pre-impact and Post-impact TC-128B Parent Material Properties

Material Source	Type	YS	UTS	EB-2in
	-	*ksi*	*ksi*	*%*
Post-impact	**Parent Material**	**64.5**	**86.5**	**37.1**
Pre-impact	**Parent Material**	**64.9**	**88.8**	**31.4**
Specification Requirement		*50 min*	*81–101*	*22 min*

Table B3 provides the tensile properties (i.e., YS, UTS, and EB-2in) for the post-test TC-128B coupons in each welded condition.

Table B3. Summary of AAR TC-128B, Steel Tensile Post-test Results (axial orientation)

Specimen	Type	YS	UTS	EB-2in
-	-	*ksi*	*ksi*	*%*
M1	Parent Material	64.2	85.8	38.3
M2	Parent Material	65.2	87.3	37.3
M3	Parent Material	64.2	86.2	35.8
Average	Parent Material	64.5	86.5	37.1
FW1	Factory Weld	-	84.9	11.1
FW2	Factory Weld	-	84.7	12.1
FW3	Factory Weld	-	84.7	12.5
Average	Factory Weld	-	84.8	11.9
CW1	Closure Weld	-	86.8	7.5
CW2	Closure Weld	-	87.0	5.2
CW3	Closure Weld	-	87.2	7.5
Average	Closure Weld	-	87.0	6.7
Specification	-	50 min	81–101	22 min

Second Phase of Testing Results

The second phase of testing included tensile testing conducted in the hoop orientation for TC-128B steel in the parent condition, HAZs from both types of welds (i.e., closure and factory), and both types of welds. Table B4 provides the tensile properties (i.e., YS, UTS, and EB-2in) for the post-test TC-128B coupons in each welded condition.

Table B4. Summary of AAR TC-128B Steel Tensile Post-test Results (hoop orientation)

Specimen	Type	YS	UTS	EB-2in
		ksi	*ksi*	*%*
	Parent Material	55.0	82.7	32.5
	Parent Material	59.6	82.6	31.5
	Parent Material	60.2	82.9	31
	Parent Material	60.6	83.3	31
Average	Parent Material	58.9	82.9	31.5
	Factory Weld	56.7	82.8	25

Specimen	Type	YS	UTS	EB-2in
		ksi	*ksi*	*%*
	Factory Weld	58.6	87.1	29
	Factory Weld	59.8	86.1	28
	Factory Weld	43.5	83.3	26
Average	Factory Weld	54.7	84.8	27
	HAZ – Factory Weld	59.8	82.8	36
	HAZ – Factory Weld	59.9	82.9	35
	HAZ – Factory Weld	60.9	82.9	29
	HAZ – Factory Weld	59.4	82.8	34
Average	HAZ – Factory Weld	60.0	82.8	33.5
	Closure Weld	79.0	96.7	40
	Closure Weld[11]	76.2	82.5	17
	Closure Weld	79.4	94.3	38
	Closure Weld	75.2	98.1	37.5
Average	Closure Weld	77.4	92.9	33.125
	HAZ - Closure Weld	59.4	83.9	34
	HAZ - Closure Weld	57.3	83.4	32
	HAZ - Closure Weld	59.7	82.8	31
	HAZ - Closure Weld	57.5	83.8	30.5
Average	HAZ - Closure Weld	58.5	83.4	31.875
Specification		50 min	81–101	22 min

Figures B59, B60, and B61 contain the YS, UTS, and EB-2in for TC-128B steel in the various material conditions, respectively.

[11] Sample CW-2 fractured near transition from reduced-width section to grip section.

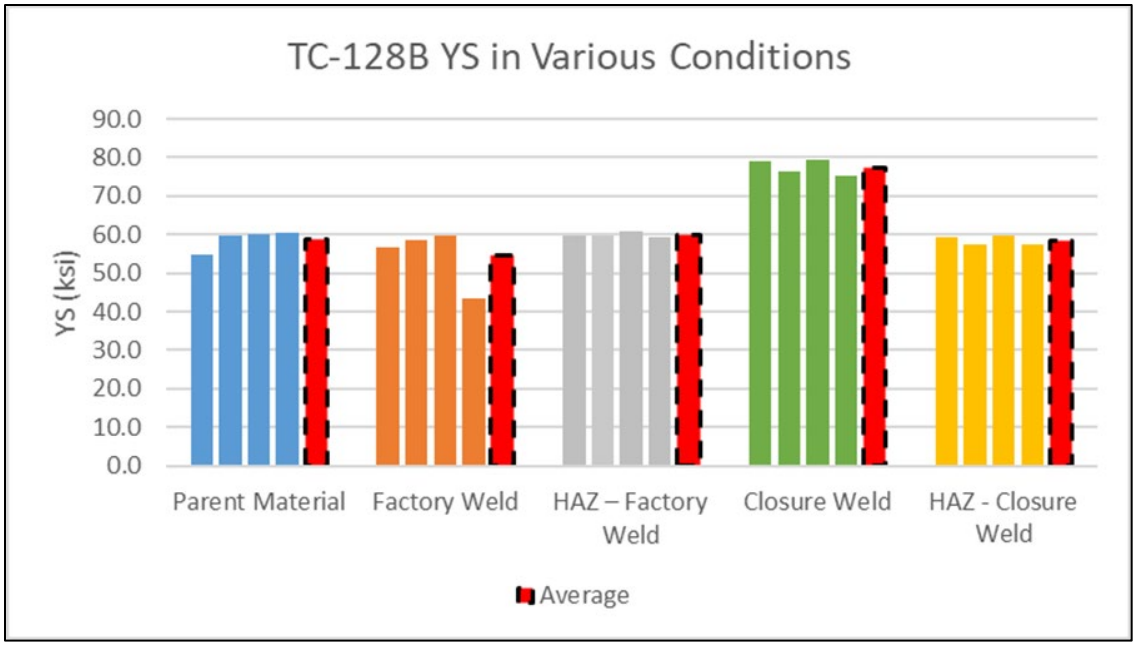

Figure B59. TC-128B Steel YS in Various Conditions

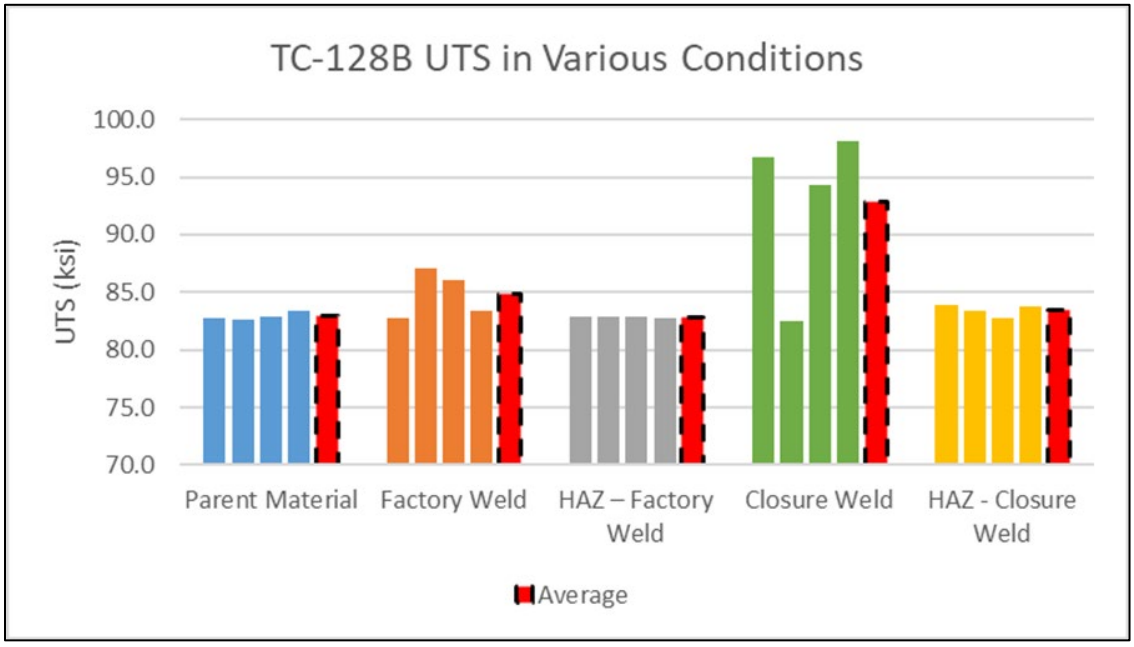

Figure B60. TC-128B Steel UTS in Various Conditions

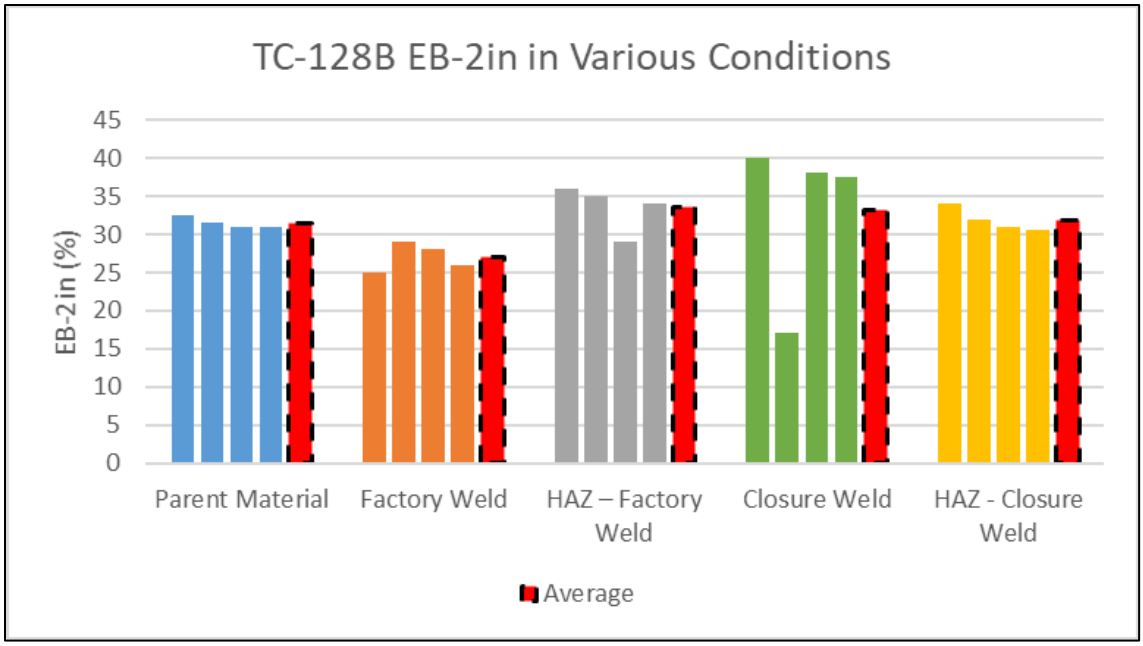

Figure B61. TC-128B Steel EB-2in in Various Conditions

The second phase of post-impact TC-128B testing also included CVN testing on coupons extracted from TC-128B in different conditions. This testing used a 10 mm by 10 mm cross-section coupon. Each CVN coupon was tested in the T-S orientation, with its long axis parallel to the "transverse" plate direction of the tank's shell and the notch pointing in the through-thickness direction of the tank's shell. CVN tests were performed on parent material, HAZs from each weld type, and each weld type. All CVN tests were performed at a temperature of 70 °F (294 K). Table B5 contains the CVN test results for TC-128B steel in the T-S orientation. The data from this table are plotted in Figure B62. The results of the CVN testing indicated that the parent material had the most consistent results of all the tested conditions. The factory-welded condition exhibited the largest scatter of results of any material condition. The closure weld exhibited energy absorption consistently lower than any other material condition.

Table B5. Summary of AAR TC-128B Steel CVN Results (T-S orientation)

Specimen	Type	Absorbed Energy
		ft-lbf
	Parent Material	113
	Parent Material	111
	Parent Material	114
	Parent Material	109
	Parent Material	112
Average	**Parent Material**	111.8
	Factory Weld	94
	Factory Weld	106
	Factory Weld	137
Average	**Factory Weld**	112.3
	HAZ – Factory Weld	124
	HAZ – Factory Weld	123

Specimen	Type	Absorbed Energy
		ft-lbf
	HAZ – Factory Weld	112
	HAZ – Factory Weld	128
Average	**HAZ – Factory Weld**	121.8
	Closure Weld	92
	Closure Weld	77
	Closure Weld	70
	Closure Weld	66
Average	**Closure Weld**	76.3
	HAZ - Closure Weld	117
	HAZ - Closure Weld	90
	HAZ - Closure Weld	108
	HAZ - Closure Weld	100
Average	**HAZ - Closure Weld**	103.8

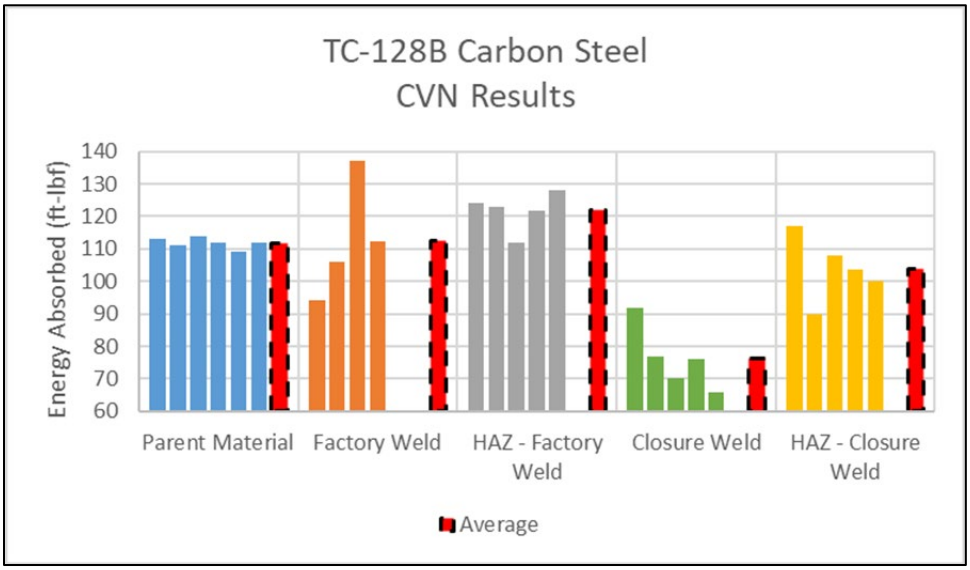

Figure B62. CVN Energy Absorbed for TC-128B Steel in Different Material Conditions (T-S orientation)

B4.3 ASTM A240, Type 304 Stainless Steel (Pre-test)

Pre-test tensile coupons were extracted from the inner tank during the manufacturing process. TTCI contracted an independent test lab to conduct tensile testing on the extracted coupons. Figure B63 shows the nominal stress-strain curves for the T304 tensile coupons. The extensometer, however, was removed when it reached the limit of its deflection (approximately 0.2 in/in), and therefore, the remainder of the stress-strain curve (up to fracture) was estimated using crosshead travel. The three T304 tensile coupons had a flat, rectangular ASTM-E8 geometry with gage dimensions of 2 inches long, 1/2 inch wide, and 1/4 inch thick.

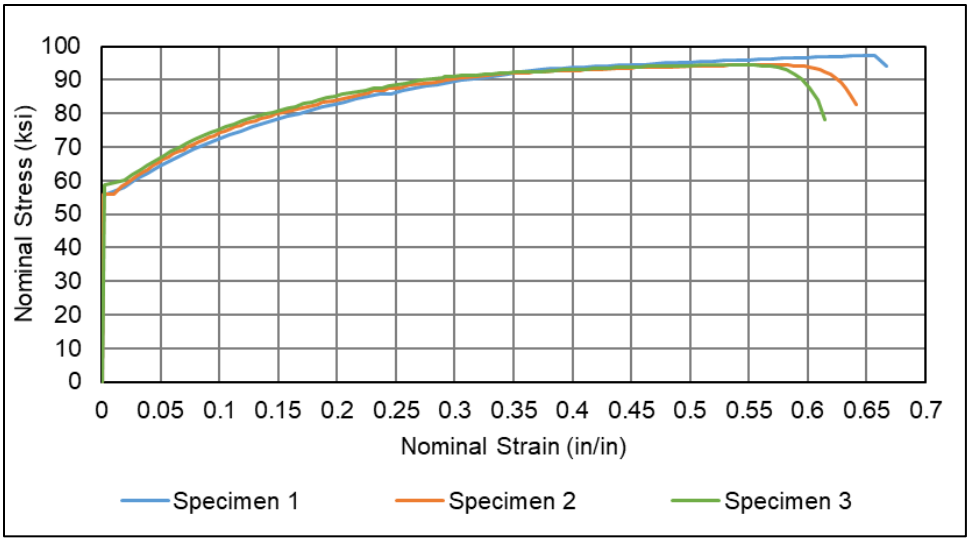

Figure B63. Nominal Stress-Strain Responses of ASTM A240, Type 304 Steel Using ASTM-E8 2-inch Gage Length Flat Dogbone (DB) Specimens

Table B6 provides the tensile properties (i.e., YS, UTS, and EB-2in) for the pre-test T304 tensile specimens.

Table B6. Summary of ASTM A240, Type 304 Steel Tensile Pre-test Results

Specimen	**YS**	**UTS**	**EB-2in**
#	*ksi*	*ksi*	*%*
1	55.6	99.9	66.7
2	55.9	94.4	64.1
3	58.6	94.5	61.5
Average	56.7	96.3	64.1
Specification	30 min	75 min	40 min

B4.4 ASTM A240, Type 304 Stainless Steel (Post-test)

Post-test tensile testing of ASTM A240, Type 304 stainless steel was performed at three different temperatures and five different strain rates. At each combination of rate and temperature, three repeat coupons were tested. Full-size coupons were tested at room temperature and at five different rates. Due to difficulties encountered by the test lab, subsize coupons were used for cryogenic temperature tests at all rates examined. To allow for a comparison between the room and cryogenic temperatures, room temperature tests were repeated using the same subsize coupon geometry as was used for cryogenic temperature tests. The subsize coupon geometry is shown in Figure B64.

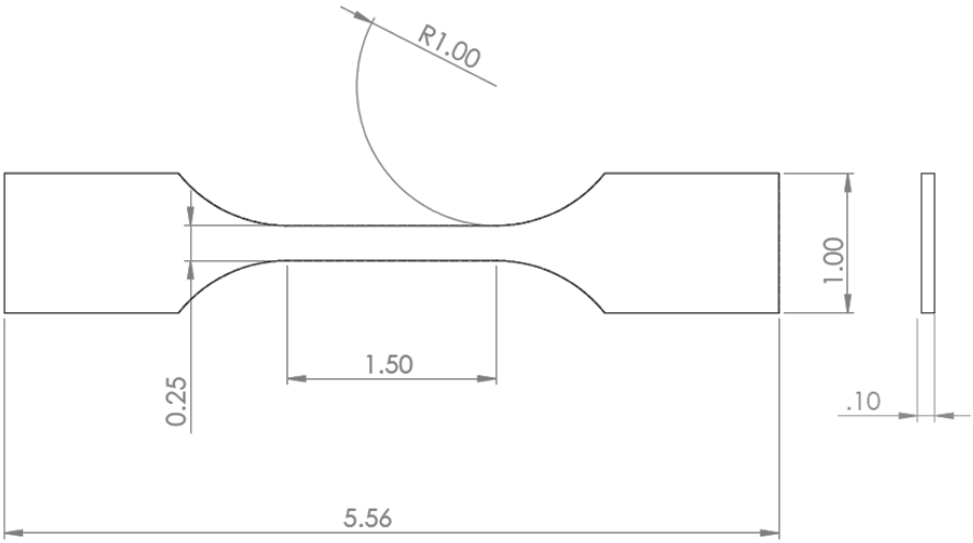

Figure B64. Subsize Tensile Coupon Dimensions

The data are presented in several ways throughout this appendix (Figure B65 through Figure B81). The nominal stress-strain responses across all strain rates are plotted for a given strain rate, and the results indicate the extensometer (i.e., used to produce engineering strain) produced some irregular results at higher strain rates. Therefore, the applied force versus displacement behavior from the test frame was also plotted for each strain rate at a given temperature. The nominal stress-strain responses for each temperature at a given strain rate were also plotted. Finally, the applied force versus displacement responses for each temperature at a given strain rate were plotted.

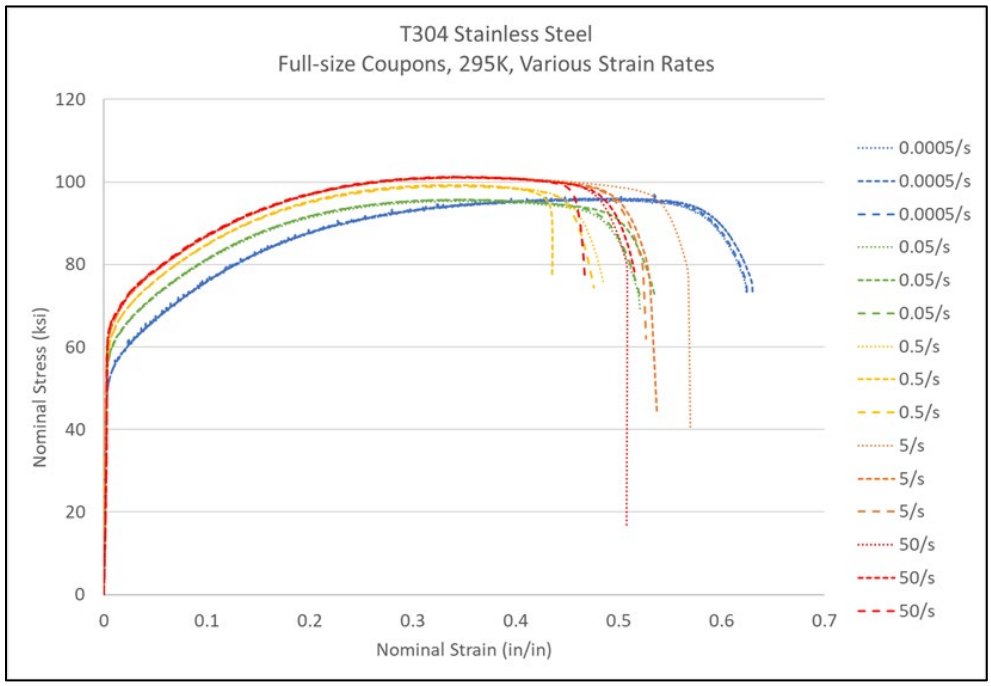

Figure B65. Nominal Stress-Strain Responses of ASTM A240, Type 304 Stainless Steel at 295 K and Various Strain Rates (full-size coupon)

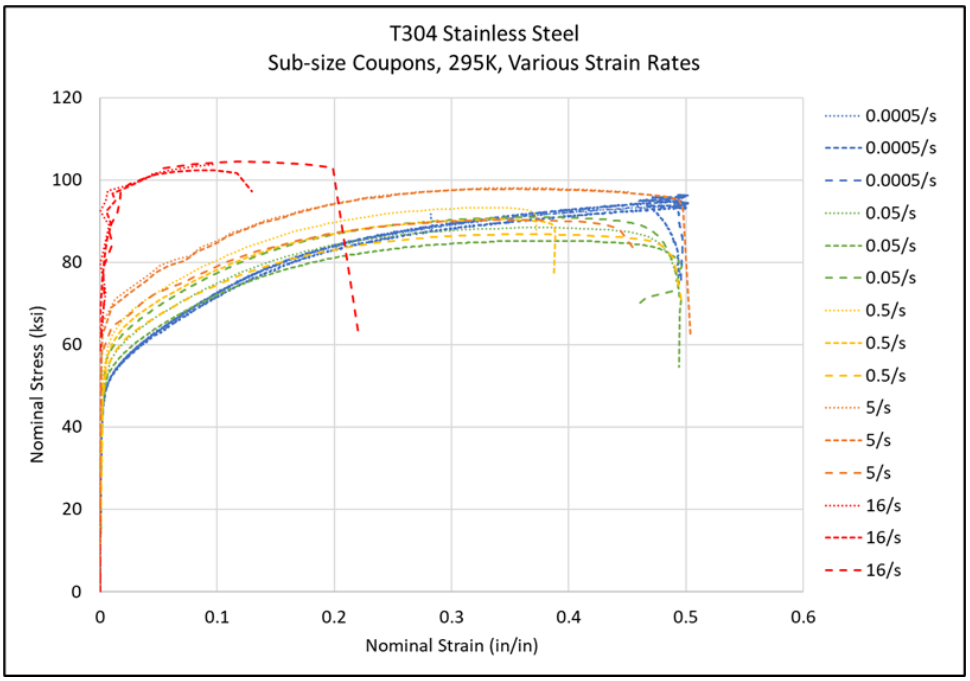

Figure B66. Nominal Stress-Strain Responses of ASTM A240, Type 304 Stainless Steel at 295 K and Various Strain Rates (subsize coupon)

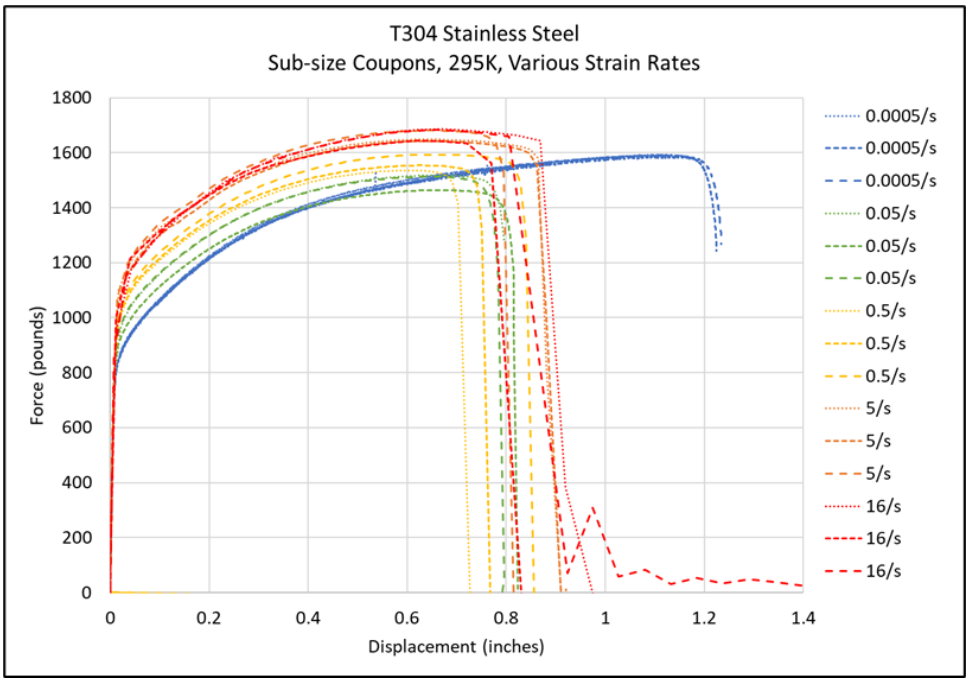

Figure B67. Force-displacement Responses of ASTM A240, Type 304 Stainless Steel at 295 K and Various Strain Rates (subsize coupon)

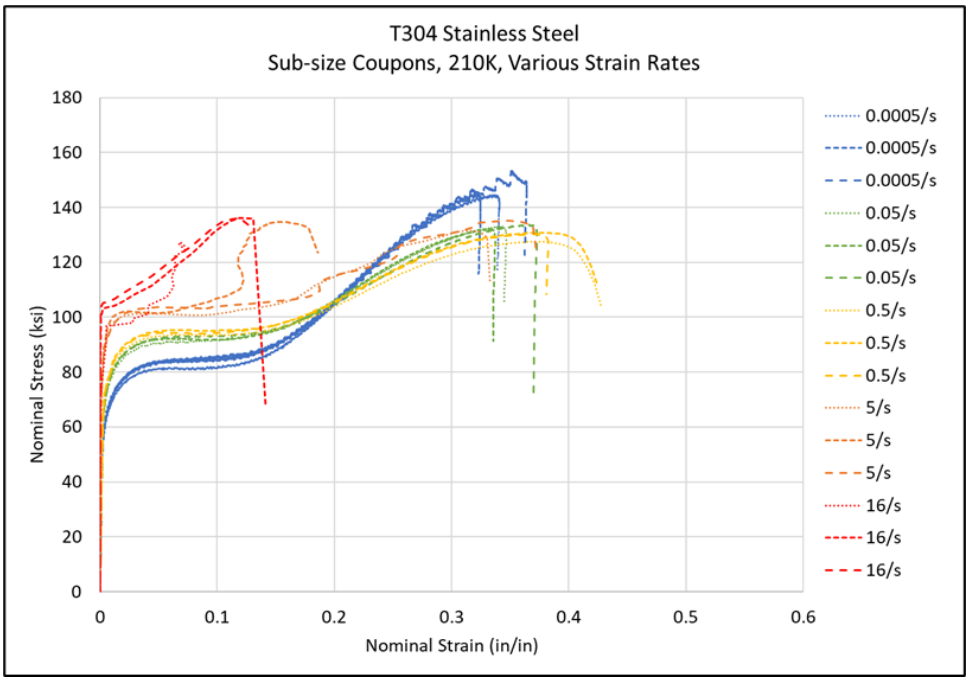

Figure B68. Nominal Stress-Strain Responses of ASTM A240, Type 304 Stainless Steel at 210 K and Various Strain Rates (subsize coupon)

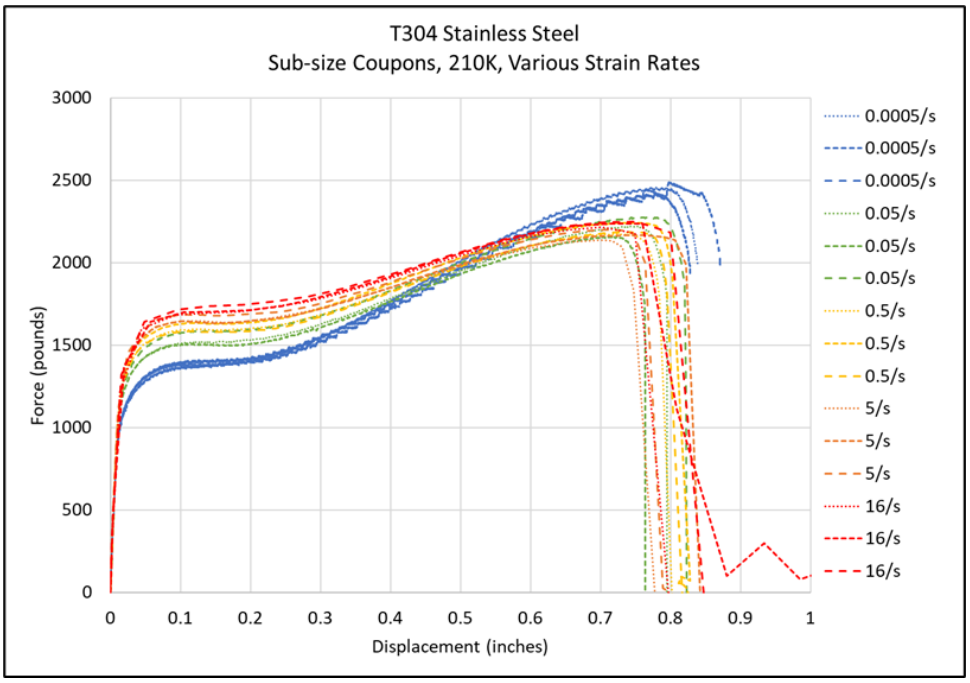

Figure B69. Force-displacement Responses of ASTM A240, Type 304 Stainless Steel at 210 K and Various Strain Rates (subsize coupon)

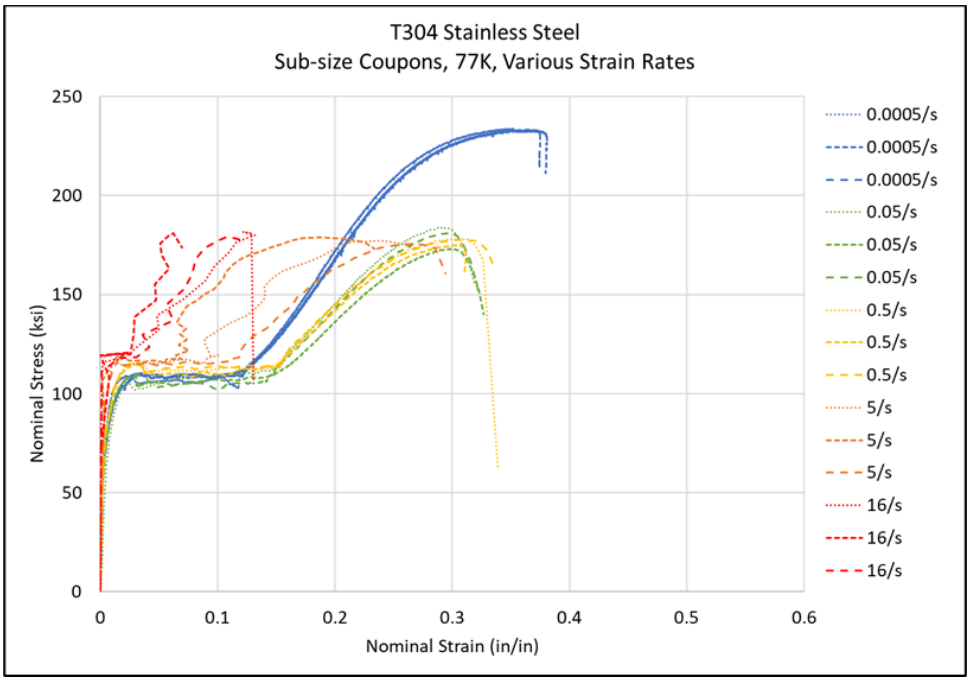

Figure B70. Nominal Stress-Strain Responses of ASTM A240, Type 304 Stainless Steel at 77 K and Various Strain Rates (subsize coupon)

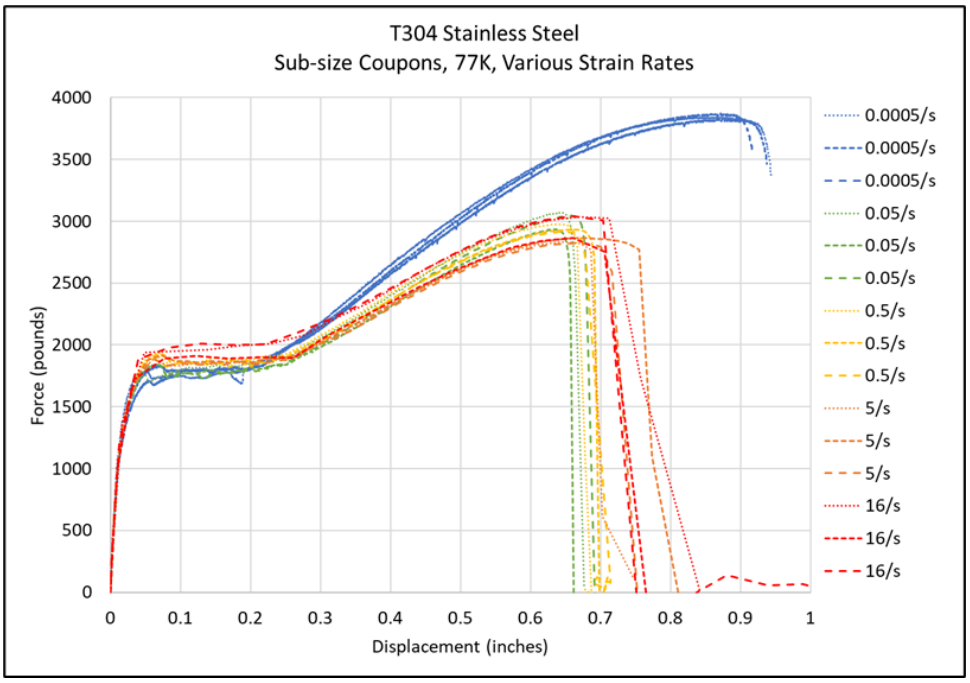

Figure B71. Force-displacement Responses of ASTM A240, Type 304 Stainless Steel at 77 K and Various Strain Rates (subsize coupon)

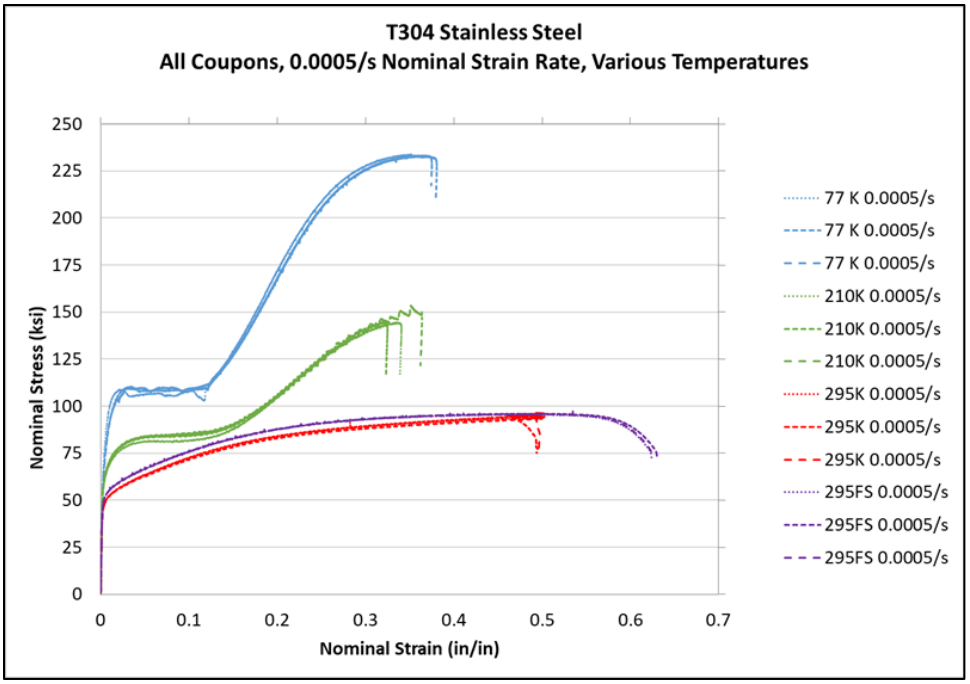

Figure B72. Nominal Stress-Strain Responses of ASTM A240, Type 304 Stainless Steel at a Strain Rate of 5E-04/s and Various Temperatures

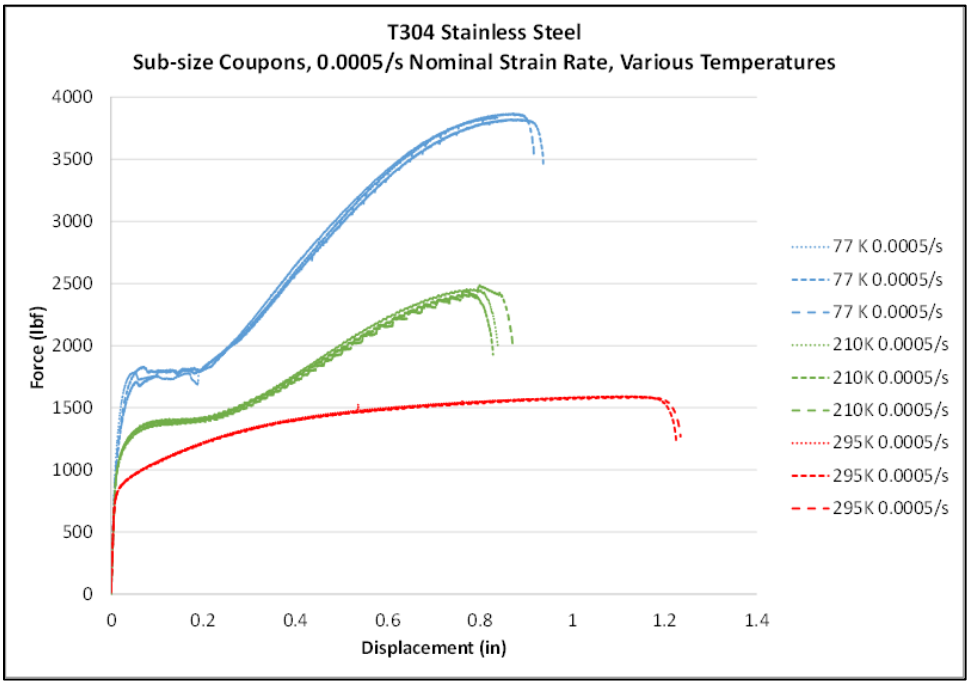

Figure B73. Force-displacement Responses of ASTM A240, Type 304 Stainless Steel at a Strain Rate of 5E-04/s and Various Temperatures

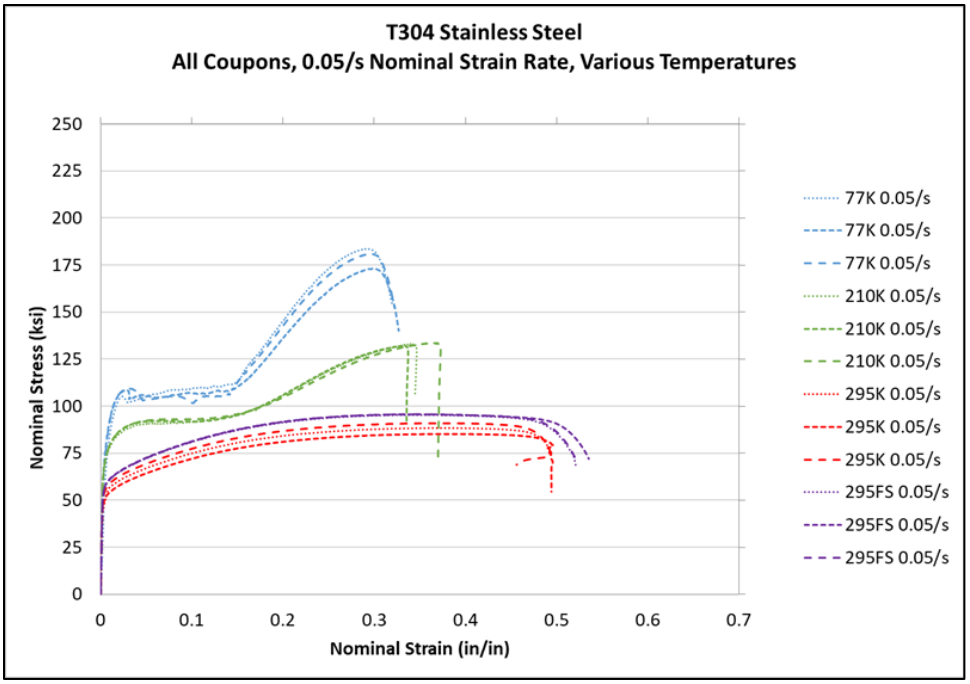

Figure B74. Nominal Stress-Strain Responses of ASTM A240, Type 304 Stainless Steel at a Strain Rate of 5E-02/s and Various Temperatures

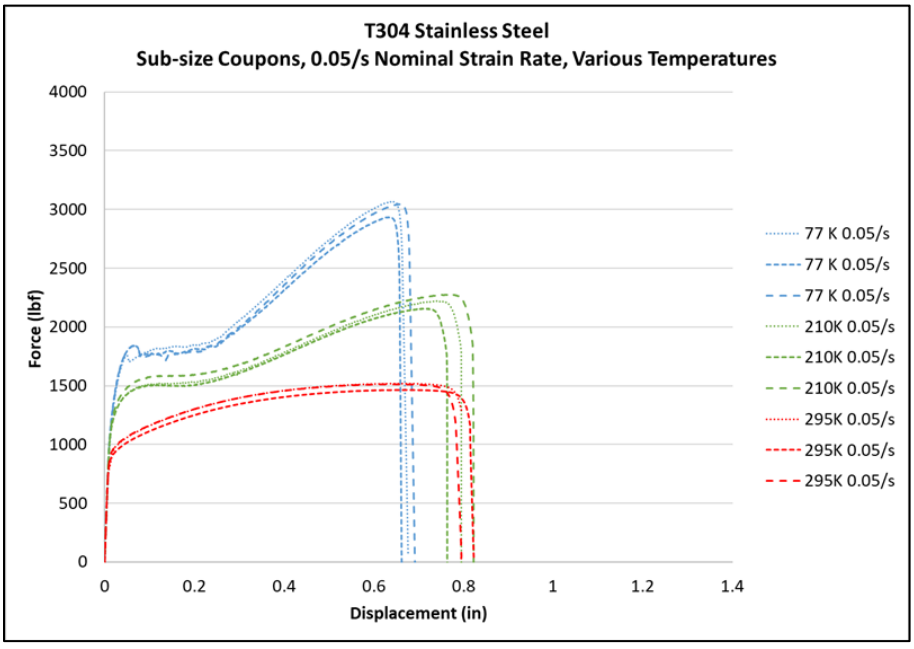

Figure B75. Force-displacement Responses of ASTM A240, Type 304 Stainless Steel at a Strain Rate of 5E-02/s and Various Temperatures

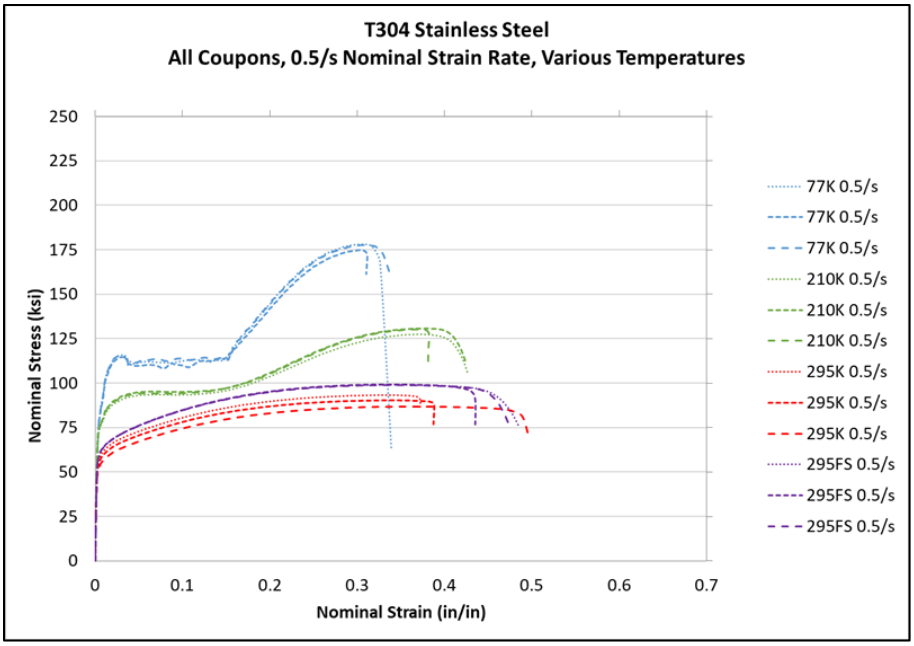

Figure B76. Nominal Stress-Strain Responses of ASTM A240, Type 304 Stainless Steel at a Strain Rate of 5E-01/s and Various Temperatures

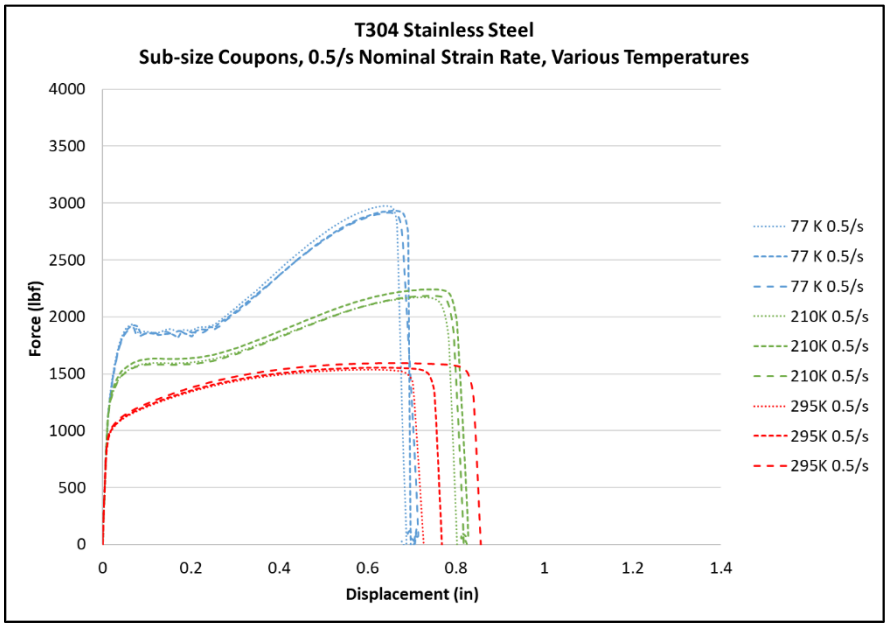

Figure B77. Force-displacement Responses of ASTM A240, Type 304 Stainless Steel at a Strain Rate of 5E-01/s and Various Temperatures

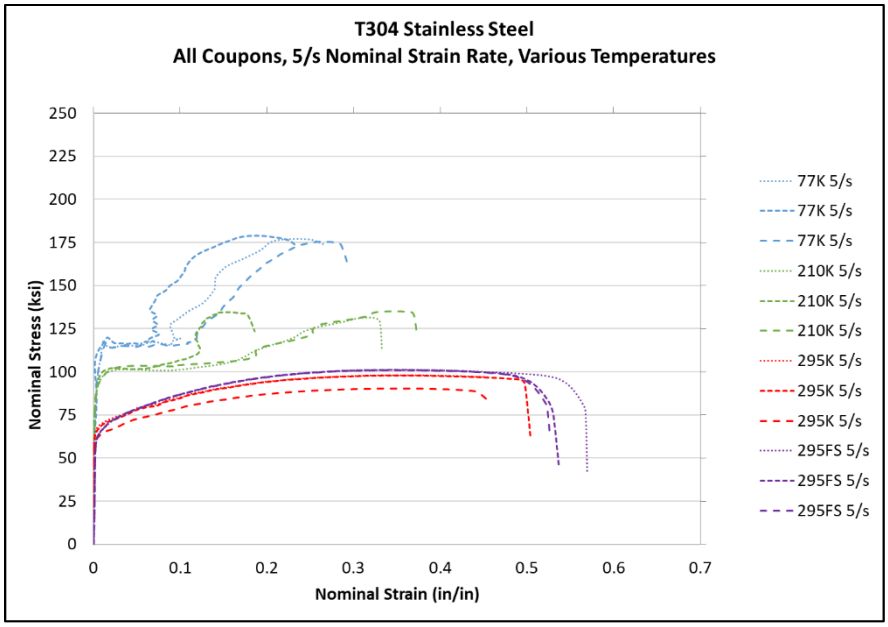

Figure B78. Nominal Stress-Strain Responses of ASTM A240, Type 304 Stainless Steel at a Strain Rate of 5/s and Various Temperatures

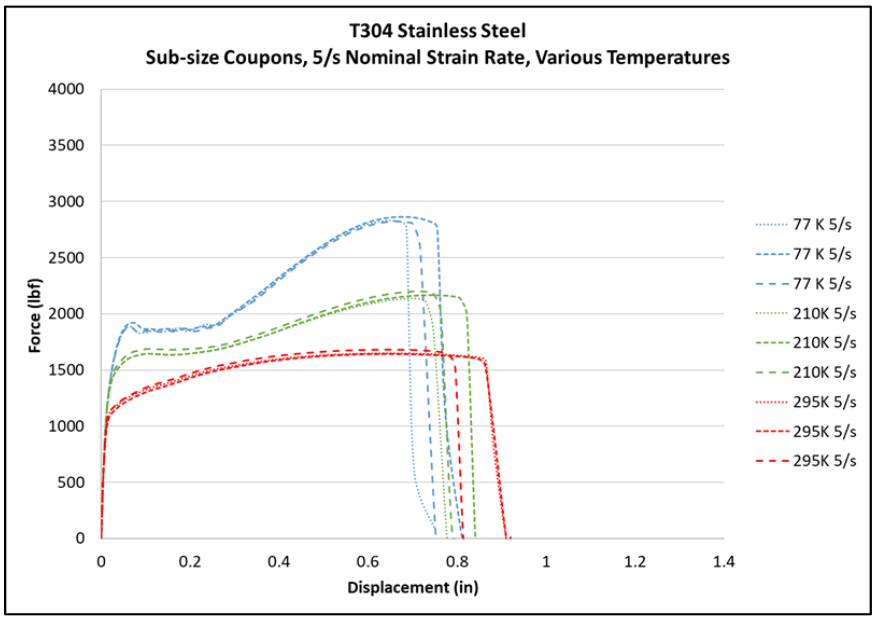

Figure B79. Force-displacement Responses of ASTM A240, Type 304 Stainless Steel at a Strain Rate of 5/s and Various Temperatures

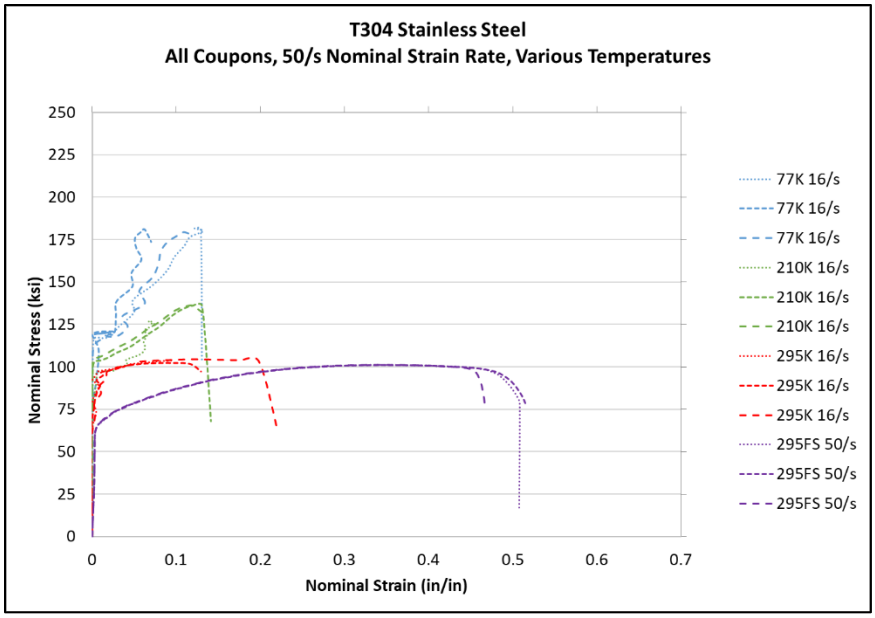

Figure B80. Nominal Stress-Strain Responses of ASTM A240, Type 304 Stainless Steel at a Strain Rate of 16/s and 50/s and Various Temperatures

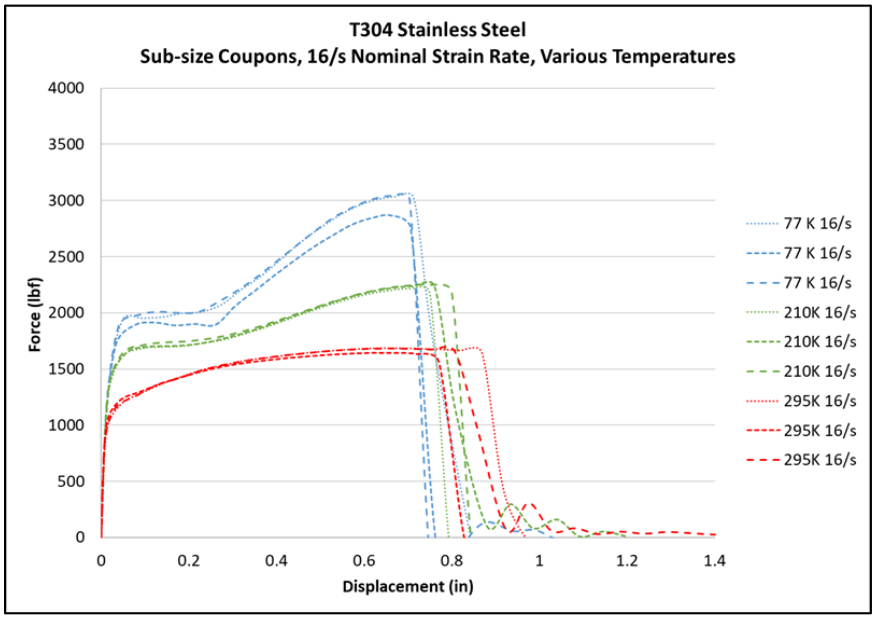

Figure B81. Force-displacement Responses of ASTM A240, Type 304 Stainless Steel at Strain Rate of 16/s and Various Temperatures

Figure B82 presents the average YS data as a graph of YS versus temperature, with a different series for each strain rate. Note that because YS was not reported for the 2-inch gage length coupons, all the data in this plot comes from subsize specimens. In general, the data show that at a given strain rate, the YS decreases as the temperature increases. At a given temperature, YS increases as the strain rate increases.

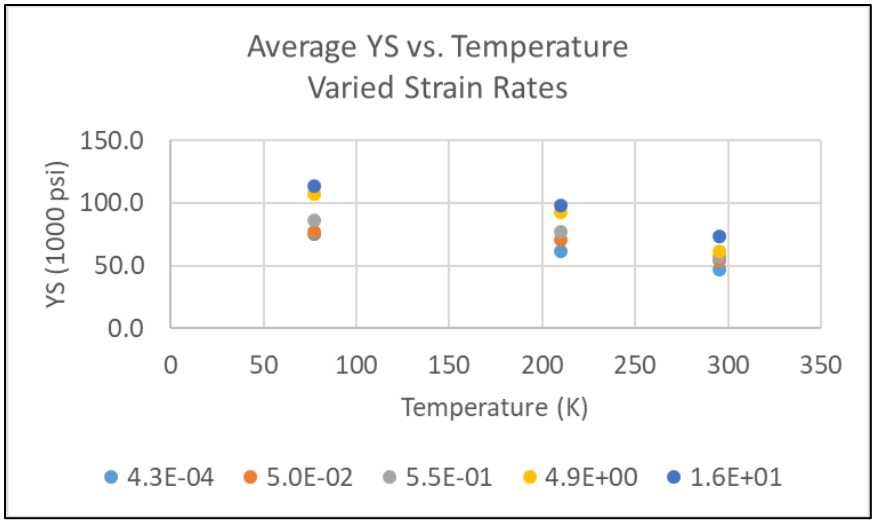

Figure B82. Graph of YS Versus Temperature for T304 Stainless Steel at Different Tensile Rates

Figure B83 presents the average YS data as a graph of YS versus strain rate with a different series for each temperature. Note that because YS was not reported for the 2-inch gage length coupons, all the data in this plot comes from subsize specimens. In general, for a given temperature, YS increases with increasing strain rate. For a given strain rate, YS increases with decreasing temperature.

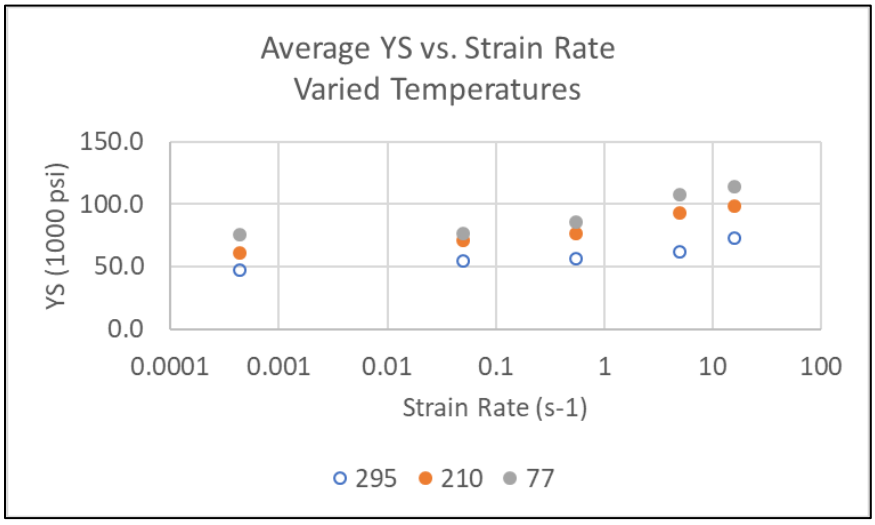

Figure B83. Graph of YS Versus Strain Rate for T304 Stainless Steel at Different Temperatures

Figure B84 presents the average UTS data as a graph of UTS versus temperature with a different series for each strain rate. The solid symbols are used for data from the subsize coupons, and the hollow symbols are used for data from the full-size coupons at 295 K. In general, the data show that at a given strain rate, the UTS decreases with increasing temperature. The UTS measured at the lowest strain rate appears significantly higher than the UTS at the elevated strain rates for all temperatures. No significant differences are observable between the data at 295 K measured using the two different coupon sizes.

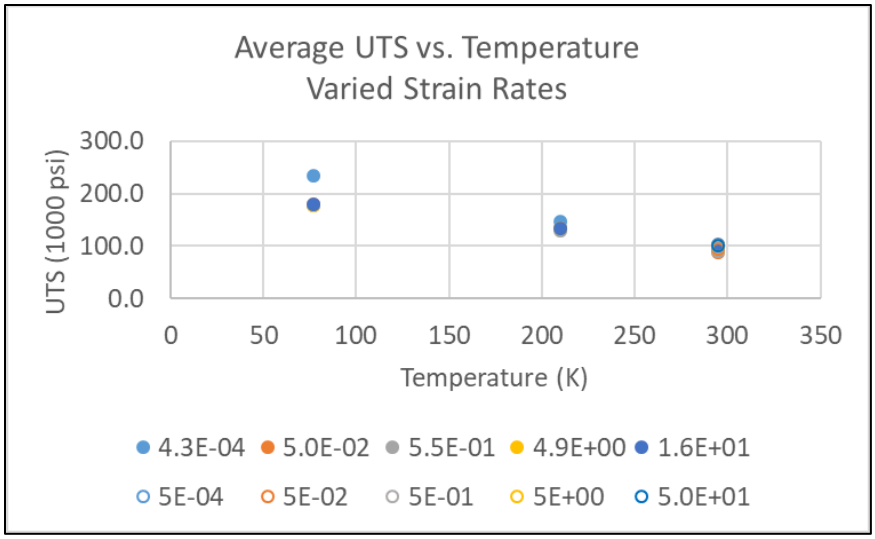

Figure B84. Graph of UTS Versus Temperature for T304 Stainless Steel at Different Tensile Rates

Figure B85 presents the average UTS data as a graph of UTS versus strain rate with a different series for each temperature. Series "295-1" contains the UTS data measured using the full-size coupon, and series "295-2" contains the UTS data measured using the subsize coupon. Note that the data in series 295-1 are plotted using the nominal strain rates, while the data in all other series are plotted using the measured strain rates. Beyond a nominal rate of 5 x 10^{-2} s^{-1}, the UTS remains fairly constant at every temperature. At each strain rate, the average UTS increases with decreasing temperature. The two sets of data measured at 295 K appear to give consistent responses.

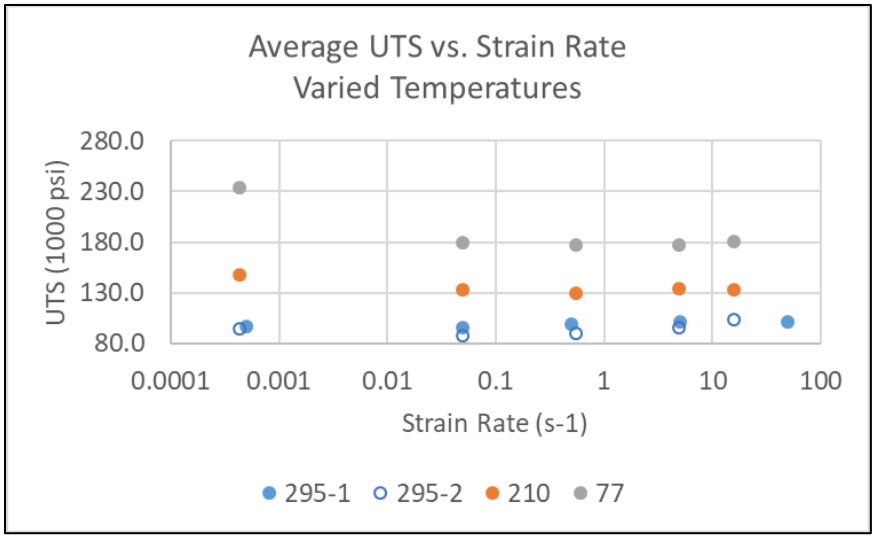

Figure B85. Graph of UTS Versus Strain Rate for T304 Stainless Steel at Different Temperatures

Figure B86 presents the average EB-2in data as a graph of EB-2in versus temperature with a different series for each strain rate. The solid symbols are used for data from the subsize coupons at 295 K, and the hollow symbols are used for data from the fullsize coupons at 295

K. Note that the full-size coupons used a 2-inch gage length, and the subsize coupons used a 1 1/2-inch gage length. In general, the data show that at a given strain rate, the EB-2in increases with increasing temperature. The EB-2in measured at the lowest strain rate is generally, but not always, higher than the EB-2in measured at the highest strain rate for a given temperature. No significant differences are observable between the data at 295 K measured using the two different coupon sizes.

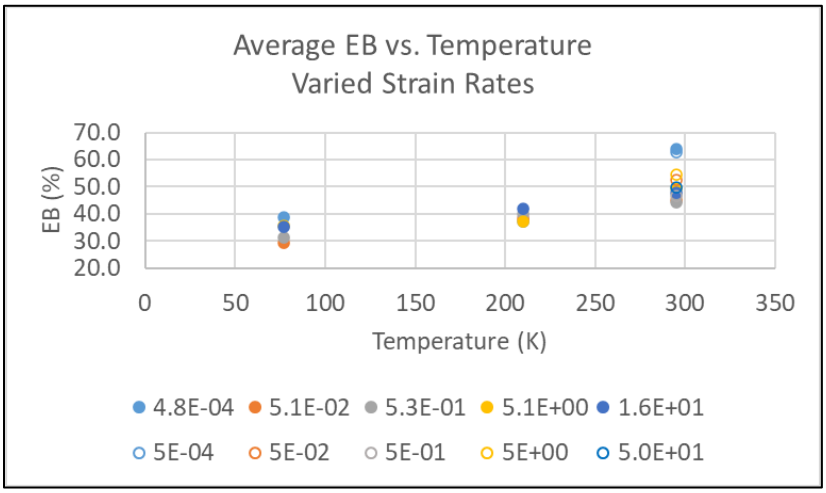

Figure B86. Graph of EB-2in Versus Temperature for T304 Stainless Steel at Different Tensile Rates

Figure B87 presents the average EB-2in data as a graph of EB-2in versus strain rate with a different series for each temperature. Series "295-1" contains the EB-2in data measured using the full-size coupon, and series "295-2" contains the EB-2in data measured using the subsize coupon. Note that the data in series 295-1 are plotted using the nominal strain rates, while the data in all other series are plotted using the measured strain rates. In general, the EB-2in is highest at 295 K for all strain rates. For a given temperature, the EB-2in tends to decrease with increasing strain rate non-monotonically. For example, at 77 K the smallest average EB-2in was observed at a nominal strain rate of 5×10^{-2} s^{-1} which is an intermediate value within the tested range.

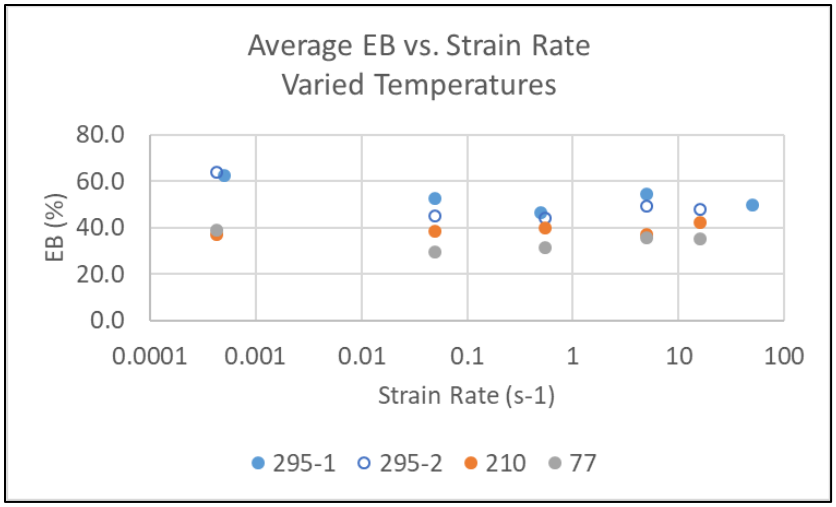

Figure B87. Graph of EB-2in Versus Strain Rate for T304 Stainless Steel at Different Temperatures

The individual and average YS data measured at each strain rate and temperature for T304 stainless steel are shown in Table B7. Figure B88 plots the data from this table as YS versus temperature with a different data series for each strain rate. Figure B89 plots the data from this table as YS versus strain rate with a different data series for each temperature.

Table B7. Summary of ASTM A240, Type 304 Steel Tensile Post-test YS Results at Varied Strain Rates and Temperatures

	Nominal Tensile Strain Rate (s^{-1})	Actual Tensile Strain Rate (s^{-1})	Subsize Coupon (1,000 psi) 295 K 71 °F	Subsize Coupon (1,000 psi) 210 K -82 °F	Subsize Coupon (1,000 psi) 77 K -321 °F
	5E-04	4.8E-04	47.5	60.4	82.5
	5E-04	4.8E-04	47.4	61.9	71.4
	5E-04	4.8E-04	47.1	62.1	73.0
Average	**5E-04**	**4.8E-04**	**47.3**	**61.5**	**75.6**
	5E-02	5.1E-02	58.3	70.0	78.4
	5E-02	5.1E-02	50.4	71.4	76.6
	5E-02	5.1E-02	54.1	71.3	76.1
Average	**5E-02**	**5.1E-02**	**54.3**	**70.9**	**77.0**
	5E-01	5.3E-01	59.4	76.1	84.6
	5E-01	5.3E-01	56.9	77.4	85.5
	5E-01	5.3E-01	54.1	77.0	87.8
Average	**5E-01**	**5.3E-01**	**56.8**	**76.9**	**85.9**
	5E+00	5.1E+00	65.5	94.3	94.0
	5E+00	5.1E+00	62.2	87.0	117.8
	5E+00	5.1E+00	57.7	97.2	110.7
Average	**5E+00**	**5.1E+00**	**61.8**	**92.8**	**107.5**

	Nominal Tensile Strain Rate (s^{-1})	Actual Tensile Strain Rate (s^{-1})	Subsize Coupon (1,000 psi) 295 K 71 °F	Subsize Coupon (1,000 psi) 210 K -82 °F	Subsize Coupon (1,000 psi) 77 K -321 °F
	5E+01	1.6E+01	72.9	91.9	116.9
	5E+01	1.6E+01	75.7	103.2	108.5
	5E+01	1.6E+01	71.4	99.3	116.8
Average	**5E+01**	**1.6E+01**	**73.3**	**98.1**	**114.1**

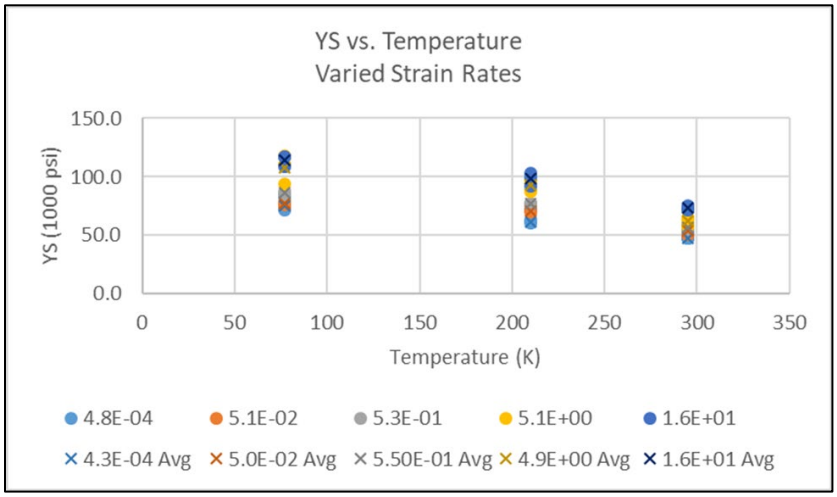

Figure B88. YS Versus Temperature at Various Strain Rates, T304 Stainless Steel

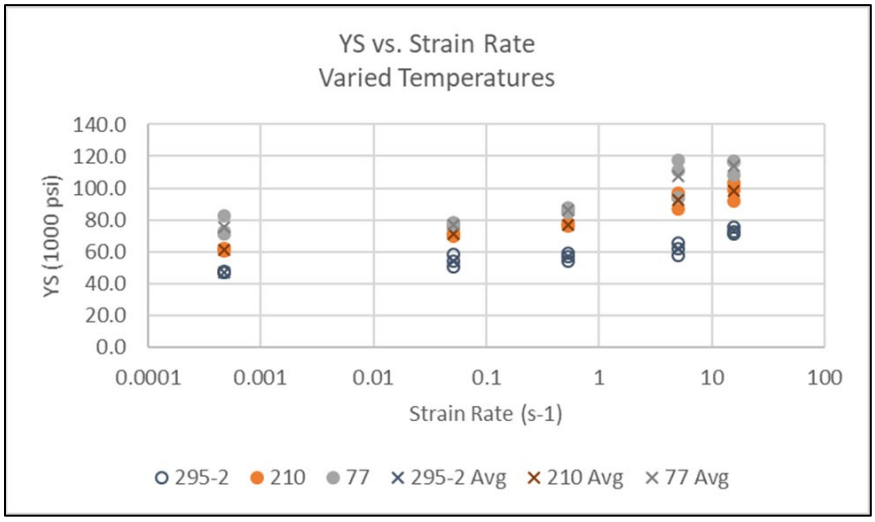

Figure B89. YS Versus Strain Rate at Various Temperatures, T304 Stainless Steel

The individual and average UTS data measured at each strain rate and temperature for T304 stainless steel are shown in Table B8 for measurements made on full-size coupons, and in Table B9 for measurements made on subsize coupons. Figure B90 plots the data from these tables as UTS versus temperature with a different data series for each strain rate. Figure B91 plots the data from these tables as UTS versus strain rate with a different data series for each temperature.

Table B8. Summary of ASTM A240, Type 304 Steel Tensile Post-test UTS Results at Varied Strain Rates and Temperatures (full-size coupons)

	Nominal Tensile Strain Rate (s^{-1})	Full-size Coupon (1,000 psi) 295 K 71 °F
	5E-04	95.9
	5E-04	97.3
	5E-04	96.3
Average	**5E-04**	**96.5**
	5E-02	95.3
	5E-02	95.7
	5E-02	95.7
Average	**5E-02**	**95.6**
	5E-01	99.1
	5E-01	99.2
	5E-01	98.9
Average	**5E-01**	**99.1**
	5E+00	101.2
	5E+00	101.2
	5E+00	101.0
Average	**5E+00**	**101.1**
	5E+01	101.2
	5E+01	101.2
	5E+01	101.3
Average	**5E+01**	**101.2**

Table B9. Summary of ASTM A240, Type 304 Steel Tensile Post-test UTS Results at Varied Strain Rates and Temperatures (subsize coupons)

	Actual Tensile Strain Rate (s^{-1})	Subsize Coupon (1,000 psi) 295 K 71 °F	Subsize Coupon (1,000 psi) 210 K -82 °F	Subsize Coupon (1,000 psi) 77 K -321 °F
	4.8E-04	93.9	144.7	234.2
	4.8E-04	96.5	145.3	232.9
	4.8E-04	94.7	153.5	233.5
Average	**4.8E-04**	**95.0**	**147.8**	**233.5**
	5.1E-02	88.4	133.1	183.7
	5.1E-02	85.2	132.1	173.1
	5.1E-02	91.0	133.6	181.0

	Actual Tensile Strain Rate (s^{-1})	Subsize Coupon (1,000 psi) 295 K 71 °F	Subsize Coupon (1,000 psi) 210 K -82 °F	Subsize Coupon (1,000 psi) 77 K -321 °F
Average	**5.1E-02**	**88.2**	**132.9**	**179.3**
	5.3E-01	93.3	127.5	178.1
	5.3E-01	90.4	130.8	174.9
	5.3E-01	86.8	130.2	177.7
Average	**5.3E-01**	**90.2**	**129.5**	**176.9**
	5.1E+00	98.0	131.5	177.1
	5.1E+00	97.9	134.6	178.9
	5.1E+00	90.3	135.1	175.5
Average	**5.1E+00**	**95.4**	**133.7**	**177.2**
	1.6E+01	104.0	127.4	181.6
	1.6E+01	102.3	136.1	181.0
	1.6E+01	104.5	136.1	179.4
Average	**1.6E+01**	**103.6**	**133.2**	**180.7**

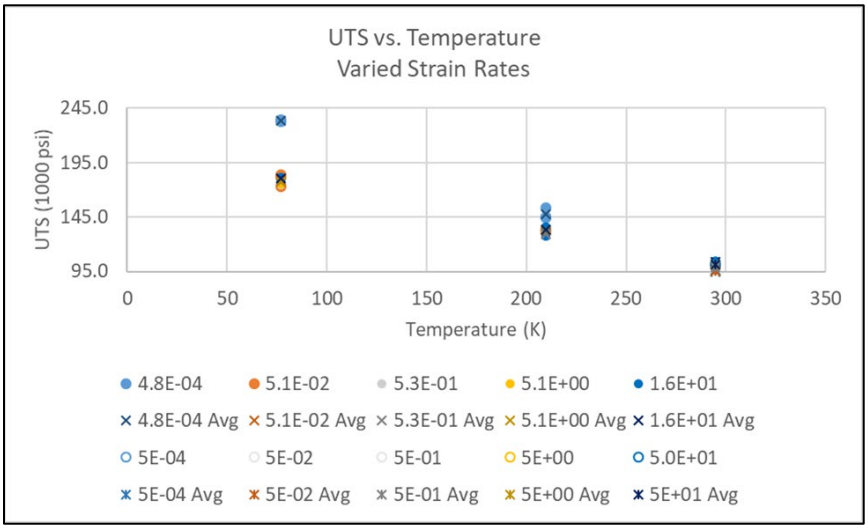

Figure B90. UTS Versus Temperature at Various Strain Rates, T304 Stainless Steel

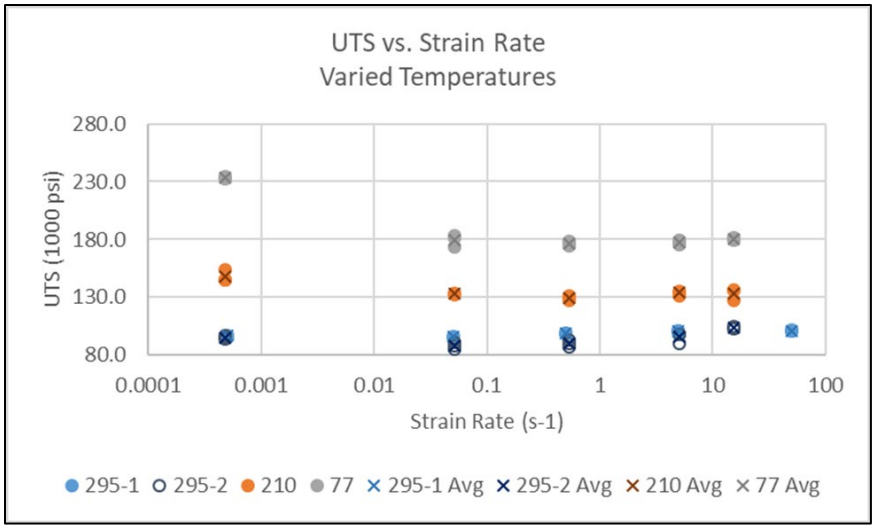

Figure B91. UTS Versus Strain Rate at Various Temperatures, T304 Stainless Steel

The individual and average EB-2in data measured at each strain rate and temperature for T304 stainless steel are shown in Table B10 for measurements made using full-size coupons and in Table B11 for measurements made using subsize coupons. Figure B92 plots the data from these tables as EB-2in versus temperature, with a different data series for each strain rate. Figure B93 plots the data from these tables as EB-2in versus strain rate, with a different data series for each temperature.

Table B10. Summary of ASTM A240, Type 304 Steel Tensile Post-test EB-2in Results at Varied Strain Rates and Temperatures (full-size coupons)

	Nominal Tensile Strain Rate (s^{-1})	Full-size Coupon (%) 295 K 71 °F
	5E-04	62.4
	5E-04	63.0
	5E-04	62.5
Average	**5E-04**	**62.6**
	5E-02	52.1
	5E-02	53.5
	5E-02	52.1
Average	**5E-02**	**52.6**
	5E-01	48.5
	5E-01	43.6
	5E-01	47.6
Average	**5E-01**	**46.6**
	5E+00	57.0
	5E+00	53.7

	Nominal Tensile Strain Rate (s^{-1})	Full-size Coupon (%) 295 K 71 °F
	5E+00	52.7
Average	**5E+00**	**54.4**
	5E+01	50.8
	5E+01	51.6
	5E+01	46.7
Average	**5E+01**	**49.7**

Table B11. Summary of ASTM A240, Type 304 Steel Tensile Post-test EB-2in Results at Varied Strain Rates and Temperatures (subsize coupons)

	Actual Tensile Strain Rate (s^{-1})	Subsize Coupon (%) 295 K 71 °F	Subsize Coupon (%) 210 K -82 °F	Subsize Coupon (%) 77 K -321 °F
	4.8E-04	60.8	36.5	39.1
	4.8E-04	67.4	37.0	39.2
	4.8E-04	63.3	38.0	38.0
Average	**4.8E-04**	**63.8**	**37.2**	**38.8**
	5.1E-02	44.7	38.3	29.5
	5.1E-02	45.5	36.7	29.4
	5.1E-02	45.1	40.7	29.4
Average	**5.1E-02**	**45.1**	**38.6**	**29.4**
	5.3E-01	41.0	40.0	30.5
	5.3E-01	42.8	40.6	32.0
	5.3E-01	48.5	38.9	31.2
Average	**5.3E-01**	**44.1**	**39.8**	**31.2**
	5.1E+00	51.4	38.3	34.4
	5.1E+00	51.2	33.3	37.7
	5.1E+00	46.0	39.6	35.1
Average	**5.1E+00**	**49.5**	**37.1**	**35.7**
	1.6E+01	51.3	42.0	35.9
	1.6E+01	43.2	42.2	35.3
	1.6E+01	48.7	42.0	34.2
Average	**1.6E+01**	**47.7**	**42.1**	**35.1**

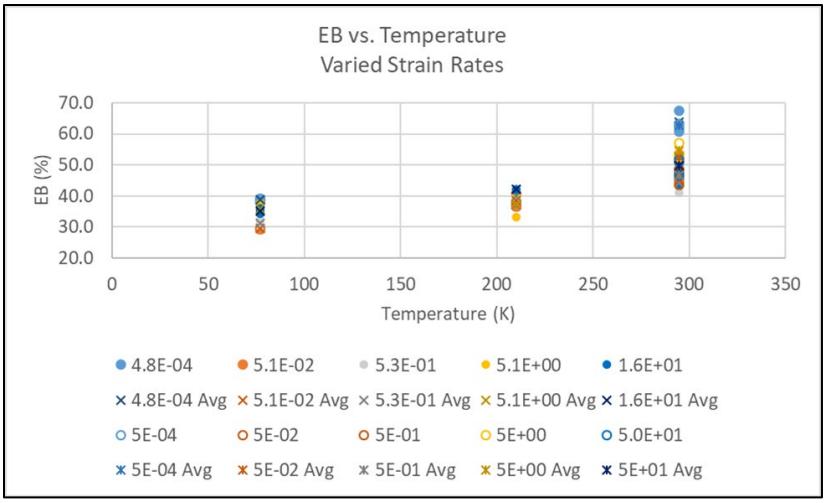

Figure B92. EB-2in Versus Temperature at Various Strain Rates, T304 Stainless Steel

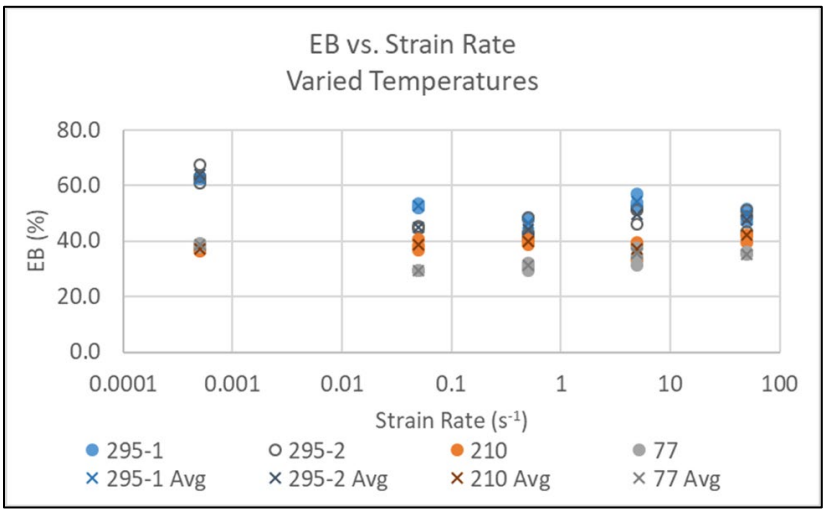

Figure B93. EB-2in Versus Strain Rate at Various Temperatures, T304 Stainless Steel

The post-test T304 material testing also included CVN testing on coupons extracted from the inner tank at different temperatures. Figure B94 shows the orientation of the CVN coupon outlined on a portion of the tank shell (left) and a cut CVN coupon aligned with the outline (right).

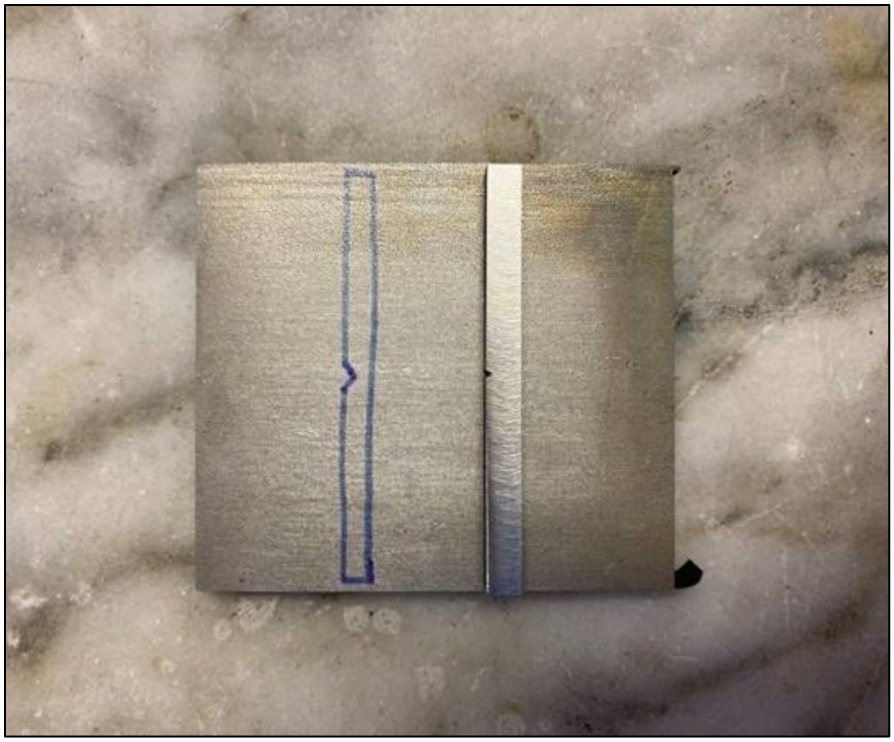

Figure B94. Orientation of CVN Coupon for T304 Stainless Steel

Table B12. Summary of ASTM A240, Type 304 Steel CVN Energy at Varied Temperatures

		295 K 71 °F	**200 K -100 °F**	**111 K -260 °F**	**77 K -321 °F**
Energy Absorbed (ft-lbf)	Coupon 1	28.5	34	30.5	29
	Coupon 2	30.5	32.5	32	22
	Coupon 3	31	35.5	29	30
	Average	**30**	**34**	**30.5**	**27**

Figure B95 presents the data from Table B12 as a plot of absorbed energy versus temperature. The individual coupon test results are shown as solid circles and the average values are plotted as "X's."

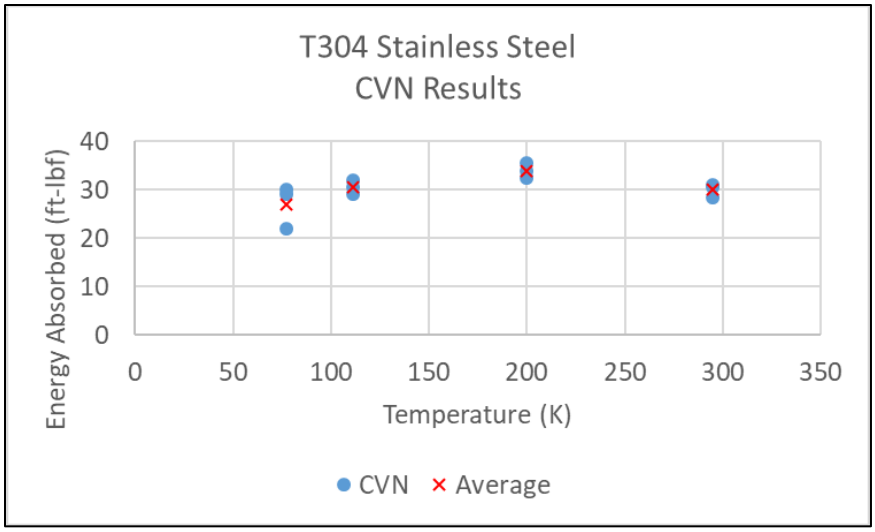

Figure B95. CVN Energy Absorbed Versus Temperature, T304 Stainless Steel

Figure B96 shows a photograph from above an exemplar CVN coupon after it had been tested. From this perspective, the CVN impact tip would have been moving from the bottom to the top of this frame. Figure B97 is a focused view of the fracture surface of the same coupon, also viewed from above. Figure B98 shows a photograph looking into the fracture surface. In this figure, the impact tip would have been moving out of the page.

Figure B96. View of Exemplar Post-test CVN Coupon

Figure B97. View of Exemplar Post-test CVN Coupon Fracture Surface

Figure B98. View of Fracture Surface Interior

Appendix C.
FEA and Test Results

For all results presented in this appendix, the acceleration data from the test and output from the FE model have been filtered using a CFC60 filter. Pre-test FEA was run at a variety of impact speeds. Following the test, post-test FEA was run using the actual test conditions.

C1. Pre-test FEA and Test Results

The appendix presents a limited set of pre-test FEA results. The pre-test FE models run at 16.7, 18, and 19 mph did not result in puncture of the inner tank. The pre-test FE model resulted in puncture of both tanks when it was run at 19.5 mph, and there was no residual energy in the impactor, i.e., the impactor rebounded. The impactor punctured both tanks and did not rebound when the pre-test FE model was run at 20 mph, i.e., there was a small amount of residual energy. Table C1 summarizes the pre-test FE model outcomes.

Table C1. Summary of Pre-test FE Models

Speed(mph)	Outer Tank State	Inner Tank State	Impactor State
16.7	No elements lost	No elements lost	Rebounding
18	Some elements lost	No elements lost	Rebounding
19	Tear along vertical edge of impactor	No elements lost	Rebounding
19.5	Tearing around edges of impactor	Tearing around edges of impactor	Rebounding
20	Tearing around edges of impactor	Tearing around edges of impactor	Penetrating

C1.1 Pre-test Model at 16.7 and 18 mph

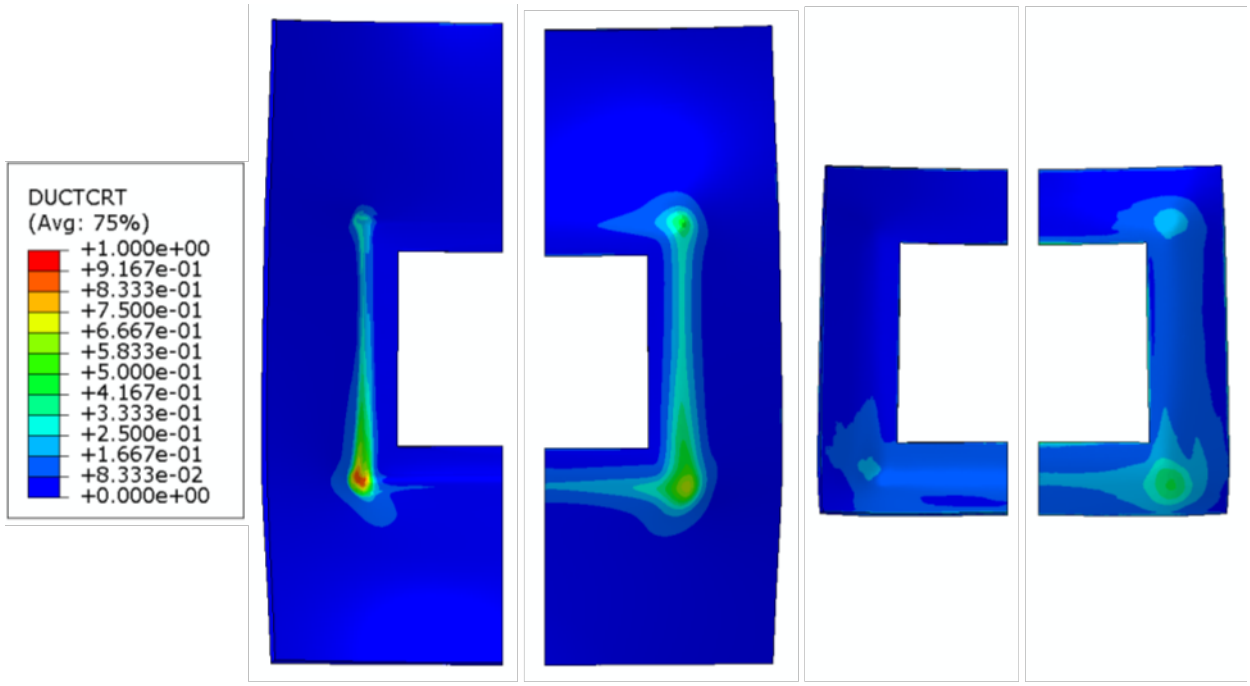

Figure C1. Outer Tank (left) and Inner Tank (right) Solid Patch Contour Plots of Damage Initiation Criterion (DUCTCRT), 16.7 mph Pre-test FE Model at 0.4 Seconds

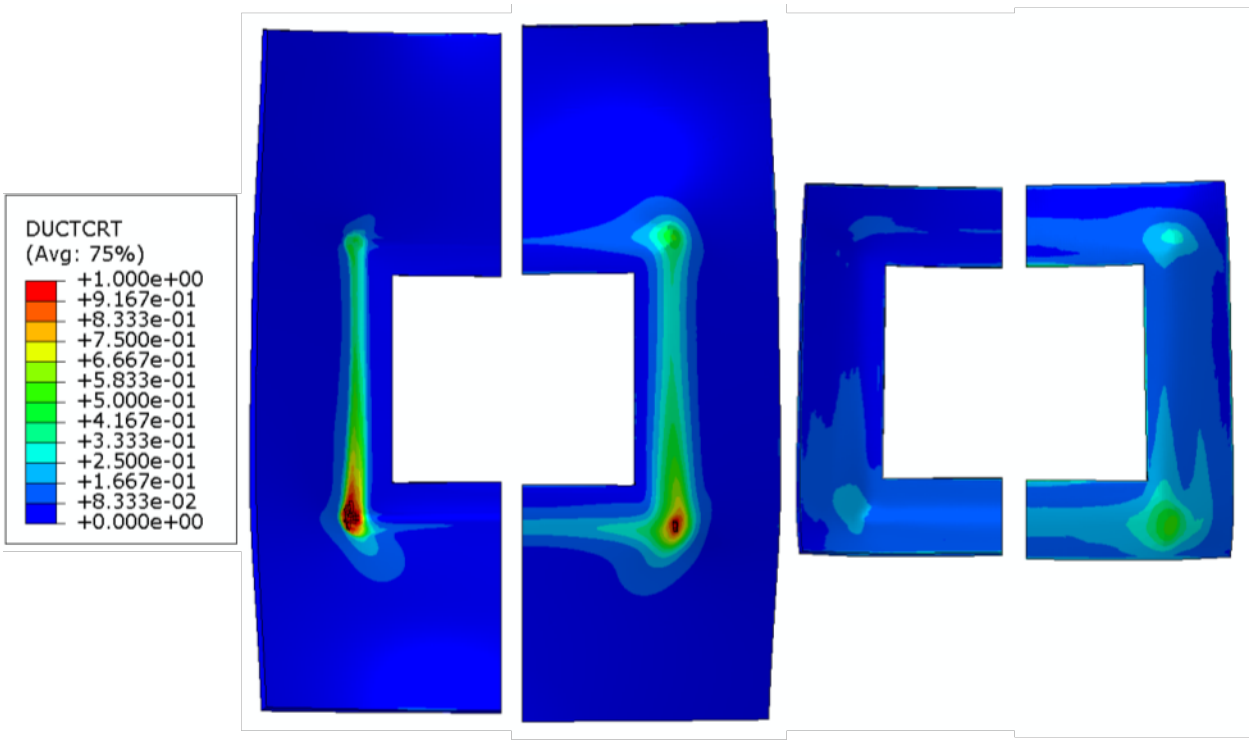

Figure C2. Outer Tank (left) and Inner Tank (right) Solid Patch Contour Plots of Damage Initiation Criterion (DUCTCRT), 18 mph Pre-test FE Model at 0.4 Seconds

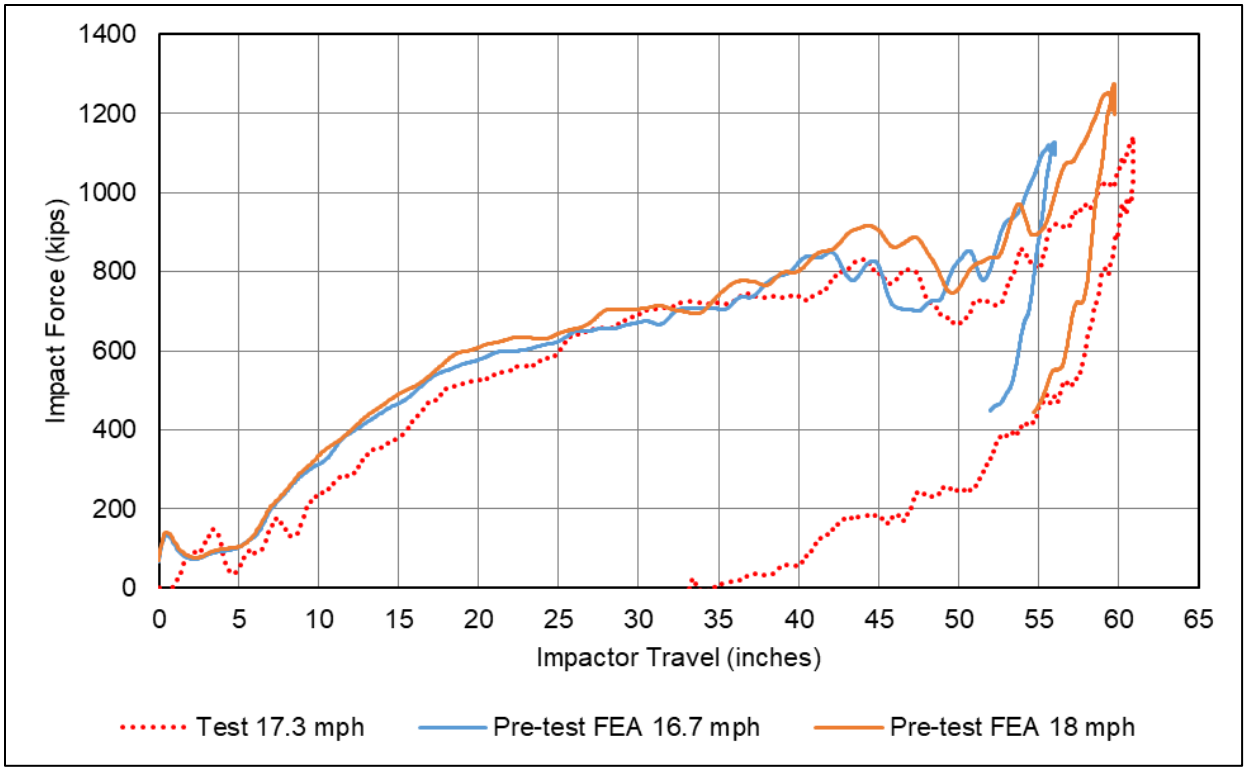

Figure C3. Impactor Force Versus Travel, Pre-test FE Model at 16.7 and 18 mph

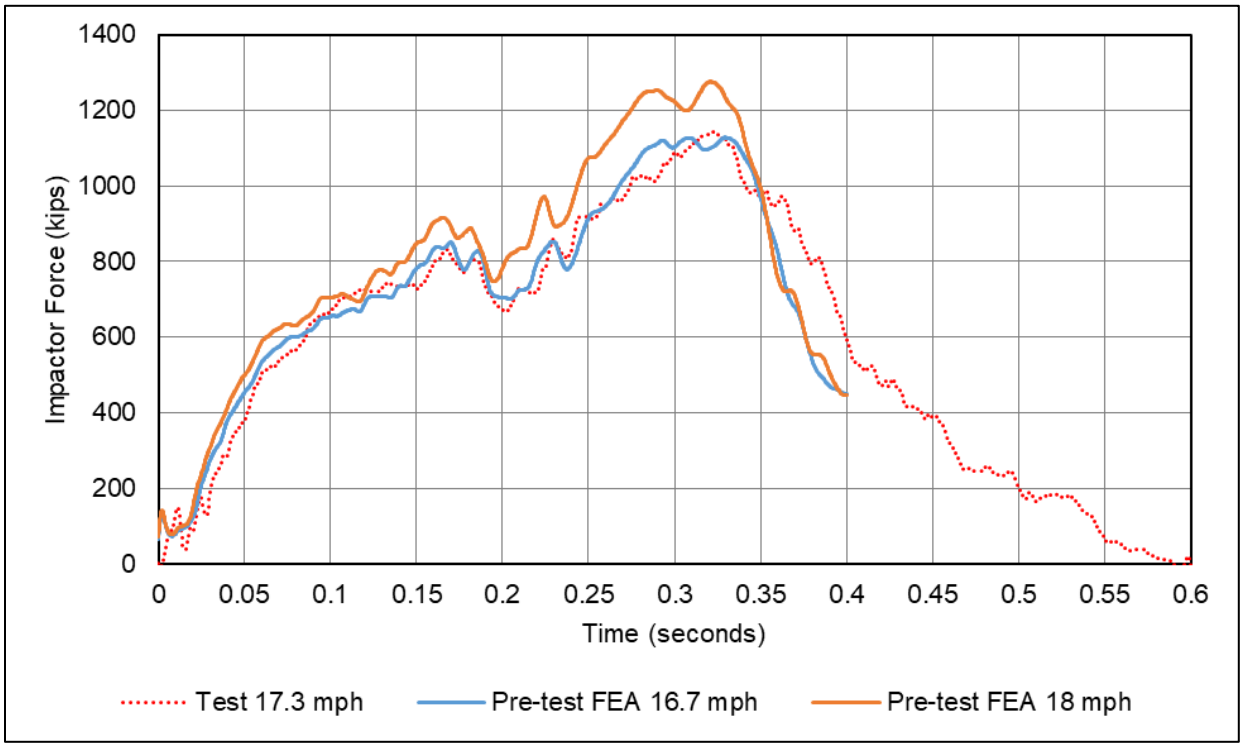

Figure C4. Impactor Force Versus Time, Pre-test FE Model at 16.7 and 18 mph

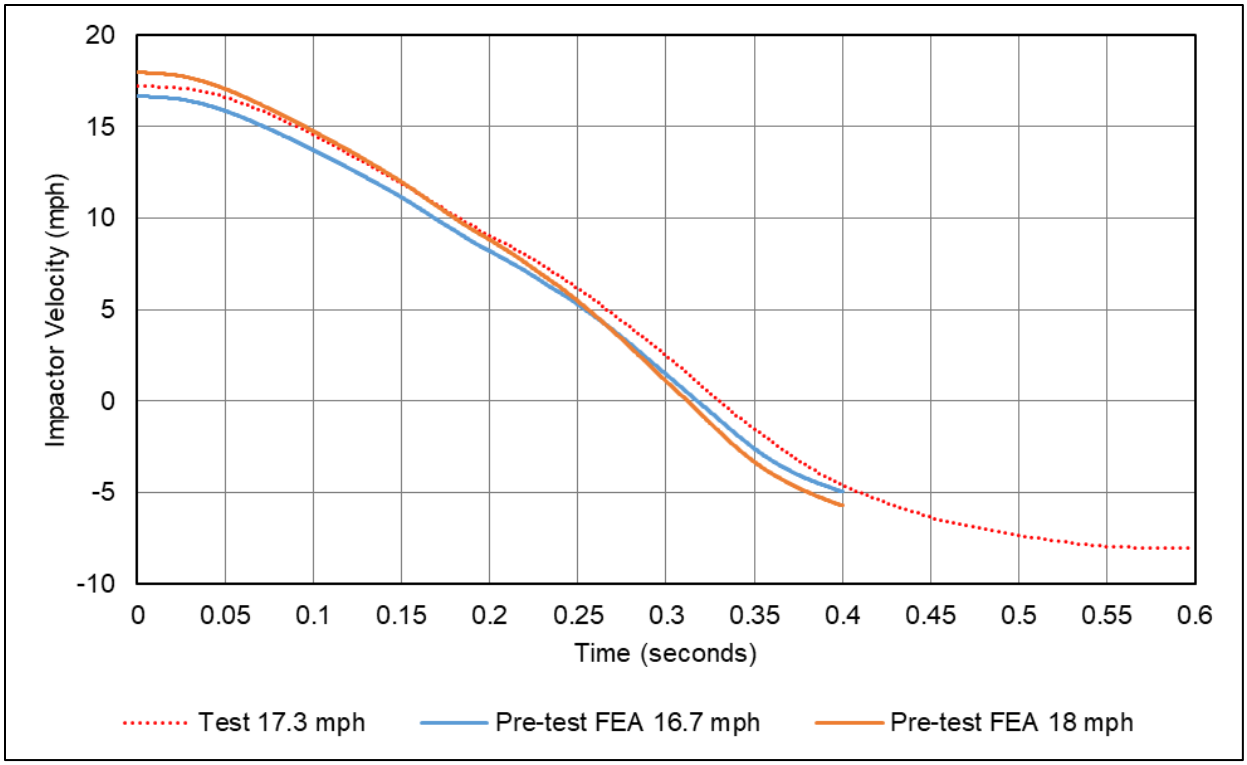

Figure C5. Impactor Velocity Versus Time, Pre-test FE Model at 16.7 and 18 mph

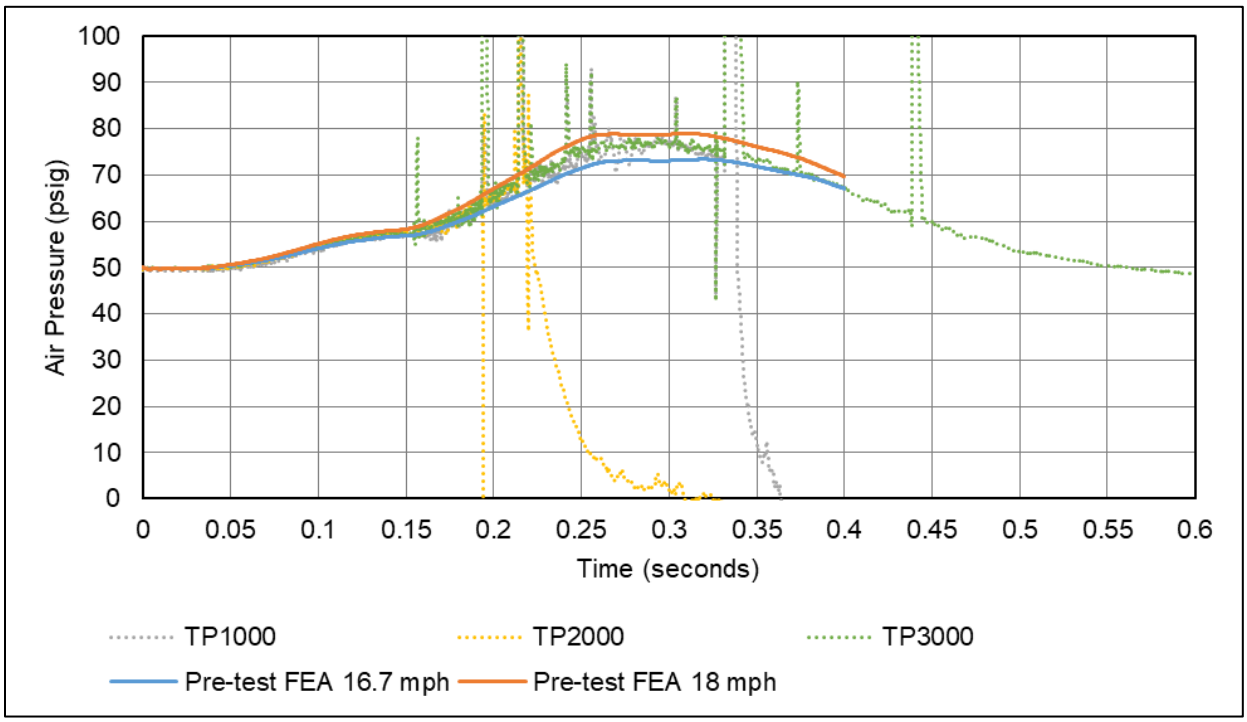

Figure C6. Outage Pressure Versus Time, Pre-test FE Model at 16.7 and 18 mph

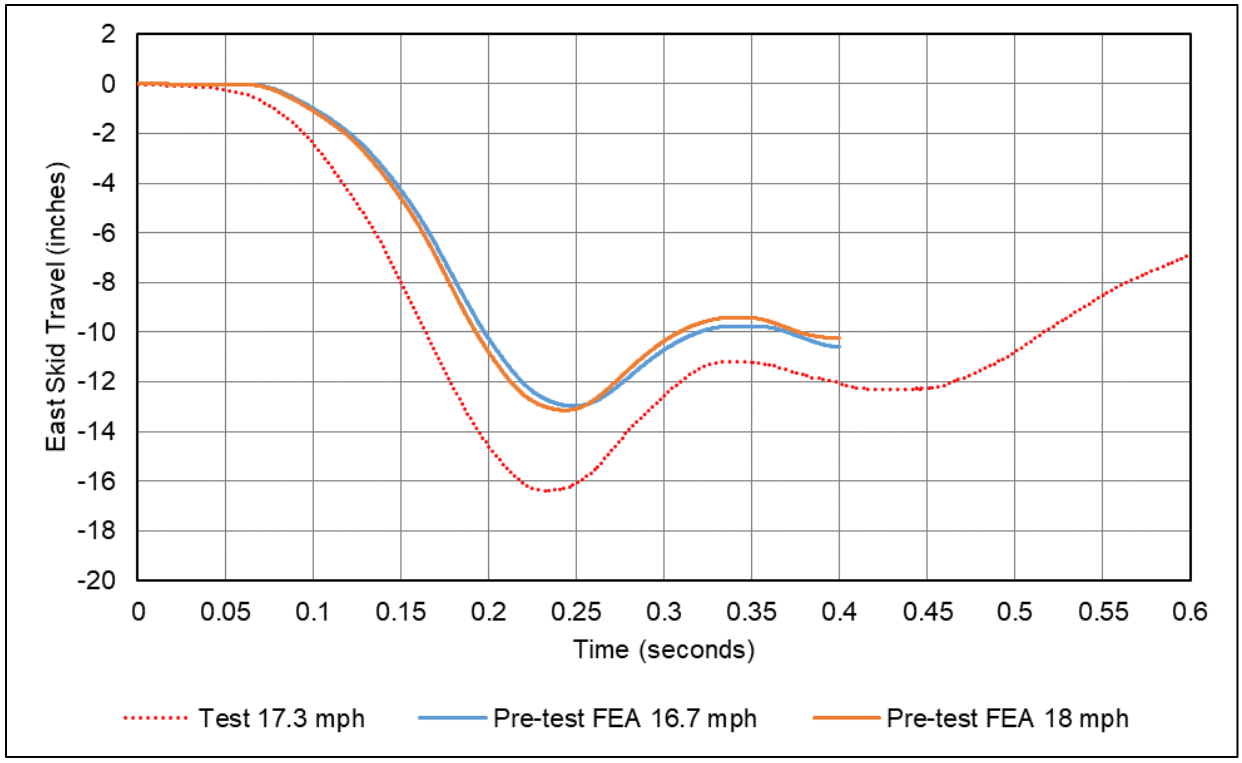

Figure C7. East Skid Travel Versus Time, Pre-test FE Model at 16.7 and 18 mph

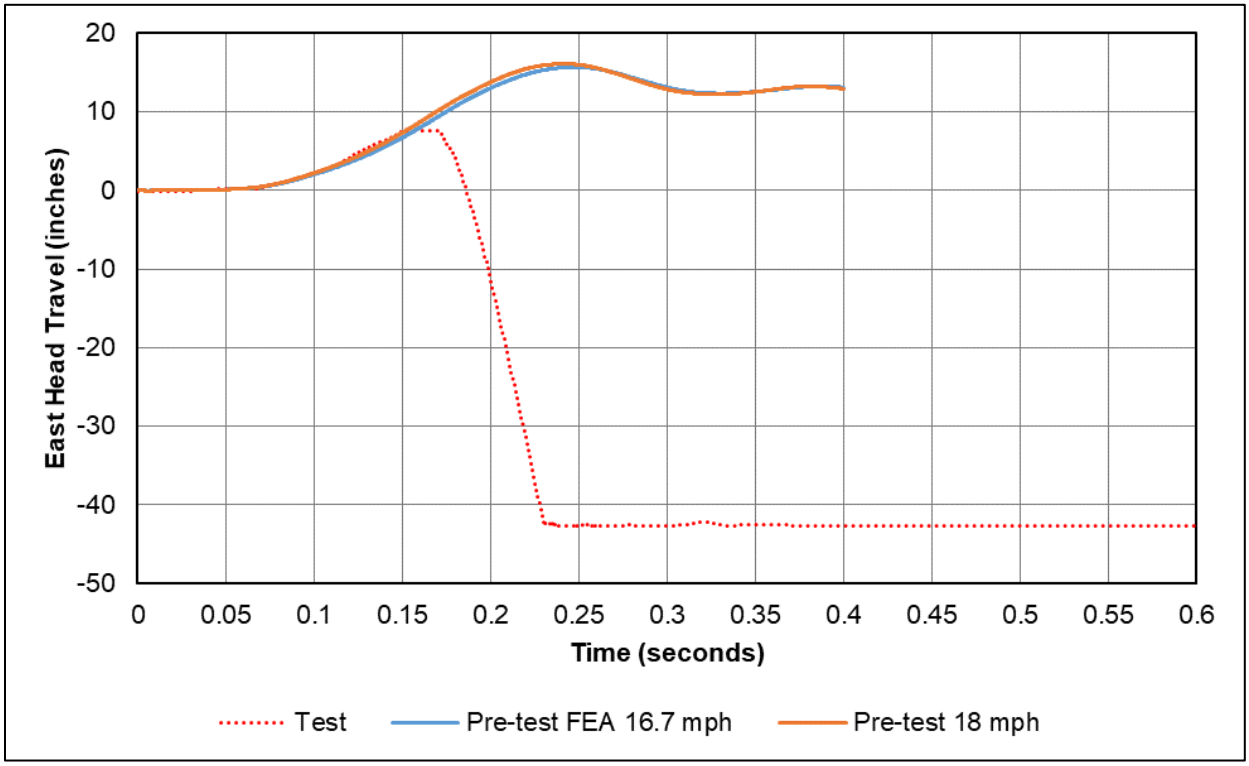

Figure C8. East Head Travel Versus Time, Pre-test FE Model at 16.7 and 18 mph

C1.1 Pre-test FE Model at 19.5 mph

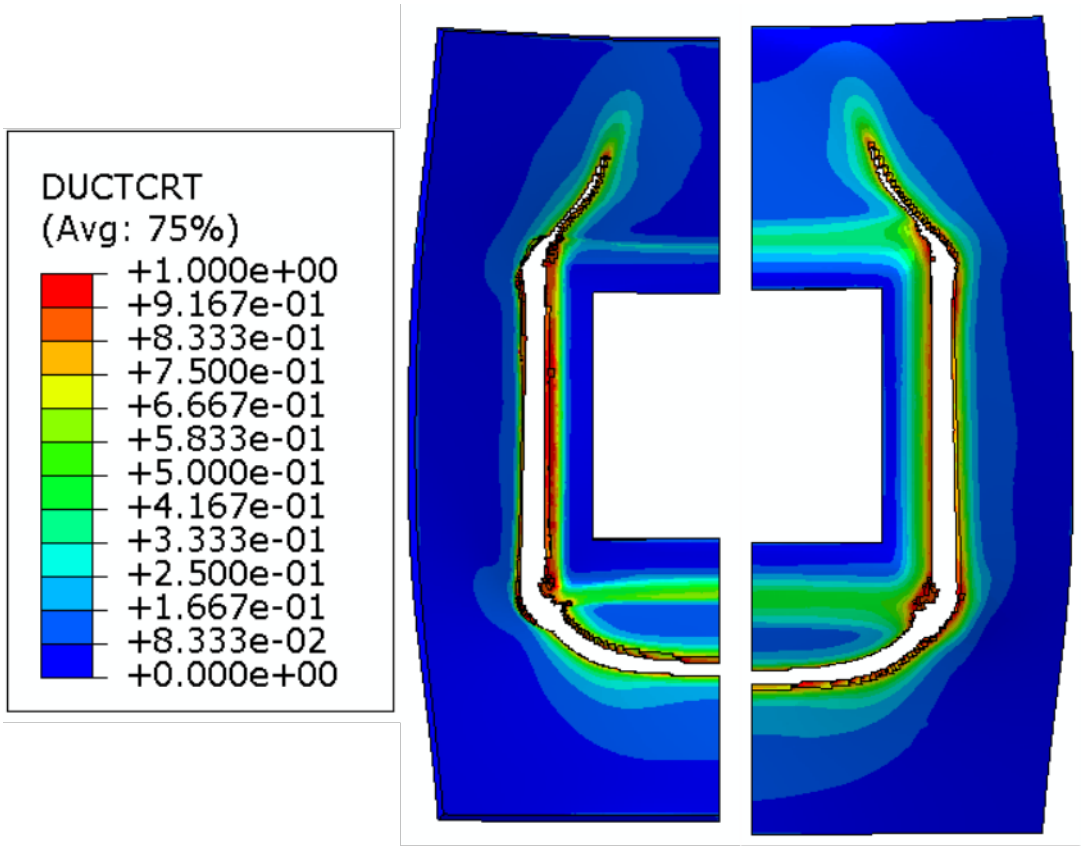

Figure C9. Outer Tank Solid Patch Exterior (left) and Interior (right) Contour Plots of Damage Initiation Criterion (DUCTCRT), 19.5 mph Pre-test FE Model at 0.336 Seconds

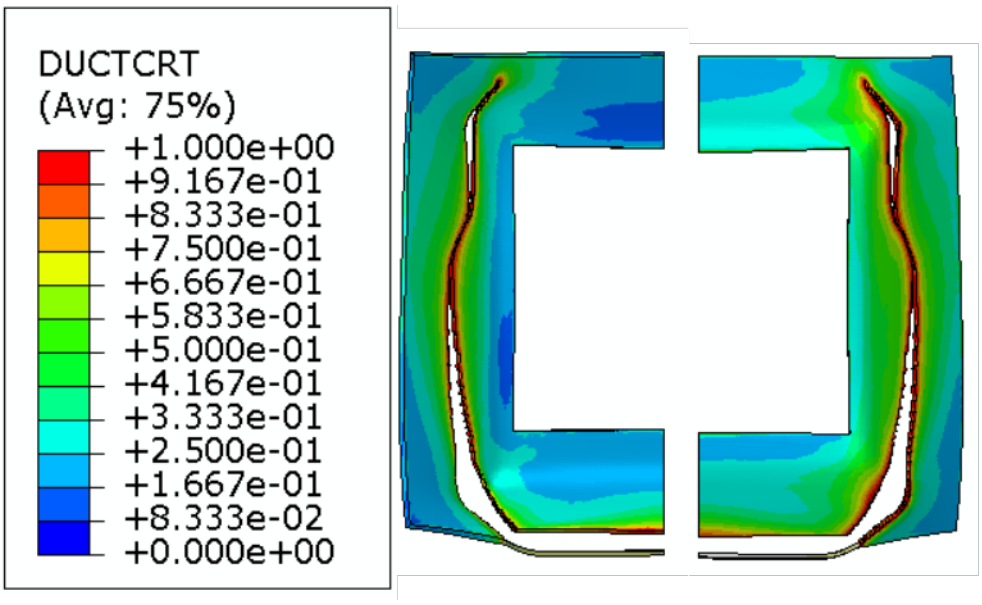

Figure C10. Inner Tank Solid Patch Exterior (left) and Interior (right) Contour Plots of Damage Initiation Criterion (DUCTCRT), 19.5 mph Pre-test FE Model at 0.336 Seconds

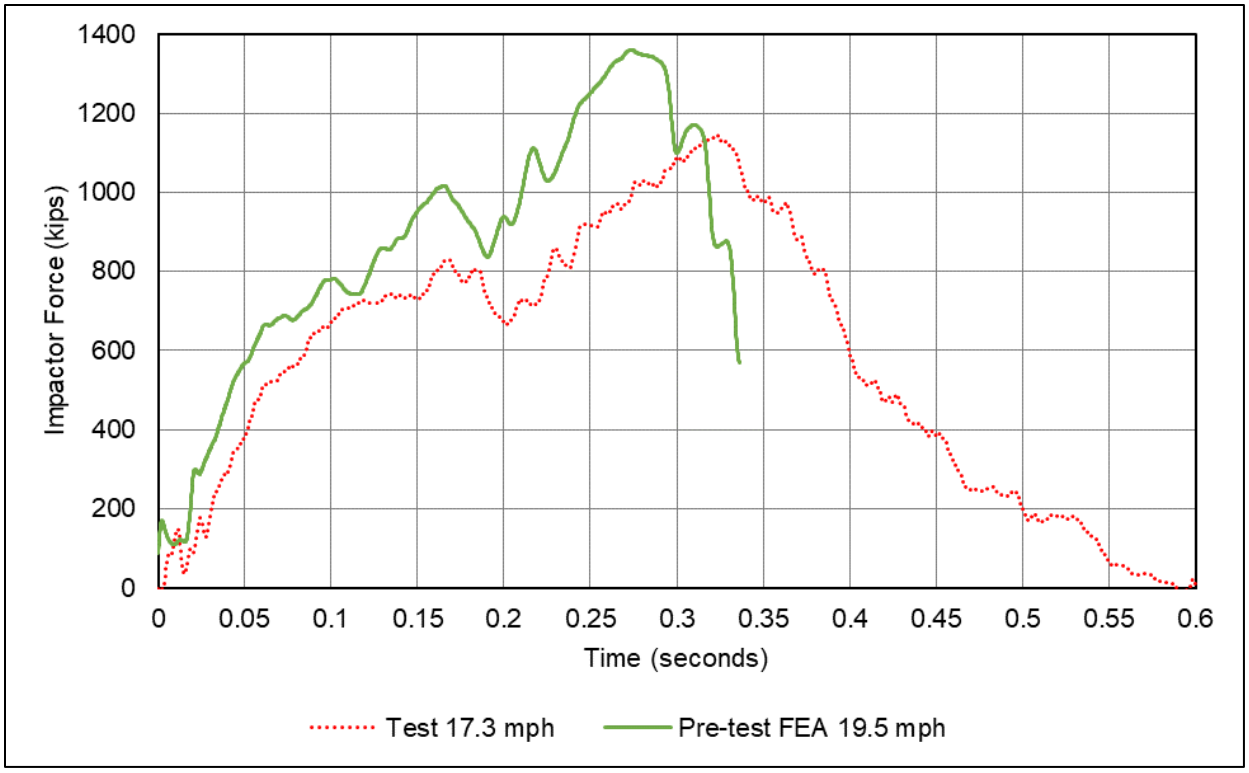

Figure C11. Impactor Force Versus Time, Pre-test FE Model at 19.5 mph

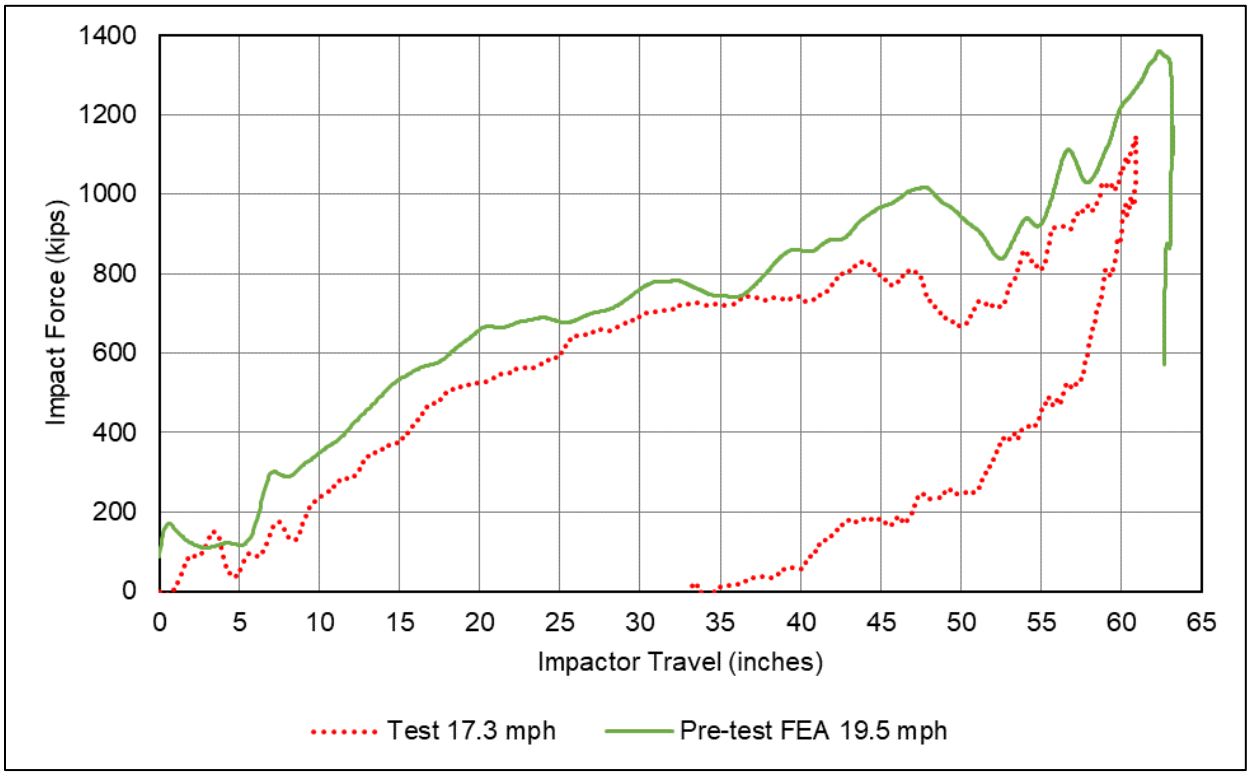

Figure C12. Impactor Force Versus Travel, Pre-test FE Model at 19.5 mph

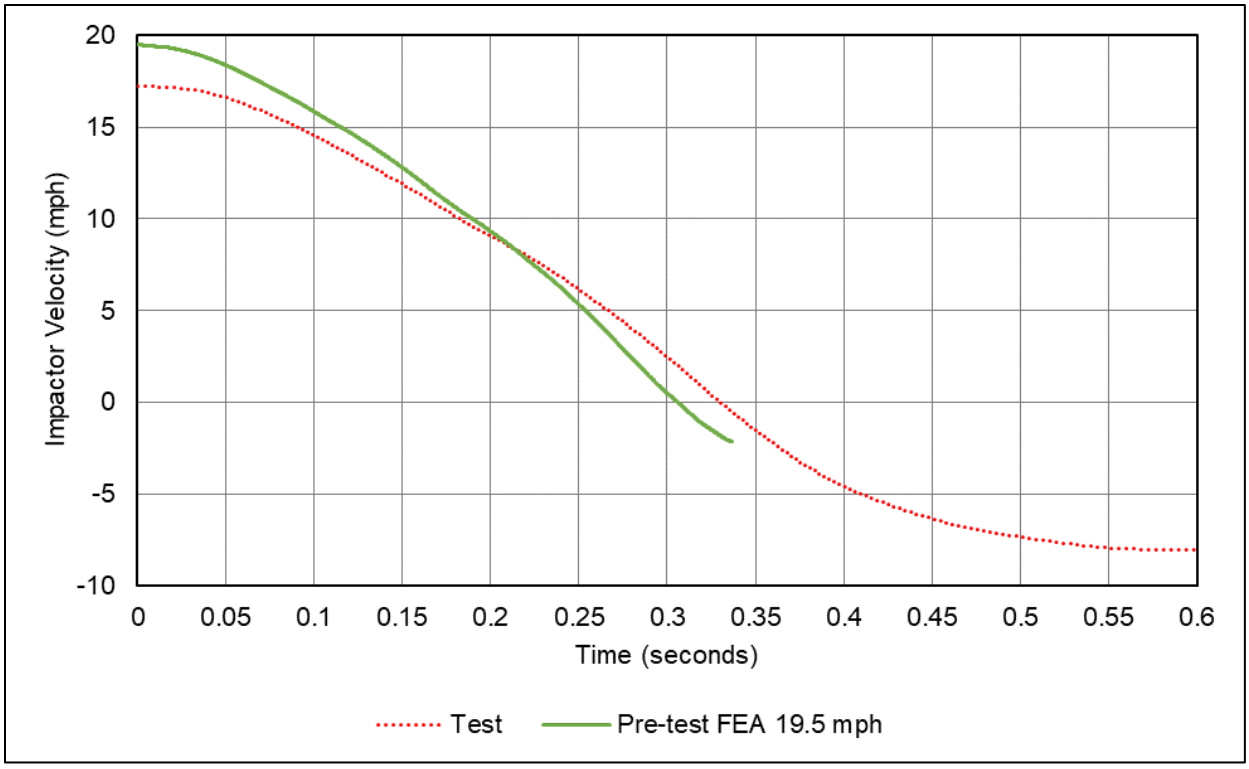

Figure C13. Impactor Velocity Versus Time, Pre-test FE Model at 19.5 mph

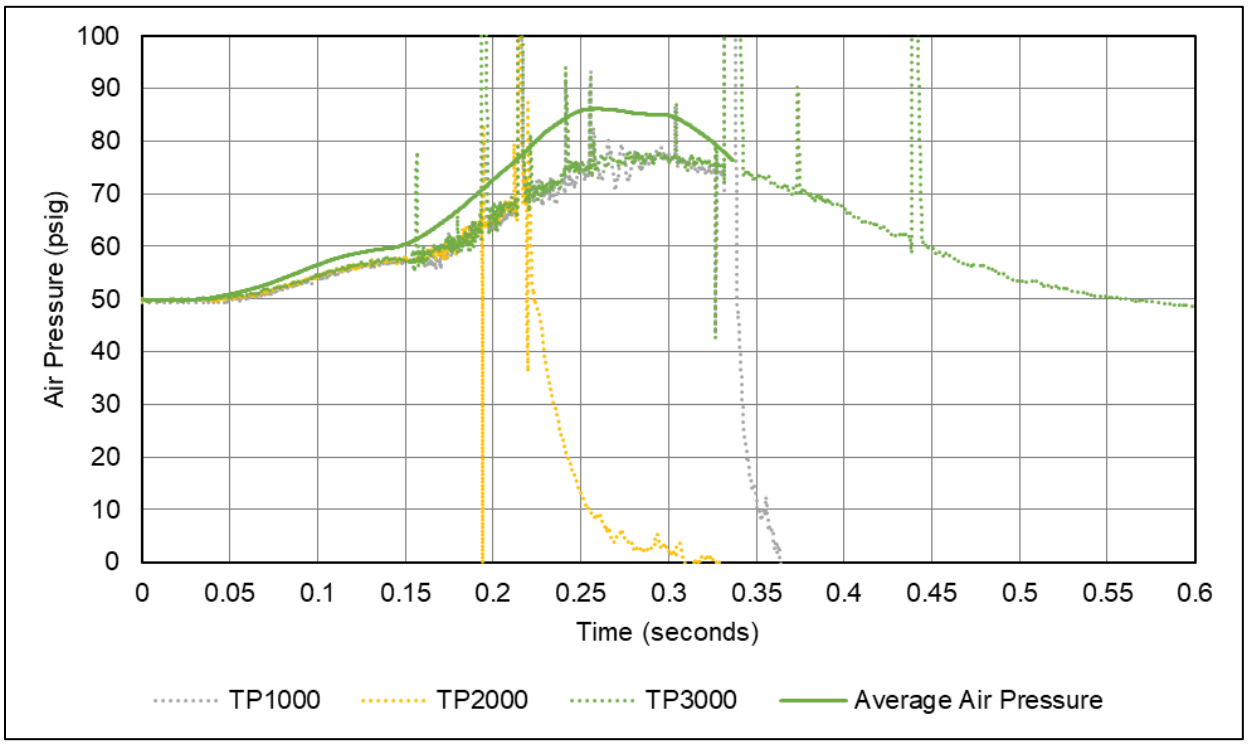

Figure C14. Outage Pressure Versus Time, Pre-test FE Model at 19.5 mph

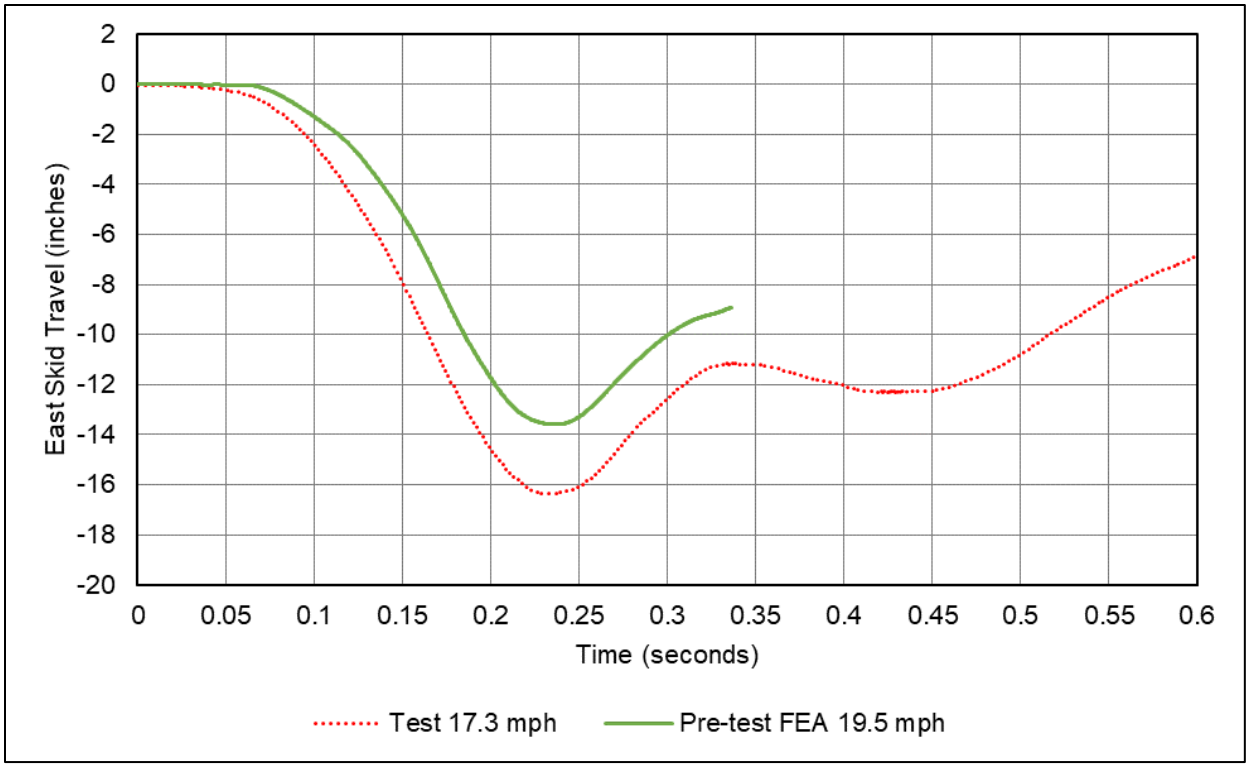

Figure C15. East Skid Travel Versus Time, Pre-test FE Model at 19.5 mph

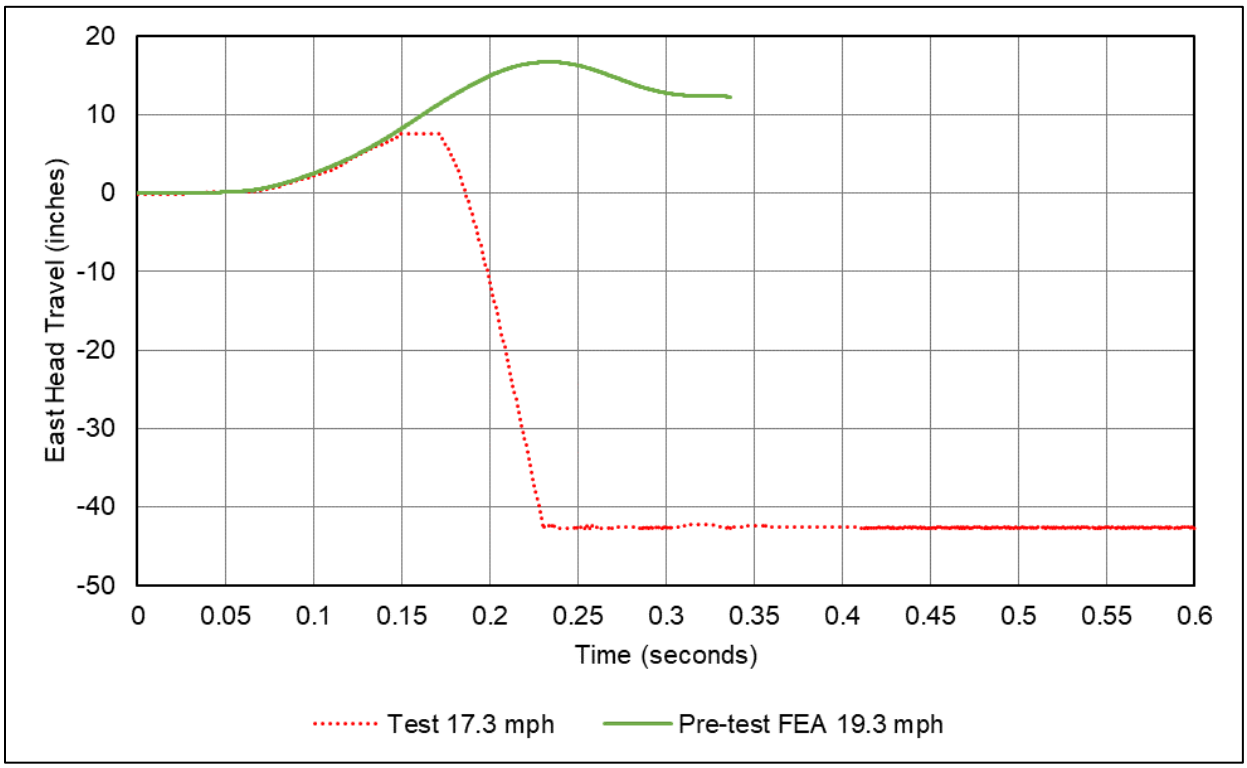

Figure C16. East Head Travel Versus Time, Pre-test FE Model at 19.5 mph

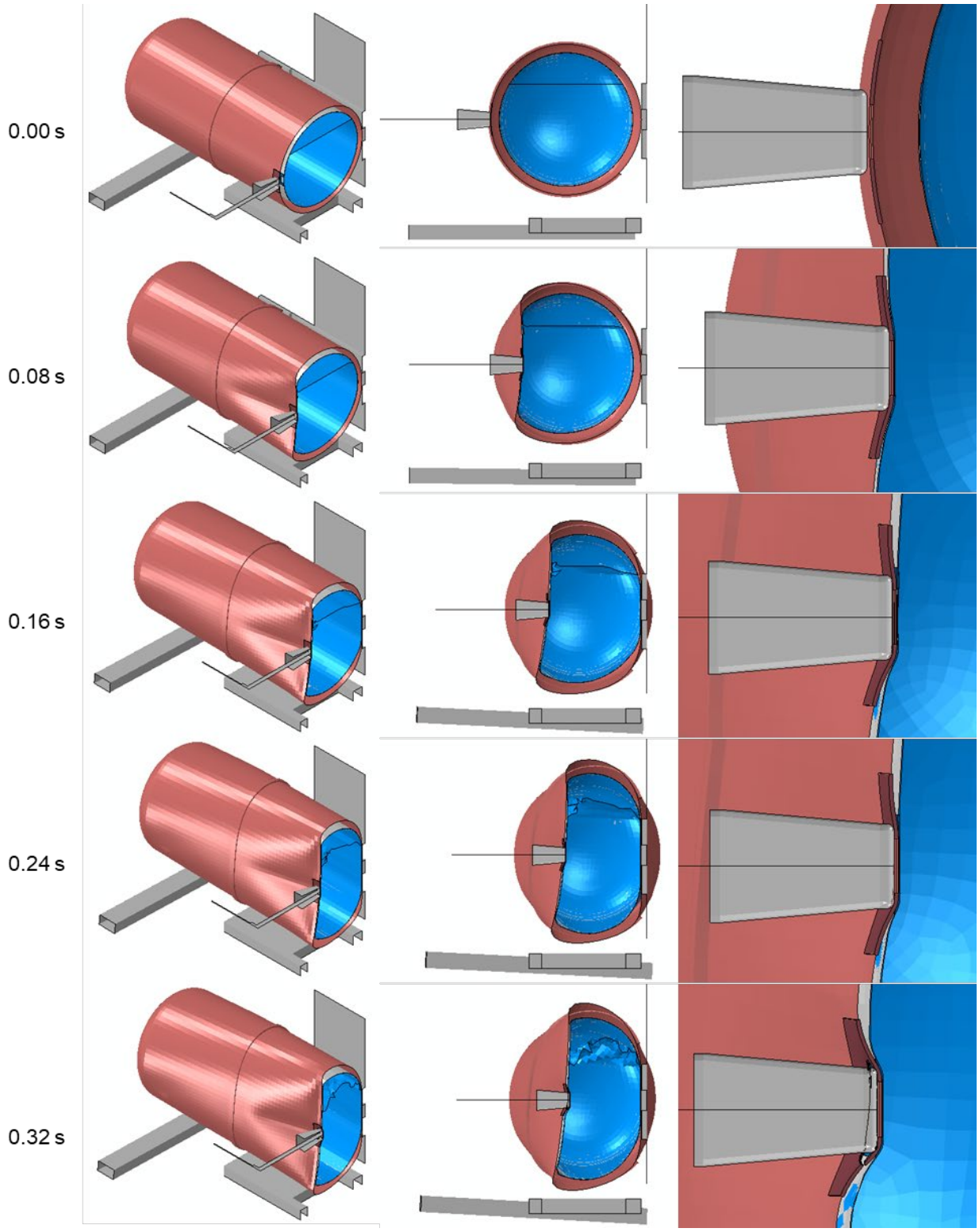

Figure C17. Isometric (left), Side (middle), and Zoomed Side (right) Views of Pre-test FE Model Impact Sequence at 19.5 mph

C2. Post-test FEA and Test Results

This appendix describes the post-test FE results. A few modeling parameters were adjusted from the pre-test to post-test FE models. The adjustments were made based on the actual test conditions and based on considerations of model runtime. The adjustments are discussed in Section 5.3.

The post-test FE results are summarized in Table C2.

Table C2. Summary of Post-test FE Models Using Pre-test Material Properties

Speed mph	Outer Tank State	Inner Tank State	Impactor State
17.3	Some elements lost	No elements lost	Rebounding

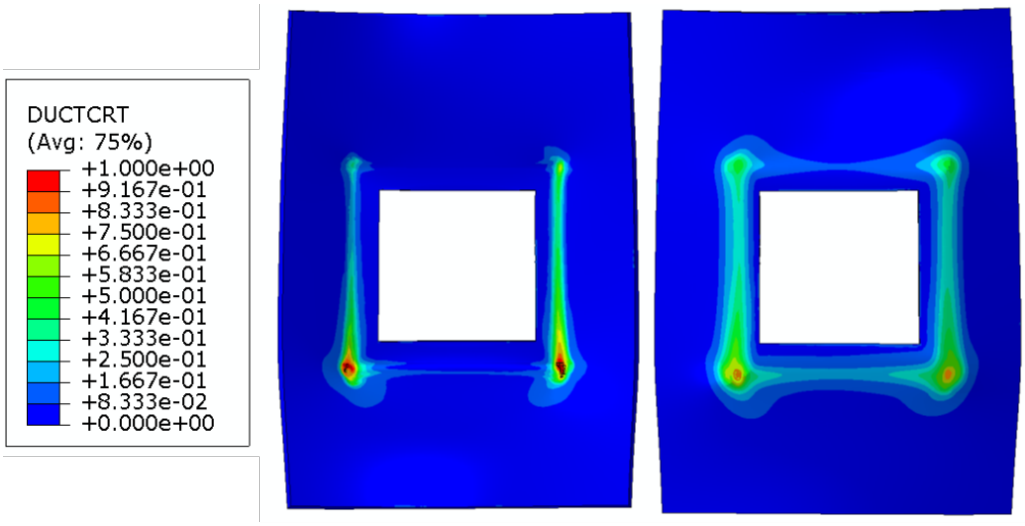

Figure C18. Outer Tank Solid Patch Exterior (left) and Interior (right) Contour Plots of Damage Initiation Criterion (DUCTCRT), 17.3 mph Post-test FE Model at 0.6 Seconds

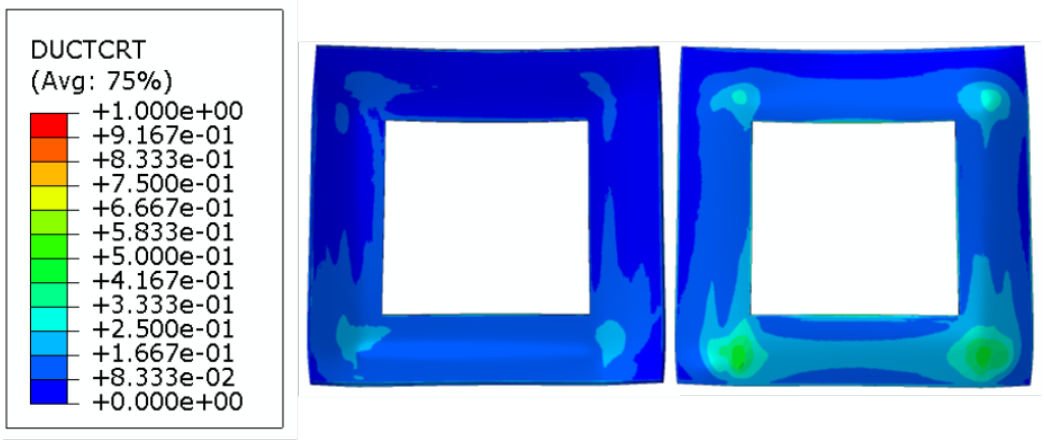

Figure C19. Inner Tank Solid Patch Exterior (left) and Interior (right) Contour Plots of Damage Initiation Criterion (DUCTCRT), 17.3 mph Post-test FE Model at 0.6 Seconds

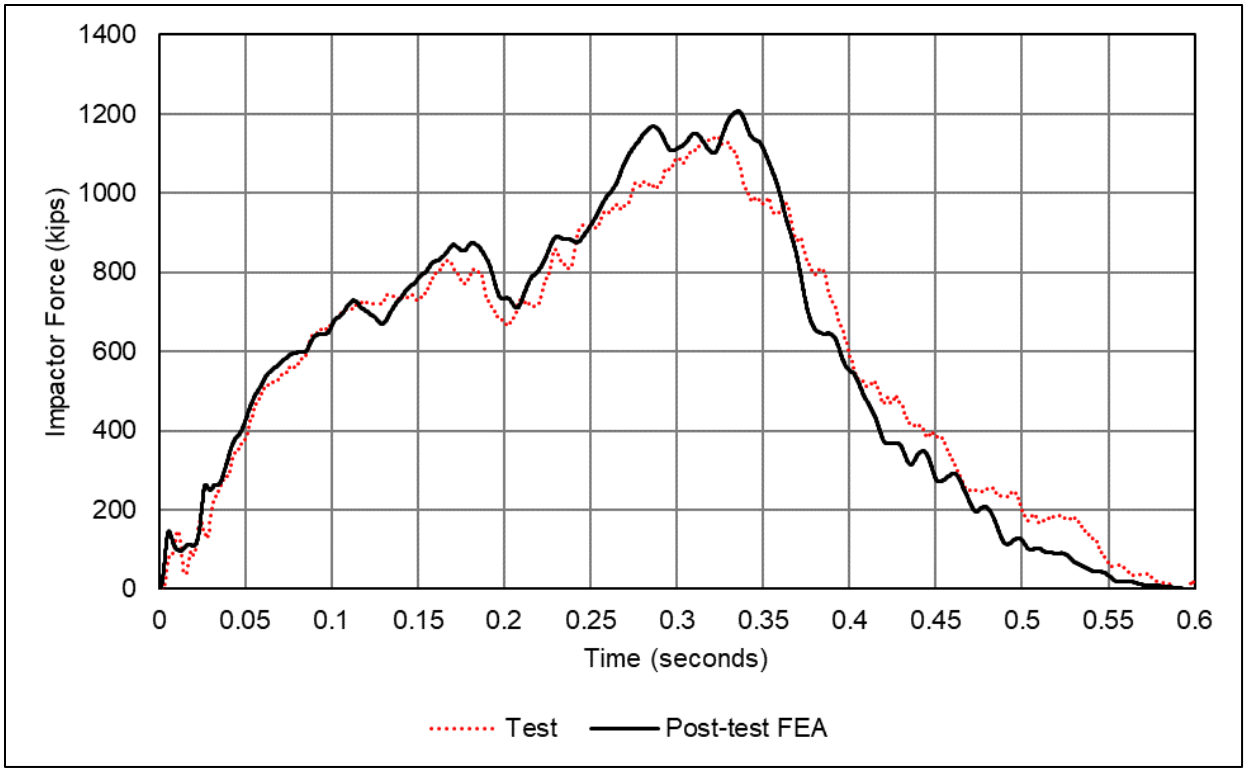

Figure C20. Impactor Force Versus Time, 17.3 mph Post-test FE Model

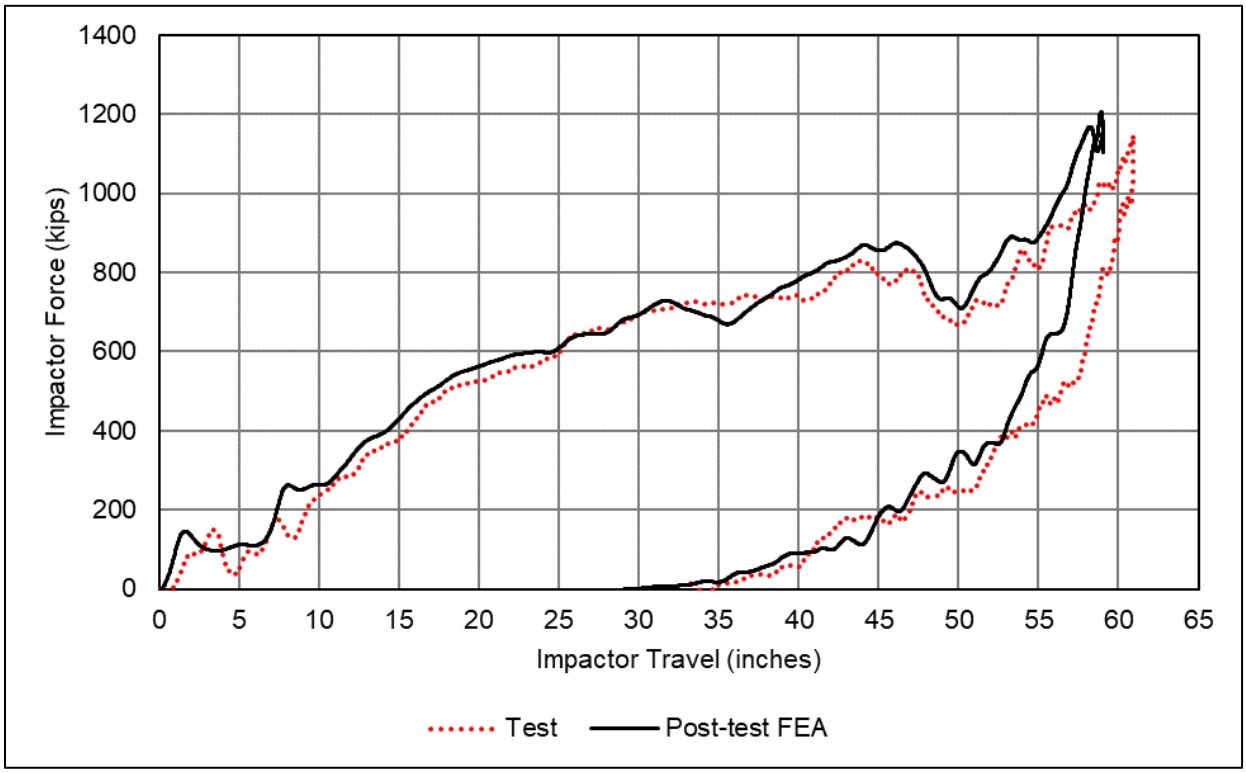

Figure C21. Impactor Force Versus Travel, 17.3 mph Post-test FE Model

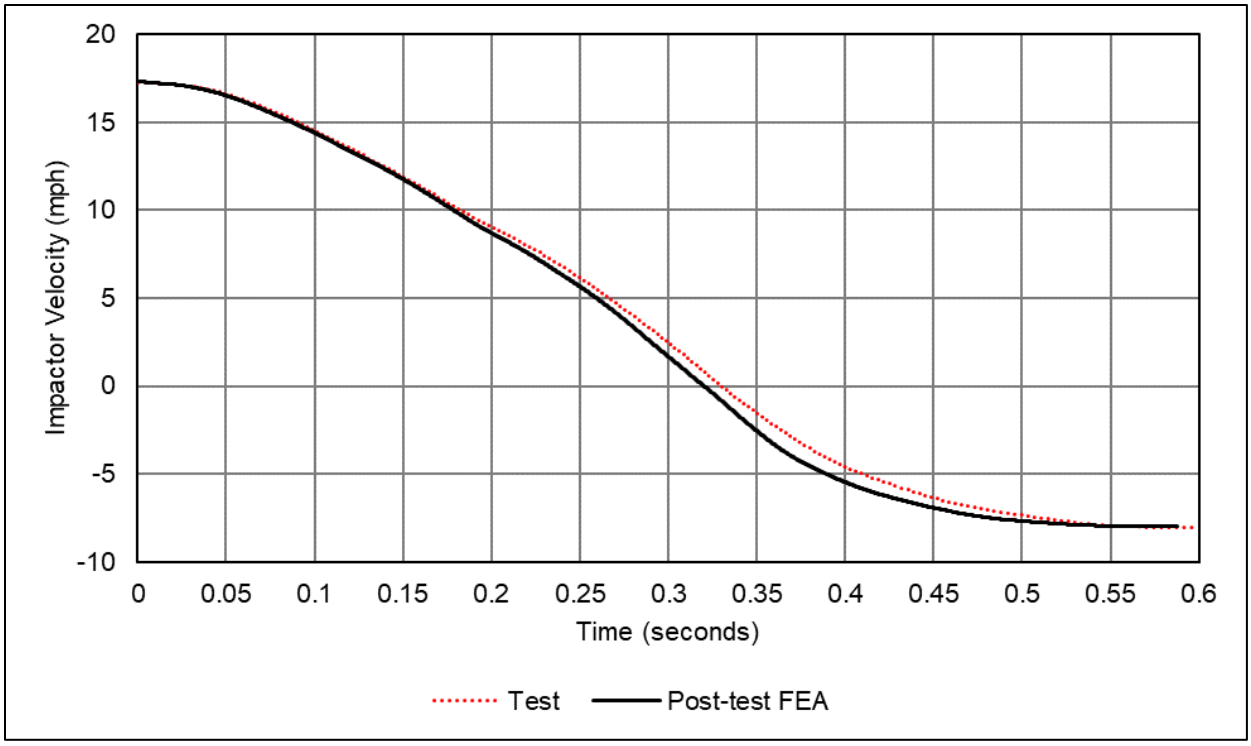

Figure C22. Impactor Velocity Versus Time, 17.3 mph Post-test FE Model

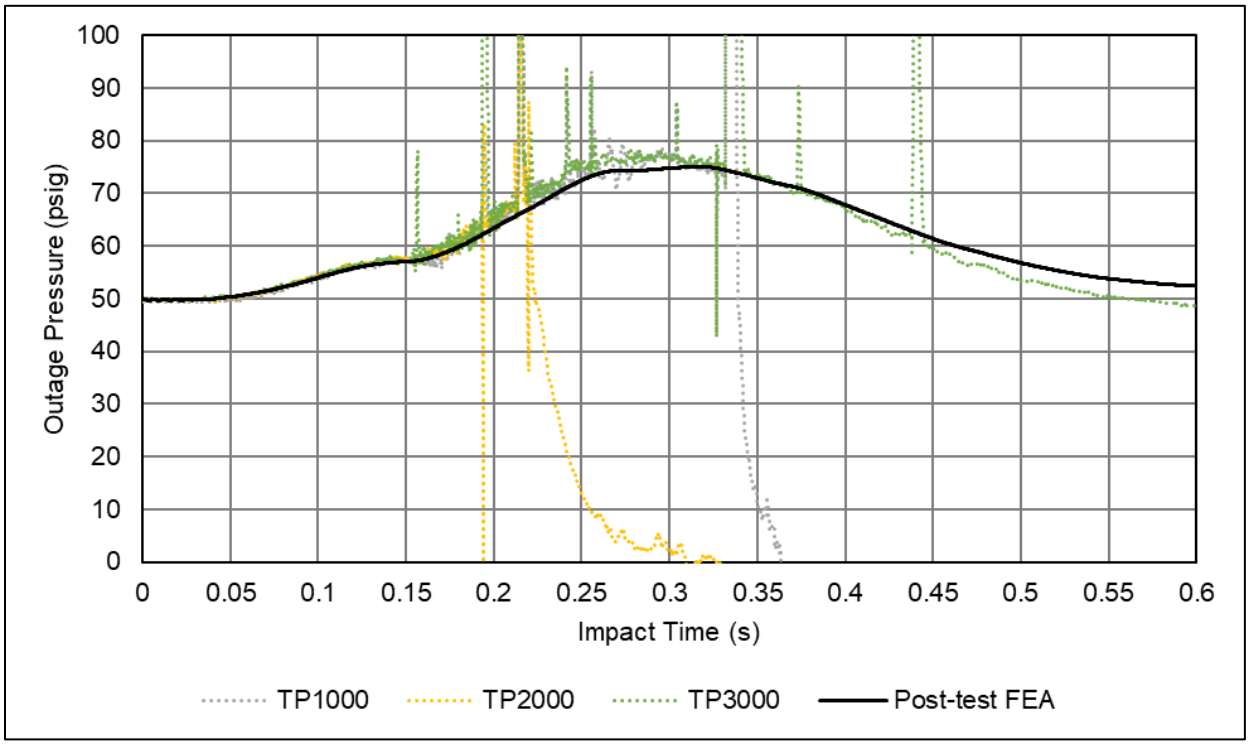

Figure C23. Outage Pressure Versus Time, 17.3 mph Post-test FE Model

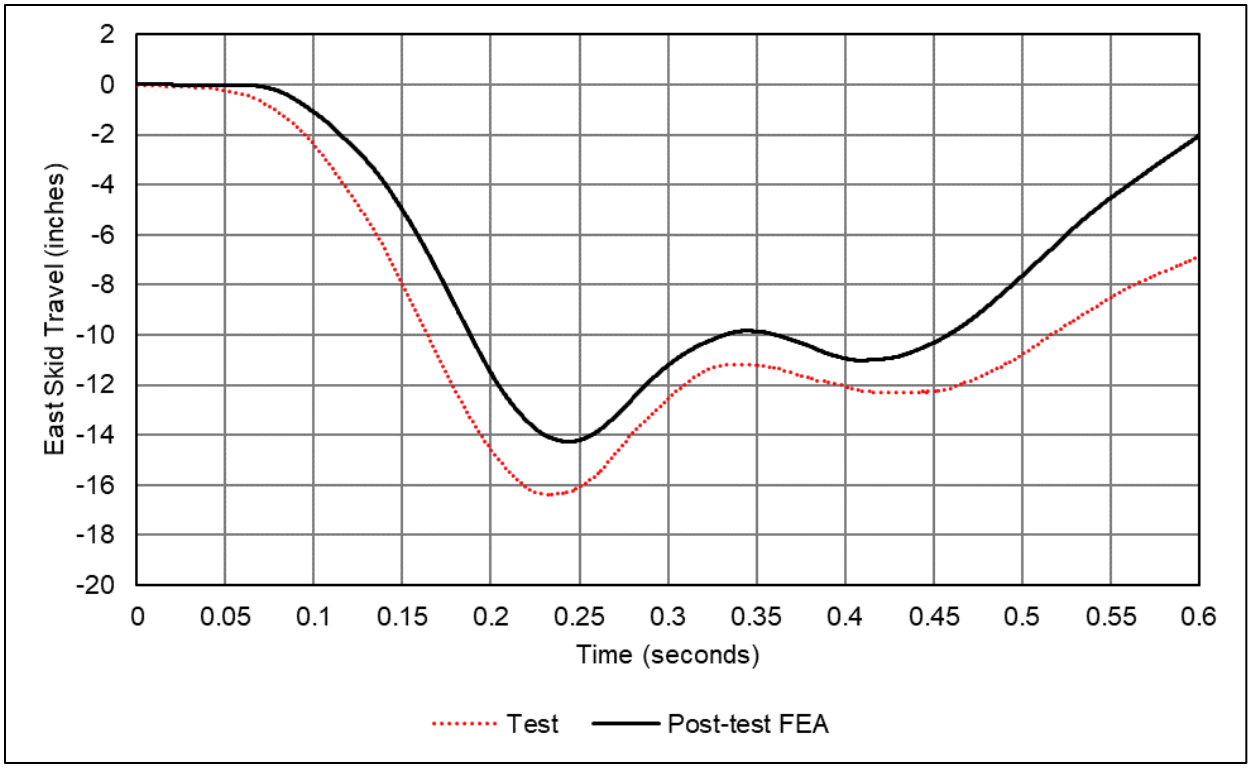

Figure C24. East Skid Travel Versus Time, 17.3 mph Post-test FE Model

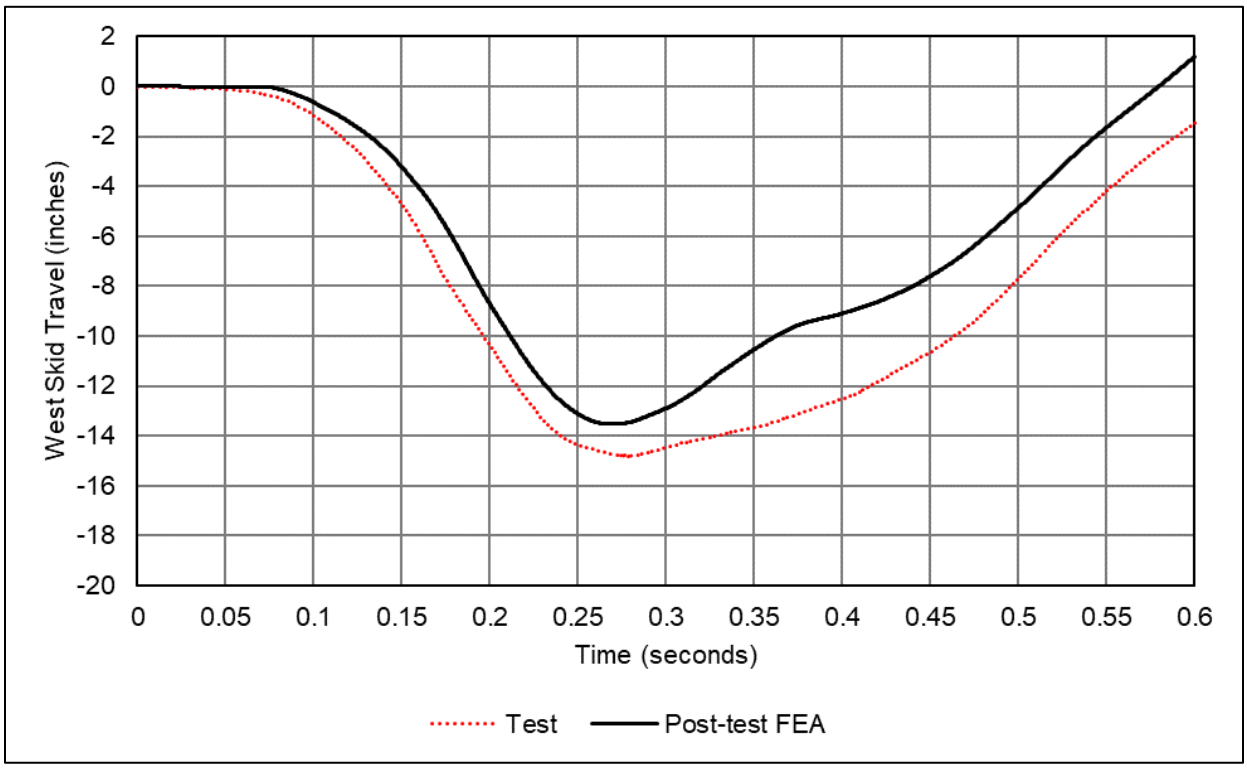

Figure C25. West Skid Travel Versus Time, 17.3 mph Post-test FE Model

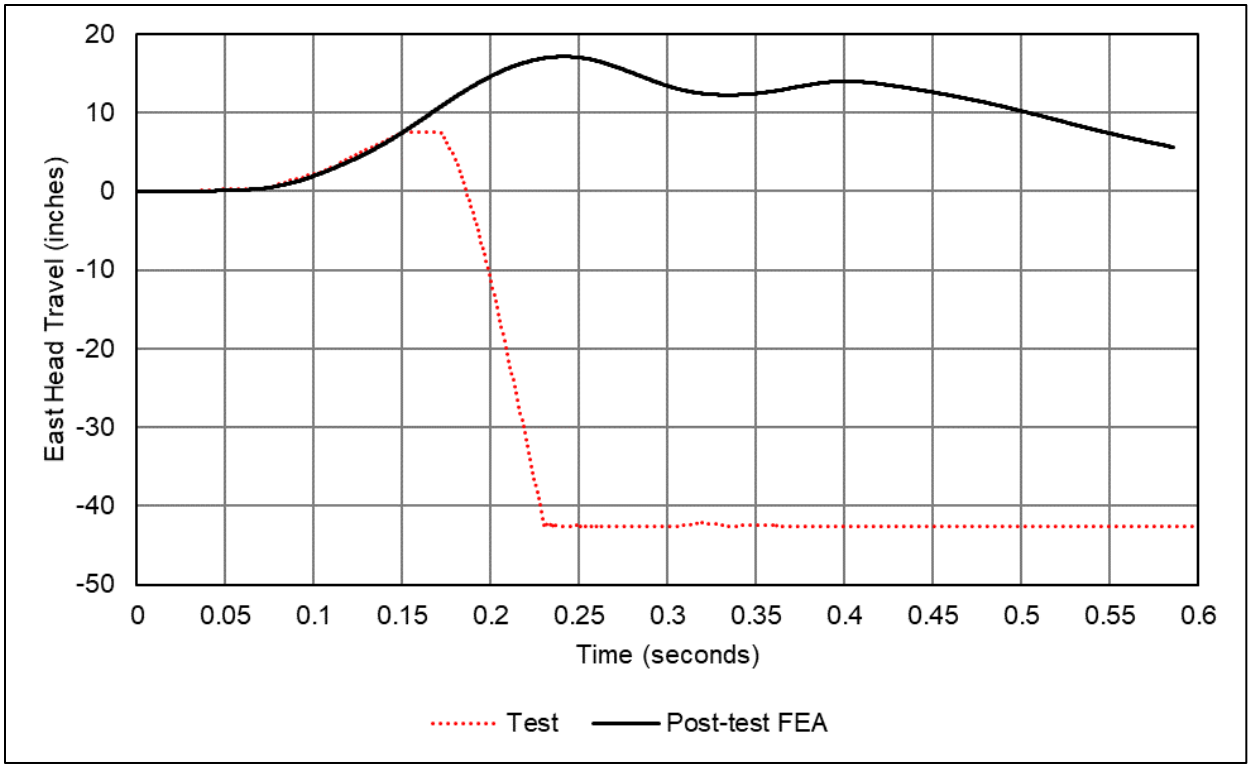

Figure C26. East Head Travel Versus Time, 17.3 mph Post-test FE Model

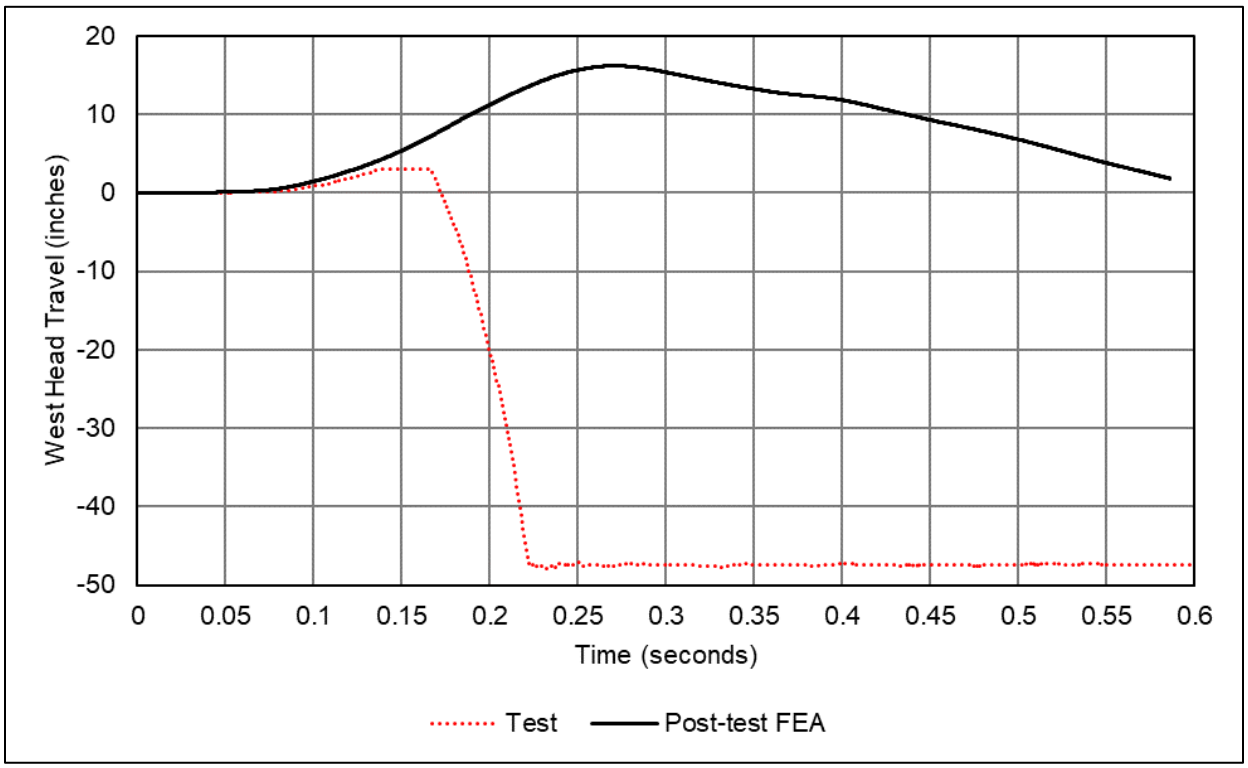

Figure C27. West Head Travel Versus Time, 17.3 mph Post-test FE Model

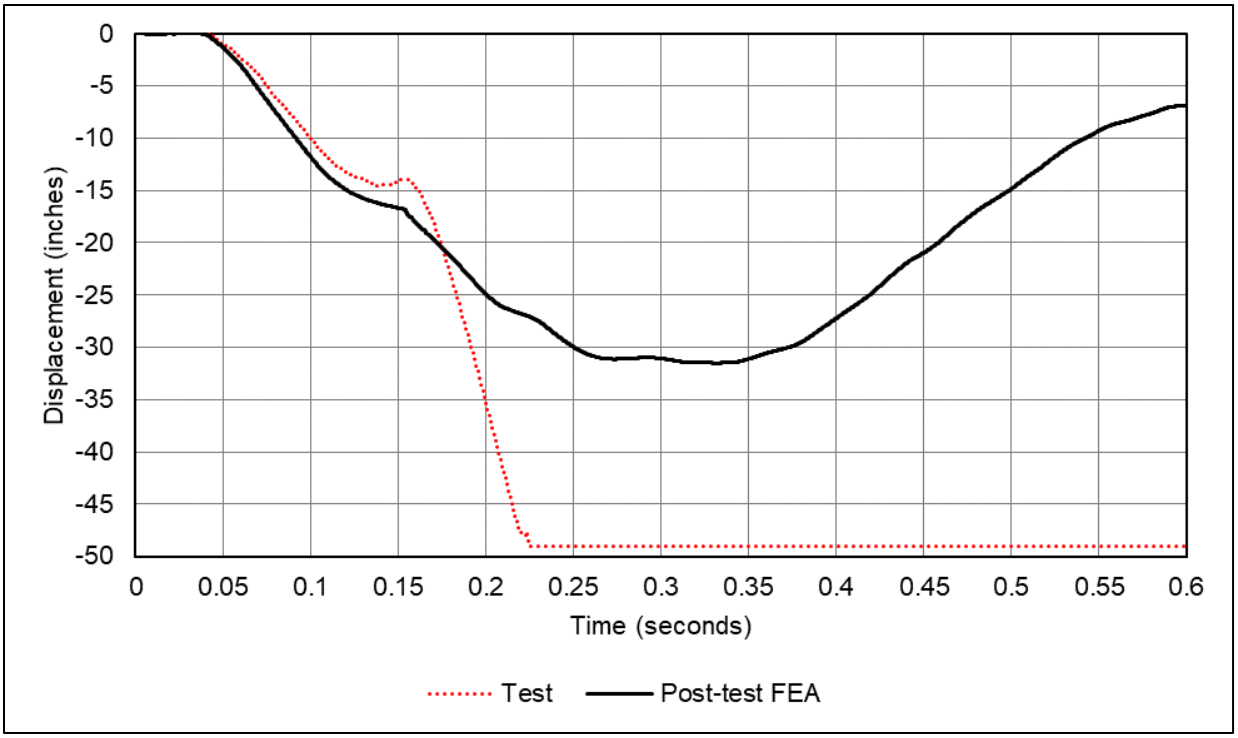

Figure C28. String Potentiometer Offset 48 inches East (TD1Y) Displacement Versus Time, 17.3 mph Post-test FE Model

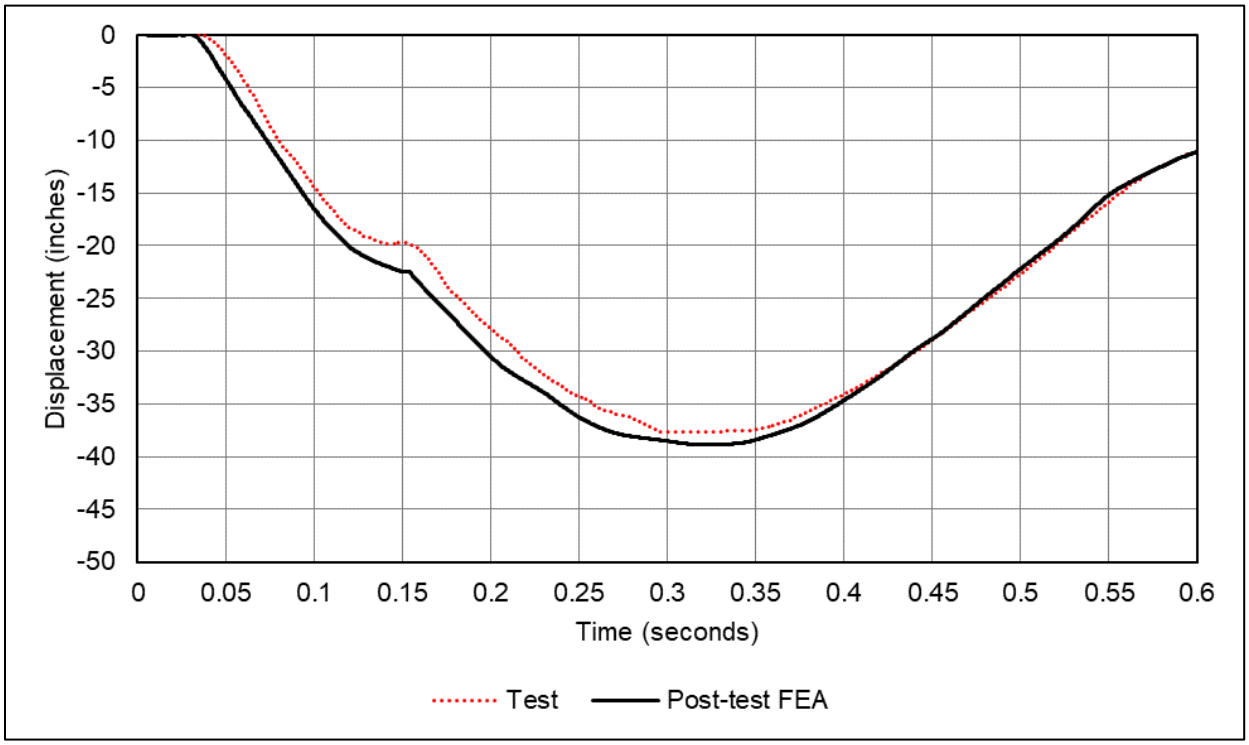

Figure C29. String Potentiometer Offset 24 inches East (TD2Y) Displacement Versus Time, 17.3 mph Post-test FE Model

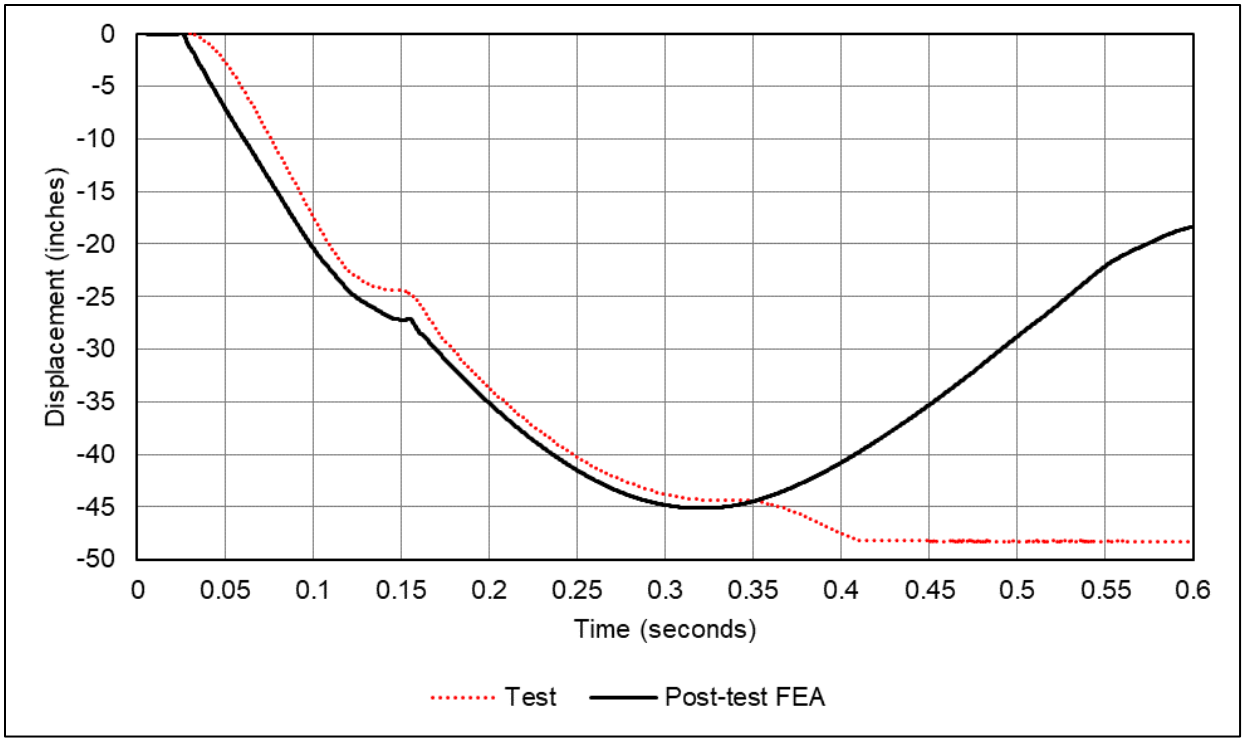

Figure C30. String Potentiometer Centered (TD3Y) Displacement Versus Time, 17.3 mph Post-test FE Model

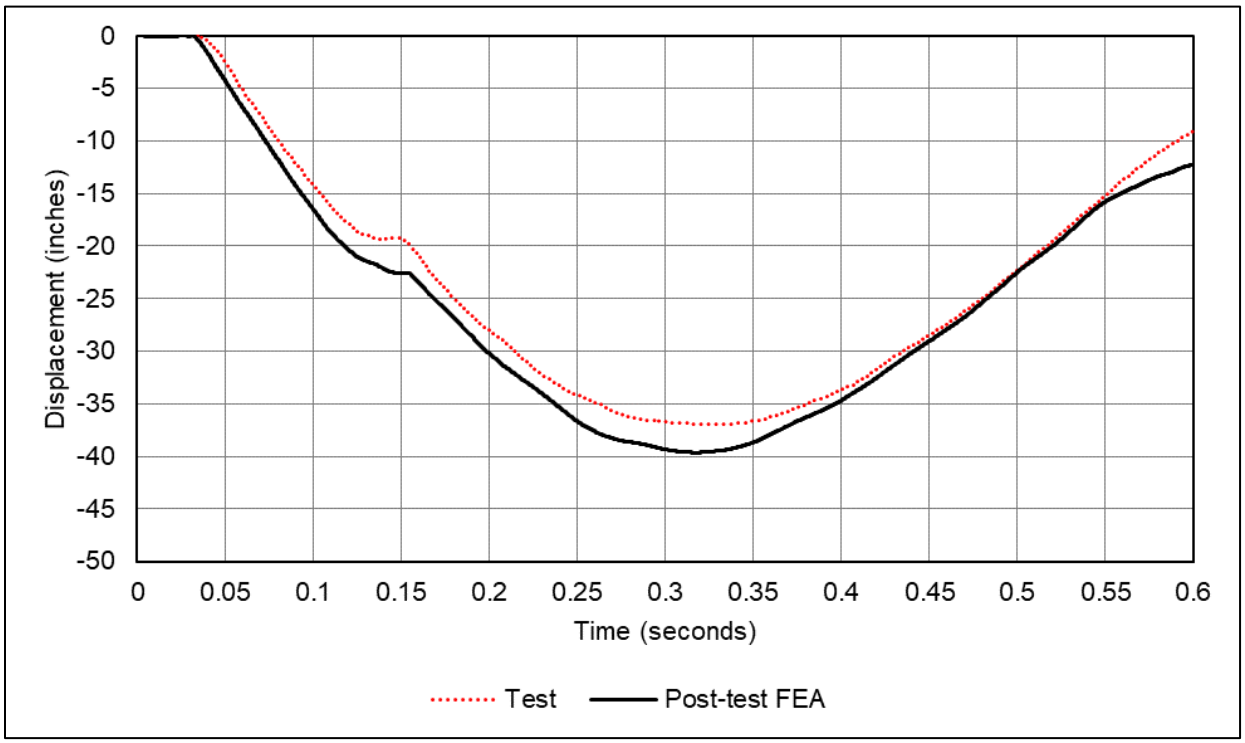

Figure C31. String Potentiometer Offset 24-inches West (TD4Y) Displacement Versus Time, 17.3 mph Post-test FE Model

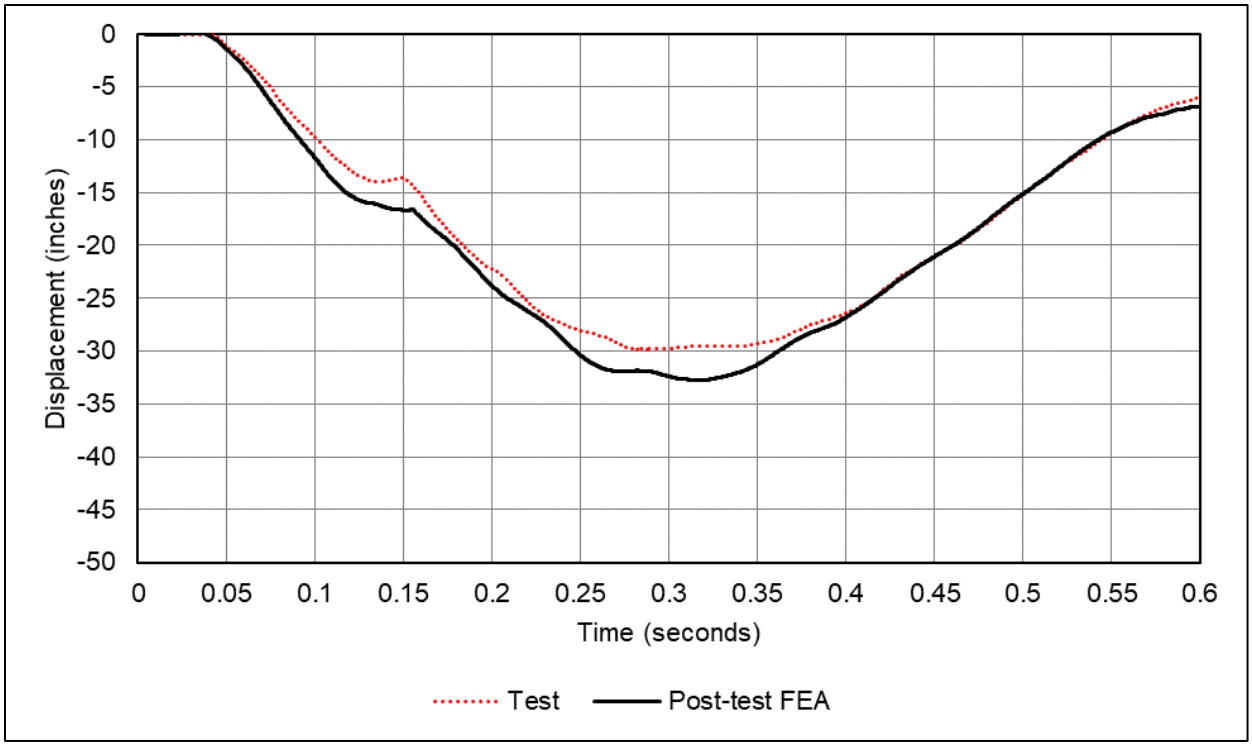

Figure C32. String Potentiometer Offset 48-inches West (TD5Y) Displacement Versus Time, 17.3 mph Post-test FE Model

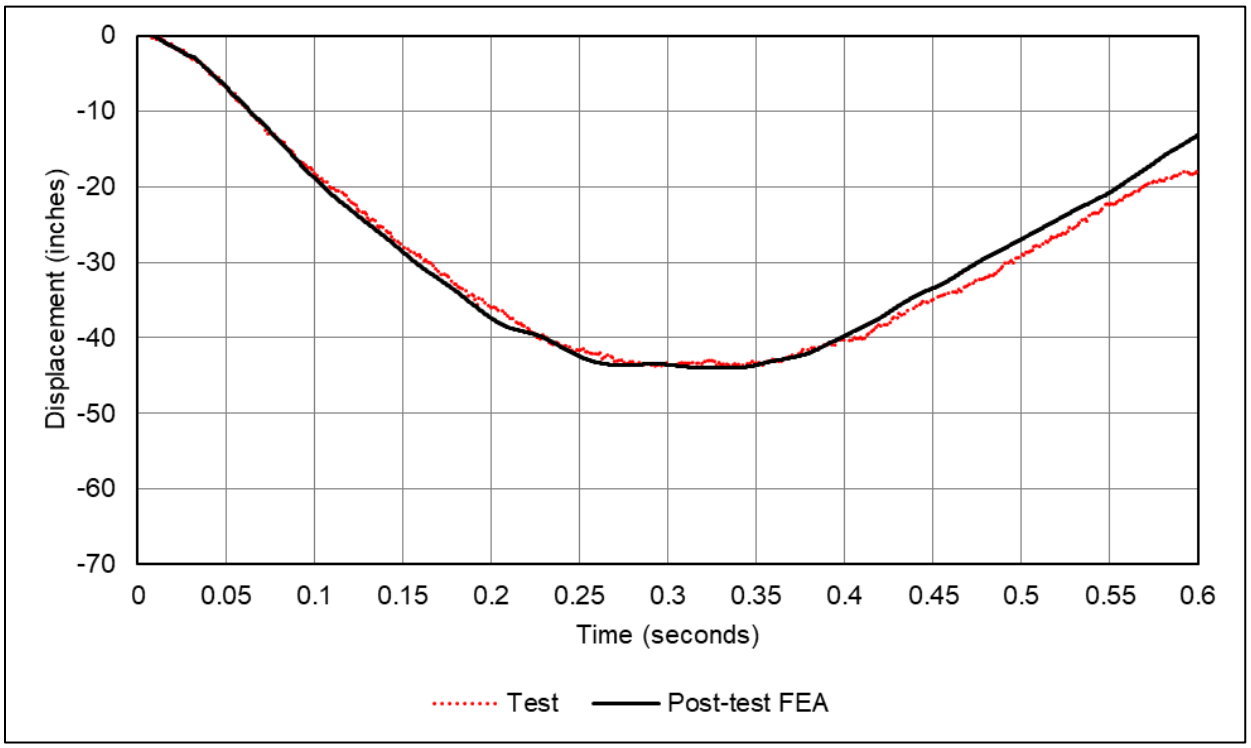

Figure C33. Laser Transducer Offset 48-inches East (BD1Y) Displacement Versus Time, 17.3 mph Post-test FE Model

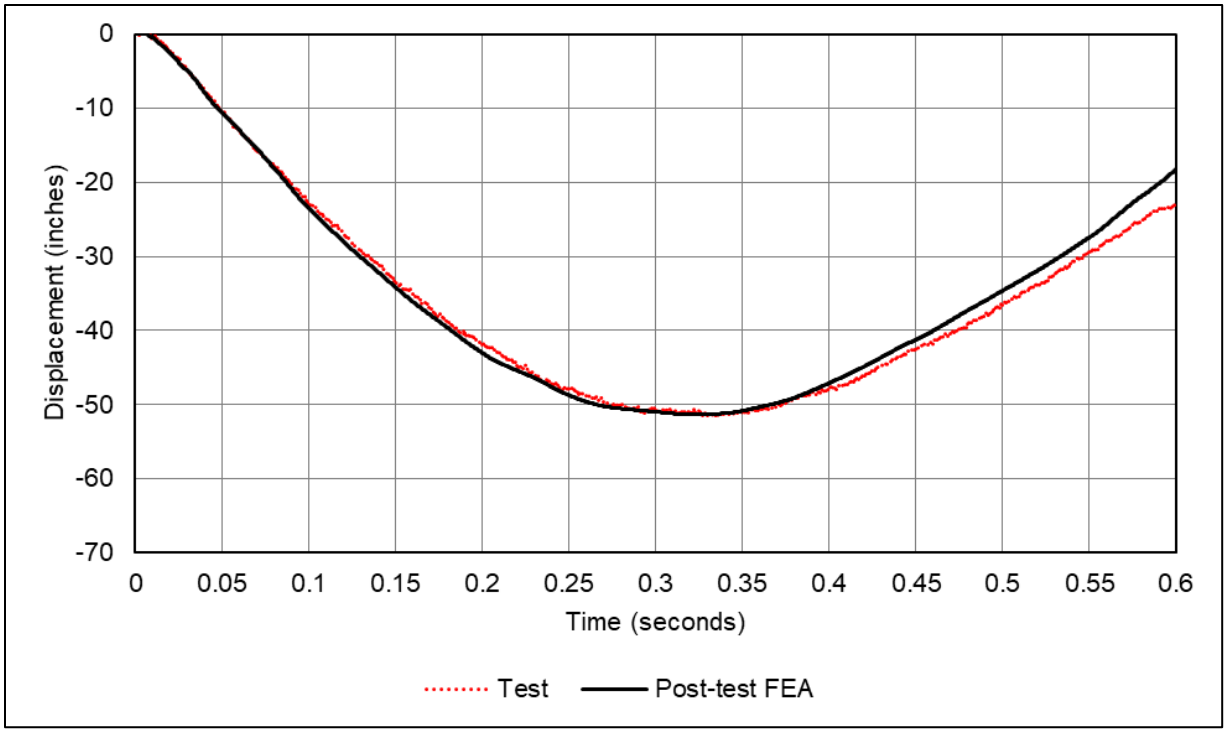

Figure C34. Laser Transducer Offset 24-inches East (BD2Y) Displacement Versus Time, 17.3 mph Post-test FE Model

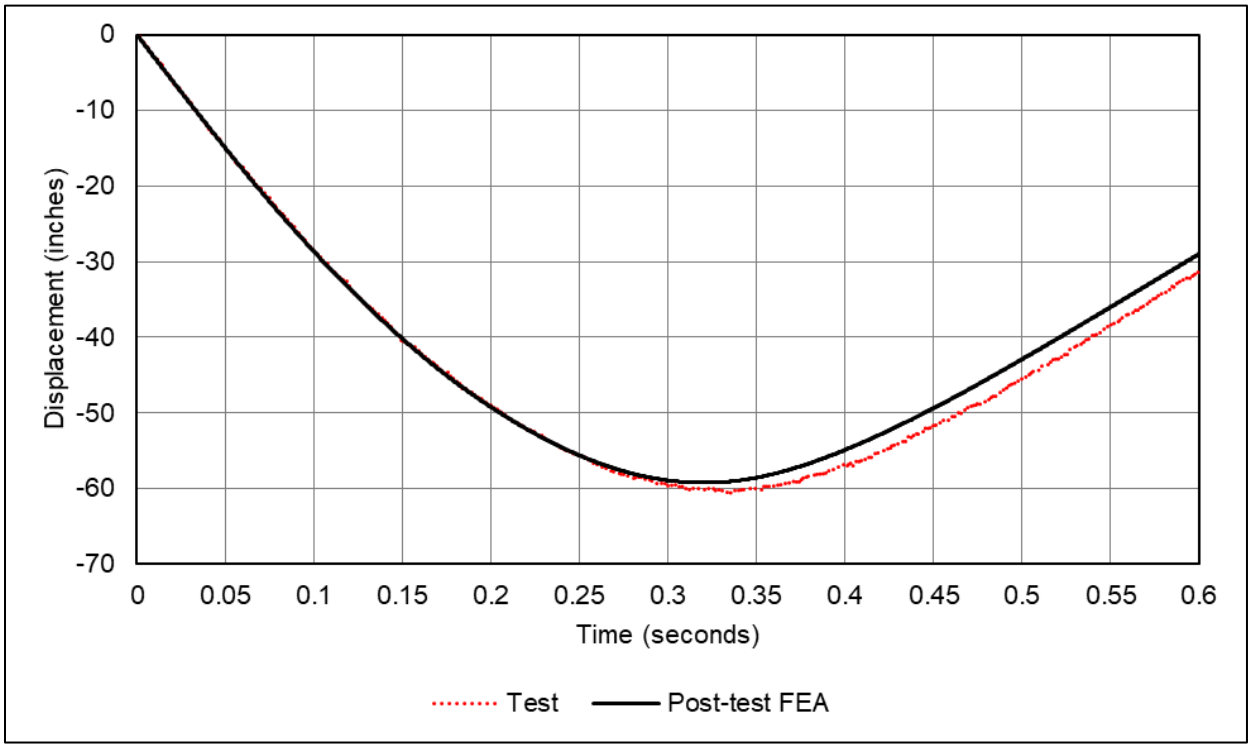

Figure C35. Laser Transducer Offset on Wall (BD3Y) Displacement Versus Time, 17.3 mph Post-test FE Model

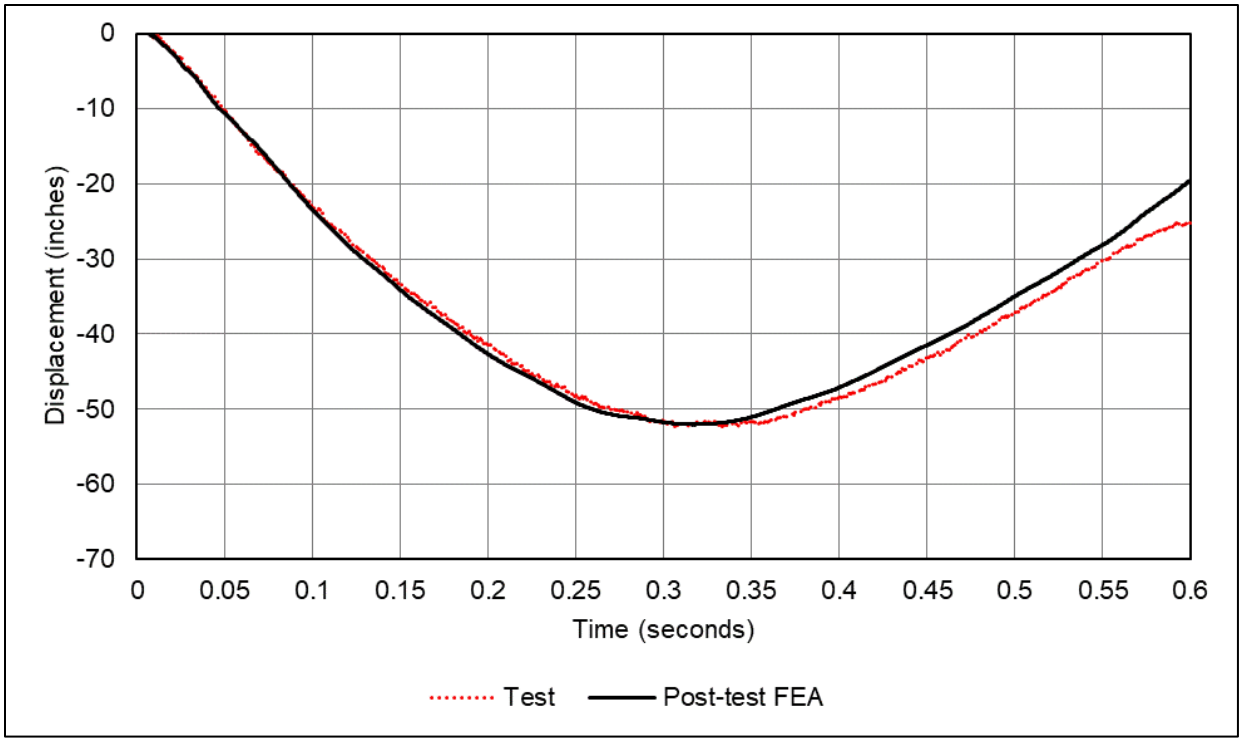

Figure C36. Laser Transducer Offset 24-inches West (BD4Y) Displacement Versus Time, 17.3 mph Post-test FE Model

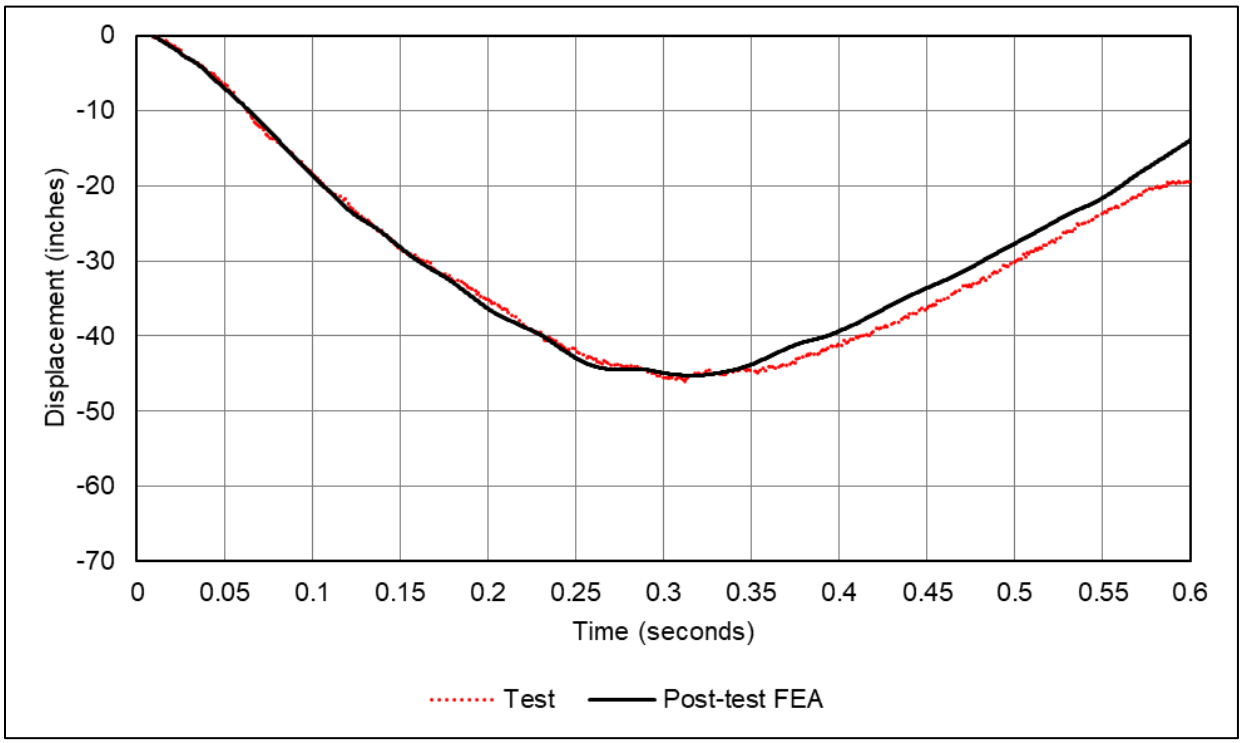

Figure C37. Laser Transducer Offset 48-inches West (BD5Y) Displacement Versus Time, 17.3 mph Post-test FE Model

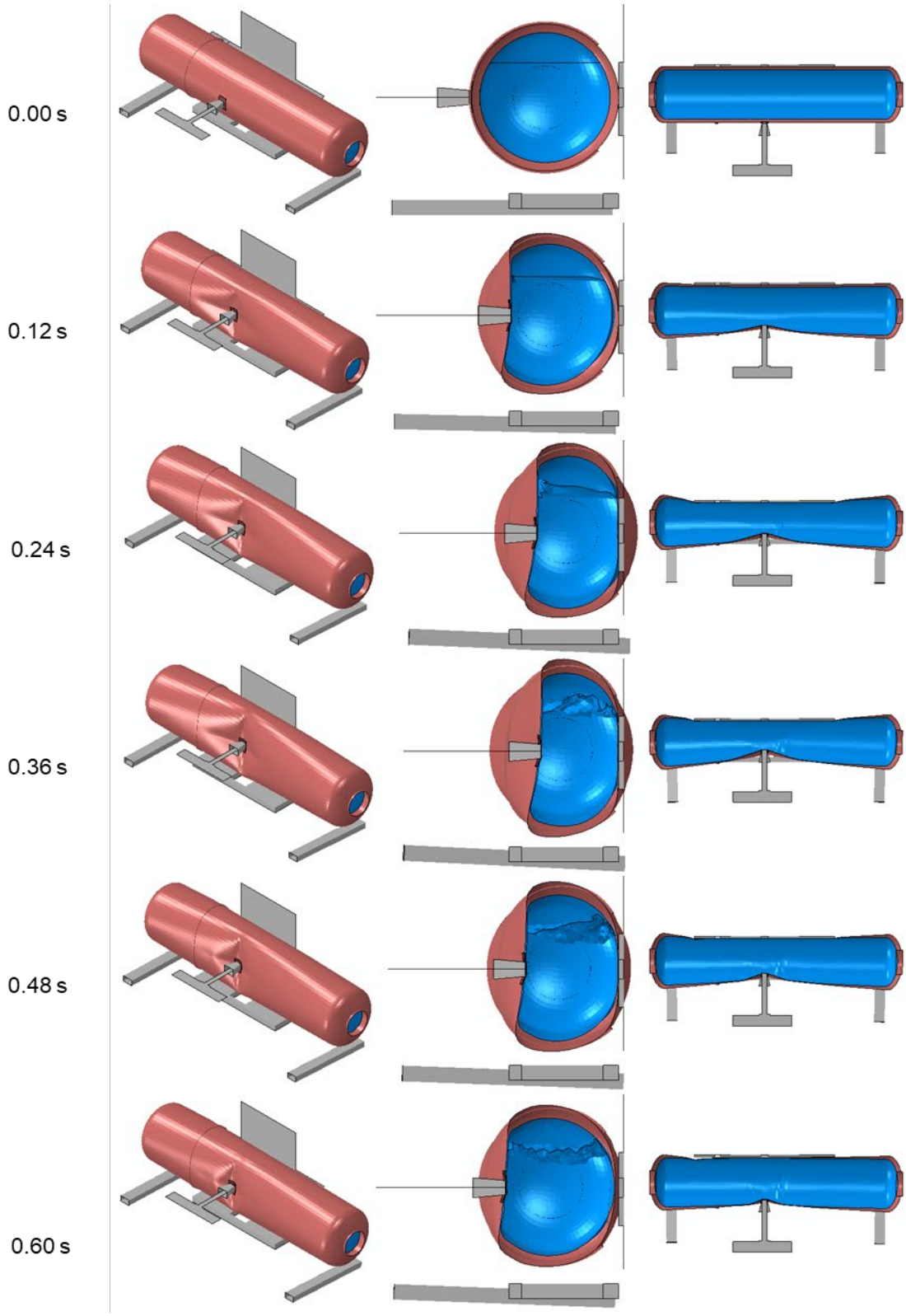

Figure C38. Isometric (left), Side Section (middle), and Top Section (right) Views of Post-test FE Model Impact Sequence at 17.3 mph

Appendix D.
Geometry in Pre-test and Post-test FE Models

This appendix contains a discussion of each of the parts that made up the assemblies for the pre- and post-test FE models. Rigid parts were used when it was important to include a part for its inertia or for its interaction through contact but where the deformation of the part could be neglected in the calculations. Four parts were modeled as rigid bodies. The remaining bodies were modeled as deformable bodies. A summary of the element types used to mesh the model assembly is provided in Table D1.

Table D1. Summary of Element Types [22]

Element Designation	Description
C3D8R	8-node linear brick element, reduced integration
CONN3D2	Connector element between two nodes or ground and a node
DCOUP3D	3-dimensional distributing coupling element
M3D3	3-node triangular membrane element
M3D4R	4-node quadrilateral membrane element (reduced integration)
MASS	Point mass
R3D3	3-dimensional, 3-node triangular facet rigid element
R3D4	3-dimensional, 4-node bilinear quadrilateral rigid element
RNODE3D	3-dimensional reference node
S3R	3-node triangular general-purpose shell, finite membrane strains (identical to element S3)
S4R	4-node general-purpose shell, reduced integration with hourglass control, finite membrane strains
SPRINGA	Axial spring between two nodes, whose line of action is the line joining the two nodes. This line of action may rotate in large-displacement analysis.

D1. Rigid Impactor

The impactor was modeled as a rigid body in the DOT-113 surrogate FE models. The geometry was a 12-inch by 12-inch indenter with 1-inch radii edges around the impact face. The geometry included the impact face, the tapered cone back to the portion of the impactor where the impactor attached to the ram arm, and a representation of the ram arm and the width of the ram car's body. The impactor, both with and without mesh, is shown in Figure D1 for the post-test FE model. A summary of the impactor mesh properties is provided in Table D2. Note that the pre-test FE model used a symmetry plane that is not shown below (refer to Figure 39).

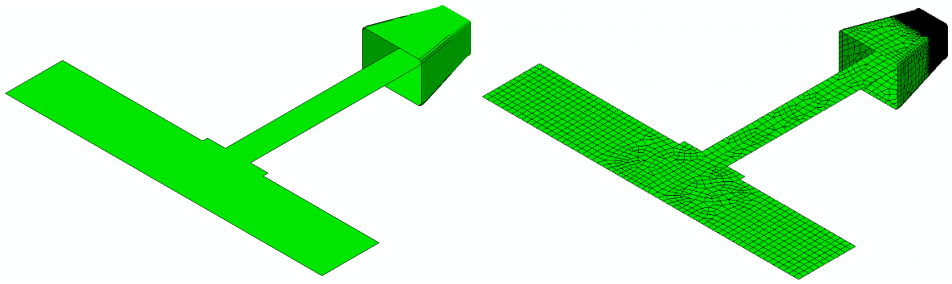

Figure D1. Impactor Geometry (left) and Mesh (right)

D2. Rigid Wall

The impact wall was modeled as a rigid body in the DOT-113 surrogate FE models. Because the wall was constrained against motion in any direction, no mass needed to be defined for this part. The wall's geometry and mesh are shown in Figure D2 for the post-test FE model. A summary of the wall mesh properties is provided in Table D3. Note that the pre-test FE model used a symmetry plane which is not shown in Figure D2 (refer to Figure 39).

Table D2. Properties of Impactor in Pre-test and Post-test FE Models

Property	Pre-test Model	Post-test Model
Type of Part	Rigid	Rigid
Symmetry	Yes	No
Number of Elements	R3D4: 42,891 R3D3: 79 RNODE3D: 13 MASS: 1	R3D4: 86,772 R3D3: 216 RNODE3D: 17 MASS: 1
Approximate Mesh Size	0.081 to 2 inches	0.081 to 2 inches
Approximate Part Weight	148,443 lbf	297,200 lbf

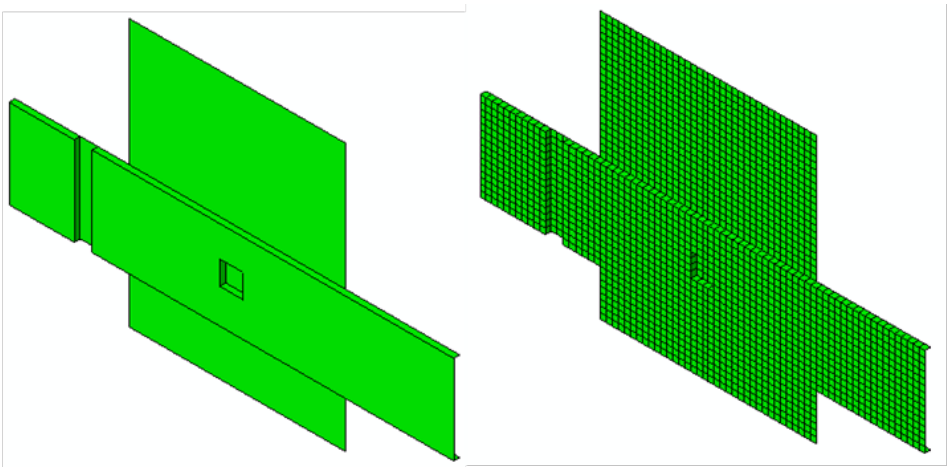

Figure D2. Rigid Wall Geometry (left) and Mesh (right)

Table D3. Properties of Rigid Wall in Pre-test and Post-test FE Models

Property	Pre-test FE Model	Post-test FE Model
Type of Part	Rigid	Rigid
Symmetry	Yes	No
Number of Elements	R3D4: 1,201 RNODE3D: 9	R3D4: 2,378 RNODE3D: 12
Approximate Mesh Size	4 inches	4 inches

D3. Rigid Skid

The trucks of the tank car surrogate were removed prior to the test. The bolster of the tank car rested directly upon a set of skids that rested upon steel plates (see Figure 5). The skids were designed to inhibit the rigid-body roll of the tank car during impact and following rebound from the rigid wall during a test. The skid geometry and mesh are shown in Figure D3. A summary of the skid mesh properties is provided in Table D4. The skid's geometry and mesh were the same in all the pre-test and post-test FE models, but only one skid (east) was included in the pre-test FE model due to symmetry (Figure 39).

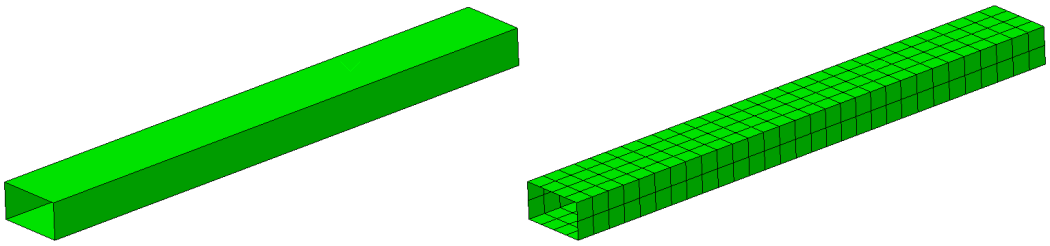

Figure D3. Skid Geometry (left) and Mesh (right)

Table D4. Properties of Skid in Pre-test and Post-test FE Models

Property	Pre-test FE Model	Post-test FE Model
Type of Part	Rigid	Rigid
Number of Elements	R3D4: 368 MASS: 2 RNODE3D: 1	R3D4: 368 MASS: 2 RNODE3D: 1
Approximate Mesh Size	6 inches	6 inches

The rigid skids used in the test weighed approximately 3,500 pounds each. This mass was included in the model through the use of a point mass at the rigid body reference node of each skid. Because the FE model is a simplified representation of the tank, it does not include such geometric details as the draft sills, draft gear, or couplers, as these features are not expected to play a significant role in the puncture response for an impact near the center of the shell. The masses of these components are included as a second point mass on the skid. For this surrogate, the additional structure at each end of the tank car was assumed to have a weight of approximately 6,100 pounds. However, the test surrogate itself did not include several tank car

components, such as the draft gear or coupler. Therefore, the additional point masses on each skid representing these components were unnecessary. However, these additional point masses were added to both the pre-test and post-test FE models without adjustment. The masses on each skid are summarized in Table D5.

Table D5. Point Masses Added to Skid Reference Point in Models

Component	Approximate Weight (lbf)
Skid	3,500
Additional point mass	6,100

D5. Inner Tank – Shell Elements

The inner tank was modeled using two different techniques. In the impact zone, the inner tank was modeled using solid "brick" elements. This part is described in Appendix D6. Away from the impact zone, the inner tank was modeled using shell elements. The shell portion of the tank is described in this section.

Figure D4 shows the shell portion of the inner tank from the post-test FE model. A summary of the inner tank shell mesh properties is provided in Table D6. Note that the pre-test FE model used a symmetry plane that is not shown in Figure D4 (refer to Figure 39). This part was globally meshed using quadrilateral reduced integration (S4R) elements and a small number of triangular shell elements (S3R). At the edges of the impact zone, the mesh was refined (0.1 inch) to provide a transition between the fine solid mesh of the impact zone and the coarse shell mesh of the distant tank. A technique referred to as shell-to-solid coupling (SSC) was used to attach the solid patch to the edges of the shell mesh on the tank. The shell part of the tank represents the midplane surface of the tank.

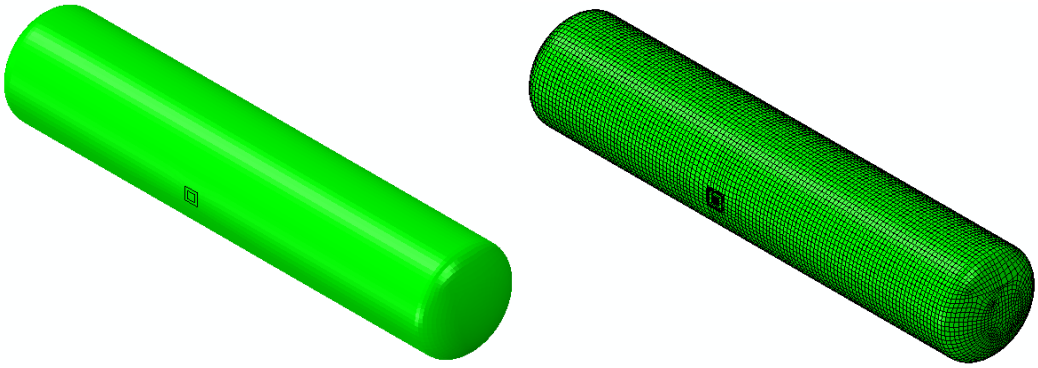

Figure D4. Post-test FE Model Inner Tank Shell Geometry (left) and Mesh (right)

Table D6. Properties of Inner Tank Shell Mesh in FE Models

Property	Pre-test FE Model	Post-test FE Model
Type of Part	Deformable, Shell	Deformable, Shell
Number of Elements	S4R: 17,307 S3R: 186	S4R: 36,465 S3R: 40
Approximate Mesh Size	0.05 to 4 inches	0.05 to 4 inches
Material	T304 Stainless Steel	T304 Stainless Steel
Shell Thickness	1/4 inch	1/4 inch
Head Thickness	1/4 inch	1/4 inch
Approximate Part Weight	5,830 lbf	12,810 lbf

D6. Inner Tank – Solid Elements

The inner tank was modeled using two different techniques. Away from the impact zone, the inner tank was modeled using shell elements. This part is described in Appendix D5. In the impact zone, the inner tank was modeled using solid "brick" elements. This part is described in this section.

Figure D5 shows the solid portion of the tank. A summary of the inner tank solid mesh properties is provided in Table D7.

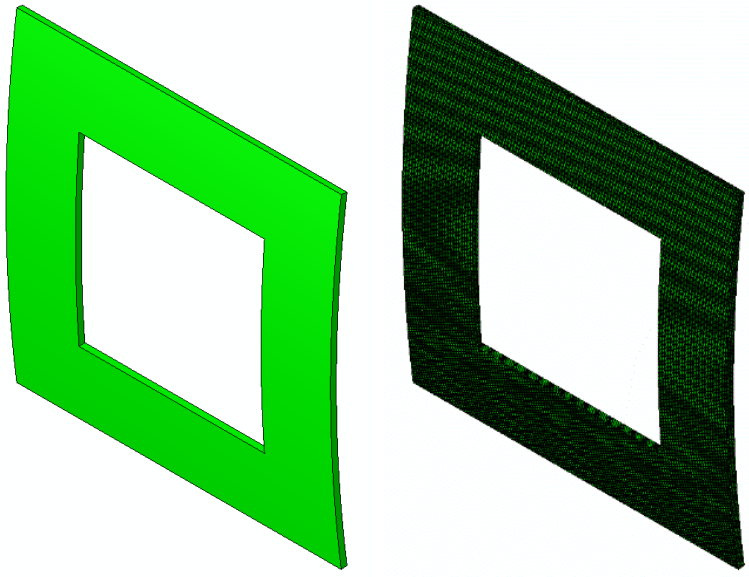

Figure D5. Inner Tank Solid Geometry (left) and Mesh (right)

Table D7. Properties of Inner Tank Solid Mesh in FE Models

Property	Pre-test FE Model	Post-test FE Model
Type of part	Deformable, solid	Deformable, solid
Number of elements	C3D8R: 132,000	C3D8R: 264,000
Approximate mesh size	0.05 inch	0.05 inch
Material	T304 stainless steel	T304 stainless steel
Thickness	1/4 inch	1/4 inch
Approximate part weight	5 lbf	9 lbf

Note that because of the fine mesh, the right-hand image appears to show the mesh as a solid-colored part. Also note that the pre-test model used a symmetry plane that is not shown in Figure D5 (refer to Figure 39). The part was meshed using five elements through the thickness of the part. This corresponded to a global mesh seed of 0.05 inches. The mesh consisted of 8-noded reduced integration hexahedral "brick" (C3D8R) elements. The solid tank mesh was attached to the shell tank mesh along the outer and inner edges using SSC. The elements along the inner and outer edges of the solid tank that were involved in the SSC were given the same elastic and plastic material responses as the rest of the solid patch, but they did not have failure behaviors defined. This was done to prevent elements involved in the SSC from being removed from the FE model, as that could cause the coupling itself to fail.

D7. Outer Tank – Shell Elements

The outer tank was modeled using two different techniques. In the impact zone, the outer tank was modeled using solid "brick" elements. This part is described in Appendix D8. Away from the impact zone, the outer tank was modeled using shell elements. The shell portion of the tank is described in this section.

Figure D6 shows the shell portion of the outer tank from the post-test model. A summary of the outer tank shell mesh properties is provided in Table D8.

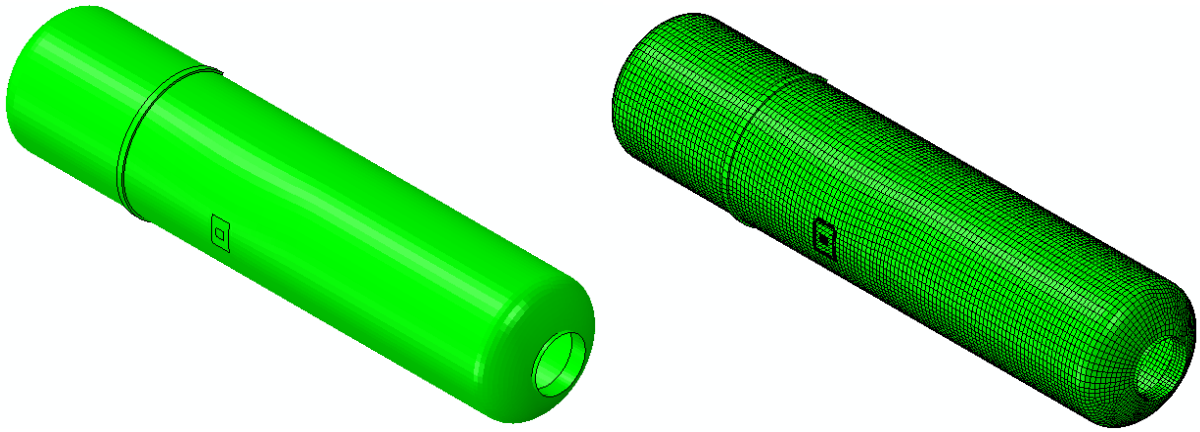

Figure D6. Outer Tank Shell Geometry (left) and Mesh (right)

Table D8. Properties of Outer Tank Shell Mesh in FE Models

Property	Pre-test FE Model	Post-test FE Model
Type of part	Deformable, shell	Deformable, shell
Number of elements	S4R: 17,307 S3R: 186	S4R: 36,465 S3R: 40
Approximate mesh size	0.081 to 4 inches	0.081 to 4 inches
Material	TC-128B carbon steel	TC-128B carbon steel
Shell thickness	0.5625 inch	0.5625 inch
Head thickness	0.5625 inch	0.5625 inch
Approximate part weight	15,640 lbf	33,906 lbf

The part includes the stiffener channel and structure connecting the outer and inner tanks. Note that the pre-test FE model used a symmetry plane that is not shown in Figure D6 (refer to Figure 39). This part was globally meshed using quadrilateral reduced integration (S4R) elements and a small number of triangular shell elements (S3R). At the edges of the impact zone, the mesh was refined (0.162 inches) to provide a transition between the fine solid mesh of the impact zone, and the coarse shell mesh of the distant tank. The shell part of the tank represents the midplane surface of the tank.

D8. Outer Tank – Solid Elements

The outer tank was modeled using two different techniques. Away from the impact zone, the outer tank was modeled using shell elements. This part is described in Appendix D7. In the impact zone, the outer tank was modeled using solid "brick" elements. This part is described in this section.

Figure D7 shows the solid portion of the outer tank. A summary of the outer tank solid mesh properties is provided in Table D9. Note that because of the fine mesh, the right-hand image appears to show the mesh as a solid-colored part. Also note that the pre-test model used a symmetry plane which is not shown in Figure D7 (refer to Figure 39). The outer tank solid patch was meshed using seven elements through the thickness. This corresponded to a global mesh

seed of 0.081 inch. The solid portion of the tank was meshed using C3D8R elements. The solid tank mesh was attached to the shell tank mesh along the outer and inner edges using SSC. The elements along the inner and outer edges of the solid tank that were involved in the SSC were given the same elastic and plastic material responses as the rest of the solid patch, but they did not have failure behaviors defined. This was done to prevent elements involved in the SSC from being removed from the model, as that could cause the coupling itself to fail.

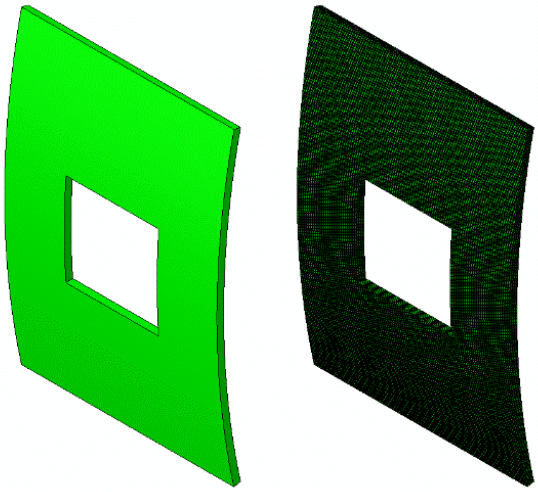

Figure D7. Outer Tank Solid Geometry (left) and Mesh (right)

Table D9. Properties of Outer Tank Solid Mesh in FE Models

Property	Pre-test FE Model	Post-test FE Model
Type of part	Deformable, Solid	Deformable, Solid
Number of elements	C3D8R: 217,224	C3D8R: 434,448
Approximate mesh size	0.081 inch	0.081 inch
Material	TC-128B Carbon Steel	TC-128B Carbon Steel
Thickness	0.5625 inch	0.5625 inch
Approximate part weight	32 lbf	64 lbf

D9. Membrane

The FE model of the DOT-113 tank car surrogate included a deformable membrane part that was non-physical and represented the extents of the lading. The liquid and gas phases of the contents of the tank were modeled within the tank using a hydraulic and a pneumatic cavity, respectively. The material properties used to describe the behavior of the air are described in Section 5.2.4, and the material properties used to describe the water are described in Section 5.2.5.

Hydraulic and pneumatic cavity modeling techniques are simplified approaches to capturing the inertial and pressure effects of the liquid lading and the pressure response of the air in the outage. For either cavity, the geometry was used to define the volume of the cavity within the model that enclosed the limits of the fluid. For the hydraulic cavity, the water in the tank was bounded by

the shell of the tank itself and by its free surface in contact with the outage. For the pneumatic cavity, the outage was bounded by the interior of the tank and the free surface of the water. Thus, the membrane part's geometry represented the interior of the tank with a horizontal plane to represent the boundary between the air and the water.

For each cavity defined within the membrane, the solver calculated the uniform pressure and temperature in each time increment during the impact. As the tank deformed from the impact, the hydraulic cavity changed shape. Because the water was highly incompressible, the indentation of the tank reduced the volume of the air in the outage. The pneumatic cavity modeled the air as an ideal gas with user-defined initial pressure and temperature and a universal gas constant. Therefore, as the volume of the tank was reduced, the volume of the pneumatic cavity decreased, and the pressure within the pneumatic cavity increased. The temperature of the air within the cavity remained constant (i.e., isothermal assumption) throughout the simulation.

Because the pneumatic and hydraulic cavities only calculated the uniform pressures and temperatures within the cavity, and not the fluid pressure or temperature at discretized points throughout the volume of the lading, the cavity techniques reduced the simulation runtime compared to techniques that represented the fluid explicitly as a mesh or collection of particles. However, the uniform behavior simplification may not be well suited to all conditions, such as an impact that features an extremely small outage or a significant variation in pressure over the volume of either the air or liquid.

Both the hydraulic and pneumatic cavity models required a geometric surface to be defined within the model that defined the boundary of each cavity. Each cavity also required a reference point defined within the volume of the cavity. This reference point was used to define the interior of the cavity, and it was also the point at which initial temperatures and pressures are defined for each cavity. As discussed in Appendix D5, the shell geometry of the tank represented the mid-plane geometry of the tank. If this geometry were used to define the outer surfaces of the pneumatic cavity, the cavity volume would be too large, since the volume enclosed was based on the mid-plane surface and not on the inner surface of the tank. The membrane part was defined to correspond to the inner surface of the tank's geometry.

The membrane part was meshed using membrane elements for both the portion of the part that is in contact with the interior of the tank and the portion of the part that defined the interface between the water and the air within the tank. The membrane elements representing the inner surface of the tank were attached to the mid-plane surface of the inner tank using a tied constraint. The membrane mesh was refined in the region of the impact zone because the inner tank mesh was also refined in this region. The geometry and mesh of the membrane part are shown in Figure D8 from the pre-test FE model which included a symmetry plane to view the interior surfaces. Note that the post-test FE model did not include a symmetry plane (refer to Figure D4).

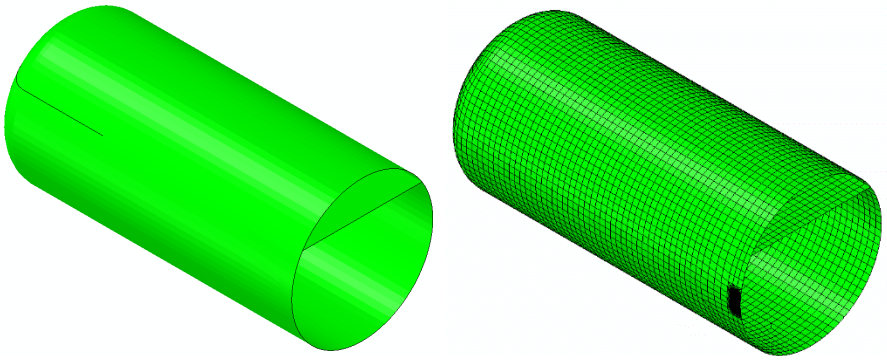

Figure D8. Membrane Geometry (left) and Mesh (right)

Because the portion of the membrane defined to divide the water and air boundary represents geometry that is not physically present within the tank, a membrane element representation was chosen to be as thin and flexible as practical within the model without causing the model to terminate due to excessively distorted membrane elements. With these constraints, a thickness of 0.05 inches was chosen for the membrane.

The height of the horizontal plane (i.e., measured from the 12 o'clock position within the inner tank, as shown in Figure D9) was adjusted in a series of incremental updates to determine the outage height corresponding to an outage of 17.6 percent. For the desired test outage of 17.6 percent, the model used an outage height of approximately 24.87 inches below the top midplane of the inner tank shell.

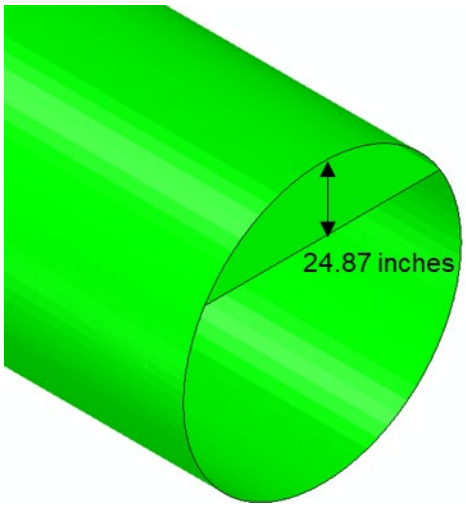

Figure D9. Reference Measurement for Outage Height within Membrane

The membrane part was also used to represent the mass of the water lading within the tank. This was done through the use of a "nonstructural mass" feature in Abaqus. The total mass of the water was calculated based on the density of water and the volume enclosed by the membrane at the desired outage level. This mass was then distributed uniformly through the membrane, including the horizontal portion of the membrane dividing the water and air phases.

The properties of the membrane part of the pre-test and post-test FE models are summarized in Table D10.

Table D10. Properties of Membrane Mesh in FE Model

Property	Pre-test FE Model	Post-test FE Model
Type of Part	Deformable, Membrane	Deformable, Membrane
Number of Elements	M3D4R: 17,097 M3D3: 108	M3D4R: 35,509 M3D3: 210
Membrane Thickness	0.05 inch	0.05 inch
Material	Membrane	Membrane
Approximate Mesh Size	4 inches	4 inches
Approximate Part Weight	66,488 lbf	132,980 lbf

D10. Rigid Ground

For both the pre-test and post-test FE models, the rigid ground was modeled with all six degrees-of-freedom (DOF) fixed. The rigid ground geometry is shown in Figure D10 (left) and the rigid ground mesh is shown in Figure D10 (right). A summary of the ground mesh properties is provided in Table D11. The same ground mesh and geometry was used in all FE models.

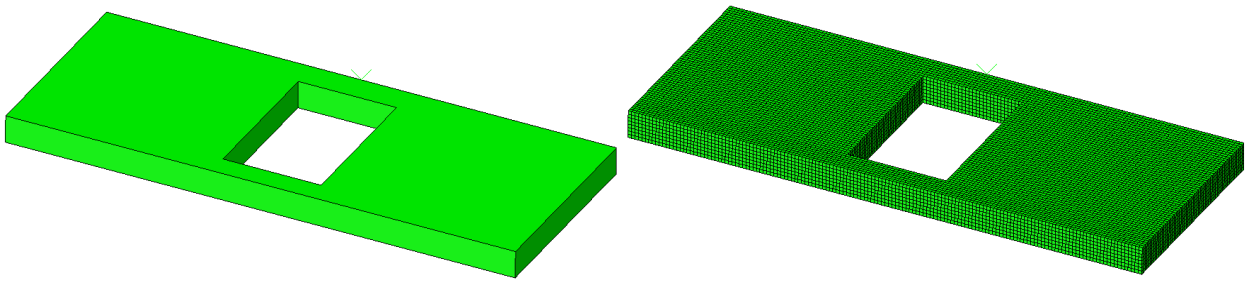

Figure D10. Rigid Ground Geometry (left) and Mesh (right)

The properties of the rigid ground mesh are summarized in Table D11.

Table D11. Properties of Ground Meshes in FE Models

Property	Pre-test FE Model	Post-test FE Model
Type of part	Rigid Body	Rigid Body
Number of elements	R3D4: 846 RNODE3D: 4	R3D4: 1,664 RNODE3D: 6
Approximate mesh size	1 1/2 inches	1 1/2 inches

Appendix E.
FE Modeling Techniques

This appendix describes the FE modeling techniques that were used in both the pre-test and post-test FE models.

E1. Rigid Impactor Boundary Conditions

The rigid impactor was constrained against all motion except for longitudinal displacement. The pre-test models were run at various speeds, and the post-test FE model was run at the measured test speed of 17.3 mph.

E2. Rigid Wall Boundary Conditions

The rigid wall was constrained against motion in all six DOF.

E3. Rigid Ground Boundary Conditions

The ground was constrained in all six DOF.

E4. Inner Tank-to-Membrane Tie

The portion of the inner tank modeled using shell elements was tied to the membrane representing the interior surface of the tank using a tied constraint. Although the size of the meshes used on both parts were similar, because they were not identical, a position tolerance of 1 inch was used.

E5. Outer Tank-to-Skid Coupling

A beam-type multi-point constraint (MPC) was used to attach the region of the end of the tank car approximating the stub sill to the skid on each end of the tank. The rigid body reference node on the skid at each end of the tank was used as the control point of the MPC. The tank car nodes subject to the constraint included nodes on the bottom of the outer tank and nodes on the bolster where the bolster would have interfaced to the stub sill. The MPC constraints are shown in Figure E1.

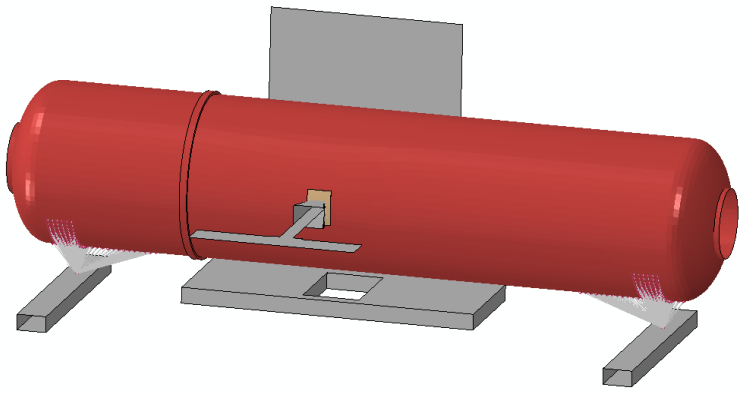

Figure E1. MPC Between Ends of Tank Car and Skids

Additionally, a “Cartesian” type of connector was used to constrain the motion of the skid in both the vertical and the longitudinal (i.e., direction of impactor travel) directions. A nonlinear damper was defined between the skid and ground to constrain longitudinal motion. This damper defined the longitudinal resistance force as a function of skid speed, such that the skid had to overcome an initially high force when it was moving slowly. Once this initial peak was overcome, the resistance offered to skid motion diminished as the skid moved more quickly. This simplified model was intended to approximate the effect of static friction being overcome as the skid initially begins its motion, followed by a reduced resistance from kinetic friction. The longitudinal relationship used in the Cartesian connector is shown in Table E1 and plotted in Figure E2.

Table E1. Longitudinal Skid Behavior

Reaction Force lbf	Skid Velocity in/s
-100	-10
-38,000	-1
0	0
38,000	1
100	10

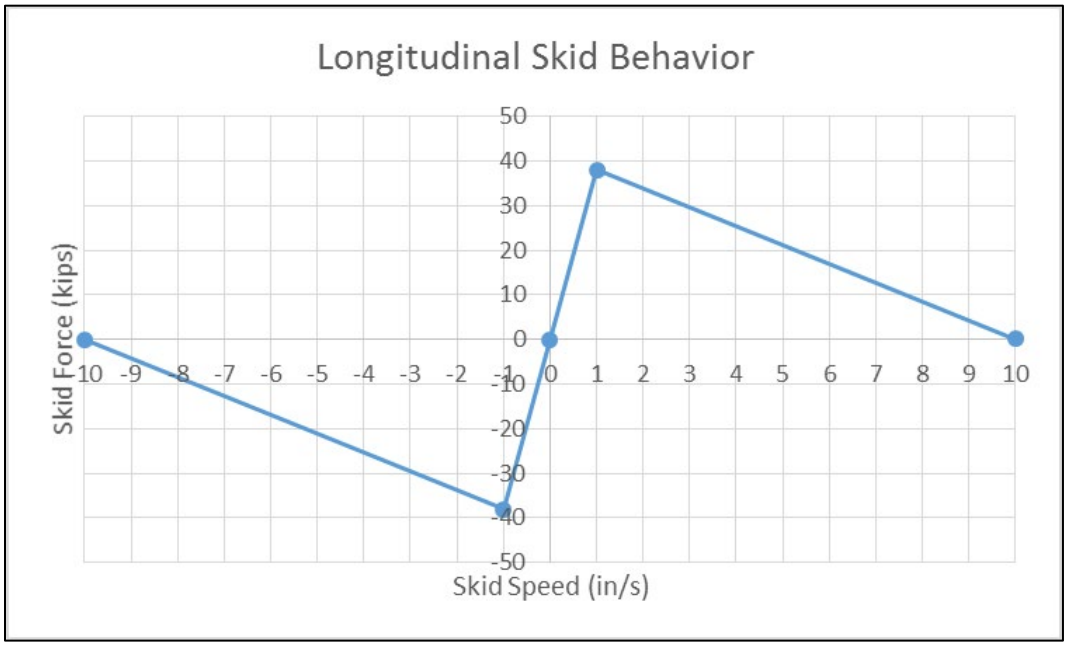

Figure E2. Longitudinal Skid Behavior

In the vertical direction, the skid used a “Stop” behavior assigned to a connector element between the skid and the ground to limit its range of motion. In the vertical downward direction, the reference point of the skid was prevented from having any displacement. In the upward direction, a limit of 100 inches was used. This number is arbitrary, but it was chosen to be larger than any anticipated vertical motion of the skid. These two vertical stops approximated the behavior of the skid on the ground during the physical test, when the skid was prevented from moving downward through contact with the ground but free to lift upward if sufficient lifting forces overcame the weight resting on it.

E6. Inner and Outer Tanks SSC

SSC constraints were used on the inner tank and the outer tank to attach each patch of solid elements in the vicinity of the impact zone to the rest of the shell-meshed tank. This type of constraint is necessary to ensure a smooth transition from solid elements that possess only translational DOF to shell elements that possess translational and rotational DOF. The shell part of each tank featured a refined mesh in the vicinity of the SSC constraint. Since the shell part corresponded to the mid-plane thickness of the tank, the shell part was aligned with the mid-plane of the solid patch. The interface between the solid elements and the shell elements is shown in Figure E3 for the outer tank and Figure E4 for the inner tank. Note that these images show the SSC region from the post-test FE model. The pre-test FE model used a symmetry plane midway across the solid patches. The pre-test FE models used the same technique, but the dimensions of the solid patch widths are halved.

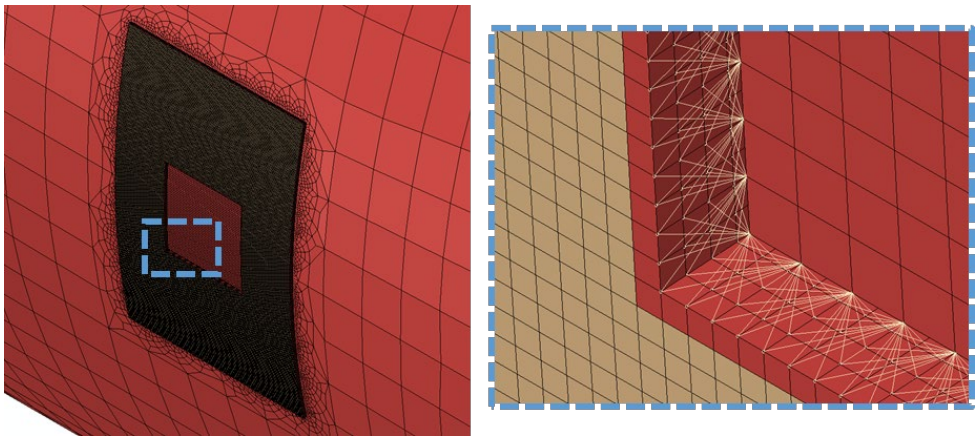

Figure E3. SSC Region on Outer Tank (left) and Detailed View of Corner (right)

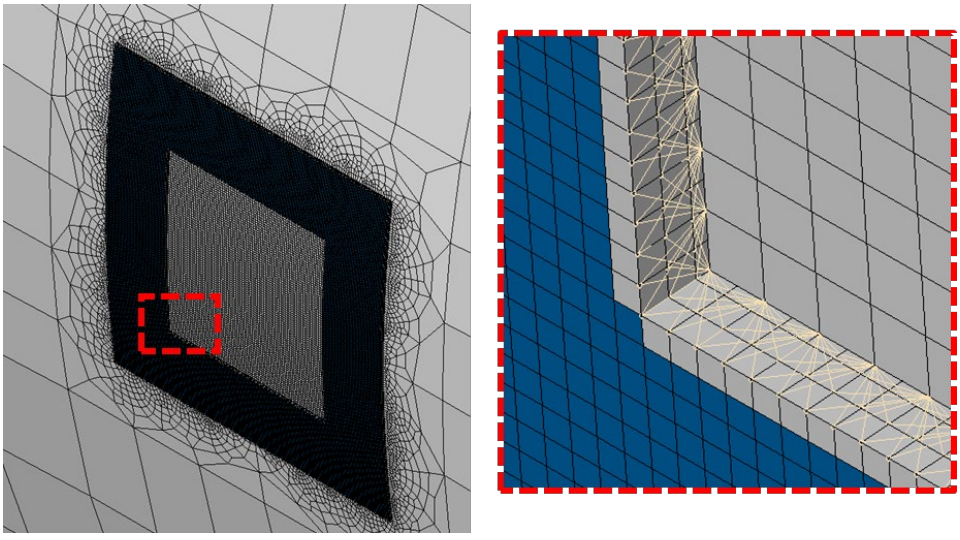

Figure E4. SSC Region on Inner Tank (left) and Detailed View of Corner (right)

E7. Pressures and Temperatures

The tested DOT-113 surrogate tank car had an initial pressure above atmospheric pressure within the inner tank and atmospheric pressure in the annular space between the tanks. The pre-test and post-test FE models attempted to replicate these pressure conditions as initial conditions on the model. Initial values for the lading temperature were defined in the FE models.

The water and air outage within the inner tank were each given an initial pressure of 50 psig. As the surfaces defining the boundaries of the water and gas phases deformed, the pressure was free to change in response. The hydraulic cavity and pneumatic cavity definitions also require the definition of the ambient pressure outside of the cavity. A value of 12.3 psi, corresponding to atmospheric pressure [31] at Pueblo, CO's, altitude of approximately 4,700 feet,[12] was used for ambient pressure. Therefore, the air within the tank was initially modeled at an absolute pressure of 62.3 psi.

The fluid cavity approach of modeling liquids and gases required an initial temperature to be defined for each cavity. Based on average historical climate data around the planned date of the DOT-113 tank car test, a temperature of 70 °F was chosen for the pre-test FE models.[13] The post-test models also used 70 °F for the lading temperature, a temperature that is consistent with the measured test-day temperature of 79 °F. The temperature was held constant for the entire duration of the pre-test and post-test simulations while the pressure and volume of the cavities were allowed to change.

E8. Springs (Displacement Transducers)

Soft springs were added to the post-test FE model to represent the string potentiometers within the inner tank and the laser transducers outside the tank car. This addition made it easier to post-process the displacement measurements from the FE model for comparison with test measurements. The springs inside the inner tank measured the internal compression in the transverse direction of the inner tank at positions corresponding to the string potentiometers spaced 2 feet apart and designated TD1Y, TD2Y, TD3Y, TD4Y, and TD5Y as well as the internal extension in the vertical direction at TD3Z.

The springs outside the tank measured external compression of the tank at positions corresponding to the laser transducers designated BD1Y, BD2Y, BD4Y, and BD5Y. A spring representing BD3Y was not implemented because BD3Y was directed at the wall and could be compared with impactor travel, an output already requested in the FE models. While laser transducers were also positioned on the wall during the test to measure separation between the wall and tank, no analogous measurements were taken from the surrogate tank car model because it remained in contact with the wall over the duration of the simulations.

Figure E5 shows three views of the FE model to describe the relative locations of the springs. The springs in the model were elastic and had an axial stiffness of 1×10^{-6} lbf/in.

[12] United States Geologic Survey. *GNIS Detail – Pueblo Memorial Airport*. USGS Geographic Names Information System (GNIS).

[13] U.S. Climate Data. Climate Pueblo – Colorado and Weather Averages Pueblo. Daily Normals Pueblo, CO, November.

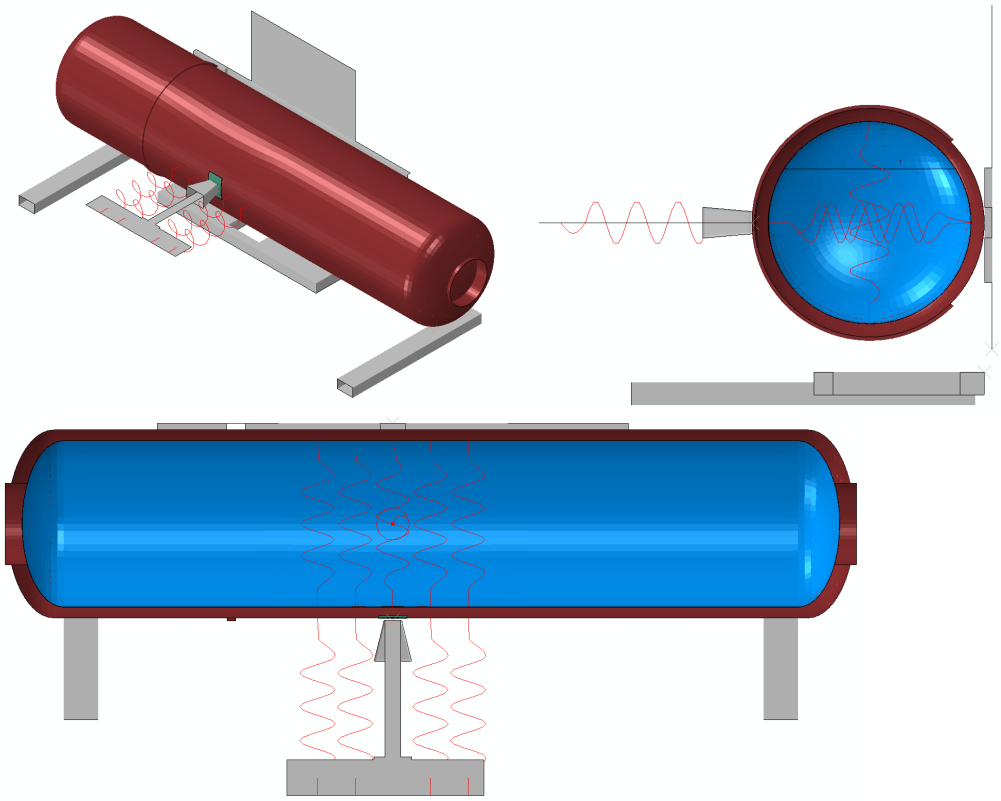

Figure E5. Post-test FE Model Isometric (top left), Side Section (top right), and Top Section (bottom) Views Showing Springs Representing Displacement Transducers

E9. Mass Scaling

Variable mass scaling was used in the FE models. Because of the need for a refined mesh of solid elements in the impact zone on both the inner and outer tanks, the puncture-capable models featured a large number of very small elements. Variable mass scaling was employed in the FE models to decrease the runtime without decreasing either the span or the resolution of the refined meshes. Variable mass scaling is a technique in which the user sets a target time increment for a set of elements within the model—up to and including all elements within the model—and the Abaqus solver increases the mass of any element required to bring the minimum time step up to the user-defined minimum. "Variable" refers to the software's ability to increase the mass of each element by a different amount based on the material and geometry of each element. While mass scaling is an efficient way of reducing runtime without re-meshing a model, care must be exercised when using this technique with highly dynamic simulations. If an overly aggressive mass scaling is applied, the amount of artificial mass added to the model in the refined mesh area can significantly affect both the overall dynamic response as well as the puncture behavior of the model.

The tensile coupon models of TC-128B and T304 steels used a variable mass scaling with a target time increment of 1×10^{-6} seconds. The puncture-capable FE models used a variable mass scaling to achieve a target time increment of 9×10^{-7} seconds over the entire model. The mass scaling factors were re-calculated for the full-scale puncture models every 2,000 increments, i.e., approximately every 1.8 milliseconds.

E10. Contact

A general contact definition was used in all models. The global contact used frictionless contact, except for metal-on-metal contact. A coefficient of friction of 0.3 was defined for regions of metal-on-metal contact. Contact exclusions were defined between the shell tank and the solid tank patch for both the inner and outer tanks. A contact thickness reduction was used on the membrane mesh in the vicinity of the impact zone.

Appendix F.
Material Behaviors in FE Models

F1. Introduction

Pre-test and post-test FE models used TC-128B carbon steel and T304 stainless steel material inputs that were calibrated from ASTM-E8 tensile test results. During construction of the DOT-113 surrogate tank car, 2-inch gage length, 1/2-inch diameter smooth round bar (SRB) coupons were machined from the outer tank and 2-inch gage length, 1/2-inch wide, and 1/4-inch thick flat dogbone (DB) coupons were cut from the inner tank. Eight TC-128B SRB coupons and three T304 DB coupons were tested to failure. The process used to create the material inputs for the FE model is described in this appendix.

F2. Simulation of Coupon Tests

FE simulations of TC-128B carbon steel and T304 stainless steel ASTM-E8 uniaxial tensile coupon tests were used to calibrate the material definitions in Abaqus/Explicit for the full-scale models of the DOT-113 surrogate side impact test. First, the plastic true stress-plastic equivalent strain (PEEQ) characteristic was specified. Then, the damage initiation envelope was calculated. Finally, a reasonable damage progression was empirically determined.

As the material responses developed using coupon models were planned for implementation in the full-scale DOT-113 surrogate model, modeling techniques for performing the coupon simulations were deliberately chosen to be similar to the modeling techniques planned for side impact analyses of the DOT-113 tank car. The same solver (Abaqus/Explicit), element types (C3D8R), and mesh sizes (0.081-inch outer tank; 0.05-inch inner tank) were chosen for the coupon models and for the DOT-113 surrogate side impact models. This was done to minimize the uncertainty associated with calibrating a material response using one set of modeling techniques but a different set of techniques to model puncture in the full-scale tank car surrogate impact simulation. If the tank car model was run using a different solver or different mesh density, the material behaviors would need to be recalibrated using coupon simulations that used similar solvers and mesh density.

For all tensile coupon simulations, a soft (1×10^{-6} lbf/in) discrete spring was included in the model to represent an extensometer attached to the ends of the gage. This spring was a representation of an extensometer in the model and simplified the process of requesting the change-in-length of the gage section from the model.

The SRB coupon model used for the TC-128B calibration is shown in Figure F1. The TC-128B coupon geometry had a 2-inch gage length and 1/2-inch diameter. Three planes of symmetry were used to reduce the number of elements in the model. The FE model used a 0.081-inch C3D8R mesh and three planes of symmetry.

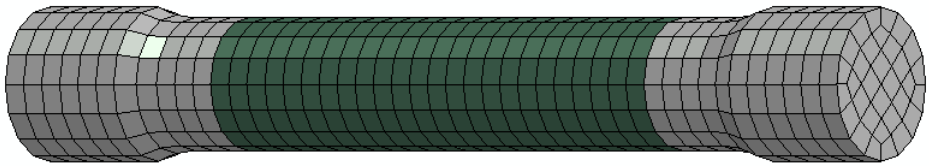

Figure F1. FE Model of TC-128B Carbon Steel Smooth Round Bar Tensile Coupon with Gage Section in Green; Mirrored Across Symmetry Planes

The DB tensile coupon FE model used for the T304 stainless steel calibration is shown in Figure F2. The DB coupon measurements were 2-inch gage length, 1/2-inch width, and 1/4-inch thickness. The FE model used a 0.05-inch C3D8R mesh and three planes of symmetry.

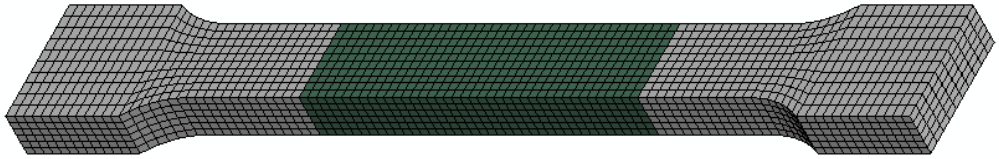

Figure F2. FE Model of T304 Stainless Steel DB Tensile Coupon with Gage Section in Green; Mirrored Across Symmetry Planes

In the full-scale puncture model of the DOT-113 tank car, the 9/16-inch-thick TC-128B carbon steel outer tank shell was meshed with seven elements across the thickness corresponding to a mesh size of approximately 0.081 inch (refer to Appendix D8). The 1/4-inch-thick T304 stainless steel inner tank shell was meshed with five elements across the thickness corresponding to a mesh size of 0.05 inch (refer to Appendix D6).

F2.1 Plastic Hardening

Abaqus requires metal plasticity to be defined in terms of true stress and PEEQ. The plastic behavior of each steel was input to the Abaqus model as isotropic hardening using a discrete number of data points. True stress and PEEQ can be calculated from nominal stress-strain tensile coupon data according to Equation F1.

Equation F1. True Stress-strain Transformation

$$\sigma_{true} = \sigma_{nom} \cdot (1 + \varepsilon_{nom})$$

$$\varepsilon^{pl} = \ln(1 + \varepsilon_{nom}) - \frac{\sigma_t}{E}$$

σ_{nom} nominal (engineering) stress

ε_{nom} nominal (engineering) strain

σ_{true} true stress

ε^{pl} plastic equivalent strain

Because necking dominates the nominal stress-strain response of the tensile coupon characteristic after the maximum force is achieved, the true stress-PEEQ relationship was extrapolated for strains beyond the strain at maximum force using the inverse method. The inverse method involves iteratively adjusting the true stress-PEEQ relationship until agreement is achieved between the tensile coupon simulation and the test results. Two methods were used to

describe the true stress-PEEQ relationships for TC-128B carbon steel and T304 stainless steel in this study, respectively.

Paredes et al. (2018) applied a Mixed Swift-Voce Law hardening expression to extrapolate true stress at high strains for TC-128B. The Mixed Swift-Voce Law is a conjunction of the Swift (power) Law [32] and the Voce (exponential/saturation) Law [33], both of which describe plastic hardening. The Mixed Swift-Voce Law is a function of PEEQ (ε^{pl}) and is formed by combining the Swift term (σ_t^{Swift}) with the Voce term (σ_t^{Voce}) using a weighting factor (α) as shown in Equation F2.

Equation F2. Swift (Power), Voce (Exponential/Saturation), and Mixed Swift-Voce Laws for Plastic Hardening

$$\sigma_t^{Swift}(\varepsilon^{pl}) = A \cdot (\varepsilon_0 + \varepsilon^{pl})^n$$

$$\sigma_t^{Voce}(\varepsilon^{pl}) = K_0 + Q \cdot \left(1 - e^{-\beta \varepsilon^{pl}}\right)$$

$$\sigma_t^{Mixed} = \alpha \cdot \sigma_t^{Swift} + (1 - \alpha)\sigma_t^{Voce}$$

The Swift-Voce constants are calibrated using the calculated true stress-PEEQ (see Equation F1) from a tensile test and performing a least squares regression fit on the Swift and Voce equations. The Swift and Voce expressions are independently fit on the test data from a PEEQ close to zero to the PEEQ at maximum force because the plastic behavior of the coupon is not dominated by necking for that range of strains. After the constants for the Swift and Voce expressions are independently determined by least-squares regression, an FE model of the uniaxial tensile test is iteratively executed while varying α until the nominal stress-strain output from the model is in agreement with the test results until the UTS is reached.

Linear extrapolation of the true stress-PEEQ strain relationship has been used for side impact puncture models in the past [5] [7] [8] [9] [13]. Recent side impact tests [14] [24] have used a Swift-Voce extrapolation for true-stress at high strains because the post-necking behavior of the coupon was better represented in the tensile coupon FE models. The Swift-Voce extrapolation technique was used for TC-128B carbon steel and T304 stainless steel for the DOT-113 surrogate tank car in the pre- and post-test FE models.

For both the linear extrapolation and the Swift-Voce Law, a single parameter can be varied while iteratively running the coupon simulations to achieve agreement with the test results via the inverse method. The parameter used for the linear extrapolation method is the slope of the extrapolated true stress-PEEQ curve for high PEEQs. The parameter used for the T304 models was the weight factor α that determined the amount of hardening at high strains, i.e., a high value for α resulted in more plastic hardening after necking initiated.

Ductile damage initiation and progression can be used in Abaqus to simulate the failure initiation and propagation experienced in the actual coupon test through element stiffness degradation and deletion. The process of calibrating a damage initiation envelope and then empirically determining a suitable damage progression value is explained in the following section.

F2.2 Bao-Wierzbicki (B-W) Damage Initiation

Figure F3 shows a schematic of the B-W triaxiality (η)-based damage initiation envelope [23] that was used in the TC-128B material failure models. Triaxiality is defined as the ratio of the hydrostatic stress (mean stress) divided by the von Mises stress (equivalent stress) and describes the general stress state of an element. The B-W envelope consists of three regions: I – Ductile Fracture, II – Mixed Fracture, and III – Shear Fracture.

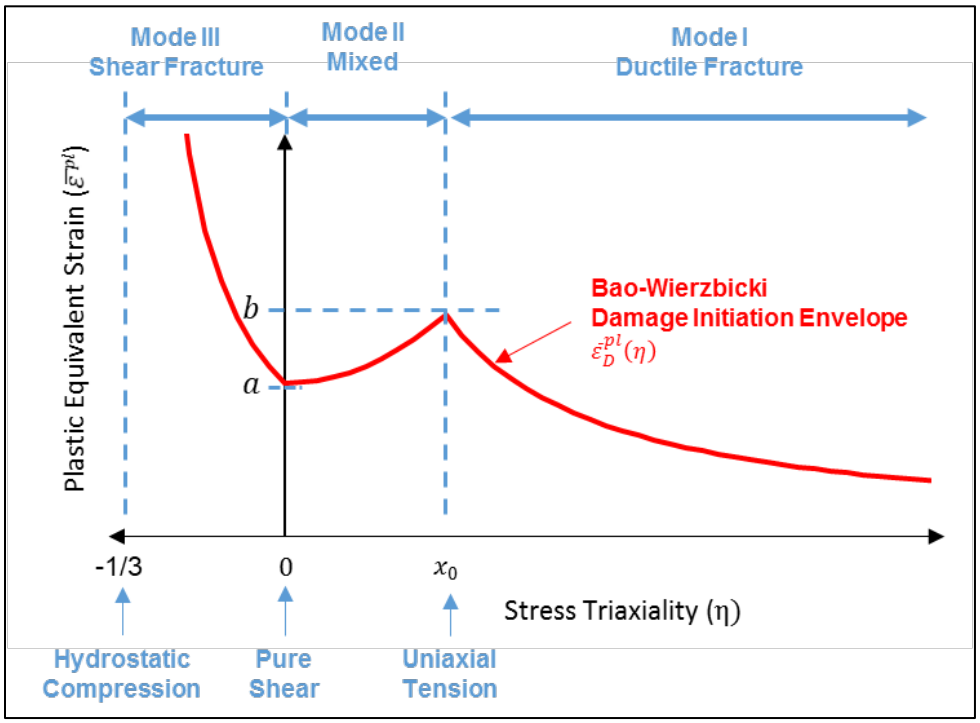

Figure F3. Schematic of B-W Damage Initiation Envelope

When η<0 the element is in a state of compression, and when η>0 the element is in a state of tension. A triaxiality of η=-1/3 corresponds to a stress state of hydrostatic compression and η=0 corresponds to pure shear. The cusp of the B-W envelope is intended to be located at the average triaxiality on the fracture surface of a smooth round bar specimen under uniaxial tension at $\eta=x_0$ and is typically close to a value of 0.4.

Three constants (a, b, x_0) govern the shape of the B-W damage initiation envelope (Equation F3) and are calibrated based on coupon test results. The critical strain to fracture in pure shear (a) corresponds to the PEEQ on the B-W envelope (ε^{pl}) when η=0 (pure shear). The critical strain to fracture in uniaxial tension (b) corresponds to ($\varepsilon_D{}^{pl}$) at the cusp of the B-W envelope when $\eta=x_0$.

Equation F3. B-W Damage Initiation Envelope

$$\varepsilon_D^{pl}(\eta) = \begin{cases} \dfrac{a}{1+3\cdot\eta} & -\dfrac{1}{3} \le \eta \le 0 \\ (b-a)\cdot\left(\dfrac{\eta}{x_0}\right)^2 + a & 0 \le \eta \le x_0 \\ \dfrac{b\cdot x_0}{\eta} & x_0 \le \eta \end{cases}$$

The complete damage initiation envelope can be developed through a series of mechanical tests on 11 unique specimen geometries intended to cover a wide range of stress triaxialities, but a simplified "quick calibration" approach that requires only one uniaxial tensile geometry to estimate the entire failure envelope was developed for industrial use by Lee and Wierzbicki [34] [35]. According to Lee, the quick calibration approach is intended to be within 10 percent agreement with a failure envelope that was developed using the complete set of 11 specimens.

The quick calibration procedure for smooth round bar tensile tests allows the calculation of the B-W envelope constants (*a, b, x_0*) by measuring the initial radius (a_0), final radius (a_f), displacement at maximum force (δ_d), and initial gage length (L_0). For flat (DB) coupons the calculation is performed by measuring initial thickness (t_0) and final thickness (t_f) instead of initial and final radius. As seen in Equation F4, the quick calibration procedure also uses the hardening exponent (n) that is used to describe the plastic hardening behavior of metals by the power law. The hardening exponent is estimated as a function of engineering strain at maximum force.

Equation F4. Quick Calibration Procedure for Smooth Round Bar (left) and Flat DB (right) Uniaxial Tensile Coupons

Smooth Round Bar	**Flat (Dogbone) Coupon**
$n = \ln\left(1+\dfrac{\delta_d}{L_0}\right)$	$n = \ln\left(1+\dfrac{\delta_d}{L_0}\right)$
$b = 2\cdot\ln\dfrac{a_o}{a_f}$	$b = \dfrac{2}{\sqrt{3}}\cdot\ln\dfrac{t_o}{t_f} + \dfrac{2\cdot n}{\sqrt{3}}\cdot\left(\sqrt{3}-1\right)$
$x_0 = \dfrac{1}{3} + \dfrac{0.22}{b}\cdot(b-n)^{1.8}$	$x_0 = \dfrac{1}{\sqrt{3}} - \dfrac{2\cdot n}{3\cdot b}\cdot\left(\sqrt{3}-1\right)$
$a = b\cdot\left(\dfrac{\sqrt{3}}{2}\right)^{1/n}$	$a = b\cdot\left(\dfrac{\sqrt{3}}{2}\right)^{1/n}$

For ductile metals in Abaqus, the damage threshold is reached when the ductile criterion (DUCTCRT) reaches a value of 1. The DUCTCRT is calculated by integrating the change in PEEQ divided by the PEEQ where damage initiates as a function of triaxiality (i.e., the B-W envelope) according to Equation F5.

Equation F5. Calculation of the DUCTCRT in Abaqus

$$DUCTCRT = \int \frac{d\varepsilon^{pl}}{\varepsilon_D^{pl}(\eta)}$$

After DUCTCRT reaches a value of 1, the stiffness of the element is degraded according to the damage progression in the material definition. In this report, exponential-displacement-based damage progression values are calibrated for each material, while previous puncture simulations used linear energy-based damage progressions [7] [8] [13].

F3. TC-128B Carbon Steel Material Behavior

Nominal stress-strain data was not available for the TC-128B SRB tensile coupons because the extensometer was removed after determining the elastic modulus by the test lab. This meant that Equation F1 could not be directly used to calculate true stress-PEEQ strain. Therefore, a TC-128B material input calibrated for a previous side impact test of a DOT-111 (CPC-1232) tank car [14] was selected since it had similar tensile properties to the TC-128B carbon steel material taken from the DOT-113 surrogate tank car. The plasticity model was calibrated by scaling it iteratively to achieve the desired YS and UTS without damage progression. The calibrated TC-128B material input is shown below in Figure F4 and given in Table F1.

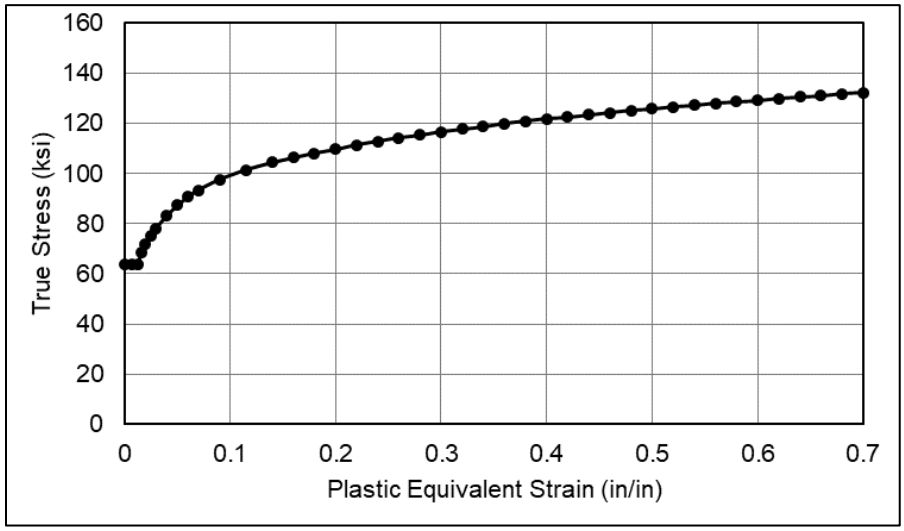

Figure F4. Plasticity Material Input for TC-128B Carbon Steel in DOT-113 Surrogate Outer Tank

Table F1. Plastic Equivalent Strain versus True Stress Input for TC-128B Carbon Steel in DOT-113 Surrogate Outer Tank

PEEQ	True Stress	PEEQ	True Stress	PEEQ	True Stress
in./in.	ksi	in./in.	ksi	in./in.	ksi
0.000E+00	6.396E+01	2.600E-01	1.142E+02	6.400E-01	1.306E+02
6.500E-03	6.396E+01	2.800E-01	1.154E+02	6.600E-01	1.312E+02
1.300E-02	6.396E+01	3.000E-01	1.166E+02	6.800E-01	1.317E+02
1.600E-02	6.838E+01	3.200E-01	1.178E+02	7.000E-01	1.323E+02
2.000E-02	7.176E+01	3.400E-01	1.188E+02	7.200E-01	1.329E+02
2.500E-02	7.514E+01	3.600E-01	1.198E+02	7.400E-01	1.334E+02
3.000E-02	7.826E+01	3.800E-01	1.208E+02	7.600E-01	1.339E+02
4.000E-02	8.346E+01	4.000E-01	1.217E+02	7.800E-01	1.345E+02
5.000E-02	8.736E+01	4.200E-01	1.226E+02	8.000E-01	1.350E+02
6.000E-02	9.074E+01	4.400E-01	1.235E+02	8.200E-01	1.355E+02
7.000E-02	9.334E+01	4.600E-01	1.243E+02	8.400E-01	1.359E+02
9.000E-02	9.750E+01	4.800E-01	1.251E+02	8.600E-01	1.364E+02
1.150E-01	1.014E+02	5.000E-01	1.258E+02	8.800E-01	1.369E+02
1.400E-01	1.045E+02	5.200E-01	1.266E+02	9.000E-01	1.373E+02
1.600E-01	1.063E+02	5.400E-01	1.273E+02	9.200E-01	1.378E+02
1.800E-01	1.081E+02	5.600E-01	1.280E+02	9.400E-01	1.382E+02
2.000E-01	1.098E+02	5.800E-01	1.287E+02	9.600E-01	1.387E+02
2.200E-01	1.114E+02	6.000E-01	1.293E+02	9.800E-01	1.391E+02
2.400E-01	1.128E+02	6.200E-01	1.299E+02	1.000E+00	1.395E+02

Damage initiation and progression behaviors were calibrated to match the average EB-2in in the eight TC-128B SRB tensile coupons. A modified version of Lee and Wierzbicki's "quick calibration" approach [34] [35] was used to develop the pre-test TC-128B damage initiation envelopes since the displacement at maximum force was not measured. For the quick calibration procedure, the average reduction in area (RA) (67.4 percent) was used to estimate the change in SRB radius, and an assumed displacement at maximum force of 0.4 inch was used as a starting point. The FE model was run iteratively and updated by modifying the displacement at maximum force until the EB-2in from the FE model was within 5 percent of the target value (31.4 percent elongation).

The constants for the B-W damage envelope are given in Table F2 and the resulting B-W envelope is plotted in Figure F5.

Table F2. B-W Damage Initiation Envelope Constants for TC-128B Carbon Steel in DOT-113 Surrogate Outer Tank

a	b	x_0
0.44695	1.1172	0.51638

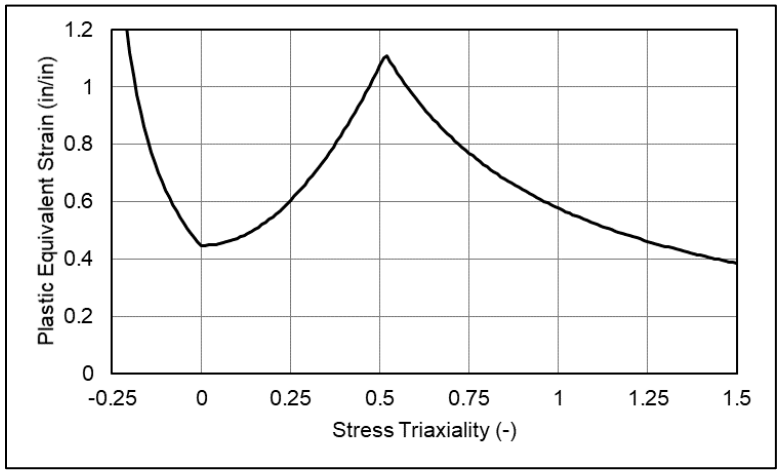

Figure F5. B-W Damage Initiation Envelope for TC-128B Carbon Steel in DOT-113 Surrogate Outer Tank

Figure F6 shows the resulting engineering stress-strain responses from the TC-128B SRB FE model. A displacement-based exponential damage progression was selected at 0.005 in/in^2 with an exponent of -1 because it gave a reasonable nominal stress-strain slope after damage initiation. A comparison of the FE model response with the average tensile properties was shown previously in Figure 41.

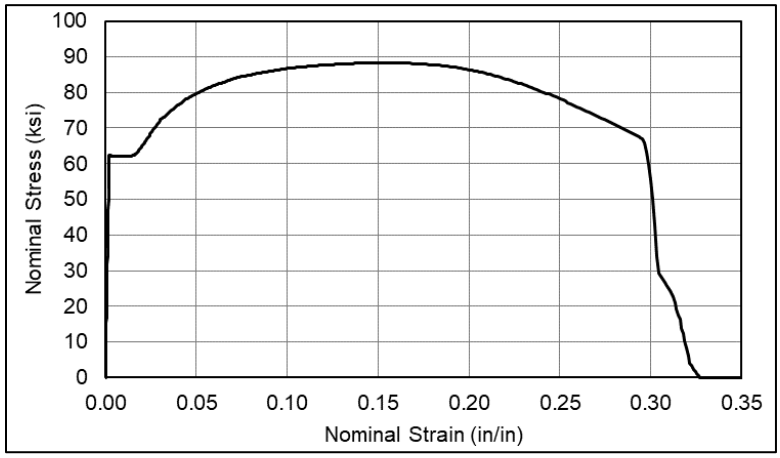

Figure F6. Nominal Stress-Strain Smooth Round Bar Tensile Coupon FE Response for TC-128B Carbon Steel in DOT-113 Surrogate Outer Tank

F4. T304 Stainless Steel Material Behavior

The mechanical properties of the T304 stainless steel composing the inner tank of the DOT-113 surrogate were characterized by tensile testing during the construction of the tank car. The plastic

hardening behavior was calculated on the nominal stress-strain data from Specimen 2 (refer to Appendix B4.2) using Equation F1. Because necking of the tensile coupon dominates the plastic hardening curve after the UTS is reached, a Swift-Voce plastic hardening equation was fit onto the calculated true stress-PEEQ strain curve from the YS to UTS. The Swift-Voce constants that resulted in the best fit were determined by a least-squares regression similar to Paredes et al. (2020). Figure F7 shows the Swift-Voce plastic hardening input for T304 stainless steel and the calculated coupon behaviors using Equation F1.

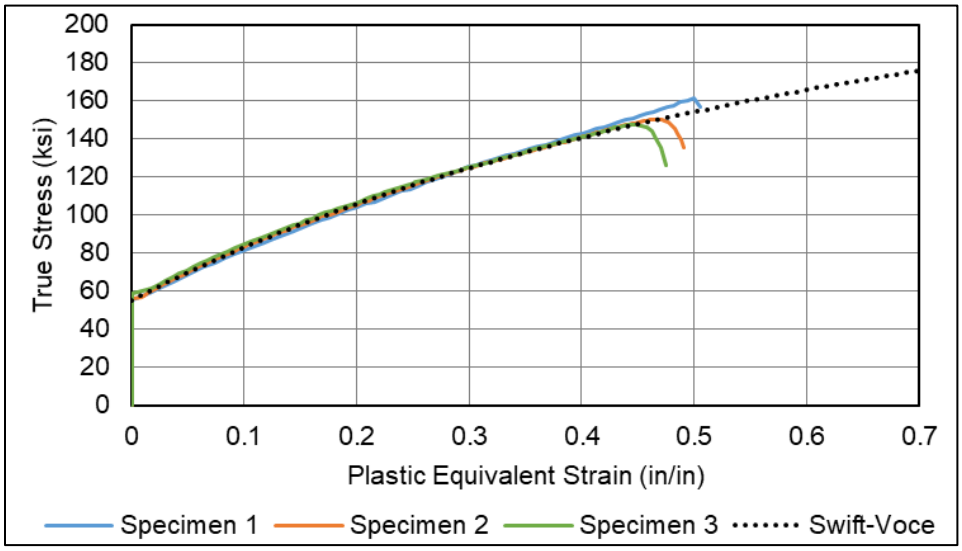

Figure F7. Mixed Swift-Voce Law for True Plastic Stress-PEEQ Strain FE Input for T304 from Pre-Test Models

The constants for the Mixed Swift-Voce expression (i.e., Equation F2) are given in Table F3.

Table F3. Constants for Mixed Swift-Voce Plastic Hardening of T304 Stainless Steel in DOT-113 Surrogate Inner Tank

Swift Hardening Law			**Voce Hardening Law**			**Weighting Factor**
A	ε_0	n	k_0	Q	β	α
ksi	-	-	*ksi*	*ksi*	-	-
212.19	0.089981	0.56389	55.261	155.71	1.9625	0.3

Because the final thickness measurements were not taken from the T304 DB tensile coupons before they were discarded, the B-W quick calibration approach could not be directly used. The B-W damage initiation envelope from the T304 inner tank in the post-test FE model of a previous DOT-113 test in 2019 was used [3]. This damage initiation envelope resulted in a reasonable damage initiation point for the T304 DB coupon models from the DOT-113 surrogate. The constants for the B-W damage envelope are given in Table F4, and the resulting B-W envelopes are plotted in Figure F8.

Table F4. B-W Damage Initiation Envelope Constants for T304 Stainless Steel in DOT-113 Surrogate Inner Tank

a	*b*	x_0
0.70565	0.98480	0.36349

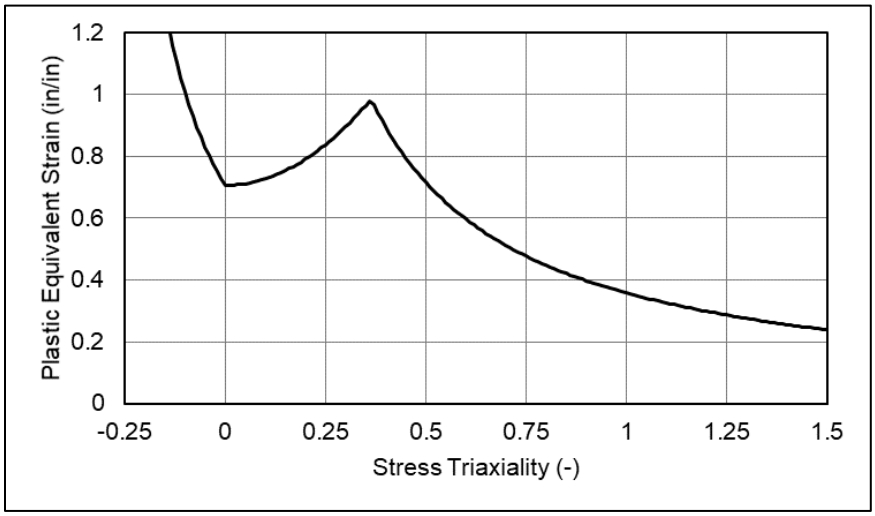

Figure F8. B-W Damage Initiation Envelope for T304 Stainless Steel in DOT-113 Surrogate Inner Tank

Figure F9 shows the resulting nominal stress-strain responses from the T304 DB FE model. A displacement-based exponential damage progression was selected at 0.005 in/in^2 with an exponent of -1 because it gave a reasonable nominal stress-strain slope after damage initiation. Qualitatively, the nominal stress-strain response from the FE model matches the overall shape of the T304 DB tensile coupon response below. A comparison of the FE model response with the average tensile properties was shown in Figure 41.

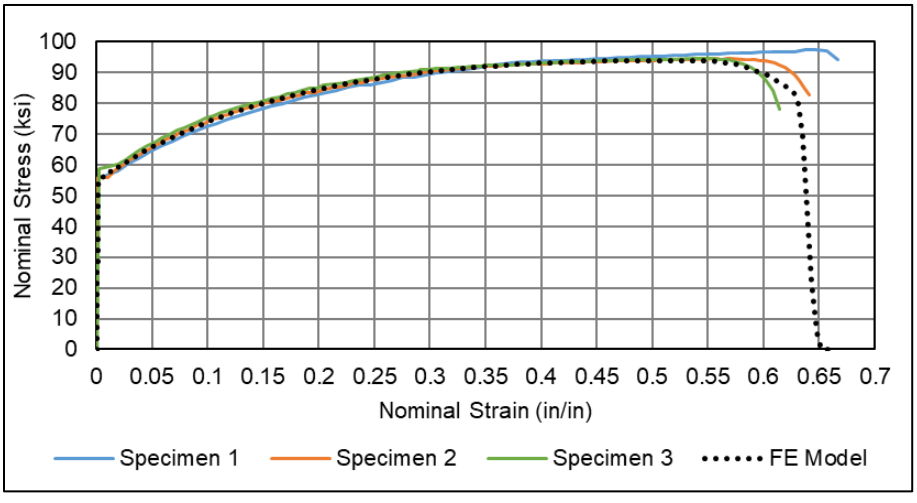

Figure F9. Nominal Stress-Strain DB Tensile Coupon FE Response for T304 Stainless Steel in DOT-113 Surrogate Inner Tank with Tensile Coupons Shown for Comparison

Appendix G.
Parametric Analyses on Tank Length and Structural Supports

The 2019 test (Test 10) of a DOT-113 tank car in this series used a retired DOT-113C120W tank car as an example of a tank car built to the existing specification [3]. The test described in this report sought to investigate the effects of a thicker outer tank made of TC-128B carbon steel on the puncture resistance of a DOT-113 tank car. As such a tank car did not exist, a purpose-built test article needed to be designed and constructed. This test article would be a simplified representation of a DOT-113 tank car that had the essential features of a DOT-113 tank car, but it was not required to have railcar-specific features such as couplers, brake rigging, or the full complement of piping necessary for service in cryogenic conditions.

Between Test 10 and Test 11, a series of simplified FE models were developed and executed to examine the effects of various simplifications to the baseline DOT-113 tank car that were under consideration for constructing the DOT-113 surrogate. These FE models examined the effects of 1) excluding certain structural features from the DOT-113 surrogate and 2) reducing the overall length of the DOT-113 surrogate compared to the baseline DOT-113 tank car.

The DOT-113 tank car used in Test 10 is shown in Figure G1. The tank car was described in Test 10's report as:

> *The inner tank was made of American Society for Testing and Materials (ASTM) A240 T304 stainless steel having a minimum thickness of 0.25 inches on its shell, and 3/8 inches for the heads. The outer tank was made of ASTM A516-70 carbon steel having a minimum thickness of 7/16 inches on the shell, and 1/2 inches on the heads. The inner tank had a nominal capacity of 32,900 gallons of water. The two tanks were separated by a 6-inch gap. This gap was filled with evacuated perlite and was capable of holding a vacuum. Additionally, this gap contained piping and structural members. The tank car had an overall length over strikers of approximately 76 feet. The car was equipped with a pressure relief valve (PRV) having a start-to-discharge pressure (STDP) of 75 psig. The PRV, as well as other loading and unloading valves, were contained in two cabinets at the two ends of the car, inboard of each bolster [3].*

Figure G1. DOT-113 Tank Car Used in Test 10

The DOT-113 surrogate planned for use in Test 11 was intended to include the essential design features that affected the puncture response of the inner and outer tanks but was simplified

compared to a complete DOT-113 tank car. The simplifications were intended to reduce the cost and complexity of fabricating a test article and represent current design practice for DOT-113 tank cars. The outer tank's material (TC-128B carbon steel) and thickness (9/16 inch) were deliberately chosen to be different from the Test 10 DOT-113 tank car to assess the effects of these changes. Table G1 contains a summary of the parameters for the Test 11 surrogate that 1) were similar to or the same as the corresponding parameters in Test 10, 2) that were intentionally different from Test 10, 3) that required further consideration.

Table G1. Comparison of Desired Parameters in Test 11 Surrogate to Test 10 DOT-113

Parameter	Target for Test 11	Relation to Parameter in Test 10
Outer Tank Material	TC-128B carbon steel	Intentionally Different
Outer Tank Thickness	9/16 inches	Intentionally Different
Outer Tank Diameter	Similar to Test 10	Similar
Inner Tank Material	T304 stainless steel	Same
Inner Tank Thickness	0.25 inches	Same
Inner Tank Diameter	Similar to Test 10	Similar
PRV STD Pressure	75 psig	Same
Lading in Test	Water	Same
Annular Space	6 inches	Same
Overall Length	TBD	~70 feet (outer tank, head seam to head seam)
Vacuum	TBD	Vacuum used in Test 10
Insulation	TBD, Representative of modern practice	Perlite used in Test 10
Stiffening Rings	TBD	Rings necessary in Test 10 for Vacuum
Piping	TBD	Complete piping for cryogenic service in Test 10
Piping Cabinets	TBD	Piping cabinets on both ends of car in Test 10
Tank Support	TBD	Tank support in Test 10 car compatible with cryogenic service

A series of non-puncture FE models were used to examine the parameters that were identified as "TBD" in Table G1. In the case of overall length, a separate parametric study looked at the effect of reducing the length of the tank car surrogate. These models used the Test 10 FE model as a starting point. The Test 10 FE model is described in detail in the Test 10 report. Non-puncture

models were used as these models have a much shorter runtime than puncture-capable models, and several iterations were planned for this investigation. Further, a non-puncture and a puncture-capable FE model should each be capable of capturing the same initial impact response, up to the onset of puncture. The primary result examined from each FE model was the force-displacement response because that is a global measurement of the overall tank car surrogate's stiffness.

The overall approach started with a non-puncture FE model having the same level of detail as in the Test 10 puncture-capable FE model but a simplified mesh and material properties. The FE model was set up to run at the test conditions of 50 psig and a 16.7 mph impact speed. Based on the results of Test 10, the puncture of the outer tank occurred at approximately 30 inches of indentation travel and a time of approximately 0.125 seconds. Therefore, the non-puncture FE model would theoretically be in agreement with the Test 10 force-time or force-displacement measurements up to that point. Note that this simplified FE model based on the Test 10 puncture-capable model was developed prior to the final post-test 10 FE model. Thus, this FE model should not be considered a validated model as several changes were subsequently made to the Test 10 post-test FE model as described in the Test 10 report [3].

Two parallel studies were performed. In the first study, each of the structural details (e.g., insulation, stiffening rings, etc.) would be removed from the FE model, and the model would be re-run to assess the influence of that detail on the overall stiffness of the model. In the second study, the tank length would be reduced, the model run, and the effect of reducing the tank's length would be assessed.

G1. Structural Detail Models

The structural details included in each non-puncture FE model are summarized in Table G2. To simplify discussion in this appendix, the models will be referred to as "Structural Detail Model #," where # corresponds to the model number listed in this table.

Table G2. Structural Detail Models for DOT-113 Surrogate

Model #	Cabinets	Piping	Tank Support	Insulation	Stiffening Rings	Vacuum
1	Yes	Yes	Yes	Yes	Yes	Yes
2	No	Yes	Yes	Yes	Yes	Yes
3	No	No	Yes	Yes	Yes	Yes
4	No	No	No	Yes	Yes	Yes
5	No	No	No	No	Yes	Yes
6	No	No	No	No	No	Yes
7	No	No	No	No	No	No

Figure G2 contains the force- and energy-displacement responses from Structural Detail Model 1 compared to Test 10. Structural Detail Model 1 included the same level of detail as the puncture-capable Test 10 model. This model was run to establish a baseline level of agreement between the non-puncture Test 10 model as well as the test data against which each change in structural

detail could be compared. As seen in this figure, the force-displacement response is in a high level of agreement up to the first peak in the test data just prior to puncture of the outer tank.

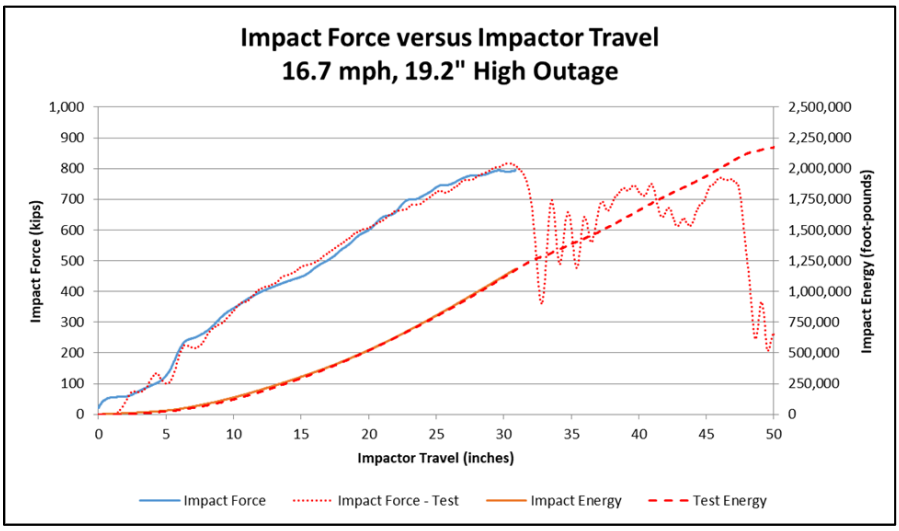

Figure G2. Structural Detail Model 1 Force-displacement and Energy-displacement Responses Compared to Test 10

Figure G3 contains the force- and energy-displacement responses from Structural Detail Model 2 compared to Test 10. Structural Detail Model 2 did not include the piping cabinets at each end. As seen in this figure, the force-displacement response underestimates the measured force at higher displacements, but it is still in relatively close agreement to the test measurements in the initial stages of response.

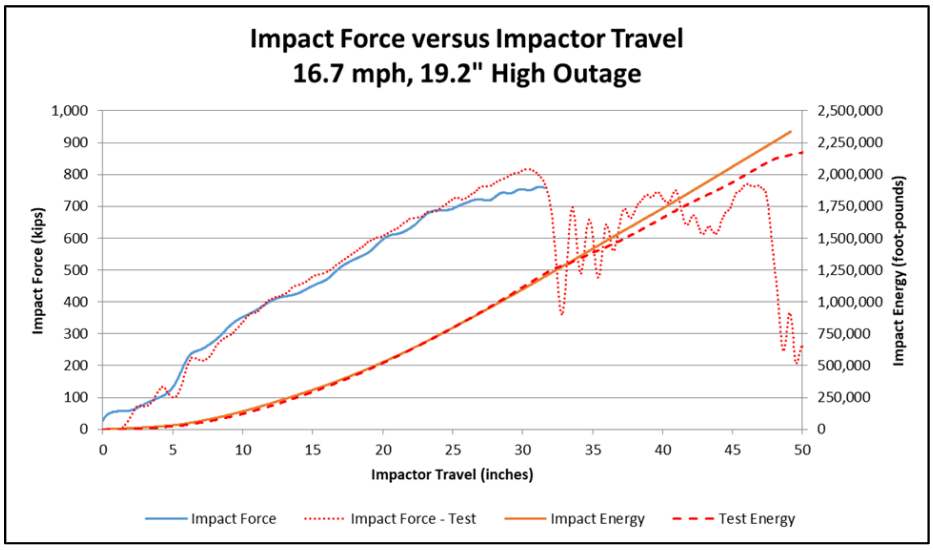

Figure G3. Structural Detail Model 2 Force-displacement and Energy-displacement Responses Compared to Test 10

Figure G4 contains the force- and energy-displacement responses from Structural Detail Model 3 compared to Test 10. Structural Detail Model 3 did not include the piping cabinets at each end of the tank or any piping. As seen in this figure, the force-displacement response underestimates the

measured force starting at approximately 17 inches, but it is still in relatively close agreement to the test measurements in the initial stages of response.

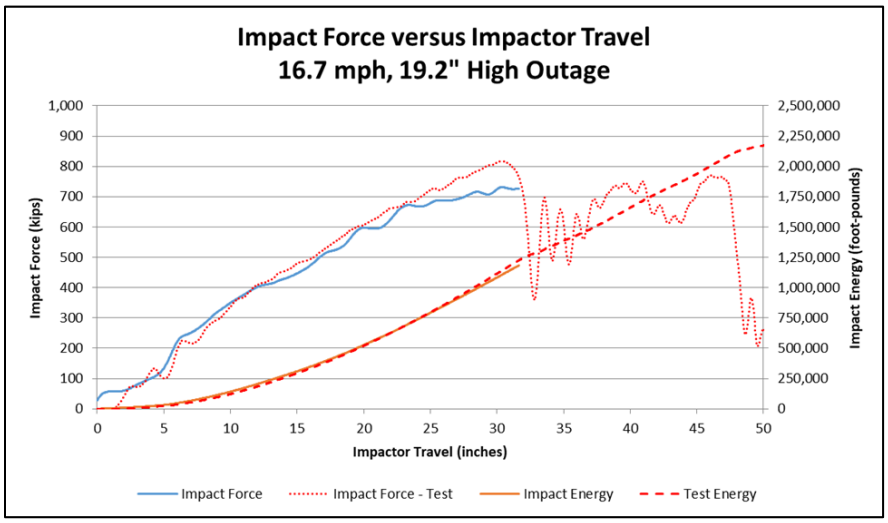

Figure G4. Structural Detail Model 3 Force-displacement and Energy-displacement Responses Compared to Test 10

Figure G5 contains the force- and energy-displacement responses from Structural Detail Model 4 compared to Test 10. Structural Detail Model 4 did not include the piping cabinets at each end of the tank, any piping, or the structural supports for the inner tank. As seen in this figure, the force-displacement response underestimates the measured force starting at approximately 17 inches, but it is still in relatively close agreement to the test measurements in the initial stages of response. Following this departure, the slope is lower than what is seen in previous models.

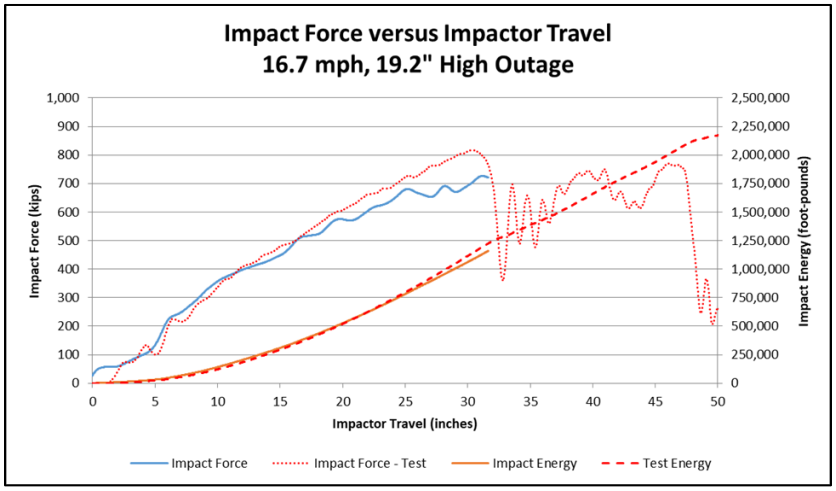

Figure G5. Structural Detail Model 4 Force-displacement and Energy-displacement Responses Compared to Test 10

Figure G6 contains the force- and energy-displacement responses from Structural Detail Model 5 compared to Test 10. Structural Detail Model 5 did not include the piping cabinets at each end of the tank, any piping, the structural supports for the inner tank, or any insulation. As seen in this figure, the force-displacement response underestimates the measured force starting much earlier than in the previous models. This observation is consistent with the Test 10 puncture models that

suggested the perlite insulation made a substantial structural contribution to the DOT-113 tank car's impact response.

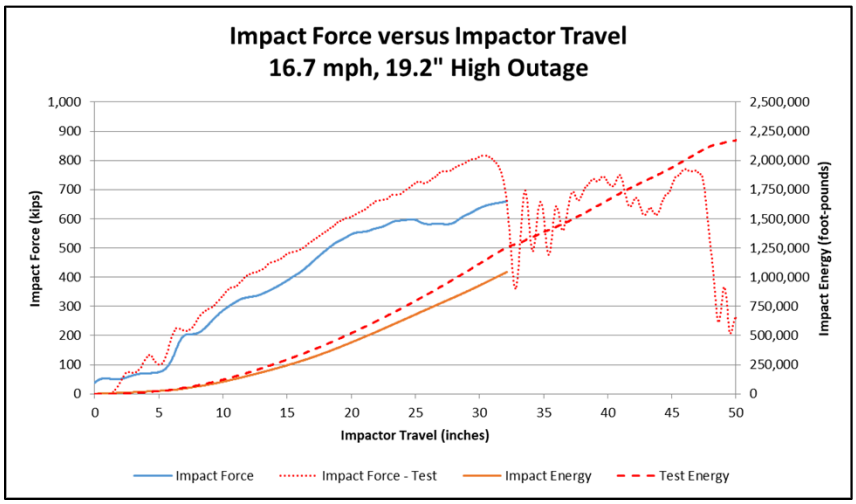

Figure G6. Structural Detail Model 5 Force-displacement and Energy-displacement Responses Compared to Test 10

Figure G7 contains the force- and energy-displacement responses from Structural Detail Model 6 compared to Test 10. Structural Detail Model 6 did not include the piping cabinets at each end of the tank, any piping, the structural supports for the inner tank, insulation, or the outer tank's stiffening rings. As seen in this figure, the force-displacement response underestimates the measured force from nearly the beginning of the simulation.

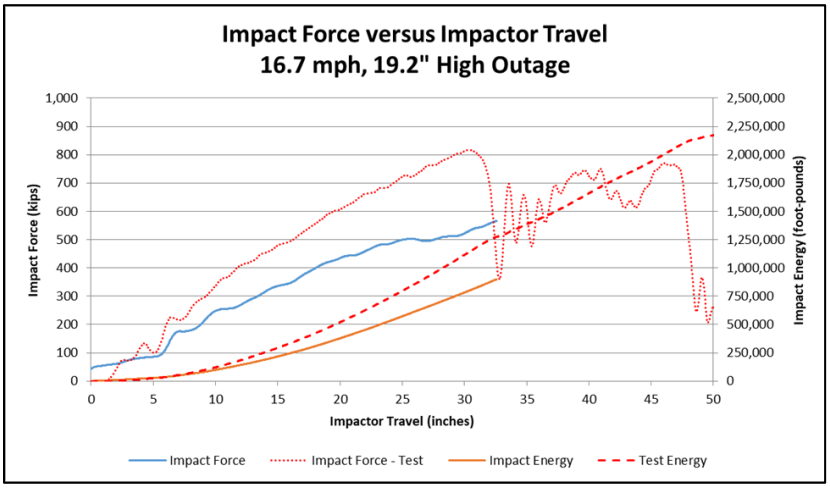

Figure G7. Structural Detail Model 6 Force-displacement and Energy-displacement Responses Compared to Test 10

Figure G8 contains the force- and energy-displacement responses from Structural Detail Model 7 compared to Test 10. Structural Detail Model 7 did not include the piping cabinets at each end of the tank, any piping, the structural supports for the inner tank, insulation, the outer tank's stiffening rings, or a vacuum in the annular space. As seen in this figure, the force-displacement response underestimates the measured force from nearly the beginning of the simulation. However, the force-displacement response for this model is stiffer than the Structural Detail

Model 6. Structural Detail Model 6 featured a simulated vacuum between the inner and outer tank, but Structural Detail Model 7 did not.

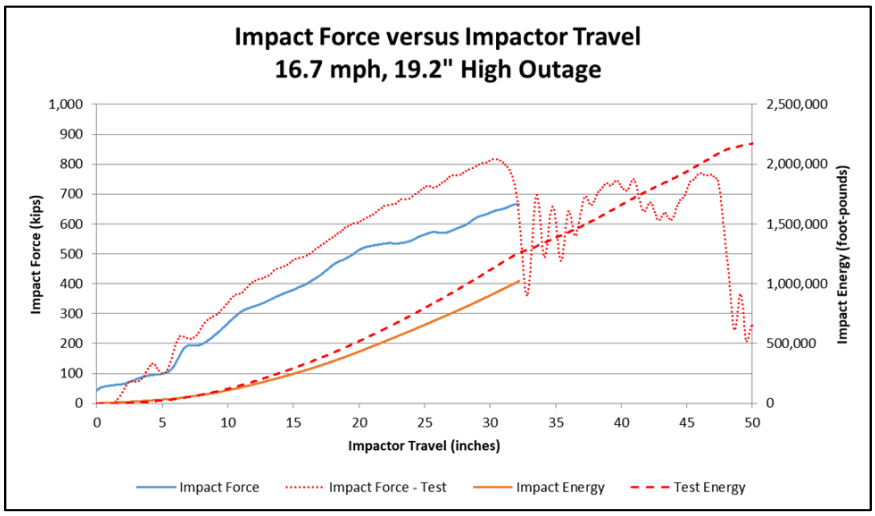

Figure G8. Structural Detail Model 7 Force-displacement and Energy-displacement Responses Compared to Test 10

Table G3 contains a summary of the peak force, displacement at peak force, and average slope from the Test 10 measurements and from each structural detail model. This table also contains a percentage difference calculation for each FE result. The percentage difference calculation is calculated as the FE result minus the test result divided by the test result.

Table G3. Peak Force, Displacement at Peak Force, and Average Slope for Structural Detail Models

	Test 10 Result							
Structural Detail Model #		**1**	**2**	**3**	**4**	**5**	**6**	**7**
Peak Force (kips)	**817**	794	761	731	726	661	565	667
Percent Difference	**-**	*-2.8*	*-6.9*	*-10.5*	*-11.1*	*-19.1*	*-30.8*	*-18.4*
Displacement at Peak Force (inches)	**30.4**	30.9	31.2	30.4	31.2	32.2	32.5	32
Percent Difference	**-**	*-1.7*	*2.7*	*0*	*2.7*	*5.9*	*7.2*	*5.5*
Average Slope to Peak Force (kips/in)	**26.9**	25.7	24.4	24.1	23.3	20.6	17.3	20.8
Percent Difference	**-**	*-4.4*	*-9.3*	*-10.5*	*-13.4*	*-23.6*	*-35.5*	*-22.6*

In summary, the absence or presence of a vacuum, the presence of stiffening rings, and the use of perlite insulation had significant effects on the force-displacement responses over the full range of simulated impact time. The exclusion of piping, piping cabinets, and the structural supports

for the tank had a slight effect on the initial stiffness but a more significant effect on surrogate stiffness as the indentation increased during the impact. Removing each structural feature examined in this study, with the exception of the vacuum, softened the force-displacement response. Removing the vacuum (i.e., allowing the annular space to remain at atmospheric pressure) increased the stiffness of the force-displacement response.

G2. Tank Length Models

The second parameter examined was the overall length of the DOT-113 surrogate. The DOT-113 tank car used in Test 10 was a long railcar with the cylindrical portion of the outer tank measuring roughly 70-feet from head weld to head weld. The tank car's length required it to be offset by 11 feet during the test to avoid fouling an adjacent right-of-way [3]. A shorter tank car was desired for the DOT-113 surrogate because that would simplify construction and allow the use of an existing DOT-117 tank as the surrogate's outer tank. A series of FE models of different lengths were run for surrogates to assess whether reducing the length of the surrogate would have a significant effect on its overall stiffness. The tank length FE models were a highly simplified representation of the DOT-113 surrogate. These FE models used a symmetry plane to reduce runtime. The FE model included the outer tank, insulation, vacuum, and inner tank. No stiffening rings, cabinet, piping, or structural supports were included in the FE models. The FE model was not capable of modeling puncture to either tank. Starting from the full-length DOT-113 tank car, the length of the tank was reduced, and the model was re-run using the same impact speed, outage volume, and initial pressure as Test 10.

The force-displacement responses of the reduced-length surrogates are plotted for each examined tank length in Figure G9. The distances listed in the legend of this figure indicate the approximate distance between the head-to-shell attachment sections of the outer tank. The model's length was varied by reducing the length of the shell, allowing the details outside the head-shell attachment section to remain the same in each model. This figure demonstrates that while the level of detail chosen for this model produces a force-displacement response that is soft compared to the Test 10 measurement, the length of the tank's shell does not have a substantial effect on the overall force-displacement responses. At the extreme short length of 28 feet, there is a slightly higher variation in force level at approximately 27 inches and a climb beginning at roughly 40 inches not seen in the other tank lengths. The model identified as "Baseline" in Figure G9 measured approximately 70 feet long for the cylindrical portion—head weld to head weld—of the outer tank. The numbers in the legend below also represent the length of the cylindrical portion of the tank car models analyzed.

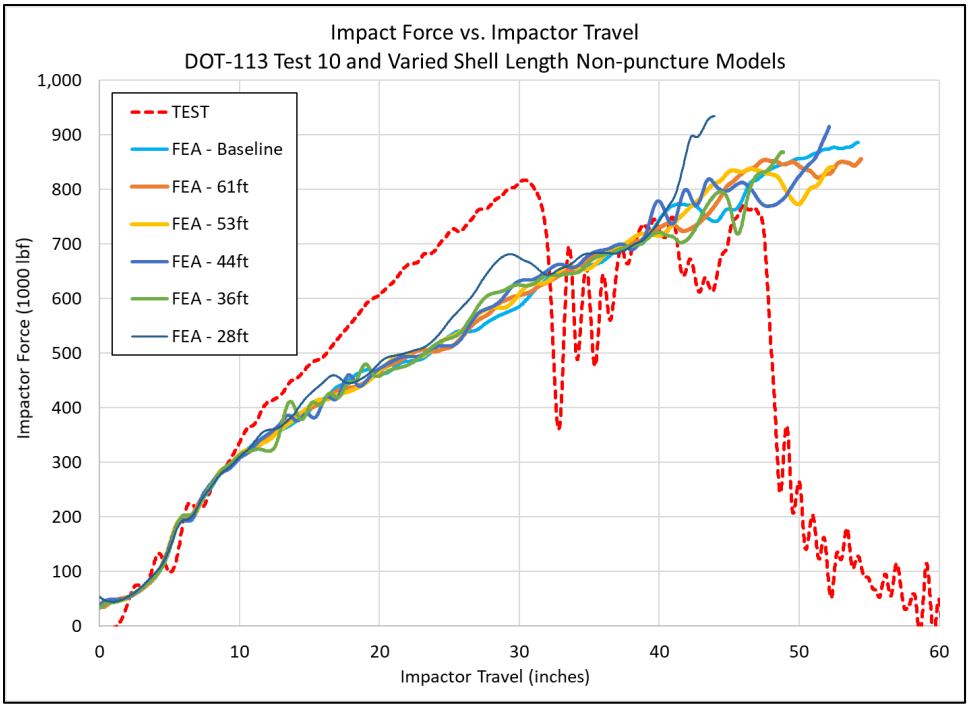

Figure G9. Various Tank Length Force-displacement and Energy-displacement Responses Compared to Test 10

G3. Conclusions

The DOT-113 surrogate for Test 11 was designed to include a stiffening ring at approximately the same distance from the point of impact as the nearest stiffening ring from the Test 10 DOT-113 tank car. The DOT-113 surrogate was designed with a length of approximately 40 feet between the head-to-shell attachments at the two ends of the outer tank. The surrogate design included tank-to-tank attachments at the heads of the tank and featured holes in the outer tank to allow the annular space to remain at atmospheric pressure. While using perlite insulation in the DOT-113 surrogate was also expected to increase its stiffness, discussions with manufacturers of DOT-113 tank cars revealed that modern designs were insulated with multi-layer insulation (MLI). While MLI was not expected to have a substantial effect on the structural response of a DOT-113 tank car, it was included in the impact zone to assess this assumption. The DOT-113 surrogate did not include piping cabinets, but it did include the piping necessary to fill, pressurize, and drain the tank car of water. Note that this piping was more limited than the piping that would be installed on a DOT-113 tank car intended for cryogenic service.

Abbreviations and Acronyms

ACRONYMS	EXPLANATION
ASTM	American Society for Testing and Materials
AAR	Association of American Railroads
B-W	Bao-Wierzbicki
CFC	Channel Frequency Class
CVN	Charpy V-notch
CFR	Code of Federal Regulations
DOF	Degrees-of-freedom
DB	Dogbone
DUCTCRT	Ductile Criterion
EB-2in	Elongation at Break with a 2-inch Gage Length
FRA	Federal Railroad Administration
FEA	Finite Element Analysis
FE	Finite Element
HMR	Hazardous Materials Regulations
HAZ	Heat-affected Zone
Hz	Hertz
HD	High Definition
HS	High-speed
kip	Kilopound (1,000 lbf)
LIDAR	Light Detection and Ranging
LNG	Liquefied Natural Gas
LN2	Liquid Nitrogen
MW	Molecular Weight
MPC	Multi-point Constraint
MLI	Multi-layer Insulation
NPRM	Notice of Proposed Rulemaking
PHMSA	Pipeline and Hazardous Materials Safety Administration
PEEQ	Plastic Equivalent
PWHT	Post-Weld Heat Treated
PRV	Pressure Relief Valve

ACRONYMS	EXPLANATION
RA	Reduction in Area
SSC	Shell-to-solid Coupling
SPH	Smoothed Particle Hydrodynamics
SRB	Smooth Round Bar
SAE	Society of Automotive Engineers
SCFM	Standard Cubic Feet per Minute
STD	Start-to-discharge
TRIAX	Stress Triaxiality
TC	Transport Canada
TTC	Transportation Technology Center (the site)
TTCI	Transportation Technology Center, Inc. (the company)
UTS	Ultimate Tensile Strength
UPM	Uniform Pressure Method
DOT	U.S. Department of Transportation
GNIS	USGS Geographic Names Information System
R	Universal Gas Constant
Volpe	Volpe National Transportation Systems Center
YS	Yield Strength